

A Comparison of  
Multivariable Design Methodologies  
for a  
Two-Degree-of-Freedom Gyro  
Torque-Rebalance Loop

by

John Ransom Coffee

S.B. Massachusetts Institute of Technology  
(1986)

SUBMITTED TO THE DEPARTMENT OF AERONAUTICS AND  
ASTRONAUTICS IN PARTIAL FULFILLMENT OF THE  
REQUIREMENTS FOR THE DEGREE OF

MASTER OF SCIENCE

at the

MASSACHUSETTS INSTITUTE OF TECHNOLOGY  
May, 1988

© John R. Coffee 1988

The author hereby grants to M.I.T. and The Charles Stark Draper Laboratory, Inc. permission to reproduce and to distribute copies of this thesis document in whole or in part.

Signature of Author \_\_\_\_\_  
Department of Aeronautics and Astronautics  
1988

Certified by \_\_\_\_\_  
Professor Wallace E. Vander Velde  
Dr

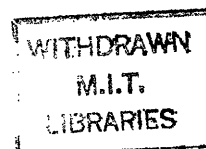
Certified by \_\_\_\_\_  
Dr. George T. Schmidt  
Dr

Accepted by \_\_\_\_\_  
Professor Harold Y. Wachman  
Chairman, Departmental Graduate Committee

MASSACHUSETTS INSTITUTE  
TECHNOLOGY

MAY 24 1988

Acro



**A Comparison of  
Multivariable Design Methodologies  
for a Two-Degree-of-Freedom Gyro  
Torque-Rebalance Loop**

by

John Ransom Coffee

Submitted to the Department of Aeronautics  
and Astronautics in partial fulfillment of the  
requirements for the degree of Master of Science

**ABSTRACT**

Multivariable design methodologies are compared in the context of controller design for the torque-rebalance loop for a strapdown two-degree-of-freedom dynamically tuned gyro described by complex coefficient differential equations. The methodologies considered are linear quadratic Gaussian with loop transfer recovery (LQG/LTR), formal loop shaping with LQG/LTR (FLS/LQG/LTR), frequency weighted LQG (FW/LQG), and classical lead compensation. The classical and multivariable methodologies are used to generate low bandwidth controller designs. The multivariable methodologies are also used to generate high bandwidth designs. The performance of the controllers are compared as well as the design methodologies themselves. The overall performance of the multivariable designs is much greater than that of the classical design, but compensators of approximately double the order are required. There is little performance difference between the multivariable designs. Of those examined, only the FW/LQG design methodology directly produces compensators that meet all of the typical torque-rebalance loop design requirements. LQG/LTR provides a simple design approach, with the design problem reduced to the selection of two scalar parameters. FLS/LQG/LTR has some promise in torque-rebalance loop design, but more expertise is needed in the selection of suitable target loops.

Thesis Supervisor: Wallace E. Vander Velde  
Title: Professor of Aeronautics and Astronautics

Technical Supervisor: George T. Schmidt, Sc.D.  
Title: Chief, Advanced Guidance Section,  
Advanced Systems Development Division,  
Air Force and Defensive Systems Department,  
The Charles Stark Draper Laboratory, Inc.

## Acknowledgement

Completion of this thesis marks the end of my career at M.I.T. I am grateful to my parents for making it possible for me to attend M.I.T. as an undergraduate.

I am especially indebted to my technical supervisor, Dr. George Schmidt of the Charles Stark Draper Laboratory, for sponsoring me as a Draper Fellow. His generous support, understanding and advice made this work possible.

I express deep gratitude to my thesis advisor, Professor Wallace VanderVelde, for taking on this thesis and providing it with direction and goals. His encouragement, assistance and concern extended far beyond the scope of this thesis and were greatly appreciated.

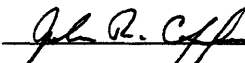
I also want to thank Professor Winston Markey for introducing me to control system design. Special thanks go to Professor Michael Athans for teaching me multivariable control and for taking the time to explain to me some of the subtleties of the LQG/LTR and FLS/LQG/LTR design methodologies.

I want to thank Tom Thorvaldsen and Mike Luniewicz for taking the time to answer my questions about the model of the gyroscope and design issues.

I extend sincere thanks to Dr. Frank Saggio and others at Smiths Industries, SLI Division, for sparking my interest in this design problem and for their interest in this work.

This work was performed at The Charles Stark Draper Laboratory under contract F04704-86-C-0160. Publication of this document does not constitute approval by The Charles Stark Draper Laboratory, Inc. or by the Air Force of the findings or conclusions contained herein. It is published for the exchange and stimulation of ideas.

I hereby assign my copyright of this thesis to The Charles Stark Draper Laboratory, Inc., Cambridge, Massachusetts.

  
\_\_\_\_\_  
John R. Coffee

Permission is hereby granted by The Charles Stark Draper Laboratory, Inc. to the Massachusetts Institute of Technology to reproduce any or all of this thesis.

# Table of Contents

<b>Abstract</b>	<b>2</b>
<b>Acknowledgement</b>	<b>3</b>
<b>Table of Contents</b>	<b>4</b>
<b>List of Figures</b>	<b>7</b>
<b>List of Tables</b>	<b>11</b>
<b>1 Introduction</b>	<b>13</b>
1.1 Overview . . . . .	13
1.2 Background . . . . .	14
1.2.1 Strapdown Gyro Operation . . . . .	14
1.2.2 Strapdown Torque-Rebalance Loop Operation . . . . .	15
1.2.3 The Complex Method . . . . .	17
1.3 Torque-Rebalance Loop Performance Requirements . . . . .	17
1.4 Thesis Goals and Design Approach . . . . .	19
<b>2 Gyro Model Description</b>	<b>20</b>
2.1 Gyro Equations of Motion . . . . .	20
2.1.1 Background . . . . .	20
2.1.2 The Tuning Condition . . . . .	21
2.1.3 Gyro Rotor Equations of Motion . . . . .	24
2.2 Torquer and Pickoff Models . . . . .	27
2.3 Linearized Equations of Motion . . . . .	28
2.4 Application of the Complex Method to the Gyro Model . . . . .	29
2.5 Summary . . . . .	30
<b>3 Properties of Block Symmetric Matrices and Systems</b>	<b>31</b>
3.1 Background . . . . .	31
3.2 Definition of Block Symmetric Systems and Complex Notation . . . . .	32
3.3 Properties of Block Symmetric Matrices . . . . .	34
3.3.1 Algebraic Properties . . . . .	34
3.3.2 Eigenvalues and Eigenvectors . . . . .	36
3.4 Properties of TITOBs Systems . . . . .	38

3.4.1	Transfer Function Description . . . . .	38
3.4.2	Transmission Zeros . . . . .	40
3.4.3	Bode Plots . . . . .	41
3.4.4	Complex SISO Nyquist Criterion . . . . .	46
3.4.5	Linear Quadratic Regulators . . . . .	49
3.5	Implementation of Block Symmetric Compensators . . . . .	50
3.6	Summary . . . . .	52
<b>4</b>	<b>Open Loop Gyro Characteristics</b>	<b>53</b>
4.1	Numerical Values . . . . .	53
4.2	Complex Modes . . . . .	55
4.3	Design Plant Model . . . . .	57
4.3.1	Integrator . . . . .	60
4.3.2	Demodulation Filter . . . . .	60
4.3.3	Spin Frequency Notch Filter . . . . .	61
4.4	Summary . . . . .	62
<b>5</b>	<b>Design Methodologies</b>	<b>63</b>
5.1	Background . . . . .	63
5.2	Overview of Methodologies and Design Approach . . . . .	64
5.3	Lead Compensation Design . . . . .	66
5.3.1	Description of Design Methodology . . . . .	66
5.3.2	Low Bandwidth Design . . . . .	66
5.3.3	Performance Limitations of First Order Lead Compensator Designs . . . . .	70
5.3.4	Summary . . . . .	72
5.4	LQG/LTR Design . . . . .	74
5.4.1	Description of Design Methodology . . . . .	74
5.4.2	Design Approach . . . . .	77
5.4.3	Linear Quadratic Target Loop Design . . . . .	77
5.4.4	Recovery of the LQ Target Loops . . . . .	84
5.4.5	Summary . . . . .	102
5.5	FW/LQG Design . . . . .	106
5.5.1	Description of Design Methodology . . . . .	106
5.5.2	Design Approach . . . . .	109
5.5.3	FW/LQ Loops . . . . .	114
5.5.4	Compensator Designs . . . . .	118
5.5.5	Summary . . . . .	125
5.6	FLS/LQG/LTR Design . . . . .	131
5.6.1	Description of Design Methodology . . . . .	131
5.6.2	Design Approach . . . . .	136
5.6.3	Linear Quadratic Target Loop . . . . .	137
5.6.4	Recovery of the LQ Target Loop . . . . .	139
5.6.5	Target Loops Based on Real Coefficient Gyro Dynamics . . . . .	144

5.6.6	Decoupling Compensators . . . . .	149
5.6.7	Summary . . . . .	159
5.7	Summary . . . . .	162
<b>6</b>	<b>Comparison of Design Methodologies and Conclusions</b>	<b>163</b>
6.1	Performance Comparisons . . . . .	163
6.1.1	Overview . . . . .	163
6.1.2	Low Bandwidth Designs . . . . .	165
6.1.3	High Bandwidth Designs . . . . .	167
6.1.4	Summary . . . . .	169
6.2	Design Procedures . . . . .	169
6.2.1	Classical Lead Compensation . . . . .	169
6.2.2	LQG/LTR . . . . .	170
6.2.3	FW/LQG . . . . .	171
6.2.4	FLS/LQG/LTR . . . . .	171
6.2.5	Summary . . . . .	172
6.3	Conclusions and Recommendations . . . . .	173
	<b>References</b>	<b>175</b>
	<b>A List of Symbols</b>	<b>177</b>
	<b>B Computer Software</b>	<b>182</b>
	<b>C Correlated Noise Kalman Filter Problem</b>	<b>183</b>
C.1	Correlated Noise Kalman Filter Derivation . . . . .	183
C.2	The CN/KF Model Based Compensator . . . . .	185
C.3	Summary of Duality . . . . .	187

# List of Figures

<b>1</b>	<b>Introduction</b>	<b>13</b>
1.1	Momentum Wheel Spinning in Inertial Space . . . . .	14
1.2	TDF-DTG Rotor and Suspension Schematic . . . . .	15
1.3	TDF-DTG Cross-Section . . . . .	16
1.4	Torque-Rebalance Loop Block Diagram . . . . .	16
<b>2</b>	<b>Gyro Model Description</b>	<b>20</b>
2.1	Suspension System Schematic Diagram . . . . .	21
2.2	Suspension System with the Shaft Deflected . . . . .	22
2.3	Orientation of C-frame and N-frame . . . . .	25
<b>3</b>	<b>Properties of Block Symmetric Matrices and Systems</b>	<b>31</b>
3.1	Stability Margins in the CCTF Bode Plot . . . . .	43
3.2	Example Feedback Loop . . . . .	44
3.3	CCTF Bode Plot of $G_c(s)$ . . . . .	45
3.4	CCTF Bode Plot of $-jG_c(s)$ . . . . .	45
3.5	Complex Unity Gain Feedback Loop . . . . .	46
3.6	Nyquist Contour . . . . .	47
3.7	Complex SISO Nyquist Plot of a TITOBS System . . . . .	48
<b>4</b>	<b>Open Loop Gyro Characteristics</b>	<b>53</b>
4.1	Bode Plot of the Gyro CCTF, $G_p(s)$ . . . . .	55
4.2	Real TITOBS System Quadrature Mode Time Response . . . . .	56
4.3	Complex System Quadrature Mode Time Response . . . . .	56
4.4	Real TITOBS System Nutation Mode Time Response . . . . .	58
4.5	Complex System Nutation Mode Time Response . . . . .	58
4.6	Torque-Rebalance Loop with Augmented Plant . . . . .	59
4.7	Design Plant Model Bode Plot . . . . .	59
4.8	Torque-Rebalance Loop with Augmented Compensator . . . . .	60
<b>5</b>	<b>Design Methodologies</b>	<b>63</b>
5.1	Design Feedback Loop . . . . .	64
5.2	Design Plant Model Augmented with Notch Filter Bode Plot . . . . .	68
5.3	Augmented Lead Compensator Bode Plot . . . . .	68
5.4	Lead Compensated System Open Loop Bode Plot . . . . .	69

5.5	Lead Compensated System Closed Loop Bode Plot . . . . .	69
5.6	Lead Compensated System Step Response . . . . .	71
5.7	Lead Compensated System Nyquist Plot . . . . .	72
5.8	Nyquist Nutation Circle for Increasing Crossover Frequency . . .	73
5.9	LQG/LTR Feedback Loop Block Diagram . . . . .	74
5.10	LQ Feedback Loop Block Diagram . . . . .	75
5.11	Block Diagram of $K_{MBC}(s)$ Modified With Notch Filter . . . . .	78
5.12	Low Bandwidth LQ Target Open Loop Bode Plot . . . . .	82
5.13	Low Bandwidth LQ Target Closed Loop Bode Plot . . . . .	82
5.14	High Bandwidth LQ Target Open Loop Bode Plot . . . . .	83
5.15	High Bandwidth LQ Target Closed Loop Bode Plot . . . . .	83
5.16	Zero Locus During Recovery of the Low Bandwidth Target . . .	85
5.17	Zero Locus During Recovery of the High Bandwidth Target . . .	85
5.18	Design LQG/LTR-1a Augmented Compensator Bode Plot . . . . .	87
5.19	Design LQG/LTR-1a Open Loop Bode Plot . . . . .	87
5.20	Design LQG/LTR-1a Closed Loop Bode Plot . . . . .	88
5.21	Design LQG/LTR-1a Step Response . . . . .	90
5.22	Design LQG/LTR-1a Nyquist Plot . . . . .	91
5.23	Design LQG/LTR-1b Augmented Compensator Bode Plot . . . . .	92
5.24	Design LQG/LTR-1b Open Loop Bode Plot . . . . .	92
5.25	Design LQG/LTR-1b Closed Loop Bode Plot . . . . .	93
5.26	Design LQG/LTR-1b Step Response . . . . .	94
5.27	Design LQG/LTR-1b Nyquist Plot . . . . .	95
5.28	Design LQG/LTR-2a Augmented Compensator Bode Plot . . . . .	96
5.29	Design LQG/LTR-2a Open Loop Bode Plot . . . . .	96
5.30	Design LQG/LTR-2a Closed Loop Bode Plot . . . . .	97
5.31	Design LQG/LTR-2a Step Response . . . . .	98
5.32	Design LQG/LTR-2a Nyquist Plot . . . . .	99
5.33	Design LQG/LTR-2b Augmented Compensator Bode Plot . . . . .	100
5.34	Design LQG/LTR-2b Open Loop Bode Plot . . . . .	100
5.35	Design LQG/LTR-2b Closed Loop Bode Plot . . . . .	101
5.36	Design LQG/LTR-2b Step Response . . . . .	103
5.37	Design LQG/LTR-2b Nyquist Plot . . . . .	104
5.38	Frequency Weighted LQ Loop Block Diagram . . . . .	108
5.39	Complete FW/LQG Feedback Loop Block Diagram . . . . .	109
5.40	Control Weighting Function Bode Plot . . . . .	111
5.41	Closed Loop LQ Bode Plot: Constant State Weighting . . . . .	112
5.42	Step Response: Constant State Weighting . . . . .	112
5.43	Resonant State Weighting Bode Plot . . . . .	114
5.44	Closed Loop LQ Bode Plot: Resonant State Weighting . . . . .	115
5.45	Step Response: Resonant State Weighting . . . . .	115
5.46	Low Bandwidth State Weighting Function Bode Plot . . . . .	116
5.47	Low Bandwidth LQ Design Open Loop Bode Plot . . . . .	117



5.48	Low Bandwidth LQ Design Closed Loop Bode Plot . . . . .	117
5.49	High Bandwidth State Weighting Function Bode Plot . . . . .	118
5.50	High Bandwidth LQ Design Open Loop Bode Plot . . . . .	119
5.51	High Bandwidth LQ Design Closed Loop Bode Plot . . . . .	120
5.52	Design FW/LQG-1 Augmented Compensator Bode Plot . . . . .	121
5.53	Design FW/LQG-1 Open Loop Bode Plot . . . . .	122
5.54	Design FW/LQG-1 Closed Loop Bode Plot . . . . .	122
5.55	Design FW/LQG-1 Step Response . . . . .	123
5.56	Design FW/LQG-1 Nyquist Plot . . . . .	124
5.57	Design FW/LQG-2 Augmented Compensator Bode Plot . . . . .	125
5.58	Design FW/LQG-2 Open Loop Bode Plot . . . . .	126
5.59	Design FW/LQG-2 Closed Loop Bode Plot . . . . .	127
5.60	Design FW/LQG-2 Step Response . . . . .	128
5.61	Design FW/LQG-2 Nyquist Plot . . . . .	129
5.62	Incorporation of the Target Loop Shape at the Plant Input . . .	132
5.63	FLS/LQG/LTR Feedback Loop Block Diagram . . . . .	133
5.64	FLS/LQG/LTR Stochastic Model . . . . .	134
5.65	Poles of $G_w(s)$ and $W(s)$ for Design FLS-0 . . . . .	138
5.66	Design FLS-0 LQ Target Open Loop Bode Plot . . . . .	140
5.67	Design FLS-0 LQ Target Closed Loop Bode Plot . . . . .	140
5.68	Design FLS-0 Augmented Compensator Bode Plot . . . . .	141
5.69	Design FLS-0 Open Loop Bode Plot . . . . .	142
5.70	Design FLS-0 Closed Loop Bode Plot . . . . .	142
5.71	Design FLS-0 Step Response to $t = 0.1 \text{ sec}$ . . . . .	145
5.72	Design FLS-0 Step Response to $t = 40 \text{ sec}$ . . . . .	145
5.73	Design FLS-0 Nyquist Plot . . . . .	146
5.74	Poles of $G_w(s)$ and $W(s)$ for Designs FLS-1 and FLS-2 . . . . .	147
5.75	Low Bandwidth Target Open Loop Bode Plot . . . . .	148
5.76	Low Bandwidth Target Closed Loop Bode Plot . . . . .	148
5.77	High Bandwidth Target Open Loop Bode Plot . . . . .	150
5.78	High Bandwidth Target Closed Loop Bode Plot . . . . .	150
5.79	Design FLS-1 Augmented Compensator Bode Plot . . . . .	151
5.80	Design FLS-1 Open Loop Bode Plot . . . . .	152
5.81	Design FLS-1 Closed Loop Bode Plot . . . . .	152
5.82	Design FLS-1 Step Response . . . . .	154
5.83	Design FLS-1 Nyquist Plot . . . . .	155
5.84	Design FLS-2 Augmented Compensator Bode Plot . . . . .	156
5.85	Design FLS-2 Open Loop Bode Plot . . . . .	157
5.86	Design FLS-2 Closed Loop Bode Plot . . . . .	157
5.87	Design FLS-2 Step Response . . . . .	159
5.88	Design FLS-2 Nyquist Plot . . . . .	160

<b>C</b>	<b>Correlated Noise Kalman Filter Problem</b>	<b>183</b>
C.1	CN/KF Feedback Loop Block Diagram . . . . .	186

# List of Tables

<b>4</b>	<b>Open Loop Gyro Characteristics</b>	<b>53</b>
4.1	Gyro Model Numerical Values . . . . .	54
<b>5</b>	<b>Design Methodologies</b>	<b>63</b>
5.1	Lead Compensator Poles and Zeros . . . . .	67
5.2	Lead Compensated System Closed Loop Poles . . . . .	70
5.3	First Order Lead Compensation Design Parameters . . . . .	73
5.4	Low Bandwidth LQ Target Closed Loop Poles and Zeros . . . . .	81
5.5	High Bandwidth LQ Target Closed Loop Poles and Zeros . . . . .	81
5.6	Design LQG/LTR-1a Compensator Poles and Zeros . . . . .	88
5.7	Design LQG/LTR-1a Closed Loop Poles . . . . .	89
5.8	Design LQG/LTR-1b Compensator Poles and Zeros . . . . .	90
5.9	Design LQG/LTR-1b Closed Loop Poles . . . . .	91
5.10	Design LQG/LTR-2a Compensator Poles and Zeros . . . . .	95
5.11	Design LQG/LTR-2a Closed Loop Poles . . . . .	97
5.12	Design LQG/LTR-2b Compensator Poles and Zeros . . . . .	101
5.13	Design LQG/LTR-2b Closed Loop Poles . . . . .	102
5.14	LQG/LTR Compensator Design Parameters . . . . .	105
5.15	Low Bandwidth Design LQ Closed Loop Poles and Zeros . . . . .	116
5.16	High Bandwidth Design LQ Closed Loop Poles and Zeros . . . . .	119
5.17	Design FW/LQG-1 Compensator Poles and Zeros . . . . .	121
5.18	Design FW/LQG-1 Closed Loop Poles . . . . .	123
5.19	Design FW/LQG-2 Compensator Poles and Zeros . . . . .	126
5.20	Design FW/LQG-2 Closed Loop Poles . . . . .	127
5.21	FW/LQG Compensator Design Parameters . . . . .	130
5.22	Design FLS-0 LQ Target Closed Loop Poles and Zeros . . . . .	139
5.23	Design FLS-0 Compensator Poles and Zeros . . . . .	143
5.24	Design FLS-0 Closed Loop Poles . . . . .	143
5.25	Low Bandwidth Target Closed Loop Poles and Zeros . . . . .	149
5.26	High Bandwidth Target Closed Loop Poles and Zeros . . . . .	149
5.27	Design FLS-1 Compensator Poles and Zeros . . . . .	153
5.28	Design FLS-1 Closed Loop Poles . . . . .	153
5.29	Design FLS-2 Compensator Poles and Zeros . . . . .	158
5.30	Design FLS-2 Closed Loop Poles . . . . .	158
5.31	FLS/LQG/LTR Compensator Design Parameters . . . . .	161

<b>6</b>	<b>Comparison of Design Methodologies and Conclusions</b>	<b>163</b>
6.1	Low (50 <i>Hz</i> ) Bandwidth Compensator Design Parameters . . . .	164
6.2	High (100 <i>Hz</i> ) Bandwidth Compensator Design Parameters . . .	165
<b>C</b>	<b>Correlated Noise Kalman Filter Problem</b>	<b>183</b>
C.1	Duality Between the FW/LQ and the CN/KF Problems . . . . .	187

# Chapter 1

## Introduction

### 1.1 Overview

This thesis presents a comparison of some multivariable design methodologies. The comparison is based on the specific example of a strapdown, two-degree-of-freedom dynamically tuned gyro torque-rebalance loop. The gyro model is expressed in terms of complex coefficient differential equations, and the controllers are designed for this complex plant description. The performance of several torque-rebalance loops designed using modern, multivariable design methodologies and by classical techniques is compared.

The thesis is organized as follows. The remainder of this chapter provides background on the two-degree-of-freedom dynamically tuned gyro, the operation of the torque-rebalance loop, and the complex method. It also describes the thesis goals and overall approach to the design problem. The gyro equations of motion are derived in Chapter 2. The complex method is applied to the linearized equations of motion to yield the complex coefficient differential equations on which the controller designs are based. Several properties of systems described by complex coefficient differential equations are summarized in Chapter 3. The design tools presented are used in the subsequent chapters in the design and analysis of the torque-rebalance loop controllers. The open loop characteristics of the linear gyro model are analyzed in Chapter 4. The controller designs are presented in Chapter 5. Each design methodology is described, and the design approach used for each methodology is presented. The unique characteristics and performance of the resulting loop designs are also discussed. Finally, a comparison of the design methodologies and conclusions are included in Chapter 6.

## 1.2 Background

### 1.2.1 Strapdown Gyro Operation

Over the past twenty years, the two-degree-of-freedom dynamically tuned gyro (TDF-DTG) has gained widespread use in strapdown inertial navigation systems as an angular rate sensor. The TDF-DTG, like single-degree-of-freedom floated instruments, uses a momentum wheel to measure angular rates.

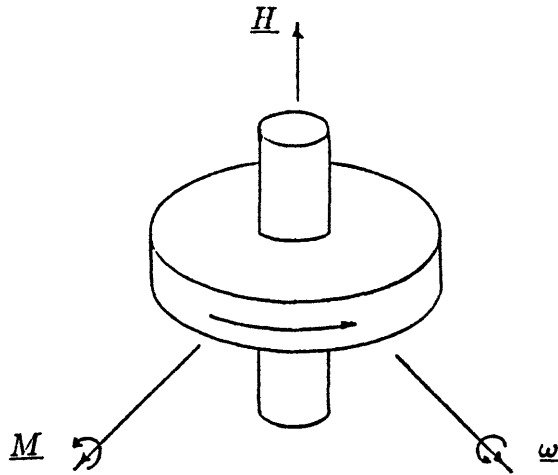


Figure 1.1: Momentum Wheel Spinning in Inertial Space

A schematic of a rotor spinning in inertial space is shown in Figure 1.1. The rotor spins with constant angular momentum,  $\underline{H}$ . The motion of the rotor is governed by the equation

$$\underline{M} = \frac{d^r}{dt} \underline{H} + \underline{\omega}_{ir}^r \times \underline{H} \quad (1.1)$$

where  $\underline{M}$  is a torque applied to the rotor and  $\underline{\omega}_{ir}^r$  is the precession of the rotor with respect to inertial space in rotor coordinates. The angular momentum in (1.1) is assumed to be constant so the derivative term is zero. If no torques are applied to the rotor, it will maintain its orientation in inertial space, conserving angular momentum. If a torque perpendicular to the spin axis is applied to the rotor, the rotor will precess at the rate  $\underline{\omega}$  about an axis perpendicular to the spin axis and the axis of the applied torque.

Figure 1.2 shows a schematic diagram of a TDF-DTG. The rotor is attached to a shaft through a suspension system made up of a gimbal and a set of flexures.

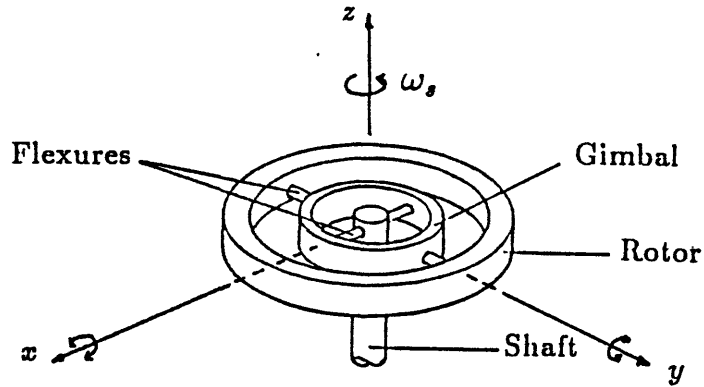


Figure 1.2: TDF-DTG Rotor and Suspension Schematic

The shaft is driven at a constant speed,  $\omega_s$ , by a motor which is attached to the gyro case (not shown). The flexures are stiff in bending but compliant in torsion, allowing the rotor, through the gimbal, to precess about the  $x$  and  $y$ -axes shown in the figure. This provides the instrument with the capability of sensing inertial angular rates on two axes simultaneously.

The torsional spring constants of the flexures, gimbal inertias, and rotor spin speed are chosen together such that the torque on the rotor due to the flexure spring rates cancels the torque due to the dynamically induced spring rate. The result is that the net average torque on the rotor due to the suspension system is zero, and the rotor behaves like a free body. This is known as the tuning condition and is described in Chapter 2.

A cross-section of a TDF-DTG is shown in Figure 1.3. The rotor is driven by the motor at the base of the gyro case. The angle between the rotor and the case is measured electromagnetically by two sets of variable inductance type pickoffs, one pair on each axis. A pair of torquer coils, fixed to the case, on each axis apply torques to the rotor electromagnetically as well. Current through the coils acts with the magnets fixed to the rotor to precess the rotor about the desired axis.

### 1.2.2 Strapdown Torque-Rebalance Loop Operation

A momentum wheel gyro employed in the strapdown mode makes use of the gyroscopic properties discussed above. A block diagram of a torque-rebalance loop is shown in Figure 1.4. In a strapdown application, the gyro case is bolted to the vehicle and is subjected to the inertial angular rates experienced by the

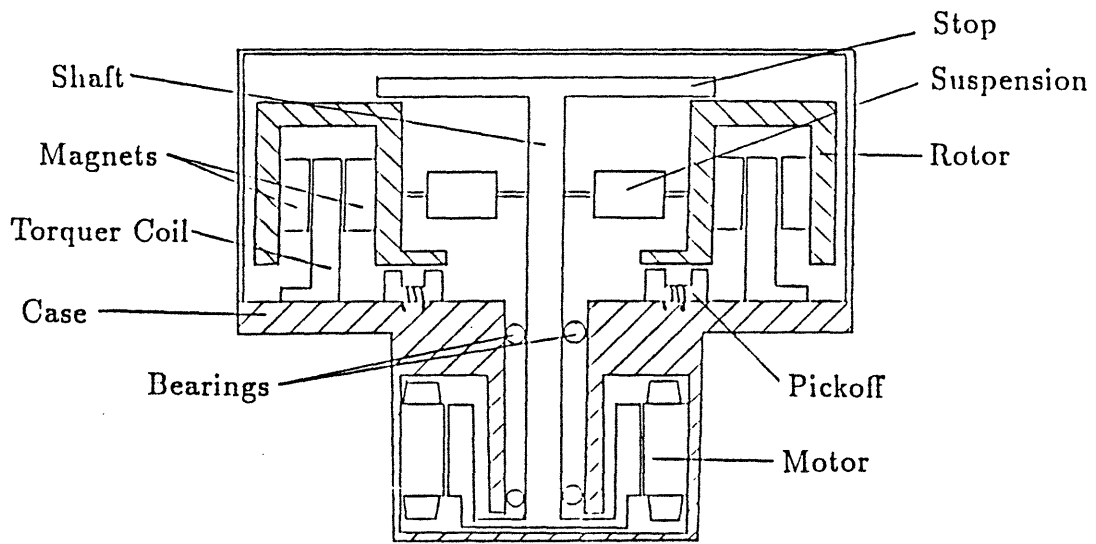


Figure 1.3: TDF-DTG Cross-Section

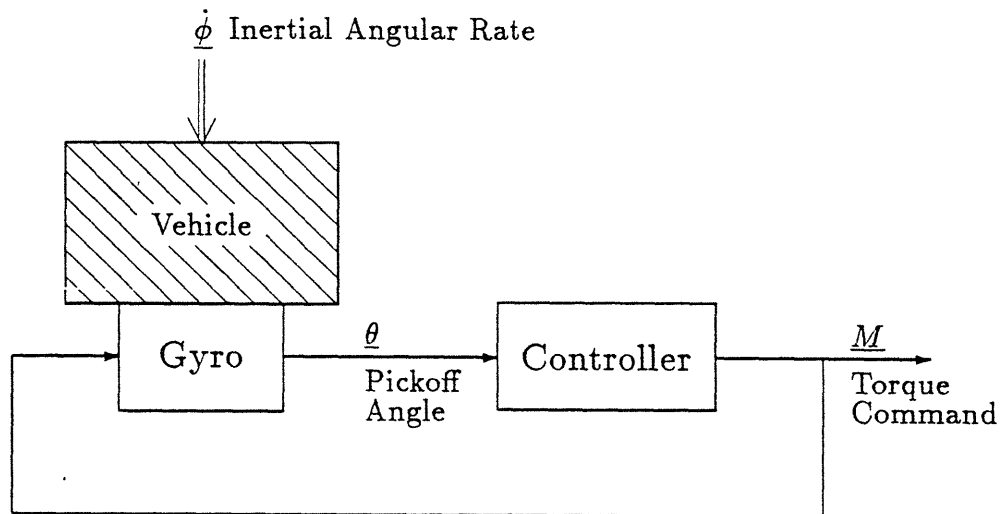


Figure 1.4: Torque-Rebalance Loop Block Diagram



vehicle. No torques are applied to the gyro rotor about its input axes by the suspension system so the rotor remains at a constant attitude with respect to inertial space. The resulting angular offset between the case and rotor,  $\theta$ , is measured by the pickoffs and is called the pickoff angle. This signal is fed to the controller which generates a commanded torque,  $\underline{M}$ , to be applied to the rotor in such away as to precess the rotor at a rate equal to the inertial angular rate applied to the gyro case, thus driving the pickoff angle back to null.

This commanded torque is also the output of the torque-rebalance loop used by the attitude update algorithm of the inertial navigation system as a measure of the inertial angular rate. This relationship can be seen in Equation (1.1) since the precession rate is equal to the inertial angular rate, and the angular momentum of the rotor is known. Thus, the torque-rebalance loop is used to keep the rotor spin axis perpendicular to the gyro input axes, keeping the pickoff angles nulled, and its output, the commanded torque, is used as a measurement of the inertial angular rates to which the gyro case is subjected.

### 1.2.3 The Complex Method

The complex method has been used to simplify the analysis of rotationally symmetric systems for quite some time. It was first applied to the analysis of a two-degree-of-freedom gyro two decades ago [13]. The primary advantage of the complex method is that it turns the two input-two output real gyro model into a single input-single output (SISO) system described by complex coefficient differential equations. This in turn allows classical SISO design tools to be used in the analysis of a nominally multi-input-multi-output (MIMO) system. The complex method is discussed in Chapter 3.

## 1.3 Torque-Rebalance Loop Performance Requirements

The torque-rebalance loop design requirements are typical of all regulator loops: good disturbance rejection, noise attenuation, and high bandwidth while maintaining sufficient stability margins. The requirements for the loop are driven by the specific dynamics of the gyro and the need for accurate inertial angular rate measurements for the inertial navigation system. The performance of the

inertial navigation system attitude algorithm depends directly on the frequency and time domain characteristics of the torque-rebalance loop. The torque command fed to the gyro must accurately reflect the angular rate environment of the vehicle so that the attitude algorithm has an accurate measurement of the inertial angular rates and so that accurate operation of the gyro can be ensured.

In order for the torque-rebalance loop to provide accurate measurements of inertial angular rates, the rotor spin axis must always be perpendicular to the gyro input axes, that is, the pickoff angles must always be nulled. Therefore, the controller must provide torque commands that will precess the gyro at the angular rates expected to be encountered by the vehicle with minimum error. In this context, the inertial angular rate applied to the gyro case can be thought of as a disturbance input that must be rejected by the regulator. This requires a high bandwidth loop with large velocity or acceleration error constants.

It is desirable for the torque command to be as free of noise as possible. Two major noise sources are vibration at the shaft spin frequency and high frequency noise due to pickoff signal modulation. Therefore, loop gain at the spin frequency must be as low as possible, effectively limiting the bandwidth of the loop to below the spin frequency. In addition, the high frequency roll off of the torque-rebalance loop gain must be as great as possible to attenuate noise at the pickoff signal modulation frequency.

The computational bandwidth of the attitude algorithm is taken to be half of the attitude update rate. The bandwidth of the torque-rebalance loop should be equal to the computational bandwidth so that the attitude algorithm will have angular rate information over its entire bandwidth. In addition, the loop gain within the bandwidth must be as near unity as possible. If the vehicle is subjected to coning motion within the torque-rebalance loop bandwidth and the closed loop gain at the coning frequency is not unity, the attitude algorithm will produce rectified attitude errors proportional to the square of the closed loop gain [4], which cannot be compensated with coning compensation algorithms.

The torque-rebalance loop design must also have sufficient stability margins so that the loop will remain stable in the presence of modelling errors, pickoff and torquer misalignments, and changes in operating conditions. The above design requirements are discussed in greater detail in Section 4.3.

## 1.4 Thesis Goals and Design Approach

Historically, classical design techniques have been used for the design of torque-rebalance loop controllers [15], [3], and [11]. Only recently have modern, multivariable design techniques been examined for use in this problem [16]. The goal of this thesis is to compare some multivariable design methodologies in the context of the torque-rebalance loop example. The methodologies considered are linear quadratic Gaussian with loop transfer recovery (LQG/LTR), formal loop shaping with LQG/LTR (FLS/LQG/LTR), frequency weighted LQG (FW/LQG), in addition to classical lead compensation. The design methodologies are described in Chapter 5.

As stated above, several torque-rebalance loop controllers are designed for a continuous time gyro model described by complex coefficient differential equations. A first order lead design, which has been typically used in classical loop designs, provides a low bandwidth baseline design. The multivariable methodologies are used to generate low bandwidth designs that are compared to the classical lead design. These methodologies can be used to generate much higher bandwidth designs; therefore, high bandwidth multivariable designs are also compared.

The performance of the controllers are compared as well as the design methodologies themselves. The results of these comparisons are summarized in Chapter 6. The overall performance of the multivariable designs is much greater than that of the classical first order lead, but they require compensators of approximately double the order of the classical design. There is little performance difference between the multivariable designs however. Of those examined, only the frequency weighted linear quadratic Gaussian design methodology produces compensators that meet all of the typical TDF-DTG torque-rebalance loop design requirements directly through the design methodology. The LQG/LTR design methodology provides the easiest design approach, with the design problem reduced to the selection of two scalar parameters. Finally, the FLS/LQG/LTR design approach has some promise in torque-rebalance loop design, but more expertise is needed in the selection of suitable target loops.

# Chapter 2

## Gyro Model Description

In this chapter, the linear model of the gyro used in the design of the torque-rebalance loop controllers is discussed. First, the dynamics of a single gimbal rotor suspension system are analyzed in order to derive the tuning condition. Then the equations of motion of the gyro rotor are derived and linearized to generate the linear model used in the design analysis. Finally, the complex method is applied to the linearized equations in order to take advantage of the rotationally symmetric properties of the gyro.

### 2.1 Gyro Equations of Motion

#### 2.1.1 Background

The dynamics of practical two degree of freedom, tuned gyroscopes have been well understood for nearly two decades. Accordingly, there are several derivations of the equations of motion available. Savet [14] derived the equations of motion for a gimballess, “vibra-beam” gyro using a Lagrangian potential. An alternative derivation is presented by Craig [6], who derived the equations of motion for a dynamically tuned gyro with  $n$  gimbals using a Newton-Euler approach. Craig [5] also performed extensive analysis on the error sources associated with a physical gyro. In a subsequent paper, Craig [4] derived the equations of motion for a physical tuned gyro under the assumption that the gyro rotor is a free body and then introduced terms corresponding to the error sources of a physical gyro into the free body equations of motion. A detailed analysis of a one and two gimbal gyros is also presented in [3].

The derivation of the equations of motion for a single gimbal, tuned gyro that is presented in this thesis follows the approach taken by Craig [4]. This analysis

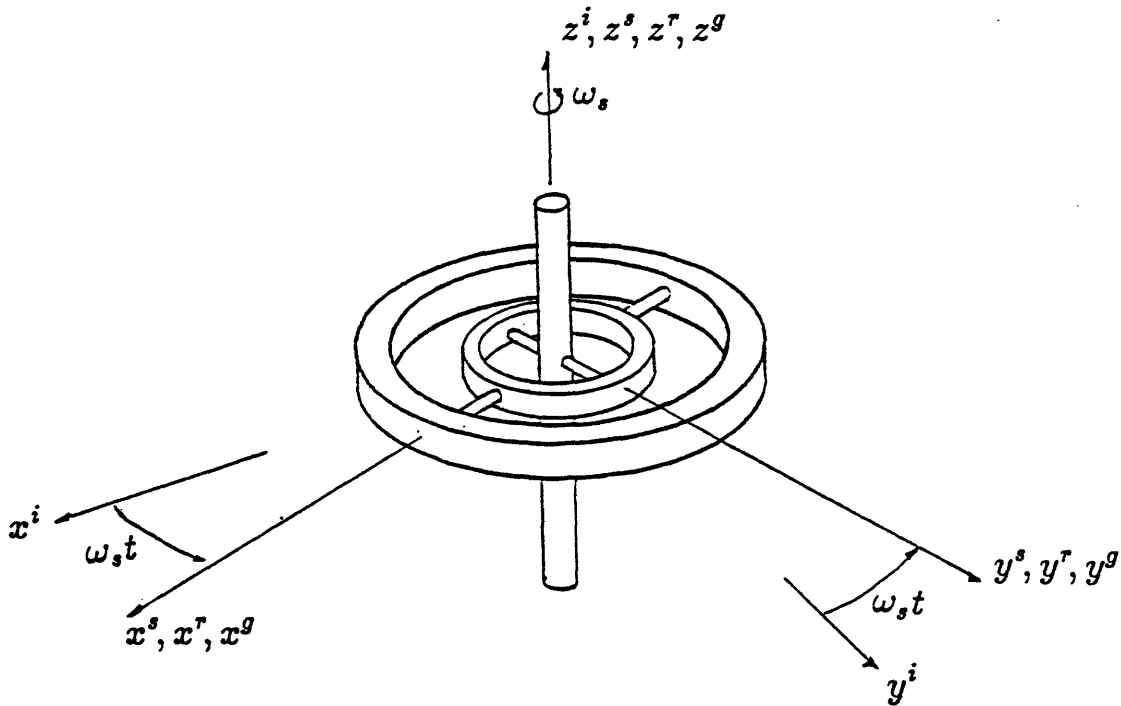


Figure 2.1: Suspension System Schematic Diagram

has been simplified somewhat to include the effects of an imperfect suspension system only, which have a first order effect on the gyro rotor motion, ignoring pickoff and torquer misalignments and other effects. A description of the overall gyro system is presented in Section 1.2.1.

### 2.1.2 The Tuning Condition

A schematic diagram of the gyro shaft, rotor, and suspension system is shown in Figure 2.1. Four reference frames are used in the analysis of the suspension system. The *i*-frame is fixed in inertial space; the *r*-frame is fixed in the gyro rotor; the *g*-frame is fixed in the gimbal, and the *s*-frame is fixed in the gyro shaft. The shaft *y*-axis,  $y^s$ , coincides with the gimbal *y*-axis, and the gimbal *x*-axis,  $x^g$ , coincides with the rotor *x*-axis,  $x^r$ . The rotor has an angular velocity of  $\omega_s$  with respect to inertial space about its *z*-axis, which is aligned with the inertial *z*-axis,  $z^i$ .

A diagram showing the shaft deflected with respect to the rotor is shown in Figure 2.2. The instantaneous attitude of the shaft relative to the rotor is

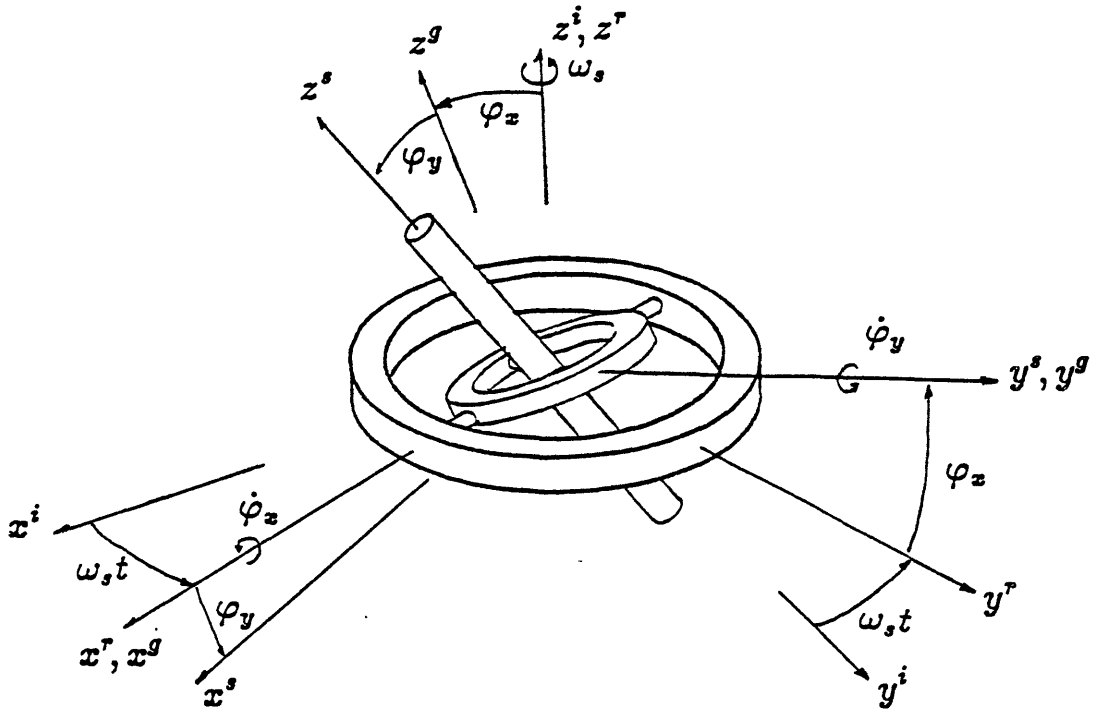


Figure 2.2: Suspension System with the Shaft Deflected

defined by the two angles,  $\varphi_x$  and  $\varphi_y$ , which are assumed to be small.

The moment applied to the rotor about the  $x^r$ -axis is the combined torsional spring constant of the outer flexures,  $K_x$ , multiplied by the deflection angle,  $\varphi_x$ .

$$M_{rx}^r = K_x \varphi_x \quad (2.1)$$

The moment applied to the rotor about the  $y^r$ -axis is the difference between the moment applied to the gimbal about the  $y^g$ -axis by the inner flexures,  $K_y \varphi_y$ , and the inertia moments of the gimbal about that axis.

$$M_{ry}^r = K_y \varphi_y - [I_{gy} \dot{\omega}_{igy}^g - (I_{gz} - I_{gx}) \omega_{igz}^g \omega_{igx}^g] \quad (2.2)$$

The components of the moments of inertia of the gimbal about the gimbal axes,  $x^g$ ,  $y^g$ , and  $z^g$ , are denoted by  $I_{gx}$ ,  $I_{gy}$ , and  $I_{gz}$  respectively.

The angular velocity of the gimbal with respect to inertial space, written in gimbal coordinates is

$$\underline{\omega}_{ig}^g = \begin{bmatrix} \omega_{igx}^g \\ \omega_{igy}^g \\ \omega_{igz}^g \end{bmatrix} = \begin{bmatrix} \dot{\varphi}_x \\ \omega_s \varphi_x \\ \omega_s \end{bmatrix}. \quad (2.3)$$

Its value is found from:

$$\begin{aligned}\underline{\omega}_{ig}^g &= \underline{\omega}_{rg}^g + \underline{\omega}_{ir}^g \\ &= \underline{\omega}_{rg}^g + C_r^g \underline{\omega}_{ir}^r\end{aligned}$$

with

$$\underline{\omega}_{rg}^g = \begin{bmatrix} \dot{\varphi}_x \\ 0 \\ 0 \end{bmatrix}, \quad \underline{\omega}_{ir}^r = \begin{bmatrix} 0 \\ 0 \\ \omega_s \end{bmatrix},$$

and where  $C_r^g$  is the direction cosine matrix relating the r-frame to the g-frame. Assuming  $\varphi_x$  and  $\varphi_y$  are small, it is shown below.

$$C_r^g = \begin{bmatrix} 1 & 0 & 0 \\ 0 & 1 & \varphi_x \\ 0 & -\varphi_x & 1 \end{bmatrix}$$

Substituting Equation (2.3) into Equation (2.2) yields the two equations for the moments applied to the rotor by the suspension system in rotor coordinates.

$$M_{rx}^r = K_x \varphi_x \quad (2.4)$$

$$M_{ry}^r = K_y \varphi_y + (-I_{gx} - I_{gy} + I_{gz}) \omega_s \dot{\varphi}_x \quad (2.5)$$

Assuming an angular displacement of the gyro case (to which the shaft is connected) with respect to inertial space about the  $x^i$ -axis of  $\phi_x$ , the angles between the rotor and shaft become

$$\varphi_x = \phi_x \cos \omega_s t \quad (2.6)$$

$$\varphi_y = -\phi_x \sin \omega_s t. \quad (2.7)$$

Substituting Equations (2.6) and (2.7) into (2.4) and (2.5) yields the following moment equations

$$M_{rx}^r = K_x \phi_x \cos \omega_s t \quad (2.8)$$

$$M_{ry}^r = -\left[ K_y + (-I_{gx} - I_{gy} + I_{gz}) \omega_s^2 \right] \phi_x \sin \omega_s t. \quad (2.9)$$

After some manipulation, Equations (2.8) and (2.9) can be written in inertial coordinates as shown in Equations (2.10) and (2.11).

$$M_{rx}^i = \frac{1}{2} \left[ (K_x + K_y) + (-I_{gx} - I_{gy} + I_{gz}) \omega_s^2 \right] \phi_x + \frac{1}{2} \left[ (K_x - K_y) - (-I_{gx} - I_{gy} + I_{gz}) \omega_s^2 \right] \phi_x \cos 2\omega_s t \quad (2.10)$$

$$M_{ry}^i = \frac{1}{2} \left[ (K_x - K_y) - (-I_{gx} - I_{gy} + I_{gz}) \omega_s^2 \right] \phi_x \sin 2\omega_s t \quad (2.11)$$

An ideal suspension system would transmit zero average moment to the rotor regardless of the time history of  $\phi_x$ . For the case of a constant  $\phi_x$ , the average moment equations are

$$M_{rx}^i = \frac{1}{2} [(K_x + K_y) + (-I_{gx} - I_{gy} + I_{gz}) \omega_s^2] \phi_x \quad (2.12)$$

$$M_{ry}^i = 0. \quad (2.13)$$

Equation (2.12) suggests the tuning condition. If the flexure torsional spring constants, gimbal moments of inertia, and rotor spin angular velocity can be chosen according to (2.14), the suspension system is said to be tuned.

$$\omega_s = \sqrt{\frac{K_x + K_y}{I_{gx} + I_{gy} - I_{gz}}} \quad (2.14)$$

As a result, the rotor is decoupled from the suspension system, and the average moments on the rotor due to the suspension system are zero.

### 2.1.3 Gyro Rotor Equations of Motion

The equations of motion of the gyro rotor are derived under the assumption that the tuning condition is met, so that the gyro rotor behaves like a free rotor in inertial space. Terms corresponding to moments due to an imperfect suspension system are added to the free body equations of motion to complete the model.

It is convenient to derive the equations of motion using coordinate systems that do not rotate with the rotor because the gyro pickoffs and torquers are fixed to the gyro case. Therefore, two new coordinate frames are defined. The n-frame is attached to the rotor but does not spin with the rotor, and the n-frame z-axis is aligned with the rotor spin axis. The c-frame is fixed in the gyro case. Figure 2.3 shows the relationship between the n-frame and the c-frame. The orientation of the n-frame with respect to the c-frame is defined by the two pickoff angles  $\theta_x$  and  $\theta_y$ .

The angular velocity of the n-frame with respect to inertial space written in the n-frame is

$$\underline{\omega}_{in}^i = \underline{\omega}_{ic}^n + \underline{\omega}_{cn}^n = C_c^n \underline{\omega}_{ic}^c + \underline{\omega}_{cn}^n \quad (2.15)$$

where

$$\underline{\omega}_{ic}^c = \begin{bmatrix} \dot{\phi}_x \\ \dot{\phi}_y \\ \dot{\phi}_z \end{bmatrix}, \quad \underline{\omega}_{cn}^n = \begin{bmatrix} \dot{\theta}_x \\ \dot{\theta}_y \\ 0 \end{bmatrix}.$$



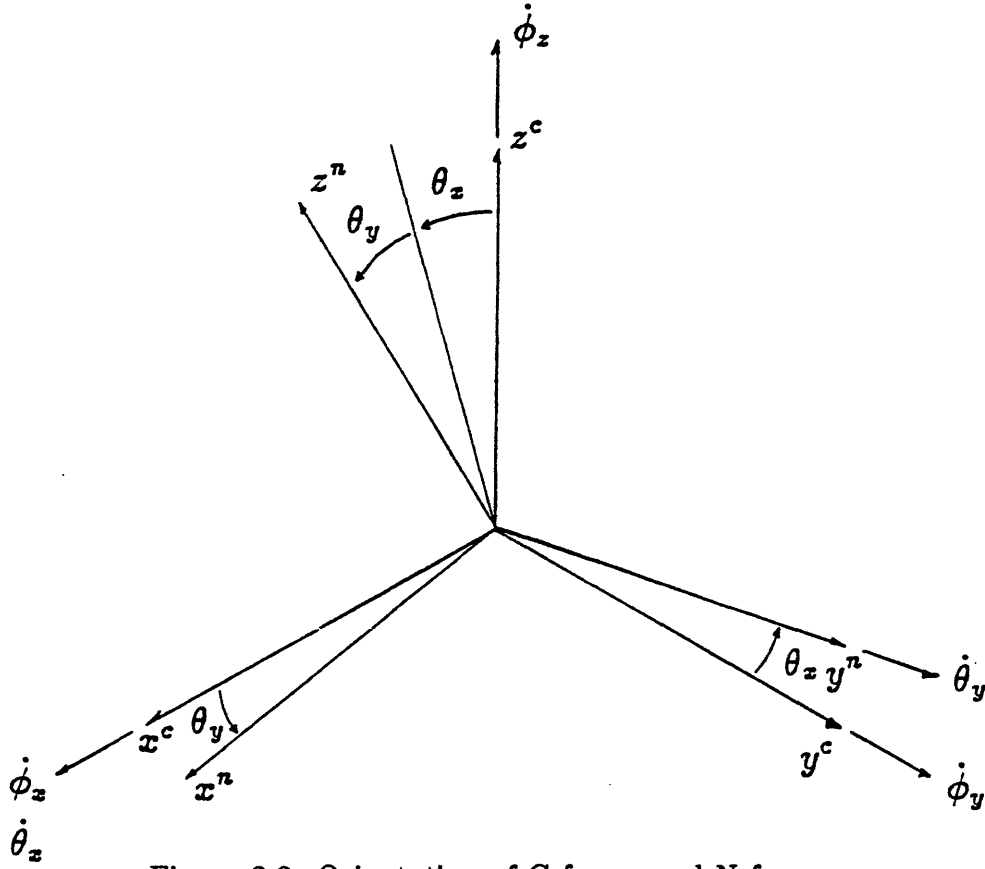


Figure 2.3: Orientation of C-frame and N-frame

The direction cosine matrix,  $C_c^n$ , for small  $\theta_x$  and  $\theta_y$  is shown below.

$$C_c^n = \begin{bmatrix} 1 & 0 & -\theta_y \\ 0 & 1 & \theta_x \\ \theta_y & -\theta_x & 1 \end{bmatrix}$$

Substituting the above quantities into Equation (2.15) yields Equation (2.16).

$$\underline{\omega}_{in}^n = \begin{bmatrix} \omega_{nx} \\ \omega_{ny} \\ \omega_{nz} \end{bmatrix} = \begin{bmatrix} \dot{\phi}_x + \dot{\theta}_x - \theta_y \dot{\phi}_z \\ \dot{\phi}_y + \dot{\theta}_y + \theta_x \dot{\phi}_z \\ \dot{\phi}_z - \theta_x \dot{\phi}_y + \theta_y \dot{\phi}_x \end{bmatrix} \quad (2.16)$$

The moment on the rotor, written in the n-frame, is equal to the rate of change of its angular momentum, as shown in Equation (2.17).

$$\underline{M}_r^n = \frac{d^i}{dt} (\underline{H}_r^n) = \frac{d^n}{dt} (\underline{H}_r^n) + \underline{\omega}_{in}^n \times \underline{H}_r^n \quad (2.17)$$

The angular momentum of the rotor is

$$\underline{H}_r^n = \begin{bmatrix} I_{rx} \omega_{nx} \\ I_{ry} \omega_{ny} \\ I_{rz} (\omega_{nz} + \omega_s) \end{bmatrix}, \quad (2.18)$$

where  $\omega_s$  is the rotor spin speed, which is assumed to be held constant by the gyro motor and is much larger than  $\omega_{nz}$ , and  $I_{rx}$ ,  $I_{ry}$ , and  $I_{rz}$  are the rotor moments of inertia about the corresponding rotor axes. Substituting (2.16) and (2.18) into (2.17) yields the following moments on the rotor, written in the n-frame.

$$\underline{M}_r^n = \begin{bmatrix} I_{rx}\dot{\omega}_{nx} + (I_{rz} - I_{ry})\omega_{ny}\omega_{nz} + I_{rz}\omega_{ny}\omega_s \\ I_{ry}\dot{\omega}_{ny} + (I_{rx} - I_{rz})\omega_{nx}\omega_{nz} - I_{rz}\omega_{nx}\omega_s \\ I_{rz}\dot{\omega}_{nz} + (I_{ry} - I_{rx})\omega_{nx}\omega_{ny} \end{bmatrix} \quad (2.19)$$

The moment on the rotor can be expressed in the case fixed coordinate frame as shown in (2.20).

$$\underline{M}_r^c = C_n^c \underline{M}_r^n \quad (2.20)$$

The motor shaft lies along the case fixed  $z^c$ -axis, and under the free rotor assumption, can only provide moments to the rotor about this axis. Moments applied to the rotor along the perpendicular axes,  $M_{rx}^c$  and  $M_{ry}^c$ , are provided by the gyro torquers.

Up to this point, the moments on the rotor have been derived under the assumption that the rotor is a free body. Actual rotor suspensions are not ideal, and their imperfections can be easily modelled as additional sources of moments on the rotor. These moments can be due to the effects of mistuning, suspension damping, and other imperfections. Craig has described several sources of errors in a dynamically tuned gyro in great detail [5].

For the purposes of this analysis, only the linear terms associated with the moments due to suspension damping will be included. These moments are shown below in Equations (2.21) and (2.22).

$$M_{sx}^c = \frac{H}{\tau}\theta_y + D_R\dot{\theta}_x \quad (2.21)$$

$$M_{sy}^c = -\frac{H}{\tau}\theta_x + D_R\dot{\theta}_y \quad (2.22)$$

Where  $H = I_{rz}\omega_s$  is the angular momentum of the rotor about its  $z^n$ -axis. The gyro quadrature time constant,  $\tau$ , is infinite in an ideal gyro. It corresponds to the rate at which the rotor will realign itself with the gyro case after an initial offset. The rotor damping term,  $D_R$ , is zero in an ideal gyro. It corresponds to viscous damping and tends to damp rotor nutation oscillations.

Combining Equations (2.20), (2.21), and (2.22) yields Equations (2.23) and

(2.24).

$$M_x = M_{rx}^n + \theta_y M_{rz}^n + M_{sx} \quad (2.23)$$

$$M_y = M_{ry}^n - \theta_x M_{rz}^n + M_{sy} \quad (2.24)$$

Expanding these equations and assuming that the rotor is symmetric so that  $I_{rx} = I_{ry} = I_{rr}$  yields:

$$\begin{aligned} M_x = & I_{rr} (\ddot{\phi}_x + \ddot{\theta}_x - \theta_y \ddot{\phi}_z - \dot{\theta}_y \dot{\phi}_z) \\ & + H (\dot{\phi}_y + \dot{\theta}_y + \theta_x \dot{\phi}_z) \\ & + (I_{rz} - I_{rr}) (\dot{\phi}_y + \dot{\theta}_y + \theta_x \dot{\phi}_z) (\dot{\phi}_z + \theta_y \dot{\phi}_x - \theta_x \dot{\phi}_y) \\ & + I_{rz} (\ddot{\phi}_z + \theta_y \ddot{\phi}_x + \dot{\theta}_y \dot{\phi}_x - \dot{\theta}_x \dot{\phi}_y - \theta_x \ddot{\phi}_y) \theta_y \\ & + \frac{H}{\tau} \theta_y + D_R \dot{\theta}_x \end{aligned} \quad (2.25)$$

$$\begin{aligned} M_y = & I_{rr} (\ddot{\phi}_y + \ddot{\theta}_y + \theta_x \ddot{\phi}_z + \dot{\theta}_x \dot{\phi}_z) \\ & - H (\dot{\phi}_x + \dot{\theta}_x - \theta_y \dot{\phi}_z) \\ & - (I_{rz} - I_{rr}) (\dot{\phi}_x + \dot{\theta}_x - \theta_y \dot{\phi}_z) (\dot{\phi}_z + \theta_y \dot{\phi}_x - \theta_x \dot{\phi}_y) \\ & - I_{rz} (\ddot{\phi}_z + \theta_y \ddot{\phi}_x + \dot{\theta}_y \dot{\phi}_x - \dot{\theta}_x \dot{\phi}_y - \theta_x \ddot{\phi}_y) \theta_x \\ & - \frac{H}{\tau} \theta_x + D_R \dot{\theta}_y \end{aligned} \quad (2.26)$$

When the gyro case is subjected to an inertial angular rate,  $\dot{\phi}$ , the gyro torquers must supply the moments,  $M_x$  and  $M_y$ , to precess the rotor at a rate equal to the inertial angular rate.

## 2.2 Torquer and Pickoff Models

The gyro torque generators apply commanded moments to the rotor electromagnetically. An electrical coil is fixed to the gyro case, and a current through the coil acts with permanent magnets on the rotor to magnetically torque the rotor. The torque generator is modelled as a simple gain,  $K_T$ , with units of torque per millivolt.

The pickoff signal generators also work electromagnetically. A coil is fixed to the gyro case, and the variation of the inductance of the coil due to rotation of the rotor about the  $x^c$ -axis and  $y^c$ -axis is measured by the pickoff. The pickoff output is amplified by a pre-amp and is modulated on a high frequency carrier

signal. The combined pickoff, pre-amp, and signal generator is modelled as a simple gain,  $K_{PO}$ , with units of millivolts per radian.

## 2.3 Linearized Equations of Motion

The equations of motion in (2.25) and (2.26) can be simplified by assuming that products including the pickoff angles,  $\theta_x$  and  $\theta_y$ , are small and retaining only the linear terms of the derivatives of  $\phi$ . These linearized equations are shown below.

$$M_x = I_{rr} (\ddot{\phi}_x + \ddot{\theta}_x) + H (\dot{\phi}_y + \dot{\theta}_y) + D_R \dot{\theta}_x + \frac{H}{\tau} \theta_y \quad (2.27)$$

$$M_y = I_{rr} (\ddot{\phi}_y + \ddot{\theta}_y) - H (\dot{\phi}_x + \dot{\theta}_x) + D_R \dot{\theta}_y - \frac{H}{\tau} \theta_x \quad (2.28)$$

The linearized model of the gyro can be expressed in the state space form shown in (2.29) and (2.30).

$$\dot{\underline{x}} = A\underline{x} + B\underline{u} + L_1 \underline{d}_1 + L_2 \underline{d}_2 \quad (2.29)$$

$$\underline{y} = C\underline{x} \quad (2.30)$$

The state vector,  $\underline{x}$ , is made up of the pickoff angles and their derivatives; the control input,  $\underline{u}$ , consists of the moments applied to the rotor by the gyro torquers; the output vector,  $\underline{y}$ , consists of the rotor pickoff angles. The additional inputs,  $\underline{d}_1$  and  $\underline{d}_2$  are the inertial angular rates and accelerations. The state space form of (2.27) and (2.28) is shown below.

$$\begin{bmatrix} \dot{\theta}_x \\ \ddot{\theta}_x \\ \dot{\theta}_y \\ \ddot{\theta}_y \end{bmatrix} = \begin{bmatrix} 0 & 1 & 0 & 0 \\ 0 & -\frac{D_R}{I_{rr}} & -\frac{H}{\tau I_{rr}} & -\frac{H}{I_{rr}} \\ 0 & 0 & 0 & 1 \\ \frac{H}{\tau I_{rr}} & \frac{H}{I_{rr}} & 0 & -\frac{D_R}{I_{rr}} \end{bmatrix} \begin{bmatrix} \theta_x \\ \dot{\theta}_x \\ \theta_y \\ \dot{\theta}_y \end{bmatrix} + \begin{bmatrix} 0 & 0 \\ \frac{1}{I_{rr}} & 0 \\ 0 & 0 \\ 0 & \frac{1}{I_{rr}} \end{bmatrix} \begin{bmatrix} M_x \\ M_y \end{bmatrix} + \begin{bmatrix} 0 & 0 \\ 0 & -\frac{H}{I_{rr}} \end{bmatrix} \begin{bmatrix} \dot{\phi}_x \\ \dot{\phi}_y \end{bmatrix} + \begin{bmatrix} 0 & 0 \\ -1 & 0 \\ 0 & 0 \\ 0 & -1 \end{bmatrix} \begin{bmatrix} \ddot{\phi}_x \\ \ddot{\phi}_y \end{bmatrix} \quad (2.31)$$

$$\begin{bmatrix} \theta_x \\ \theta_y \end{bmatrix} = \begin{bmatrix} 1 & 0 & 0 & 0 \\ 0 & 0 & 1 & 0 \end{bmatrix} \begin{bmatrix} \theta_x \\ \dot{\theta}_x \\ \theta_y \\ \dot{\theta}_y \end{bmatrix} \quad (2.32)$$

## 2.4 Application of the Complex Method to the Gyro Model

The complex method has been used to simplify the analysis of a large class of systems with rotationally symmetric dynamics. It has been applied to the two-degree-of-freedom-dynamically tuned gyro by Lipman [13], Craig [6], and others. The application of the complex method to two input-two output block symmetric (TITOBS) systems has been analyzed in great detail by Johnson [12], and many of his results, discussed in Chapter 3, are used in the remainder of this thesis.

The complex method is applied to the gyro equations of motion by defining the following complex variables:

$$\begin{aligned}\theta_c &= \theta_x + j\theta_y \\ \dot{\phi}_c &= \dot{\phi}_x + j\dot{\phi}_y \\ M_c &= M_x + jM_y.\end{aligned}$$

Expressing Equations (2.29) and (2.30) in terms of the complex pickoff angle,  $\theta_c$ , complex inertial angular rate,  $\dot{\phi}_c$ , and complex moment command,  $M_c$ , yields the set of complex state space equations shown in (2.33) and (2.34).

$$\begin{bmatrix} \dot{\theta}_c \\ \ddot{\theta}_c \end{bmatrix} = \begin{bmatrix} 0 & 1 \\ j\frac{H}{I_{rr}} & (-\frac{D_R}{I_{rr}} + j\frac{H}{I_{rr}}) \end{bmatrix} \begin{bmatrix} \theta_c \\ \dot{\theta}_c \end{bmatrix} + \begin{bmatrix} 0 \\ \frac{1}{I_{rr}} \end{bmatrix} M_c + \begin{bmatrix} 0 \\ j\frac{H}{I_{rr}} \end{bmatrix} \dot{\phi}_c + \begin{bmatrix} 0 \\ -1 \end{bmatrix} \ddot{\phi}_c \quad (2.33)$$

$$\theta_c = \begin{bmatrix} 1 & 0 \end{bmatrix} \begin{bmatrix} \theta_c \\ \dot{\theta}_c \end{bmatrix} \quad (2.34)$$

Clearly, there are several advantages to representing the system in complex form. The two primary reasons that this is done are that a TITOBS system is transformed into a SISO system and that the order of the system is reduced by a factor of two. Additional properties of TITOBS systems and their complex representations are discussed in Chapter 3.

It is also convenient at this point to introduce the torquer and pickoff gains into the state equations, and to also write the angles in units of degrees instead of radians. This results in Equations (2.35) and (2.36), where  $M'_c$  is the torque

command in millivolts and  $\theta'_c$  is the pickoff angle output, also in millivolts.

$$\begin{bmatrix} \dot{\theta}_c \\ \ddot{\theta}_c \end{bmatrix} = \begin{bmatrix} 0 & 1 \\ j\frac{H}{\tau I_{rr}} & (-\frac{D_R}{I_{rr}} + j\frac{H}{I_{rr}}) \end{bmatrix} \begin{bmatrix} \theta_c \\ \dot{\theta}_c \end{bmatrix} + \begin{bmatrix} 0 \\ K_T \frac{180}{\pi} \frac{1}{I_{rr}} \end{bmatrix} M'_c + \begin{bmatrix} 0 \\ j\frac{H}{I_{rr}} \end{bmatrix} \dot{\phi}_c + \begin{bmatrix} 0 \\ -1 \end{bmatrix} \ddot{\phi}_c \quad (2.35)$$

$$\theta'_c = \begin{bmatrix} K_{PO} \frac{\pi}{180} & 0 \end{bmatrix} \begin{bmatrix} \theta_c \\ \dot{\theta}_c \end{bmatrix} \quad (2.36)$$

Throughout the remainder of this thesis, the terms in Equations (2.35) and (2.36) are referred to as the corresponding terms in Equations (2.37) and (2.38).

$$\dot{\underline{x}}_p = A_p \underline{x}_p + B_p u_p + L_{1p} \dot{\phi}_c + L_{2p} \ddot{\phi}_c \quad (2.37)$$

$$y_p = C_p \underline{x}_p \quad (2.38)$$

The SISO complex coefficient transfer function from the moment command input,  $u_p$ , to the pickoff angle output,  $y_p$ , is determined from the state space representation of the system as shown in Equation (2.39).

$$G_p(s) = C_p (sI - A_p)^{-1} B_p \quad (2.39)$$

## 2.5 Summary

In this chapter, the equations of motion for the two-degree-of-freedom, dynamically tuned gyro are derived. These equations lead to a linear model of the gyro used in design and analysis of torque-rebalance loop controllers for the gyro. The complex method is applied to the linear equations of motion, yielding a single input-single output description of the gyro.

## Chapter 3

# Properties of Block Symmetric Matrices and Systems

In this Chapter, some properties of block symmetric systems are presented, with special attention to real, two input–two output block symmetric (TITOBS) systems. After some background is presented, block symmetric matrices are defined, and the relationship between block symmetric systems and their corresponding complex representations is discussed. Next, some properties of block symmetric matrices are presented. Then some properties of TITOBS systems and their corresponding complex single input–single output (SISO) forms are examined. Included in this section is a discussion of the use of Bode plots of complex systems and the complex SISO Nyquist criterion for control system design. Lastly, the implementation of block symmetric dynamic compensators in digital computers by taking advantage of the complex method is analyzed.

### 3.1 Background

The linear model of the two–degree–of–freedom tuned gyroscope, along with many other systems with rotational symmetry, is a block symmetric system. This block symmetric nature can be taken advantage of by using the complex method, and the complex method has been used to simplify the analysis of several systems with rotational dynamics. As was discussed in Chapter 2, the complex method has been used to derive the equations of motion of the tuned gyro and has also been used to arrive at a complex coefficient transfer function description of the linearized gyro model ([13] and [6]). The use of the complex method also has advantages in control system design, analysis, and implementation for block symmetric systems, especially TITOBS systems.

Since TITOBS systems can be transformed into complex SISO systems via the complex method, classical SISO design tools can be used in the design of a nominally MIMO system. Root locus, Bode plots, and the Nyquist criterion can be used, but must be interpreted differently for complex systems than for real systems. A 1974 NASA report [15] used the complex versions of root locus and Bode plots in the design of a tuned rotor gyro torque-rebalance loop controller. Johnson [12] derived the rules for the root locus of complex systems and also developed interpretations of Bode plots and the Nyquist criterion for complex systems; both of which are used extensively in this thesis.

The reduction in system order and number of inputs and outputs afforded by the complex method offers a possibility of computational savings in compensator design. Compensators for block symmetric systems implemented in digital computers can benefit from reduced memory storage requirements if the complex version of the compensator is used.

### 3.2 Definition of Block Symmetric Systems and Complex Notation

This chapter describes several properties of real, block symmetric matrices and systems. A  $2n \times 2m$  real matrix,  $S$ , is block symmetric if it can be partitioned as shown in Equation (3.1).

$$S = \begin{bmatrix} S_r & -S_i \\ S_i & S_r \end{bmatrix} \quad (3.1)$$

The real sub-matrices,  $S_r$  and  $S_i$ , both have dimension  $n \times m$ . The complex matrix,  $S_c$ , corresponding to the real block symmetric matrix,  $S$ , is defined in (3.2).

$$S_c = S_r + jS_i \quad (3.2)$$

A real, linear, time invariant system that is block symmetric can be described by a corresponding system in complex form. This is shown to be true for the gyro model at the end of Chapter 2. Consider the real, block symmetric system shown below in state space form

$$\dot{\underline{x}}(t) = A\underline{x}(t) + B\underline{u}(t) \quad (3.3)$$

$$\underline{y}(t) = C\underline{x}(t) \quad (3.4)$$



with the control law

$$\underline{u}(t) = -G\underline{x}(t) \quad (3.5)$$

where the matrices  $A$ ,  $B$ ,  $C$ , and  $G$  are properly sized, block symmetric, and are partitioned as

$$A = \begin{bmatrix} A_r & -A_i \\ A_i & A_r \end{bmatrix} \quad B = \begin{bmatrix} B_r & -B_i \\ B_i & B_r \end{bmatrix}$$

$$C = \begin{bmatrix} C_r & -C_i \\ C_i & C_r \end{bmatrix} \quad G = \begin{bmatrix} G_r & -G_i \\ G_i & G_r \end{bmatrix},$$

and the state, control, and output vectors are partitioned as

$$\underline{x} = \begin{bmatrix} \underline{x}_r \\ \underline{x}_i \end{bmatrix} \quad \underline{u} = \begin{bmatrix} \underline{u}_r \\ \underline{u}_i \end{bmatrix} \quad \underline{y} = \begin{bmatrix} \underline{y}_r \\ \underline{y}_i \end{bmatrix}.$$

Next, consider the corresponding complex system shown below

$$\dot{\underline{x}}_c(t) = A_c \underline{x}_c(t) + B_c \underline{u}_c(t) \quad (3.6)$$

$$\underline{y}_c(t) = C_c \underline{x}_c(t) \quad (3.7)$$

with the control law

$$\underline{u}_c(t) = -G_c \underline{x}_c(t) \quad (3.8)$$

where the complex matrices and vectors are defined as

$$A_c = A_r + jA_i$$

$$B_c = B_r + jB_i$$

$$C_c = C_r + jC_i$$

$$G_c = G_r + jG_i$$

$$\underline{x}_c = \underline{x}_r + j\underline{x}_i$$

$$\underline{u}_c = \underline{u}_r + j\underline{u}_i$$

$$\underline{y}_c = \underline{y}_r + j\underline{y}_i.$$

The real, block symmetric system described by Equations (3.3) through (3.5) is fully described by the real and imaginary parts of the corresponding complex system in Equations (3.6) through (3.8). This result has some important implications. First, the size of the complex state vector is half the size of the real state vector, since its real and imaginary parts contain the information of the

full size, real vector. Also, the size of the control and output vectors are likewise halved in the complex description of the system. This is particularly useful if the original real system is TITOBS, since the real system is transformed into a complex SISO system. This allows modified classical SISO design tools such as root locus, Bode plots and Nyquist plots to be used for the design of what is physically a two input–two output system. Finally, block symmetric compensators implemented in digital computers can also benefit from the use of the complex form of the system, since the memory required to store the smaller complex matrices is less than that required for real block symmetric matrices.

### 3.3 Properties of Block Symmetric Matrices

This section summarizes some of the properties of block symmetric matrices and their relationships to the corresponding complex matrices. Most of the results in this section are due to Johnson [12], and the proofs of the following results can be found there.

#### 3.3.1 Algebraic Properties

##### Sum

The sum of two compatible, block symmetric matrices is block symmetric. If  $R$  and  $S$  are real, block symmetric matrices with

$$R = \begin{bmatrix} R_r & -R_i \\ R_i & R_r \end{bmatrix} \quad S = \begin{bmatrix} S_r & -S_i \\ S_i & S_r \end{bmatrix}$$

then their sum is shown below

$$\begin{aligned} T &= R + S \\ &= \begin{bmatrix} \mathcal{Re}\{T_c\} & -\mathcal{Im}\{T_c\} \\ \mathcal{Im}\{T_c\} & \mathcal{Re}\{T_c\} \end{bmatrix} \end{aligned}$$

where

$$\begin{aligned} T_c &= R_c + S_c \\ R_c &= R_r + jR_i \\ S_c &= S_r + jS_i. \end{aligned}$$

## Product

The product of two compatible block symmetric matrices is block symmetric. If  $R$  and  $S$  are real, block symmetric matrices with

$$R = \begin{bmatrix} R_r & -R_i \\ R_i & R_r \end{bmatrix} \quad S = \begin{bmatrix} S_r & -S_i \\ S_i & S_r \end{bmatrix}$$

then their product is shown below

$$\begin{aligned} T &= RS \\ &= \begin{bmatrix} \mathcal{Re}\{T_c\} & -\mathcal{Im}\{T_c\} \\ \mathcal{Im}\{T_c\} & \mathcal{Re}\{T_c\} \end{bmatrix} \end{aligned}$$

where

$$\begin{aligned} T_c &= R_c S_c \\ R_c &= R_r + jR_i \\ S_c &= S_r + jS_i. \end{aligned}$$

## Matrix Exponential

The matrix exponential of a block symmetric matrix is block symmetric. If  $S$  is a real, square, block symmetric matrix with

$$S = \begin{bmatrix} S_r & -S_i \\ S_i & S_r \end{bmatrix}$$

then the matrix exponential is shown below

$$\begin{aligned} T &= I + S + \frac{1}{2!}S^2 + \frac{1}{3!}S^3 + \dots \\ &= \begin{bmatrix} \mathcal{Re}\{T_c\} & -\mathcal{Im}\{T_c\} \\ \mathcal{Im}\{T_c\} & \mathcal{Re}\{T_c\} \end{bmatrix} \end{aligned}$$

where

$$\begin{aligned} T_c &= I + S_c + \frac{1}{2!}S_c^2 + \frac{1}{3!}S_c^3 + \dots \\ S_c &= S_r + jS_i. \end{aligned}$$

This result follows directly from the sum and product properties.

## Matrix Inverse

The inverse of a block symmetric matrix, if it exists, is block symmetric. If  $S$  is a real, square, block symmetric matrix with

$$S = \begin{bmatrix} S_r & -S_i \\ S_i & S_r \end{bmatrix}$$

its inverse is

$$S^{-1} = \begin{bmatrix} \mathcal{R}e\{S_c^{-1}\} & -\mathcal{I}m\{S_c^{-1}\} \\ \mathcal{I}m\{S_c^{-1}\} & \mathcal{R}e\{S_c^{-1}\} \end{bmatrix}$$

where

$$S_c = S_r + jS_i.$$

The inverse exists if the  $\det(S_c) \neq 0$ .

## Determinant

The determinant of a real, square, block symmetric matrix,  $S$ , with

$$S = \begin{bmatrix} S_r & -S_i \\ S_i & S_r \end{bmatrix}$$

is

$$\det(S) = [\det(S_r + jS_i)] [\det(S_r - jS_i)] \quad (3.9)$$

$$= [\det(S_c)] [\det(S_c)]^* \quad (3.10)$$

where

$$S_c = S_r + jS_i$$

and  $*$  denotes complex conjugate.

### 3.3.2 Eigenvalues and Eigenvectors

The eigenvalues of a real, square, block symmetric matrix come in complex conjugate pairs for both real and complex eigenvalues. The eigenvalues of the real, block symmetric matrix,  $S$ , with

$$S = \begin{bmatrix} S_r & -S_i \\ S_i & S_r \end{bmatrix}$$

are the eigenvalues,  $\lambda_k$ , of the complex matrix

$$S_c = S_r + jS_i$$

and their complex conjugates,  $\lambda_k^*$ . Therefore, the eigenvalues of a block symmetric matrix can be found from the eigenvalues of the corresponding complex matrix.

The right eigenvectors of the real,  $2n \times 2n$ , block symmetric matrix,  $S$ , can be found from the eigenvalue problem shown in Equation (3.11)

$$S \underline{v}_k = \lambda_k \underline{v}_k \quad k = 1, 2, 3, \dots, 2n \quad (3.11)$$

where  $\underline{v}_k$  is the  $k$ th right eigenvector and  $\lambda_k$  is the  $k$ th eigenvalue, generally complex. Equation (3.11) can be partitioned as shown in (3.12).

$$\begin{bmatrix} S_r & -S_i \\ S_i & S_r \end{bmatrix} \begin{bmatrix} \underline{v}_u \\ \underline{v}_l \end{bmatrix}_k = \lambda_k \begin{bmatrix} \underline{v}_u \\ \underline{v}_l \end{bmatrix}_k \quad (3.12)$$

The  $n \times 1$  sub-vectors,  $\underline{v}_u$  and  $\underline{v}_l$ , are the upper and lower partitions of the  $2n \times 1$  right eigenvectors.

The right eigenvectors of the corresponding complex,  $n \times n$  matrix,  $S_c$ , can be found from the eigenvalue problem shown in Equation (3.13)

$$S_c \underline{v}_c = \lambda_c \underline{v}_c \quad (3.13)$$

where

$$\begin{aligned} S_c &= S_r + jS_i \\ \underline{v}_c &= \underline{v}_r + j\underline{v}_i, \end{aligned}$$

and the subscripts have been removed to simplify the notation. The vector,  $\underline{v}_c$ , is an  $n \times 1$  right eigenvector and  $\lambda_c$  is its associated eigenvalue, generally complex.

The eigenvectors,  $\underline{v}$ , of the real, block symmetric matrix  $S$  can be found from the eigenvectors,  $\underline{v}_c$ , of the corresponding complex matrix,  $S_c$ . The exact relationship between these eigenvectors depends upon whether the associated eigenvalues are real or complex.

For a real eigenvalue of  $S_c$ ,  $s = \lambda_c$ , the eigenvalues of  $S$  are  $s = \lambda_c$  and  $s = \lambda_c^* = \lambda_c$ . The associated eigenvectors of  $S$  are

$$\underline{v} = \begin{bmatrix} \text{Re} \{ \underline{v}_c \} \\ \text{Im} \{ \underline{v}_c \} \end{bmatrix} \quad \text{and} \quad \underline{v} = \begin{bmatrix} \text{Re} \{ \underline{v}_c \} \\ -\text{Im} \{ \underline{v}_c \} \end{bmatrix}. \quad (3.14)$$

For a complex eigenvalue of  $S_c$ ,  $s = \lambda_c$ , the eigenvalues of  $S$  come in the complex conjugate pair,  $s = \lambda_c$  and  $s = \lambda_c^*$ . The associated eigenvectors of  $S$  are, respectively

$$\underline{v} = \begin{bmatrix} v_c \\ -jv_c \end{bmatrix} \quad \text{and} \quad \underline{v}^* = \begin{bmatrix} v_c^* \\ jv_c^* \end{bmatrix}. \quad (3.15)$$

Equations (3.14) and (3.15) can be used to find the eigenvectors of a block symmetric matrix from the eigenvectors of its corresponding complex matrix. They can also be used to find the eigenvectors of the complex matrix from those of the block symmetric matrix. A more detailed discussion and proof of (3.14) and (3.15) is given by Johnson [12].

### 3.4 Properties of TITOBS Systems

In this section, some properties of TITOBS systems are discussed. The transfer function matrix of a TITOBS system is considered. The complex method yields the SISO complex coefficient transfer function (CCTF). This SISO transfer function allows the use of the complex versions of the Bode and Nyquist tools. Transmission zeros of TITOBS systems are also examined.

#### 3.4.1 Transfer Function Description

The transfer function matrix of a real, linear, time invariant system relates the Laplace transform of the input vector to the Laplace transform of the output vector. This relation is shown in Equation (3.16).

$$\underline{Y}(s) = G(s)\underline{U}(s) \quad (3.16)$$

The vector  $\underline{U}(s)$  is the Laplace transform of the input  $\underline{u}(t)$ , and the vector  $\underline{Y}(s)$  is the Laplace transform of the output  $\underline{y}(t)$ . The transfer function matrix,  $G(s)$ , can be found from the state space representation of the system from

$$G(s) = C(sI - A)^{-1}B \quad (3.17)$$

where the matrices,  $A$ ,  $B$ , and  $C$  are defined in Equations (3.3) and (3.4).

If the system is a TITOBS system, then (3.16) can be partitioned in the following manner,

$$\begin{bmatrix} Y_r(s) \\ Y_i(s) \end{bmatrix} = \begin{bmatrix} G_r(s) & -G_i(s) \\ G_i(s) & G_r(s) \end{bmatrix} \begin{bmatrix} U_r(s) \\ U_i(s) \end{bmatrix} \quad (3.18)$$

where all of the partitioned elements are *scalars*. The complex method is now used to generate the complex coefficient transfer function (CCTF),  $G_c(s)$ , which is a scalar function and is shown in Equation (3.19).

$$G_c(s) = G_r(s) + jG_i(s) \quad (3.19)$$

The complex version of (3.18) becomes

$$Y_c(s) = G_c(s)U_c(s). \quad (3.20)$$

The complex time domain input to the system can be partitioned into its real and imaginary parts as

$$u_c(t) = u_r(t) + ju_i(t),$$

and its Laplace transform is

$$U_c(s) = U_r(s) + jU_i(s).$$

The Laplace transform of the output is

$$Y_c(s) = Y_r(s) + jY_i(s),$$

and the complex time domain system output,  $y_c(t)$ , can be found from the inverse Laplace transform of  $Y_c(s)$ :

$$\begin{aligned} y_c(t) &= y_r(t) + jy_i(t) \\ y_r(t) &= \mathcal{R}e \{ \mathcal{L}^{-1} \{ Y_c(s) \} \} \\ y_i(t) &= \mathcal{I}m \{ \mathcal{L}^{-1} \{ Y_c(s) \} \} \end{aligned}$$

where  $\mathcal{L}^{-1}$  denotes inverse Laplace transform.

One important fact about the CCTF is that it is not conjugate symmetric. Ordinary, real coefficient transfer functions have the property that,

$$G(s^*) = G^*(s)$$

however, for the explicitly complex transfer function,

$$\begin{aligned} G_c(s^*) &= G_r(s^*) + jG_i(s^*) \\ &= G_r^*(s) + jG_i^*(s) \end{aligned}$$

but,

$$G_c^*(s) = G_r^*(s) - jG_i^*(s);$$

therefore, for nonzero  $G_i(s)$ ,

$$G_c(s^*) \neq G_c^*(s).$$

The result of this lack of symmetry is that the frequency response of the complex system is different for positive and negative frequencies, yielding two different Bode plots. Also, the Nyquist plot of a complex system is not symmetric about the real axis. Conjugate symmetry does hold if  $G_c(s)$  has real coefficients only.

### 3.4.2 Transmission Zeros

The transmission zeros of a TITOBS system are the zeros of the corresponding CCTF and their complex conjugates. The transmission zeros of a MIMO system come from the solution to the generalized eigenvalue problem shown in Equation (3.21)

$$(z_k M - L) \underline{v}_k = 0 \quad (3.21)$$

where

$$M = \begin{bmatrix} I & 0 \\ 0 & 0 \end{bmatrix} \quad \text{and} \quad L = \begin{bmatrix} A & B \\ -C & 0 \end{bmatrix},$$

and  $z_k$  is the  $k$ th transmission zero and  $\underline{v}_k$  is the associated right generalized eigenvector.

The transmission zeros are the roots of

$$\det(z_k M - L) = 0 \quad (3.22)$$

$$\det[z_k I - A] \det[C(z_k I - A)^{-1} B] = 0 \quad (3.23)$$

$$\det[z_k I - A] \det[G(z_k)] = 0 \quad (3.24)$$

if there are no pole-zero cancellations, that is  $\det[z_k I - A] \neq 0$ . With this condition, the transmission zeros are the solutions to Equation (3.25).

$$\det[G(z_k)] = 0 \quad (3.25)$$

If the system is a TITOBS system, the transfer function can be expanded as in Equation (3.18). Using the determinant rule in Equation (3.9),

$$\begin{aligned} \det[G(s)] &= [\det(G_r(s) + jG_i(s))] [\det(G_r(s) - jG_i(s))] \\ &= [\det(G_c(s))] [\det(G_c(s^*))] \\ &= G_c(s)G_c(s^*) \end{aligned}$$



since  $G_c(s)$  is a scalar function. Therefore, the transmission zeros of a TITOBS system come from the solution to

$$G_c(s) = 0 \quad \text{and} \quad G_c(s^*) = 0 \quad (3.26)$$

so that if  $z_k$  is a zero of the CCTF,  $G_c(s)$ , it is also a transmission zero of the corresponding TITOBS system, as is  $z_k^*$ .

### 3.4.3 Bode Plots

Frequency domain analysis of linear systems is conducted by employing Bode plots in the case of SISO systems, which can be extended to analysis using singular values in the case of MIMO systems. For the special MIMO case of the TITOBS system, which can be described by a SISO complex coefficient transfer function, an interpretation of the traditional Bode plot can be developed. The Bode plot of the complex system contains the singular value information associated with the typical MIMO singular value plot of the TITOBS system, and also contains phase information associated with Bode plots of real SISO transfer functions.

The singular values,  $\sigma_k(s)$ , of a  $2m \times 2m$  real, linear system are the non-negative square roots of the eigenvalues of the real matrix,  $G(s)G^H(s)$ , where  $2m$  is the number of system inputs and outputs and  $G^H(s)$  is the complex conjugate transpose of  $G(s)$ . In more compact notation,

$$\sigma_k(s) = \left[ \lambda_k \{ G(s)G^H(s) \} \right]^{\frac{1}{2}} \geq 0 \quad (3.27)$$

where the eigenvalues,  $\lambda_k$ , come from Equation (3.28).

$$\det [\lambda_k I - G(s)G^H(s)] = 0 \quad (3.28)$$

If  $G(s)$  is a TITOBS system, it can be partitioned as follows

$$G(s) = \begin{bmatrix} G_r(s) & -G_i(s) \\ G_i(s) & G_r(s) \end{bmatrix} \quad G^H(s) = \begin{bmatrix} G_r^*(s) & G_i^*(s) \\ -G_i^*(s) & G_r^*(s) \end{bmatrix}$$

where the partitioned elements are real coefficient, SISO transfer functions. Substituting the partitioned matrices into (3.28), making use of the rule for the determinant, and simplifying yields (3.29).

$$\begin{aligned} & \det [\lambda_k I - (G_r(s) + jG_i(s))(G_r(s) + jG_i(s))^*] \cdot \\ & \det [\lambda_k I - (G_r(s) - jG_i(s))(G_r(s) - jG_i(s))^*] = 0 \end{aligned} \quad (3.29)$$

Noting the following relations,

$$\begin{aligned} G_c(s) &= G_r(s) + jG_i(s) \\ G_c^*(s^*) &= G_r(s) - jG_i(s) \end{aligned}$$

Equation (3.29) becomes

$$\det [\lambda_k I - G_c(s)G_c^*(s)] \det [\lambda_k I - G_c(s^*)G_c^*(s^*)] = 0 \quad (3.30)$$

with solutions

$$\begin{aligned} \lambda_k &= G_c(s)G_c^*(s) \\ \lambda_k &= G_c(s^*)G_c^*(s^*) \end{aligned}$$

The square roots of these eigenvalues are the minimum and maximum singular values of the TITOBS system. They are also the magnitudes of  $G_c(s)$  and  $G_c(s^*)$ . For  $s = j\omega$ , the singular values of  $G(j\omega)$  are the magnitudes of  $G_c(j\omega)$  and  $G_c(-j\omega)$ , which can be found from the Bode magnitude plot of  $G_c(j\omega)$  for positive and negative frequencies.

The phase of the CCTF  $G_c(s)$  is less well defined than its magnitude. The phase angle of  $G_c(j\omega)$  for  $\omega > 0$  is the amount of phase by which the output *leads* the input. This is not true, however, for negative frequencies. The phase angle of  $G_c(-j\omega)$  for  $\omega > 0$  is the amount of phase by which the output *lags* the input. In order for the phase angle to have the same meaning (output leading the input) for both positive and negative frequencies, the magnitude and phase of  $G_c^*(-j\omega)$  for  $\omega > 0$  is used in the Bode plot of the complex system. The magnitude of  $G_c^*(-j\omega)$  is equal to the magnitude of  $G_c(-j\omega)$ , and the phase of  $G_c^*(-j\omega)$  is the amount of phase by which the output *leads* the input. This convention was adopted by Johnson [12]. An additional advantage of this convention is that a Bode plot of a transfer function with real coefficients will have the same phase for both positive and negative frequencies. The one disadvantage of this convention is that the corresponding complex SISO Nyquist plot is not apparent from inspection of the Bode plot, since  $G_c(j\omega)$  is plotted for both positive and negative frequencies in the Nyquist plot.

The CCTF Bode plots are used extensively in the remainder of this thesis. Adopting the notation of Johnson [12], the transfer function  $G_c(j\omega)$  for  $\omega > 0$  is referred to as the forward transfer function, and  $G_c^*(-j\omega)$  for  $\omega > 0$  is referred

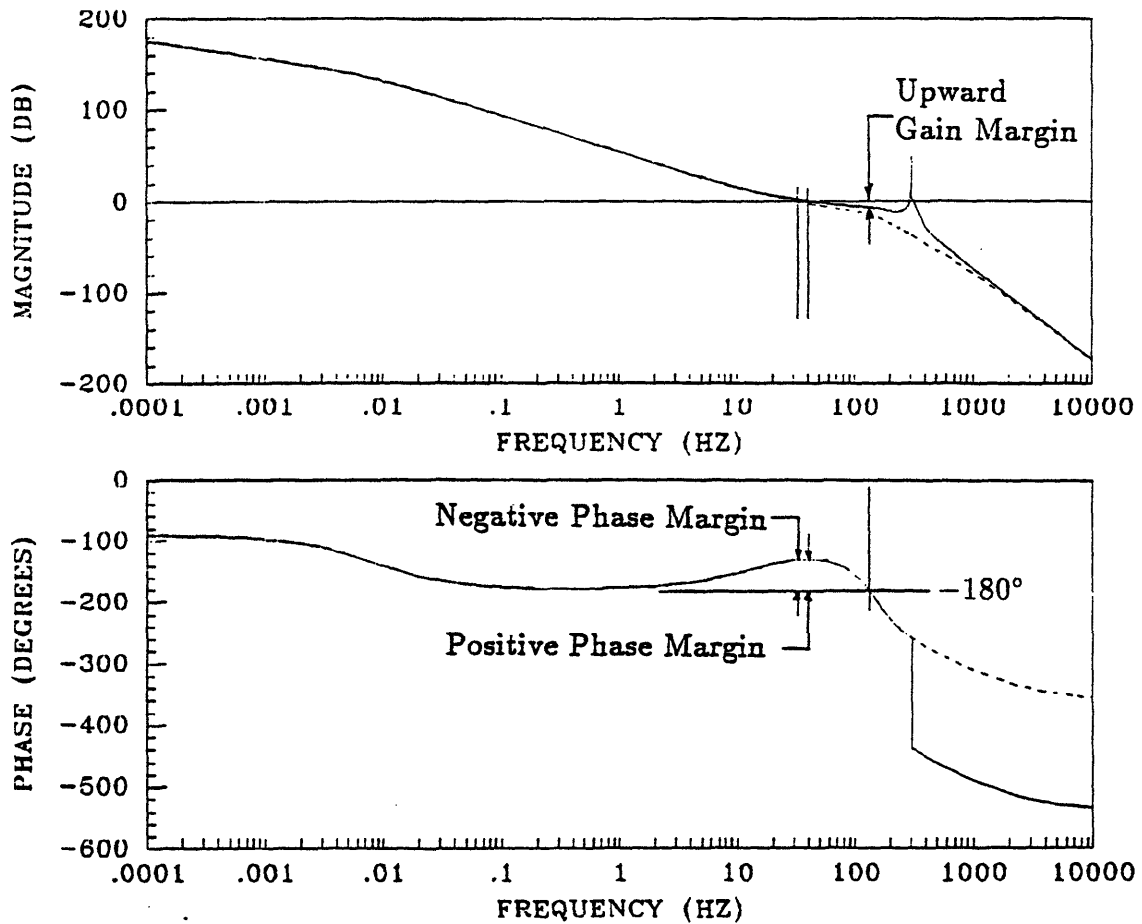


Figure 3.1: Stability Margins in the CCTF Bode Plot

to as the backward transfer function. An example of a Bode plot of a CCTF is shown in Figure 3.1. The solid lines in the plot represent the gain and phase of the forward transfer function, and the broken lines represent the gain and phase of the backward transfer function.

The stability margins that are discussed in the next section can be read off of the CCTF Bode plot. Figure 3.1 shows an open loop CCTF Bode plot with the stability margins indicated. The precise definitions of these margins are discussed in the next section.

The Bode plot interpretation of these margins is similar to that of the traditional margin for real coefficient transfer functions. From the Nyquist stability criterion, the phase of the forward and backward transfer functions cannot pass through  $-180^\circ$  while the magnitude of the respective transfer function is greater than unity. The amount by which the phase of these transfer functions is greater

than  $-180^\circ$  when the magnitudes of the transfer functions are unity is the phase margin. Since the magnitudes of the forward and backward transfer functions can crossover at different frequencies, the positive and negative phase margins can have different values. Another way of stating the Nyquist criterion is that the magnitude of the forward and backward transfer functions must be below unity while the phases of the respective transfer functions pass through  $-180^\circ$ . The upward gain margin is the minimum amount by which the magnitude of either transfer function can be increased before its magnitude becomes unity.

The CCTF Bode plot offers some directional information in terms of the feedback required to stabilize a TITOBS system. Consider the feedback loop in Figure 3.2 and the Bode plot of the CCTF  $G_c(s)$  shown in Figure 3.3. The magnitude plot indicates that the low frequency behavior of the system is that of an integrator, with the magnitude both transfer functions rolling off at  $20\text{ dB/decade}$ . The phase angle of a transfer function with real coefficients is  $-90^\circ$  for an integrator, but the phase at low frequencies in this case is  $0^\circ$  for the forward transfer function and  $-180^\circ$  for the backward transfer function.

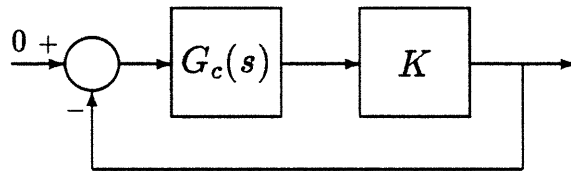


Figure 3.2: Example Feedback Loop

Compensation of this system with a purely real gain,  $K = k_0$ , will result in an unstable closed loop system, since the open loop phase at low frequencies is  $-180^\circ$  for the backward transfer function, while the gain is greater than unity, indicating no phase margin. Therefore, the open loop gain must be of the form  $K = -jk_0$ , where  $k_0$  is a real constant. The multiplication of the loop gain by the negative, pure imaginary gain introduces the “missing” phase needed to bring the phase of both the forward and backward transfer functions to  $-90^\circ$  in agreement with the magnitude plot. (Remember that the backward transfer function is defined to be  $G_c^*(-j\omega)$ .) A Bode plot of the new open loop system of  $-jG_c(s)$ , with  $k_0 = 1$ , is shown in Figure 3.4.

The physical significance of a pure imaginary compensator gain is cross feed-

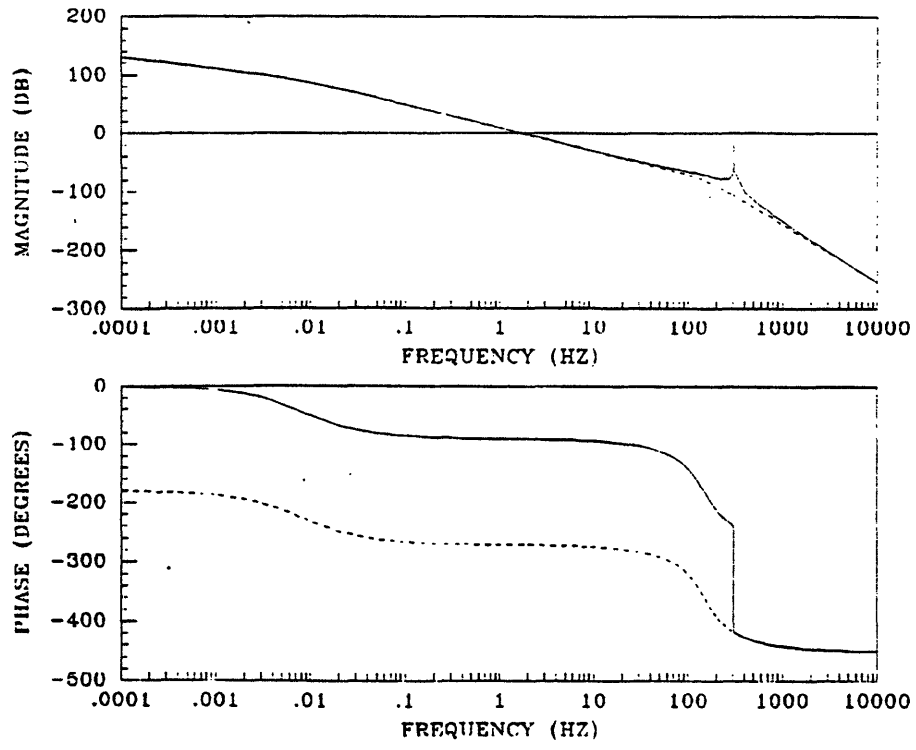


Figure 3.3: CCTF Bode Plot of  $G_c(s)$

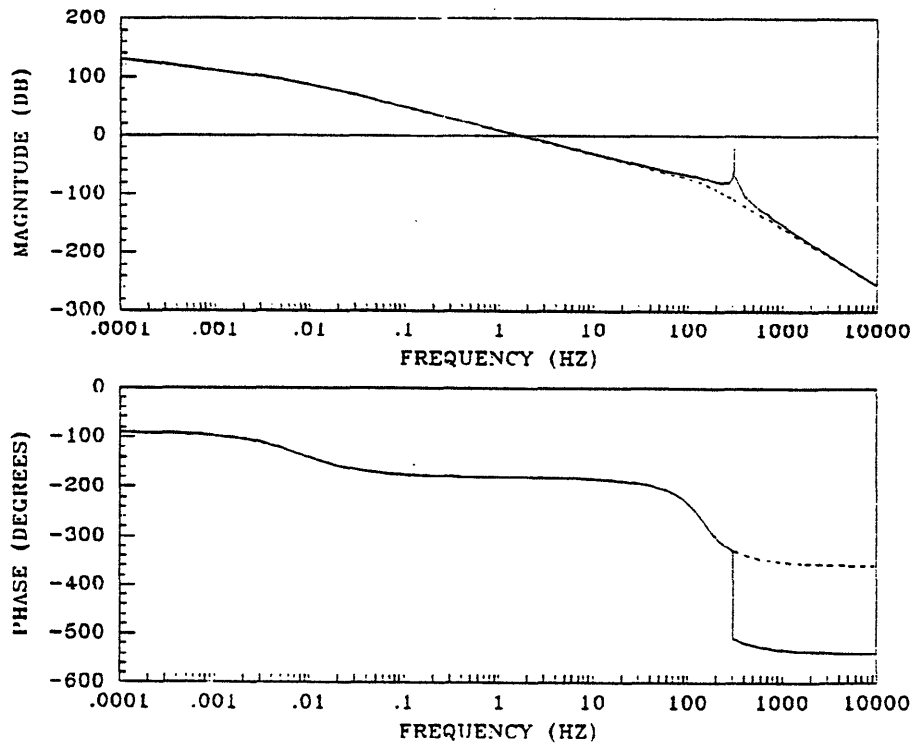


Figure 3.4: CCTF Bode Plot of  $-jG_c(s)$

back. Assuming the control law of the example,

$$u_c = -(-jk_0)y_c$$

and expanding into real and imaginary parts yields

$$\begin{aligned} u_r + ju_i &= jk_0(y_r + jy_i) \\ &= -k_0y_i + jKy_r \end{aligned}$$

The negative imaginary part of the output is feedback to the real part of the input, and the real part of the output is feedback to the imaginary part of the input. For the case of the TITOBS gyro, this would mean that the negative  $y$ -pickoff angle is feedback to the  $x$ -moment command, and the  $x$ -pickoff angle is feedback to the  $y$ -moment command.

### 3.4.4 Complex SISO Nyquist Criterion

The use of the complex method to transform a TITOBS system into a complex SISO system allows the use of the classical Nyquist criterion to investigate the stability of the system. The complex SISO Nyquist criterion is identical to the classical version except that the transfer function in question has complex coefficients.

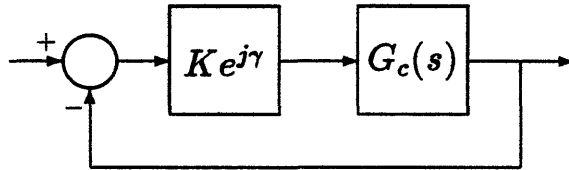


Figure 3.5: Complex Unity Gain Feedback Loop

A complex unity gain feedback system is shown in Figure 3.5. The nominal open loop system is the CCTF  $G_c(s)$ . The perturbation,  $Ke^{j\gamma}$ , is the complex form of a block symmetric perturbation to the nominal TITOBS plant,  $G(s)$ . The nominal closed loop poles of the system are the zeros of the complex coefficient characteristic equation,

$$1 + G_c(s) = 0 \tag{3.31}$$

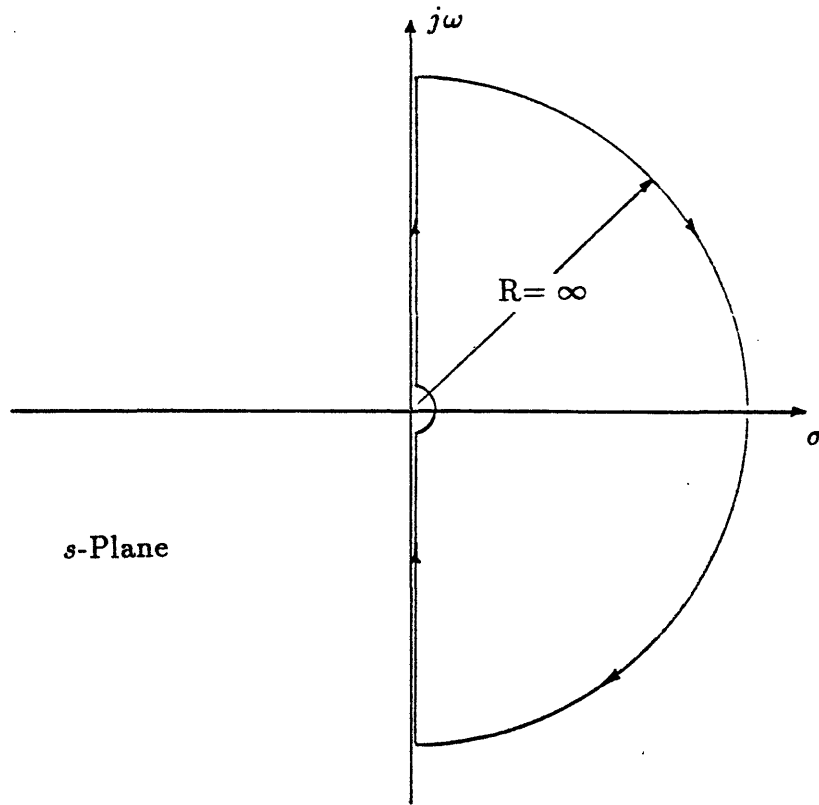


Figure 3.6: Nyquist Contour

In order for the closed loop system to be stable, the number of closed loop poles in the right half  $s$ -plane,  $Z$ , must be zero. Stability of the system can be determined by using the Nyquist criterion, which can be written as

$$N = N \{-1, G_c(s), N_R\} = P - Z \quad (3.32)$$

where  $N$  is the number of counterclockwise encirclements of the  $-1$  point by the clockwise mapping of the Nyquist contour,  $N_R$ , by  $G_c(s)$ . The Nyquist contour is chosen to enclose the open right half  $s$ -plane as shown in Figure 3.6.  $P$  is the number of poles of  $G_c(s)$  encircled by  $N_R$  in the  $s$ -plane, and  $Z$  is the number of zeros of  $G_c(s)$  encircled by  $N_R$  in the  $s$ -plane. Again, for stability  $Z$  must be zero, so the Nyquist criterion is

$$N = N \{-1, G_c(s), N_R\} = P \quad (3.33)$$

This is the usual SISO Nyquist criterion except that the open loop transfer function,  $G_c(s)$ , is a CCTF. The resulting complex SISO Nyquist plot is not

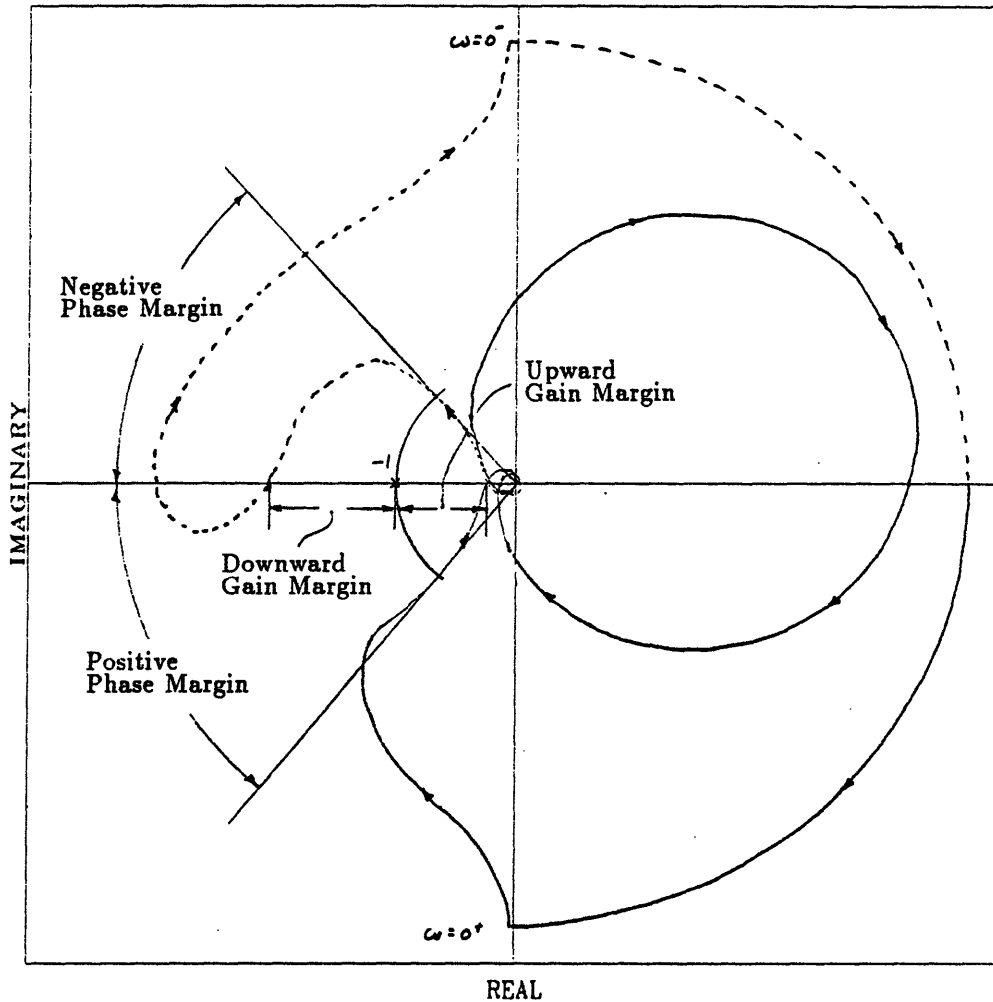


Figure 3.7: Complex SISO Nyquist Plot of a TITOBS System

symmetric about the real axis. An example of a complex SISO Nyquist plot is shown in Figure 3.7. The solid line represents the plot of  $G_c(s)$  for the part of  $N_R$  above the real axis in the  $s$ -plane while the broken line represents the plot of  $G_c(s)$  for the part of  $N_R$  below the real axis. The lack of conjugate symmetry of  $G_c(s)$  can be clearly seen in the plot.

Gain and phase margins for the complex system are defined in the usual way from the complex SISO Nyquist plot. These gain and phase margins are labeled in Figure 3.7. Referring to the complex perturbation in Figure 3.5, the gain and phase margins are defined as follows. The upward and downward gain margin is the amount by which the gain,  $K$ , can be increased and decreased on all feedback paths simultaneously with  $\gamma = 0$  before the number of encirclements of the  $-1$  point changes, and the system becomes unstable. Similarly, the negative and



positive phase margin is the amount by which the phase,  $\gamma$ , can be increased and decreased on all feedback paths simultaneously with  $K = 1$  before the number of encirclements of the  $-1$  point changes, and the system becomes unstable. These stability margins are valid for the real TITOBs system only if the perturbations are block symmetric. These complex stability margins will be used extensively in the remainder of this thesis.

### 3.4.5 Linear Quadratic Regulators

Feedback controllers for block symmetric systems which are based on linear quadratic design methodologies have block symmetric form. This result is summarized by Johnson [12]. This is important since it allows the use of the CCTF Bode plots and complex SISO Nyquist plots with linear quadratic regulator (LQR) designs. This result also applies to Kalman filter designs and linear quadratic Gaussian (LQG) problems.

Consider the deterministic LQR problem of designing a feedback controller to minimize the quadratic cost functional,

$$J = \int_0^{\infty} [\underline{x}^T(t)Q_{xx}\underline{x}(t) + 2\underline{x}^T(t)Q_{xu}\underline{u}(t) + \underline{u}^T(t)Q_{uu}\underline{u}(t)] dt$$

starting from an initial condition,  $\underline{x}(0)$ , for the stabilizable linear system given by

$$\dot{\underline{x}}(t) = A\underline{x}(t) + B\underline{u}(t).$$

The state weighting matrix,  $Q_{xx}$ , is positive semi-definite, and the control weighting matrix,  $Q_{uu}$ , is positive definite. The optimal steady state feedback control law is

$$\underline{u}(t) = -G\underline{x}(t).$$

If the system is block symmetric and the weighting matrices,  $Q_{xx}$ ,  $Q_{xu}$ , and  $Q_{uu}$  are block symmetric, then the resulting optimal feedback gain matrix,  $G$ , is block symmetric. Furthermore, the closed loop system matrix,  $A - BG$ , is also block symmetric.

### 3.5 Implementation of Block Symmetric Compensators

In this section, the use of the complex method is examined for the digital implementation of block symmetric compensators. The use of the complex representation of a block symmetric compensator offers the possibility of reduced storage requirements over implementation of the real compensator. Two types of block symmetric compensators are analyzed: gain compensators and dynamic compensators.

The implementation of the discrete control law,

$$\underline{u}[n] = -G\underline{y}[n] \quad (3.34)$$

where  $G$  is a  $2m \times 2m$  matrix, and there are  $2m$  system outputs ( $\underline{y}$ ) and  $2m$  controls ( $\underline{u}$ ), requires the storage of the feedback gain matrix,  $G$ . Storage space is needed for  $4m^2$  real numbers.

If the system is block symmetric, (3.34) can be partitioned as,

$$\begin{bmatrix} \underline{u}_r[n] \\ \underline{u}_i[n] \end{bmatrix} = - \begin{bmatrix} G_r & -G_i \\ G_i & G_r \end{bmatrix} \begin{bmatrix} \underline{y}_r[n] \\ \underline{y}_i[n] \end{bmatrix} \quad (3.35)$$

which can be reduced to

$$\underline{u}_c[n] = -G_c \underline{y}_c[n] \quad (3.36)$$

where

$$\begin{aligned} G_c &= G_r + jG_i \\ \underline{u}_c[n] &= \underline{u}_r[n] + j\underline{u}_i[n] \\ \underline{y}_c[n] &= \underline{y}_r[n] + j\underline{y}_i[n] \end{aligned}$$

The  $m \times m$  gain matrix,  $G_c$ , has  $m^2$  complex elements. Storage of the real and imaginary parts of these elements requires memory for  $2m^2$  real numbers, or half of the memory required for the block symmetric gain matrix.

A dynamic compensator has the form

$$\dot{\underline{z}}(t) = F\underline{z}(t) + G\underline{y}(t) \quad (3.37)$$

$$\underline{u}(t) = H\underline{z}(t) \quad (3.38)$$

where there are  $2m$  inputs and outputs and  $2n$  states,  $\underline{z}$ . The discrete version of the compensator is assumed to have the form

$$\underline{z}[n+1] = F'\underline{z}[n] + G'\underline{y}[n] \quad (3.39)$$

$$\underline{u}[n] = H'\underline{z}[n] \quad (3.40)$$

where

$$\begin{aligned} F' &= e^{FT} \\ G' &= \int_0^T e^{F\tau} G d\tau \\ H' &= H \end{aligned}$$

and where  $T$  is the sampling interval. Implementation of these equations requires that the matrices  $F'$ ,  $G'$ , and  $H'$  be stored in the computer. Storage for  $4n^2 + 8mn$  real numbers is needed.

If the compensator is block symmetric, then the memory required can again be reduced by a factor of two, to  $2n^2 + 4mn$  if the complex version of the equations is used. The complex system is found in the same manner as in Equations (3.6) through (3.7).

There is no savings of the amount of required mathematical operations in either case. Although the sizes the matrices and vectors are reduced by the use of the complex method, the subsequent arithmetic becomes complex. There is no reduction in the number of real arithmetic operations in a matrix-vector multiplication, as is performed in a compensator, when the complex method is used.

There can be a savings of arithmetic operations when a matrix-matrix multiplication is performed. The multiplication of two  $2n \times 2n$  real, block symmetric matrices requires  $8n^3$  real multiplies and  $4n^2(2n-1)$  real adds. The multiplication of the two corresponding complex  $n \times n$  matrices requires  $4n^3$  real multiplies and  $2n^2(2n-1)$  real adds, a savings of a factor of two. This suggests that a computational savings can be made in design and analysis by taking advantage of the complex method. However, present design software, such as MATRIXX and Control-C, do not allow complex matrices in many numerical routines, such as Riccati equation solvers. Furthermore, these built-in routines are fast enough such that making them faster would not speed the design process significantly.

## 3.6 Summary

In this chapter some properties of block symmetric matrices and systems are presented. The complex method can be used to transform a TITOBS system into a complex SISO system. The complex coefficient transfer function is a frequency domain description of the complex SISO system, and the classical SISO design tools, Bode and Nyquist plots, can be extended to CCTF systems. Finally, the use of the complex form of a block symmetric system in the design and implementation of compensators is investigated.

## Chapter 4

# Open Loop Gyro Characteristics

In this chapter, the model of the open loop gyro is discussed, and numerical values for the complex, linear model are introduced. The open loop complex frequency response, from the commanded complex moment input to the complex pickoff angle output, is examined, and a modal analysis is performed, comparing the complex modes to their real counterparts. The addition of required loop dynamics to the gyro model is discussed and the design plant model is defined.

### 4.1 Numerical Values

The numerical values of the parameters discussed in Chapter 2 are shown in Table 4.1. The rotor spin speed in Chapter 2,  $\omega_s$ , in *radians/sec*, is  $2\pi f_s$ . Substituting these values into Equations (2.35) and (2.36) yields the state space representation of the open loop gyro model in Equations (4.1) and (4.2).

$$\begin{bmatrix} \dot{\theta}_c \\ \ddot{\theta}_c \end{bmatrix} = \begin{bmatrix} 0 & 1 \\ j95.8333 & (-0.2083 + j1916.67) \end{bmatrix} \begin{bmatrix} \theta_c \\ \dot{\theta}_c \end{bmatrix} + \begin{bmatrix} 0 \\ 62.2292 \end{bmatrix} M'_c + \begin{bmatrix} 0 \\ j1916.67 \end{bmatrix} \dot{\phi}_c + \begin{bmatrix} 0 \\ -1 \end{bmatrix} \ddot{\phi}_c \quad (4.1)$$

$$\theta'_c = \begin{bmatrix} 3490.66 & 0 \end{bmatrix} \begin{bmatrix} \theta_c \\ \dot{\theta}_c \end{bmatrix} \quad (4.2)$$

The open loop transfer function defined in Equation (2.39) is shown in Equation (4.3).

$$G_p(s) = \frac{217221.0}{s^2 - (-0.20833 + j1916.67)s - j95.8333} \quad (4.3)$$

Table 4.1: Gyro Model Numerical Values

Gyro Parameter	Symbol	Value	Units
Rotor spin speed	$f_s$	200	$Hz$
Polar moment of inertia	$I_{gz}$	7.32	$gm\text{-}cm^2$
Transverse moment of inertia	$I_{rr}$	4.80	$gm\text{-}cm^2$
Rotor angular momentum	$H$	9200	$dyne\text{-}cm\text{-}sec$
Gyro viscous damping	$D_R$	1.0	$dyne\text{-}cm\text{-}sec$
Quadrature time constant	$\tau$	20.0	$sec$
Pickoff gain	$K_{PO}$	200000	$mV/rad$
Torquer gain	$K_T$	5.2133	$dyne\text{-}cm/mV$

The eigenvalues of the complex  $A_p$  matrix are shown below.

$$\lambda_1 = -0.05 + j0.00000413$$

$$\lambda_2 = -.15833 + j1916.7$$

The first eigenvalue corresponds to the quadrature mode, the first order damping due to the quadrature time constant discussed in Chapter 2. The second corresponds to the lightly damped nutation mode. It has a natural frequency of  $f_n = 305.05 Hz$ , and damping, due to the viscous damping term,  $D_R$ , of  $\zeta_n = 8.26 \times 10^{-5}$ . The frequency of the nutation is determined by the rotor spin speed and rotor moments of inertia.

$$f_n = \frac{I_{gz}}{I_{rr}} f_s$$

The eigenvectors corresponding to the eigenvalues above are

$$\underline{v}_1 = \begin{bmatrix} 0.59296 + j0.80368 \\ -0.02965 - j0.04018 \end{bmatrix}$$

$$\underline{v}_2 = \begin{bmatrix} -6.0548 \times 10^{-8} - j5.2174 \times 10^{-4} \\ 0.9999998 - j3.3448 \times 10^{-5} \end{bmatrix}$$

A bode plot of the CCTF,  $G_p(s)$ , is shown in Figure 4.1. The solid lines in the plot correspond to positive frequencies, and the broken lines correspond to negative frequencies. In the magnitude plot, the responses for the positive and negative frequencies correspond to the maximum and minimum singular values of the corresponding real, TITOBS system. Note the lightly damped nutation resonance.

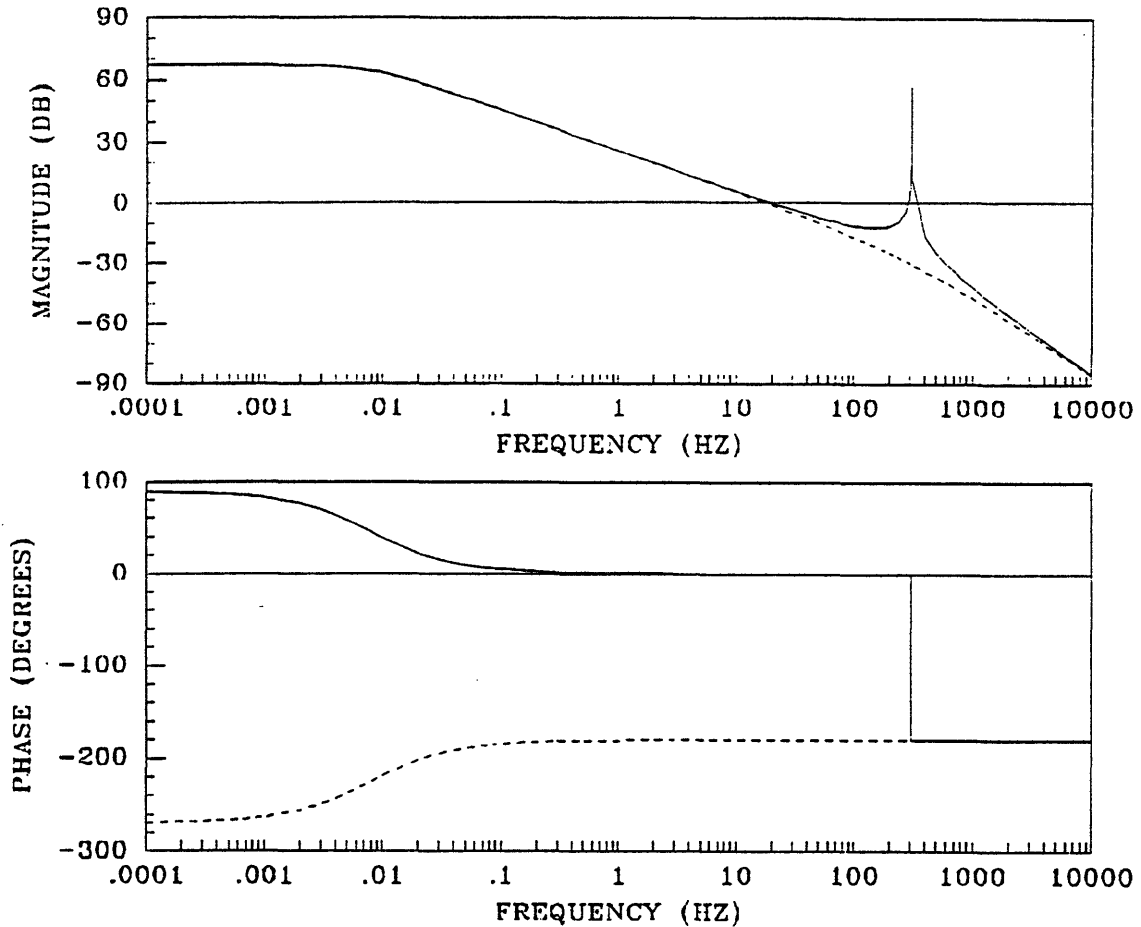


Figure 4.1: Bode Plot of the Gyro CCTF,  $G_p(s)$

## 4.2 Complex Modes

The complex method provides an alternate view of the gyro modes. The eigenvalues of the complex system contain some directional information. If the real, TITOBS system is analyzed, this directional information can only be found from the eigenvectors. This result is discussed in detail by Johnson [12].

Figure 4.2 shows a plot of the response of the real TITOBS gyro to an initial condition selected to excite the quadrature mode only. Both pickoff angles,  $\theta_x$  and  $\theta_y$ , have an essentially first order decay with the time constant,  $\tau = 20 \text{ sec}$ . In comparison, Figure 4.3 shows a plot of the response of the complex pickoff angle to the corresponding complex initial condition. The imaginary part of the complex pickoff angle is plotted versus its real part. Here the complex pickoff angle approaches the origin asymptotically.

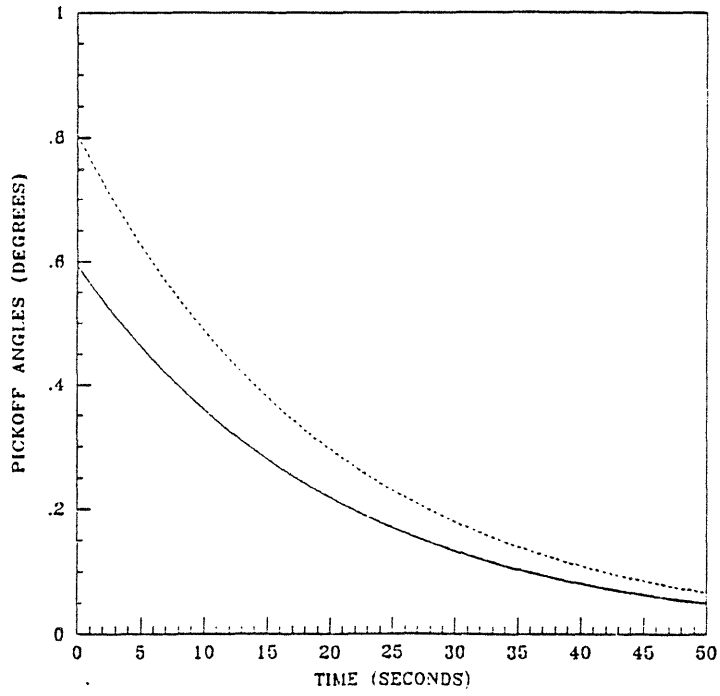


Figure 4.2: Real TITOBS System Quadrature Mode Time Response

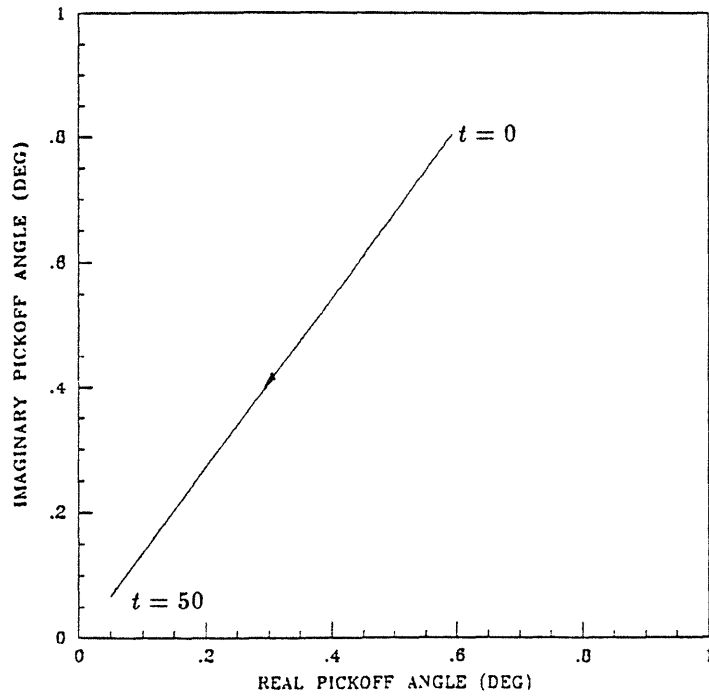


Figure 4.3: Complex System Quadrature Mode Time Response



Figure 4.4 shows a plot of the response of the real TITOBS gyro to an initial condition selected to excite the nutation mode only. Both pickoff angles,  $\theta_x$  and  $\theta_y$ , have a lightly damped sinusoidal oscillation at the nutation frequency of approximately 305 Hz;  $\theta_x$  leads  $\theta_y$  by  $90^\circ$ .

Figure 4.5 shows a plot of the response of the complex pickoff angle due to the corresponding complex initial condition. The imaginary part of the complex pickoff angle is plotted versus its real part. The complex pickoff angle spirals toward the origin of the complex plane in a counterclockwise manner. The direction of the spiral can be predicted by the sign of the complex part of the eigenvalue. A positive sign, as is the case here, indicates a counterclockwise spiral. A negative imaginary part indicates a clockwise spiral.

### 4.3 Design Plant Model

In order to meet performance specifications, certain dynamics are required to be included in the forward loop of the torque–rebalance loop. A block diagram of the torque–rebalance loop is shown in Figure 4.6. The gyro is denoted by  $G_p(s)$  while the required dynamics are a demodulation filter,  $G_d(s)$ , and an integrator. These, along with a notch filter which is not shown, are discussed below. For compensator design, the gyro plant is augmented with the demodulation filter and the integrator at the plant output to form the *design plant model*,  $G_x(s)$ .

$$G_x(s) = \frac{1}{s} G_d(s) G_p(s) \quad (4.4)$$

In state space form, the augmented plant is

$$\dot{\underline{x}}(t) = A_x \underline{x}(t) + B_x u_p(t) \quad (4.5)$$

$$y(t) = C_x \underline{x}(t) \quad (4.6)$$

which can be partitioned into

$$\begin{bmatrix} \dot{x}_i \\ \dot{x}_d \\ \dot{x}_p \end{bmatrix} = \begin{bmatrix} 0 & C_d & 0 \\ 0 & A_d & B_d C_p \\ 0 & 0 & A_p \end{bmatrix} \begin{bmatrix} x_i \\ x_d \\ x_p \end{bmatrix} + \begin{bmatrix} 0 \\ 0 \\ B_p \end{bmatrix} u_p$$

$$y = \begin{bmatrix} 1 & 0 & 0 \end{bmatrix} \begin{bmatrix} x_i \\ x_d \\ x_p \end{bmatrix}$$

This is outlined in Figure 4.6. A Bode plot of  $G_x(s)$  is shown in Figure 4.7.

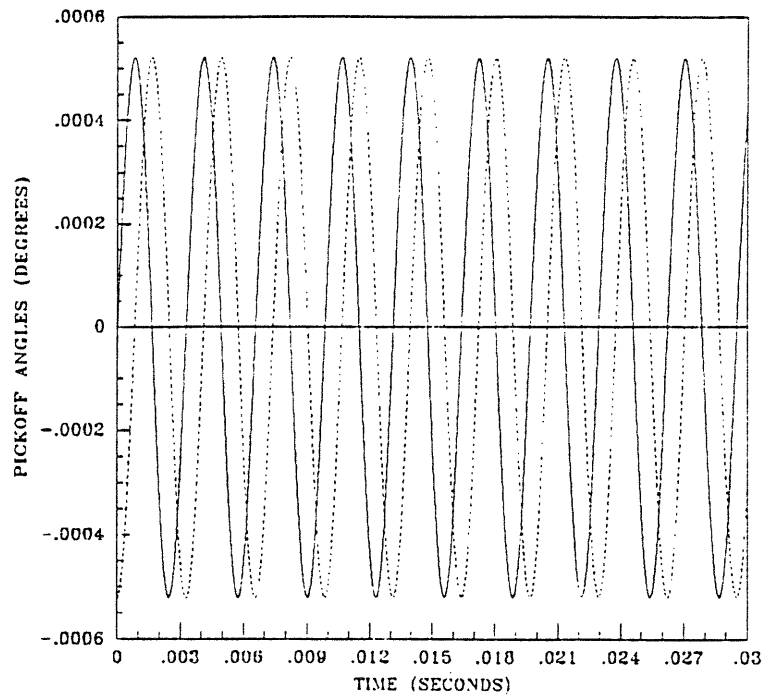


Figure 4.4: Real TITOBS System Nutation Mode Time Response

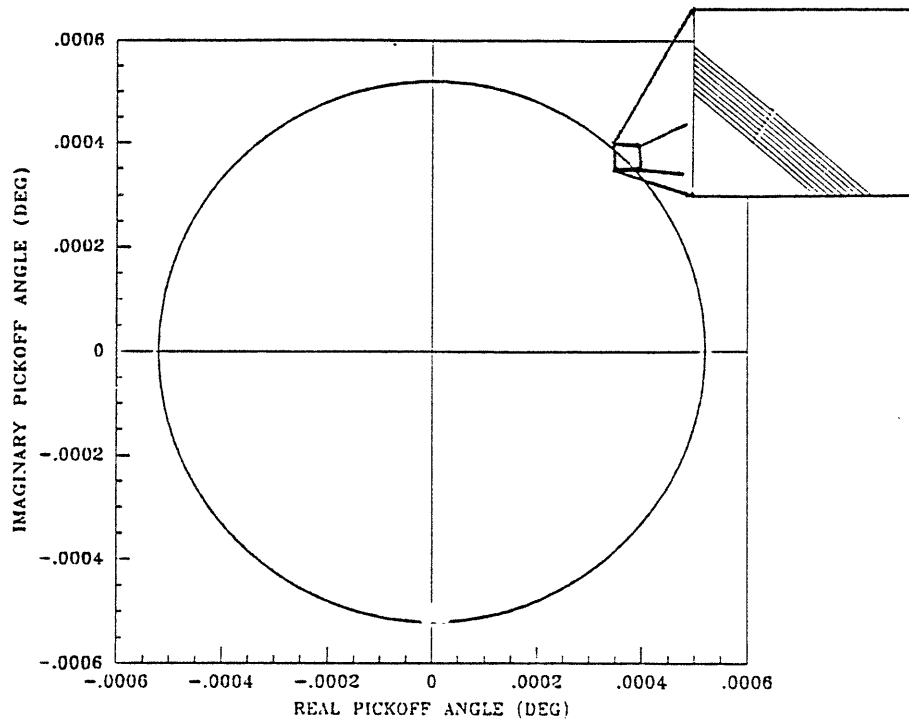


Figure 4.5: Complex System Nutation Mode Time Response

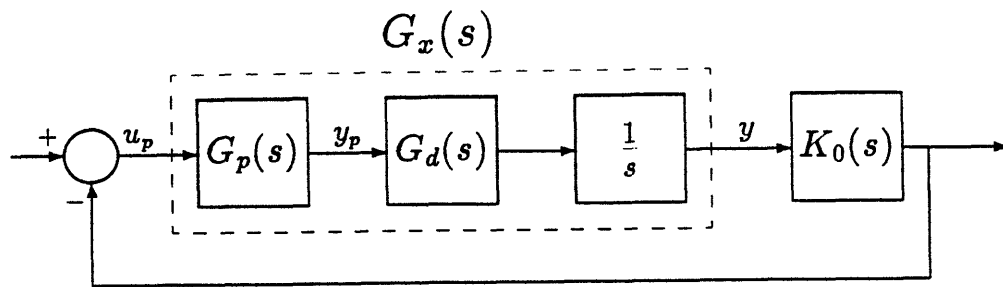


Figure 4.6: Torque-Rebalance Loop with Augmented Plant

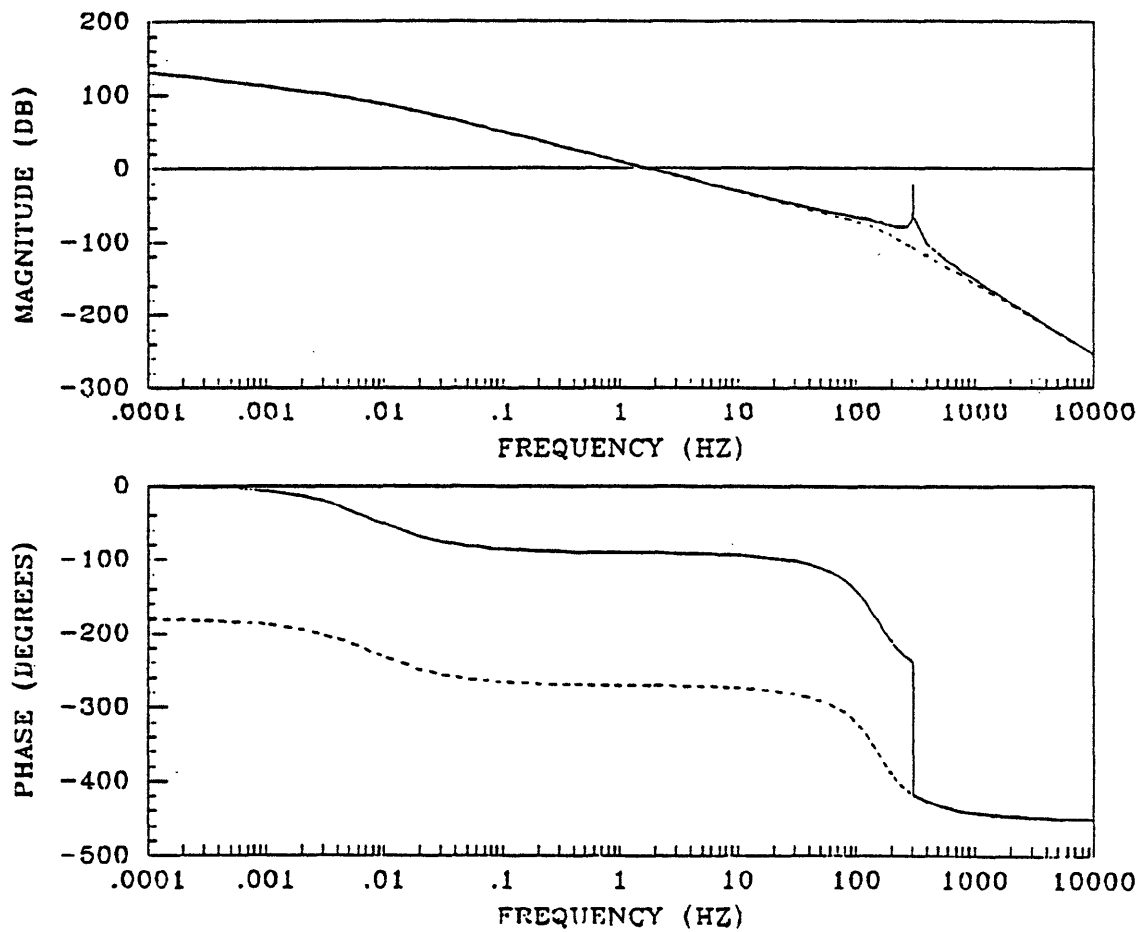


Figure 4.7: Design Plant Model Bode Plot

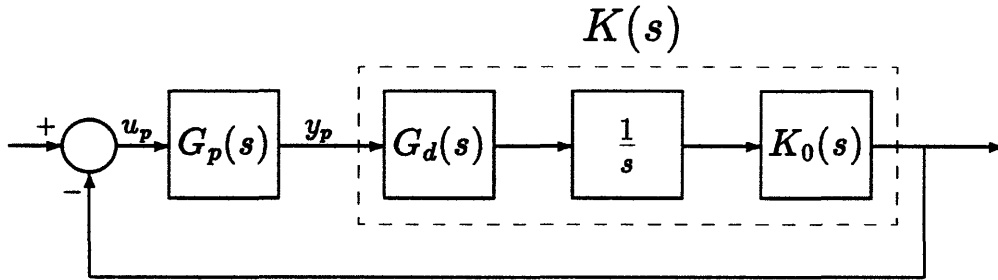


Figure 4.8: Torque-Rebalance Loop with Augmented Compensator

The compensator,  $K_0(s)$ , is designed with respect to the design plant model. Once the compensator is designed, the required dynamics are absorbed into the compensator at the compensator input to form the final compensator,  $K(s)$ .

$$K(s) = \frac{1}{s} K_0(s) G_d(s) \quad (4.7)$$

The resulting feedback loop is shown in Figure 4.8.

### 4.3.1 Integrator

One design requirement is that there be zero steady state error in commanded moment when the gyro case is subjected to a step input in inertial angular rate,  $\dot{\phi}_c$ . This requires a Type I system which is achieved through the addition of an integrator into the forward loop. With the integrator in the loop, the torquers precess the rotor at a rate equal to  $\dot{\phi}_c$ . Clearly, if there were a steady state error in the commanded moment, the rotor would eventually hit the stops. An integrator in a CCTF is equivalent to an integrator on each output of the real, TITOBS system.

In some cases, a Type II system is required so that there is zero steady state error in commanded moment to a step input in inertial angular acceleration. However, only Type I systems are considered in this thesis.

### 4.3.2 Demodulation Filter

The gyro pickoff/signal generator modulates the pickoff angle information on a high frequency carrier signal. The high frequency roll off of the torque-rebalance loop frequency response is desired to be as great as possible such that

the attenuation at the carrier frequency is high. The attenuation is increased by including a low pass demodulation filter at the gyro output. The filter used in this thesis is a second order low pass filter of the form shown in Equation (4.8).

$$G_d(s) = \frac{\omega_d^2}{s^2 + 2\zeta_d\omega_d s + \omega_d^2} \quad (4.8)$$

where

$$\omega_d = 2\pi \cdot 150 \text{ Hz}$$

$$\zeta_d = 0.5.$$

The filter can also be described in state space form by the appropriate system matrices,  $A_d$ ,  $B_d$ , and  $C_d$ . The filter is placed on both outputs of the TITOBS system so the CCTF in Equation (4.8) has real coefficients. The poles of  $G_d(s)$  are  $-471 \pm j816.35$ .

### 4.3.3 Spin Frequency Notch Filter

Another design requirement is the implementation of a notch filter at the gyro rotor spin frequency of 200 Hz. This is required because it is expected that there is a large amount of noise in the gyro output at this frequency, and it is undesirable for the moment command to contain this noise, since it is the output of the loop. The notch filter is not included in the design plant model because different design methodologies require that it be implemented in different ways in the compensator,  $K_0(s)$ .

For designs which require a notch filter to be explicitly included in the compensator, such as lead compensation, the transfer function of a suitable notch filter is shown below in Equation (4.9).

$$G_n(s) = \frac{s^2 + 2\zeta_z\omega_z s + \omega_n^2}{s^2 + 2\zeta_p\omega_n s + \omega_n^2} \quad (4.9)$$

where

$$\omega_n = 2\pi \cdot 200 \text{ Hz}$$

$$\zeta_z = 0.00001$$

$$\zeta_p = 0.167.$$

The filter can also be described in state space form by the appropriate system matrices,  $A_n$ ,  $B_n$ ,  $C_n$ , and  $D_n$ . The filter is placed on both outputs of the real,

TITOBS system so the CCTF in Equation (4.9) has real coefficients. The poles of  $G_n(s)$  are  $-209.86 \pm j1239.0$ , and the zeros are  $-0.001256 \pm j1256.6$ .

## 4.4 Summary

In this chapter, numerical values of the gyro parameters are introduced into the gyro model. The open loop response of the gyro is examined in the frequency domain and in the time domain. The forward loop dynamics, required to meet performance specifications, are discussed, and the gyro model is augmented with these dynamics to form the design plant model.

# Chapter 5

## Design Methodologies

The design methodologies employed in this thesis for the design of two-degree-of-freedom, dynamically tuned gyro torque-rebalance loop controllers are described in this chapter. After some background on the design of TDF-DTG controllers, an overview of the design methodologies used and the overall design approach taken is presented. Then each of the methodologies is described and applied to the complex form of the linear gyro model. The design results and the characteristics of the design methodologies are compared in Chapter 6.

### 5.1 Background

Very little work has been published on the design of controllers specifically for strapdown tuned gyros. A NASA report [15] used complex root locus and bode techniques for controller design. The complex root locus was also used in [11]. Another NASA report [3] compared the performance of a controller with both auto and cross feedback to a controller designed to diagonalize the system transfer function matrix. The report found little difference in the performance of the two designs. The use of modern control design methodologies on the TDF-DTG problem has only been examined relatively recently in an internal CSDL memo [16]. In it, the performance of some optimal regulators are compared to a classical lead compensation design. It was found that an optimal regulator design could be used to significantly extend the bandwidth of the torque-rebalance loop beyond that possible with classical designs.

## 5.2 Overview of Methodologies and Design Approach

The primary goal of this thesis is to compare multivariable design methodologies in the design of TDF–DTG torque–rebalance loop controllers. The design methodologies considered in this chapter are classical first order lead compensation of the complex system, linear quadratic Gaussian with loop transfer recovery (LQG/LTR), frequency weighted linear quadratic Gaussian (FW/LQG), and LQG/LTR with formal loop shaping (FLS/LQG/LTR). Two loop design bandwidths are considered for the gyro model used in this thesis, a low (50 Hz) bandwidth design and a high (100 Hz) bandwidth design. Each design methodology is used to generate a 50 Hz bandwidth design, which is nearly the maximum attainable with lead compensation, and the remaining methodologies are also used to generate 100 Hz bandwidth designs. This approach allows comparison of all of the methodologies for the low bandwidth design and a comparison of the multivariable designs at the higher bandwidth that they allow.

The feedback loop considered in the design and analysis of the TDF–DTG torque–rebalance loop is shown in Figure 5.1. The signals  $u_p$  and  $y_p$  are the moment command input and pickoff angle output of the gyro, respectively. The reference input signal,  $u_{pi}$ , is fictitious and is equal to zero. Therefore, the output of the loop,  $u_{po}$ , is the negative of the moment command to the gyro. The transfer function from  $u_{pi}$  to  $u_{po}$  is used as a measure of loop performance, since the moment command to the gyro, the output of the loop, is a measure of the inertial angular rate applied to the gyro case.

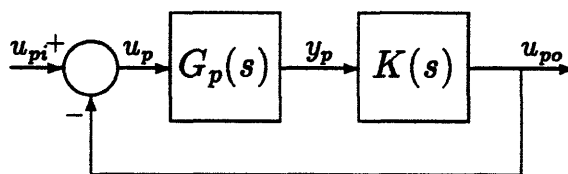


Figure 5.1: Design Feedback Loop

The design tools discussed in Chapter 3 are used extensively to determine the performance and stability margins of the designs. With reference to Figure 5.1, Bode plots of the open loop transfer function from the plant moment command



input to the output of the compensator,  $K(s)G_p(s)$ , are used to determine the velocity error constant,  $K_v$ , which is used as an indication of steady state errors in pickoff angle and moment command due to step inputs of angular acceleration. Nyquist plots of the same transfer function are used to determine the stability margins of the complex description of the system. Bode plots of the closed loop transfer function from the fictitious signal,  $u_{pi}$ , to the compensator output are used to determine loop bandwidth and  $M_p$ , the maximum closed loop peaking within the bandwidth. The bandwidth of the system is considered to be the frequency at which the magnitude falls below  $-3 dB$  or the phase falls below  $-90^\circ$ , whichever is lower on either the forward or backward transfer function. The gain of the closed loop system at  $10 kHz$  is used as a measure of the high frequency attenuation. The response of the closed loop system to a step in inertial angular rate applied to the gyro case is also used as a measure of system performance. The maximum deviation of the pickoff angles from null, time required to drive the pickoff angles back to null, and the peak overshoot and settling time of the moment commands are examined.

## 5.3 Lead Compensation Design

### 5.3.1 Description of Design Methodology

Lead compensation of a complex system is identical to classical lead compensation of real SISO systems except that the compensator gain may be complex. The first order lead compensator has the form shown in Equation (5.1)

$$K_L(s) = K \left[ \frac{\frac{s}{a} + 1}{\frac{s}{b} + 1} \right] \quad a < b \quad (5.1)$$

where  $a$  and  $b$  are real and  $K$  is a generally complex gain.

The notch filter described in Equation (4.9) must be explicitly included in the compensator, so the design plant model is augmented with the notch filter before the lead compensator is designed. A Bode plot of the gyro augmented with an integrator, demodulation filter, and with the notch filter is shown in Figure 5.2. The design goal is to select  $K$ ,  $a$ , and  $b$  in order to obtain the desired closed loop bandwidth and stability margins.

### 5.3.2 Low Bandwidth Design

With reference to Figure 5.2 and the discussion of CCTF Bode plot interpretations in Chapter 3, it is clear that the lead compensator gain,  $K$ , must be purely imaginary and negative. The resulting compensator output,  $u_{po}$ , is returned to the gyro input,  $u_p = M'_c$  with negative feedback. The TITOBS interpretation of this is cross feedback with no auto feedback. That is,

$$M'_c = jK(s)\theta'_c$$

or

$$M'_x = -K(s)\theta'_y$$

$$M'_y = K(s)\theta'_x$$

where  $K(s)$  is the real coefficient, augmented compensator: the lead compensator with integrator, demodulation filter, and notch filter. The compensator,  $K(s)$ , is placed on both outputs of the TITOBS System.

In order to achieve a bandwidth of 50 Hz, the lead compensator pole,  $b$ , is placed at  $s = -2\pi \cdot (1000 \text{ Hz}) \approx -6283.2$  so that its phase contribution is

Table 5.1: Lead Compensator Poles and Zeros

Poles	Zeros
0.0	-80.0
-6238.2	$-0.001256 + j1256.6$
$-209.86 + j1239.0$	$-0.001256 - j1256.6$
$-209.86 - j1239.0$	
$-471.00 + j816.35$	
$-471.00 - j816.35$	

negligible at 50 Hz. Then the magnitude of  $K$  and the zero location,  $a$ , are adjusted so that the bandwidth requirement could be met while maintaining reasonable phase margins. Care is exercised to keep the zero location far enough away from the origin to prevent slowing of the step response of the loop. The final lead compensator design is shown in Equation (5.2).

$$K_L(s) = -j170 \left[ \frac{\frac{s}{80} + 1}{\frac{s}{6283.2} + 1} \right] \quad (5.2)$$

A Bode plot of the overall compensator,  $K(s)$ : lead compensator augmented with the notch filter, demodulation filter, and integrator, is shown in Figure 5.3. Note that the magnitude of the forward and backward transfer functions are identical, indicating no coupling between the channels of the TITOBS compensator. The compensator poles and zeros are listed in Table 5.1, and the compensator integrator gain is  $-j170$ , giving a velocity error constant of 110.9 dB. A Bode plot of the compensated open loop system is shown in Figure 5.4 while a Bode plot of the closed loop system is shown in Figure 5.5. The system has a  $-90^\circ$  bandwidth of just over 50 Hz and a  $-3$  dB bandwidth of 145 Hz. The  $M_p$  of the forward transfer function is 3.95 dB while the  $M_p$  of the backward transfer function is 2.37 dB. The closed loop gain at 10 kHz is  $-170$  dB. The closed loop poles of the system are listed in Table 5.2.

The response of the system to a 1 deg/sec step in the  $y$ -axis inertial angular rate, or  $\dot{\phi}_c = j$  1deg/sec, is shown in Figure 5.6. The real and imaginary parts of the pickoff angle and the real and imaginary parts of the commanded moments are plotted versus time. Related to the TITOBS system, the real and imaginary parts are the  $x$ -axis and  $y$ -axis pickoff angles and  $x$ -axis and  $y$ -axis moment commands, respectively. The solid lines denote the  $x$ -axis response and

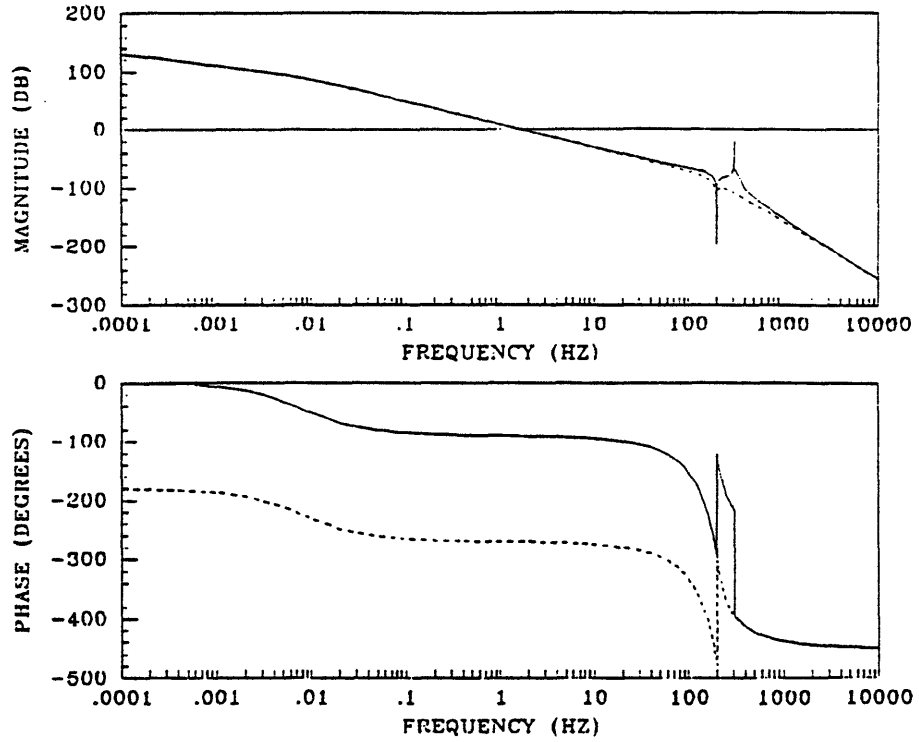


Figure 5.2: Design Plant Model Augmented with Notch Filter Bode Plot

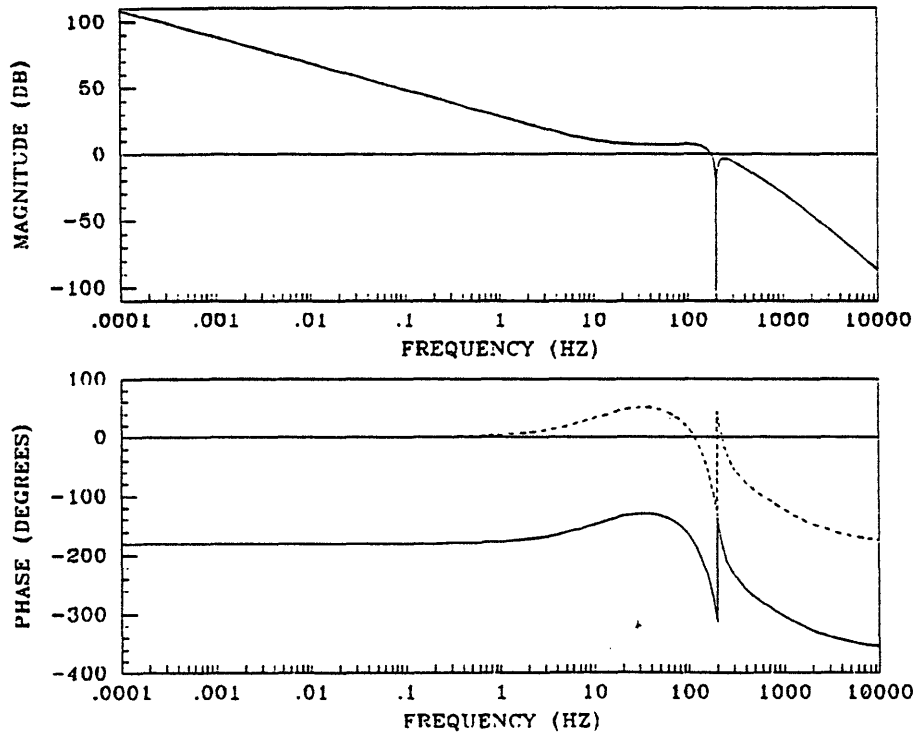


Figure 5.3: Augmented Lead Compensator Bode Plot

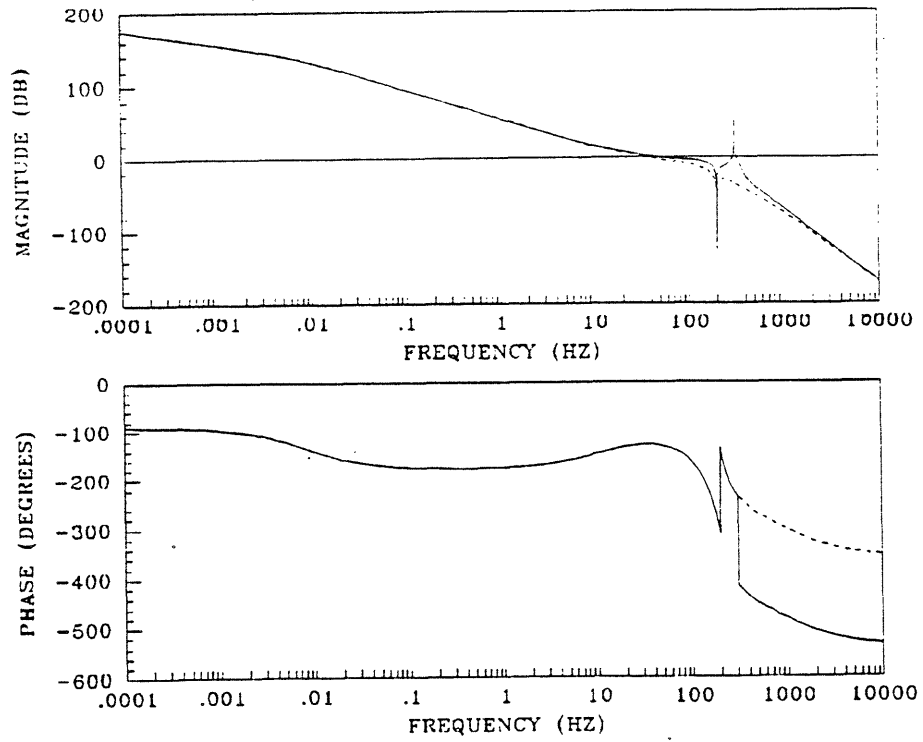


Figure 5.4: Lead Compensated System Open Loop Bode Plot

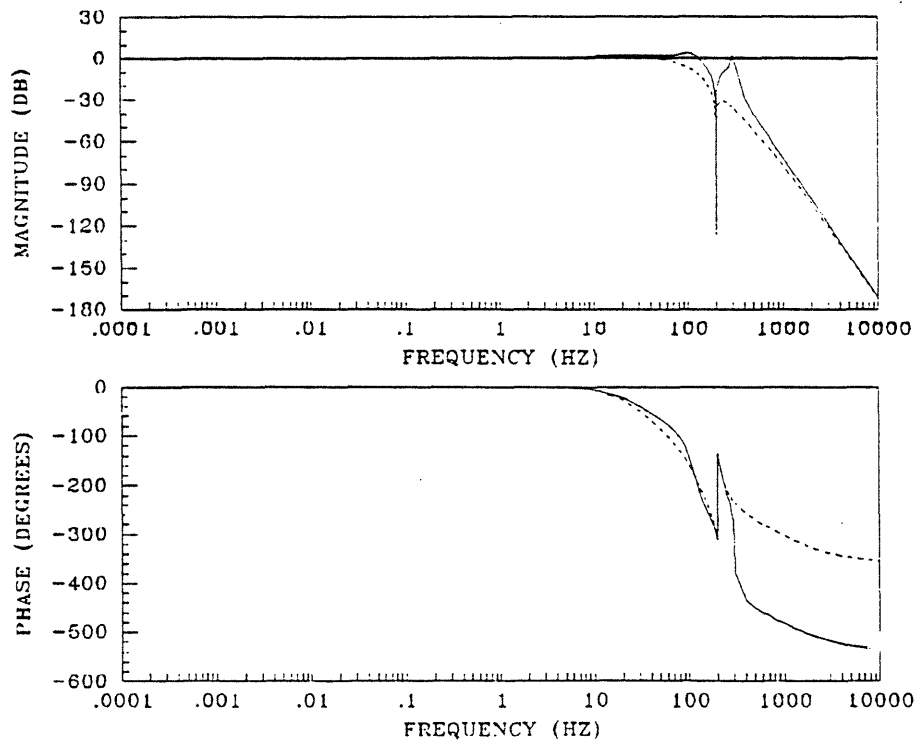


Figure 5.5: Lead Compensated System Closed Loop Bode Plot

Table 5.2: Lead Compensated System Closed Loop Poles

Closed Loop Poles	
$-6282.6 + j1.8300$	$-142.05 + j36.488$
$-54.742 + j1883.2$	$-171.88 - j92.496$
$-232.43 + j1333.8$	$-214.29 - j1259.0$
$-166.27 + j693.01$	$-380.82 - j680.12$

the broken lines denote the  $y$ -axis response. The response of the pickoff angles has significant oscillation at the nutation frequency, while there is little in the moment command response. The maximum deviation of the  $y$ -axis pickoff angle is  $0.0042^\circ$  while the  $x$ -axis moment command has an overshoot of 31% and a settling time of about 0.035 seconds.

A Nyquist plot of the lead compensated system is shown in Figure 5.7. The stability margins obtained from the plot indicate a negative phase margin of  $50^\circ$ , a positive phase margin of  $49^\circ$ , an upward gain margin of  $4.73 \text{ dB}$ , and an infinite downward gain margin. An interesting feature of this and the subsequent Nyquist plots is the large circle occupying the right half of the plane. This is due to the nutation resonance, where the frequency response has a large magnitude and the phase rapidly goes through  $-180^\circ$ , tracing out the circle.

### 5.3.3 Performance Limitations of First Order Lead Compensator Designs

The  $50 \text{ Hz}$  bandwidth design is nearly the highest attainable with classical first order lead compensation. Slightly higher bandwidths are possible, but with reduced phase margins. The loss of phase can be alleviated somewhat by increasing the demodulation filter cutoff frequency; however, there is a fundamental limit on the bandwidth imposed by the nutation resonance.

Consider the schematic Nyquist plot in Figure 5.8 showing the nutation circle for increasing system crossover frequency. For the  $50 \text{ Hz}$  bandwidth design, the phase just before the nutation resonance is approximately  $-230^\circ$ , and after the nutation resonance it is approximately  $-410^\circ$ , tracing out the circle in the right half of the Nyquist plane. As the crossover frequency is increased, compensator phase lead is also increased to maintain reasonable positive phase margins.

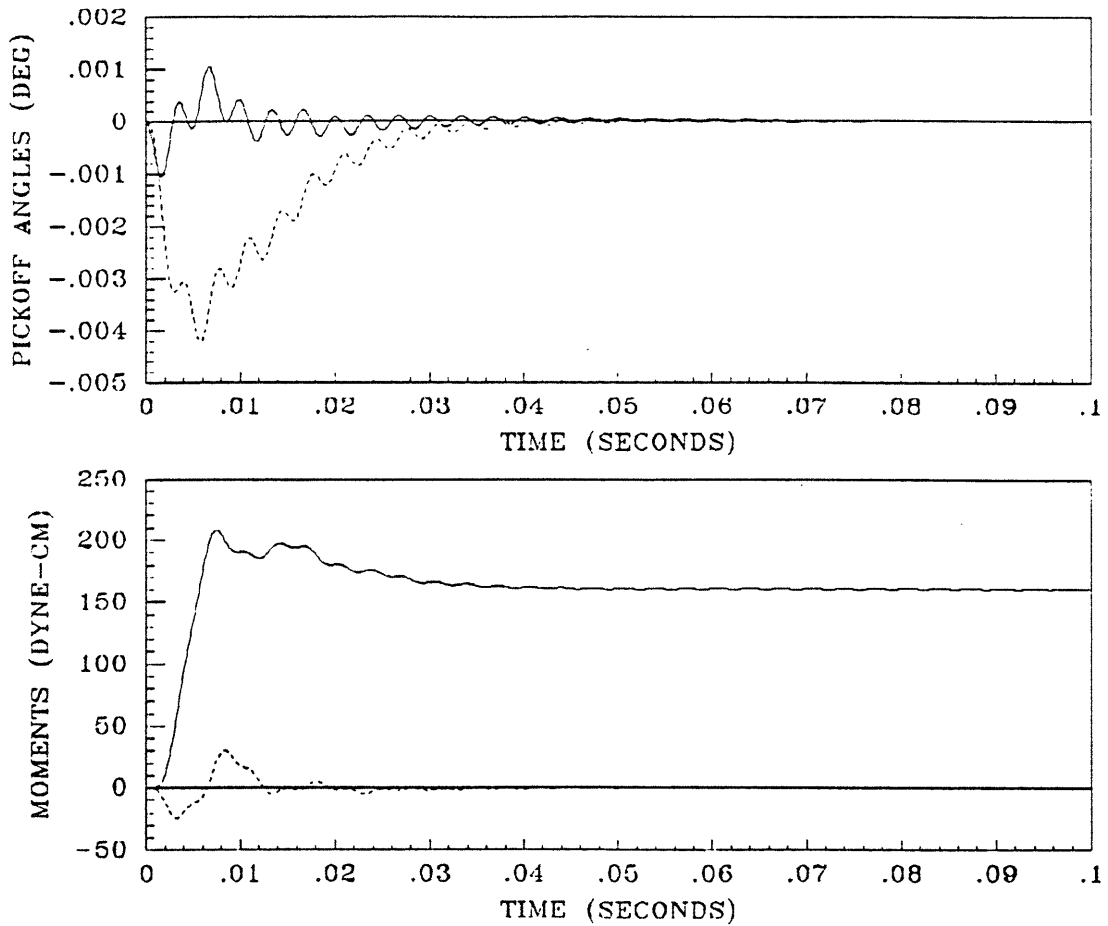


Figure 5.6: Lead Compensated System Step Response

This in turn, increases the phase at nutation, rotating the nutation circle in a counterclockwise manner, reducing the available negative phase margin. The diameter of the circle increases due to the increased crossover frequency. If the phase just before nutation becomes greater than  $-180^\circ$ , then the nutation circle will encircle the  $-1$  point, causing the system to become unstable.

Therefore, the requirement that the phase be less than  $-180^\circ$  just before nutation places a strict limit on the achievable bandwidth for lead compensated systems. An alternative requirement is that the phase must be greater than  $0^\circ$  just before nutation. This requirement is met by linear quadratic designs, discussed below, but cannot be met with simple, first order lead compensation.

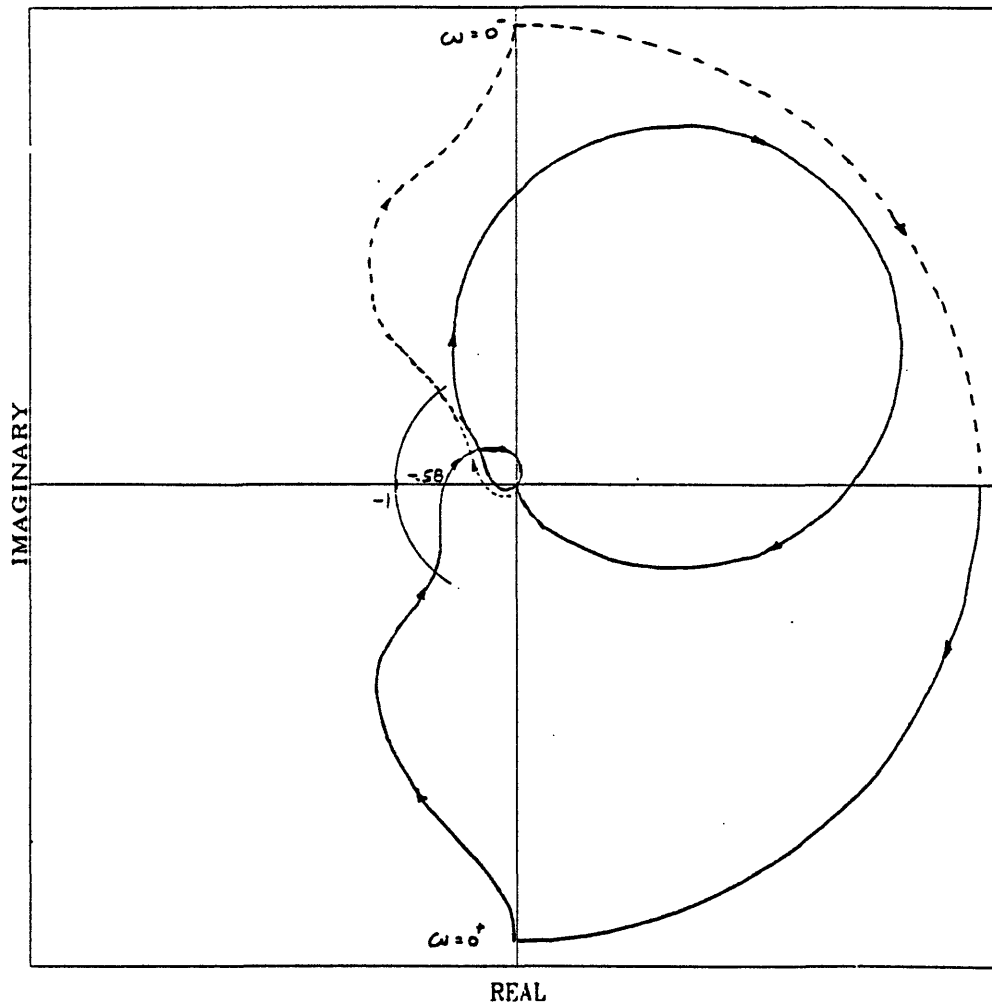


Figure 5.7: Lead Compensated System Nyquist Plot

### 5.3.4 Summary

The stability and performance of the first order lead design are summarized in Table 5.3. The upward gain margin is very small while the downward gain margin is infinite. The bandwidth of 50 Hz is nearly the maximum attainable with this design methodology due to the nutation phase restriction. Another feature of the design is that although the  $-90^\circ$  bandwidth is 50 Hz, the  $-3\text{ dB}$  bandwidth is 145 Hz. This implies the loop will pass significant high frequency angular rate information with large phase lags. In addition, if the attitude algorithm computational bandwidth is set at 50 Hz, this could cause significant errors due to coning motion as discussed in Section 1.3.



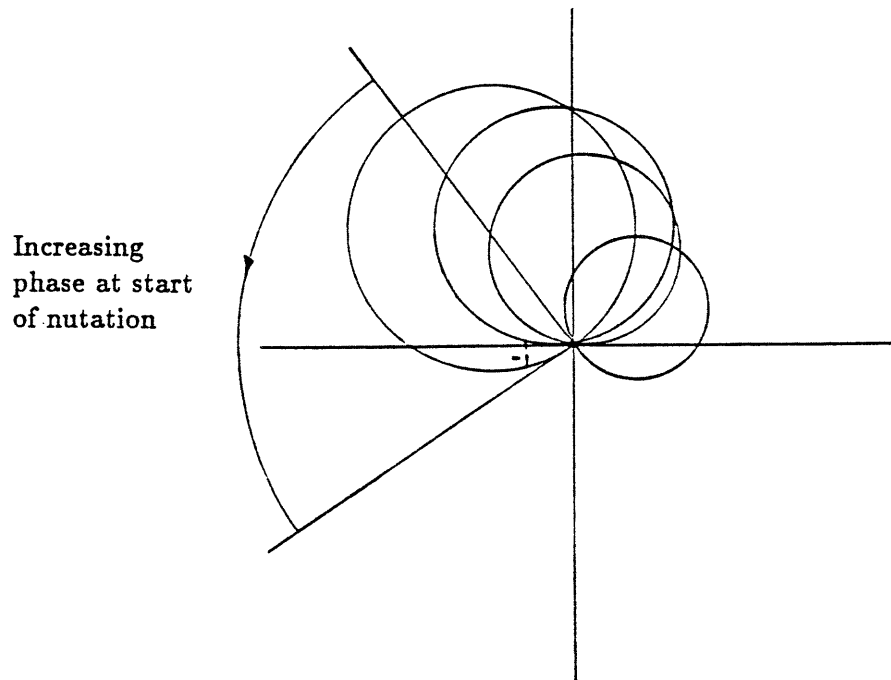


Figure 5.8: Nyquist Nutation Circle for Increasing Crossover Frequency

Table 5.3: First Order Lead Compensation Design Parameters

Parameters	Units	Lead Design
Upward Gain Margin	<i>dB</i>	4.73
Downward Gain Margin	<i>dB</i>	$\infty$
Negative Phase Margin	<i>deg</i>	50
Positive Phase Margin	<i>deg</i>	49
$-90^\circ$ Bandwidth	<i>Hz</i>	50
$-3\text{ dB}$ Bandwidth	<i>Hz</i>	145
Forward TF $M_p$	<i>dB</i>	3.95
Backward TF $M_p$	<i>dB</i>	2.37
Velocity Error Constant	<i>dB</i>	110.9
CL Gain at 10 <i>kHz</i>	<i>dB</i>	-170
Moment Command Overshoot	<i>%</i>	31
Settling Time	<i>sec</i>	0.035
Pickoff Angle Deviation	<i>deg</i>	0.0042

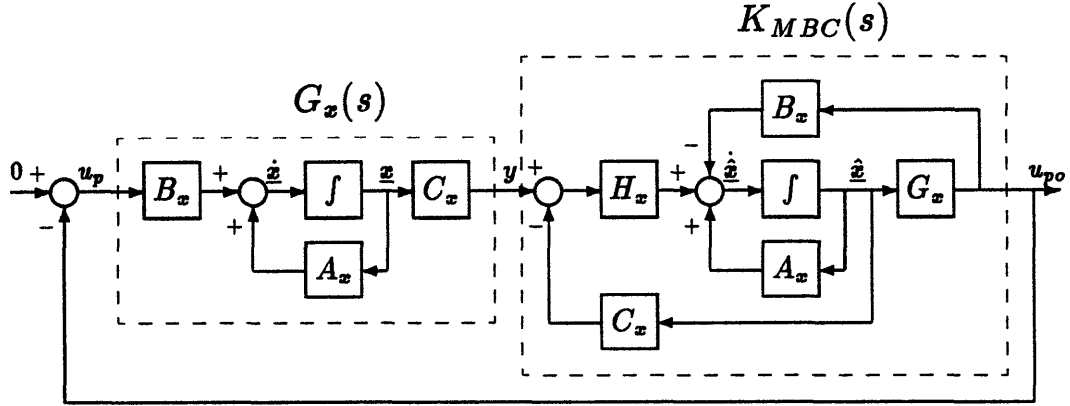


Figure 5.9: LQG/LTR Feedback Loop Block Diagram

## 5.4 LQG/LTR Design

### 5.4.1 Description of Design Methodology

The linear quadratic Gaussian with loop transfer recovery (LQG/LTR) design methodology has been described by Doyle and Stein [7] and extended by Athans and Stein [2]. LQG/LTR combines a linear quadratic regulator and a Kalman filter to produce a model based compensator,  $K_{MBC}(s)$ , of the form shown in Figure 5.9. In the figure, the design plant model transfer function is denoted by  $G_x(s)$ . The gain matrix  $G_x$  is the optimal feedback gain that is the solution to a linear quadratic regulator problem and  $H_x$  is the steady state Kalman filter gain matrix.

The gain matrix,  $G_x$ , is the solution to the deterministic LQR problem to minimize the cost functional

$$J = \int_0^{\infty} [\underline{x}^H(t) Q_{xx} \underline{x}(t) + u_p(t)^* Q_{uu} u_p(t)] dt \quad (5.3)$$

constrained by the complex augmented system dynamics,

$$\dot{\underline{x}}(t) = A_x \underline{x}(t) + B_x u_p(t) \quad (5.4)$$

and the control law,

$$u_p(t) = -G_x \underline{x}(t) \quad (5.5)$$

where  $\underline{x}$  is the complex augmented state vector discussed in Section 4.3, and  $u_p$  is the complex scalar moment command to the gyro. The state vector weighting

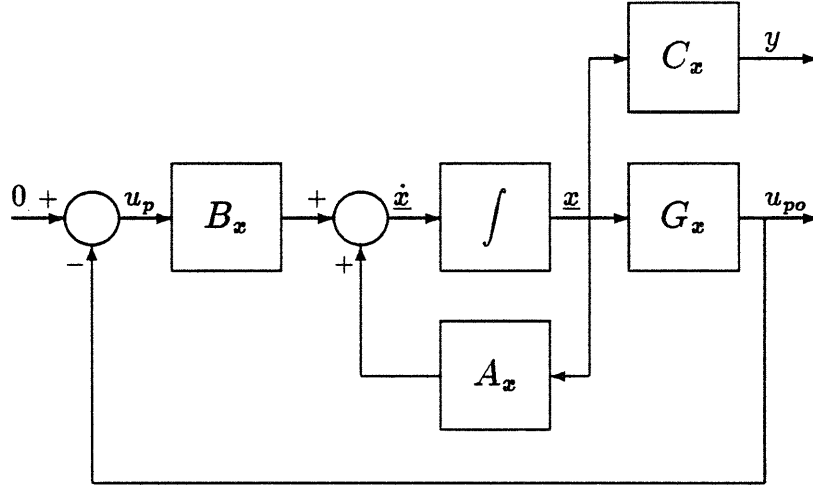


Figure 5.10: LQ Feedback Loop Block Diagram

matrix is positive semi-definite, and  $Q_{xx} = N^H N$ , where  $N$  is an auxiliary output matrix. The control weighting is a positive scalar,  $Q_{uu} = \rho$ . Assuming  $[A_x, B_x]$  stabilizable and  $[A_x, N]$  detectable,  $G_x$  comes from the solution to the algebraic Riccati equation,

$$0 = SA_x + A_x^H S + Q_{xx} - \frac{1}{\rho} S B_x B_x^H S \quad (5.6)$$

$$G_x = \frac{1}{\rho} B_x^H S \quad (5.7)$$

where  $H$  denotes complex conjugate transpose.

The weighting parameters,  $Q_{xx}$  and  $Q_{uu}$ , are chosen to shape the frequency response of the LQ loop,

$$G_{LQ}(s) = G_x (sI - A_x)^{-1} B_x \quad (5.8)$$

which can be found by breaking the LQ feedback loop at the plant input. A block diagram of the LQ feedback loop is shown in Figure 5.10.

A Kalman filter is used in the model based compensator to generate state estimates,  $\hat{x}(t)$ , for the linear quadratic regulator full state feedback. The LQG/LTR design methodology uses the “accurate measurement” Kalman filter problem to recover the good performance and stability properties of the LQ loop,  $G_{LQ}(s)$ , in the feedback loop of Figure 5.9.

Consider the stochastic, linear, time invariant system

$$\dot{\underline{x}}(t) = A_x \underline{x}(t) + B_x \xi(t) \quad (5.9)$$

$$y_p(t) = C_x \underline{x}(t) + \theta(t) \quad (5.10)$$

where the process noise,  $\xi(t)$ , is a scalar, zero mean, Gaussian, white noise process with covariance,

$$E \{ \xi(t) \xi(t - \tau) \} = \Xi \delta(\tau),$$

and the measurement noise,  $\theta(t)$ , is a scalar, zero mean, Gaussian, white noise process with covariance,

$$E \{ \theta(t) \theta(t - \tau) \} = \mu \delta(\tau),$$

and the process noise input matrix is identical to the control input matrix.

Assuming  $[A_x, B_x]$  stabilizable and  $[A_x, C_x]$  detectable, the Kalman filter gain matrix,  $H_x$ , comes from the solution to the algebraic Riccati equation

$$0 = \Sigma A_x^H + A_x \Sigma + B_x \Xi B_x^H - \frac{1}{\mu} \Sigma C_x^H C_x \Sigma \quad (5.11)$$

$$H_x = \frac{1}{\mu} \Sigma C_x^H \quad (5.12)$$

If the augmented plant,  $G_x(s)$ , has no non-minimum phase zeros, then, point-wise in  $s$ ,

$$\lim_{\mu \rightarrow 0} K_{MBC}(s) G_x(s) = G_{LQ}(s). \quad (5.13)$$

Also, since  $G_x(s)$  is a scalar transfer function, the loop broken at the plant input,  $K_{MBC}(s) G_x(s)$ , has the same transfer function as the loop broken at the plant output,  $G_x(s) K_{MBC}(s)$ , so the properties of the LQ loop,  $G_{LQ}(s)$ , can be recovered in the feedback loop broken at either point. The value of  $\mu$  determines the frequency to which the LQ loop is recovered. This is referred to as the recovery bandwidth.

The LQG/LTR design procedure is as follows:

1. Design a target LQ loop that has the desired performance and stability properties by choosing  $N$  to shape the loop and  $\rho$  to achieve the desired bandwidth.
2. Recover the target LQ loop in the feedback loop to the desired bandwidth by choosing the design parameter  $\mu$ .

During the recovery process, as  $\mu \rightarrow 0$ , the model based compensator has the following properties [1]:

- The zeros of  $K_{MBC}(s)$  start at some open loop poles of  $G_x(s)$  and approach the zeros of  $G_{LQ}(s)$ .
- Some of the poles of  $K_{MBC}(s)$  cancel the undesirable zeros of  $G_x(s)$ .
- The rest of the poles of  $K_{MBC}(s)$  go to infinity in a stable manner.

### 5.4.2 Design Approach

A total of four LQG/LTR designs are examined. Two are based on a 50 Hz bandwidth LQ target loop, one recovered to provide a bandwidth of 50 Hz and the other recovered a decade beyond the nutation frequency. The other two designs are based on a 100 Hz LQ target loop, one recovered to provide a bandwidth of 100 Hz and the other recovered a decade beyond the nutation frequency.

One major drawback to the LQG/LTR methodology is that an LQ target loop with a notch filter beyond the crossover frequency cannot be generated with the constant weightings in the cost functional in Equation (5.3). (A notch filter can be generated with the use of a frequency weighted cost functional, which is treated in Section 5.5.) In addition, since the target loop is recovered asymptotically, a sharp notch filter may not be recovered adequately for practical values of  $\mu$ , leading to a recovered notch at the wrong frequency with the wrong depth. These problems are solved by designing and recovering LQ target loops without notch filters, and then incorporating the notch filter in Equation (4.9) at the output of the model based compensator. A block diagram of the model based compensator modified with the notch filter is shown in Figure 5.11. This *ad hoc* implementation of the notch filter destroys the optimality and guaranteed stability properties of the recovered LQ loop, so a separate check of the feedback loop stability must be performed.

### 5.4.3 Linear Quadratic Target Loop Design

#### Loop Shaping

The LQ target loops are designed using the design plant model and the design parameters  $N$  and  $\rho$ , as discussed at the beginning of this section. The two

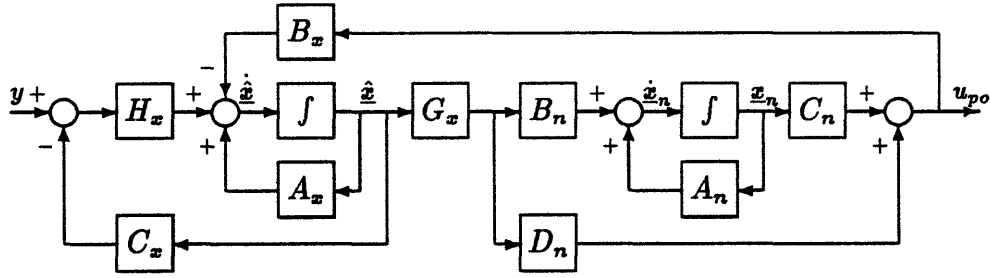


Figure 5.11: Block Diagram of  $K_{MBC}(s)$  Modified With Notch Filter

open loop LQ target Bode plots are shown in Figures 5.12 and 5.14. Two design characteristics of these loops require discussion. First, the magnitudes of the forward and backward transfer functions are matched at high and low frequencies, which is the equivalent of matching the singular values of the real TITOBS system at these frequencies. Second, the highest attenuation in the forward transfer function between crossover and nutation is placed at the spin frequency to augment the effect of the notch filter on the forward transfer function in the recovered design.

The shape of the magnitude of the frequency response of the LQ loop can be controlled through the use of the state and control weightings,  $N$  and  $\rho$ . In particular, the magnitude responses of the forward and backward transfer functions can be matched at high and low frequencies in a systematic way. This ensures that the magnitude response of the system at high and low frequencies is identical for every input direction [1]. The frequency of the highest attenuation in the forward transfer function can also be easily controlled.

Consider the TITOBS version of the LQR problem stated in Equation (5.3). The TITOBS LQ loop is

$$G_{LQ}(s) = G_x (sI - A_x)^{-1} B_x \quad (5.14)$$

where all of the matrices in Equation (5.14) are the corresponding block symmetric versions of those in Equations (5.3) and (5.4). In the ‘cheap control’ limit of the LQ problem,

$$\lim_{\rho \rightarrow 0} \sqrt{\rho} G_x = N. \quad (5.15)$$

Therefore, assuming  $\rho \ll 1$ , Equation (5.14) can be written as

$$G_{LQ}(j\omega) \approx \frac{1}{\sqrt{\rho}} N (j\omega I - A_x)^{-1} B_x. \quad (5.16)$$

where  $j\omega$  is substituted for  $s$ . The goal is to select  $N$  in such a way that the singular values of the TITOBLS LQ loop are matched at high and low frequencies, that is

$$\lim_{\omega \rightarrow 0} \sigma_k \{G_{LQ}(j\omega)\} = \frac{k_l / \sqrt{\rho}}{\omega} \quad (5.17)$$

$$\lim_{\omega \rightarrow \infty} \sigma_k \{G_{LQ}(j\omega)\} = \frac{k_h / \sqrt{\rho}}{\omega} \quad (5.18)$$

where  $k_l$  and  $k_h$  are real constants. This is equivalent to matching the magnitudes of the forward and backward transfer functions of the CCTF LQ loop at these frequencies, since the minimum and maximum singular values of the TITOBLS system are the magnitudes of the forward and backward transfer functions. Therefore, the magnitudes of the LQ forward and backward transfer functions are shown below, where the matrices are once again those of the complex representation of the system.

$$|G_{LQ}(j\omega)| \approx \frac{1}{\sqrt{\rho}} |N (j\omega I - A_x)^{-1} B_x| \quad (5.19)$$

$$|G_{LQ}(-j\omega)| \approx \frac{1}{\sqrt{\rho}} |N (-j\omega I - A_x)^{-1} B_x| \quad (5.20)$$

Partitioning the terms of  $N (sI - A_x)^{-1} B_x$  yields,

$$\begin{bmatrix} N_L & N_M & N_H \end{bmatrix} \begin{bmatrix} sI & -C_d & 0 \\ 0 & sI - A_d & -B_d C_p \\ 0 & 0 & sI - A_p \end{bmatrix}^{-1} \begin{bmatrix} 0 \\ 0 \\ B_p \end{bmatrix}$$

where the subscripts,  $L$ ,  $M$ , and  $H$ , indicate the partitions of  $N$  that control the shape of the LQ loop at low, middle, and high frequencies as is shown below. After some manipulation,

$$\begin{aligned} N (sI - A_x)^{-1} B_x &= N_L \frac{1}{s} C_d (sI - A_d)^{-1} B_d C_p (sI - A_p)^{-1} B_p + \\ &N_M (sI - A_d)^{-1} B_d C_p (sI - A_p)^{-1} B_p + \\ &N_H (sI - A_p)^{-1} B_p. \end{aligned} \quad (5.21)$$

In the low and high frequency limits,

$$\lim_{s \rightarrow 0} N (sI - A_x)^{-1} B_x = N_L \frac{1}{s} [C_d A_d^{-1} B_d C_p A_p^{-1} B_p] \quad (5.22)$$

$$\lim_{s \rightarrow \infty} N (sI - A_x)^{-1} B_x = N_H \frac{1}{s} B_p. \quad (5.23)$$

Choosing the following values for the partitions of  $N$

$$\begin{aligned} N_L &= [C_d A_d^{-1} B_d C_p A_p^{-1} B_p]^{-1} \\ N_M &= \begin{bmatrix} 0 & 0 \end{bmatrix} \\ N_H &= k_h [B_p^H B_p]^{-1} B_p^H \end{aligned}$$

yields the following limits for Equations (5.22) and (5.23)

$$\lim_{s \rightarrow 0} N (sI - A_x)^{-1} B_x = \frac{1}{s} \quad (5.24)$$

$$\lim_{s \rightarrow \infty} N (sI - A_x)^{-1} B_x = k_h \frac{1}{s} \quad (5.25)$$

and for  $s = j\omega$ ,

$$\lim_{\omega \rightarrow 0} |G_{LQ}(j\omega)| \approx |G_{LQ}(-j\omega)| \approx \frac{1/\sqrt{\rho}}{\omega} \quad (5.26)$$

$$\lim_{\omega \rightarrow \infty} |G_{LQ}(j\omega)| \approx |G_{LQ}(-j\omega)| \approx \frac{k_h/\sqrt{\rho}}{\omega} \quad (5.27)$$

With  $N$  specified in this way, the design problem is reduced to determining the two scalar design parameters,  $k_h$  and  $\rho$ . The value of  $\rho$  determines the bandwidth of the LQ loop. Increasing  $\rho$  lowers the bandwidth, while decreasing  $\rho$  raises the bandwidth. Recall that for the above approximations to hold,  $\rho$  must be much less than unity. The value of  $k_h$  controls the point of highest attenuation in the forward transfer function between crossover and nutation. Reducing  $k_h$  for a given value of  $\rho$  moves the point down in frequency, while increasing  $k_h$  moves the point up in frequency. The effects of  $\rho$  and  $k_h$  are somewhat coupled so they must be iteratively adjusted to achieve the desired results.

The matrix  $N_M$  provides two additional degrees of freedom in shaping the LQ loop, which have not been exploited here. It can be used to control the loop shape in the middle frequencies, but is not used here because  $N_L$  and  $N_H$  provide adequate control of the loop shape. A good choice of  $N_M$  could provide a better loop shape than is possible with just matching the transfer function magnitudes at high and low frequencies, and it is possible to chose  $N$  such that the magnitudes are matched at all frequencies, that is

$$|G_{LQ}(j\omega)| \approx |G_{LQ}(-j\omega)| \approx \frac{1/\sqrt{\rho}}{\omega}$$

for all  $\omega$ . The recovery of this loop generates a compensator that completely inverts the plant. This produces a loop with unacceptable time response characteristics which are discussed in more detail in Section 5.6.



Table 5.4: Low Bandwidth LQ Target Closed Loop Poles and Zeros

Poles	Zeros
$-134.45 + j1917.7$	$-57.441 + j1271.5$
$-474.06 + j818.00$	$-469.60 + j817.69$
$-470.72 - j815.75$	$-466.00 - j802.92$
$-135.11 + j122.05$	$-122.92 - j12.155$
$-119.00 - j125.18$	

Table 5.5: High Bandwidth LQ Target Closed Loop Poles and Zeros

Poles	Zeros
$-351.64 + j1921.7$	$-163.72 + j1280.3$
$-503.91 + j842.02$	$-470.25 + j751.99$
$-465.12 - j808.81$	$-463.49 - j823.86$
$-320.80 + j235.30$	$-254.46 - j54.320$
$-257.63 - j277.45$	

### LQ Target Loops

Bode plots of the open and closed loop low bandwidth LQ target are shown in Figures 5.12 and 5.13. The LQ design parameters shown below are chosen to give a  $-3$  dB bandwidth of 50 Hz.

$$Q_{uu} = 2.5 \times 10^{-12}$$

$$N = \begin{bmatrix} -j4.4118 \times 10^{-4} & 0 & 0 & 0 & 3.3586 \times 10^{-6} \end{bmatrix}$$

The resulting closed loop LQ poles and zeros are shown in Table 5.4.

Bode plots of the open and closed loop high bandwidth LQ target are shown in Figures 5.14 and 5.15. The LQ design parameters shown below are chosen to give a  $-3$  dB bandwidth of 100 Hz.

$$Q_{uu} = 1.0 \times 10^{-13}$$

$$N = \begin{bmatrix} -j4.4118 \times 10^{-4} & 0 & 0 & 0 & 1.7677 \times 10^{-6} \end{bmatrix}$$

The resulting closed loop LQ poles and zeros are shown in Table 5.5.

Another interesting feature of open loop LQ targets is that the phases of forward and backward transfer functions are not equal at low frequencies. Considering the discussion of CCTF Bode plots in Chapter 3 and the results of the

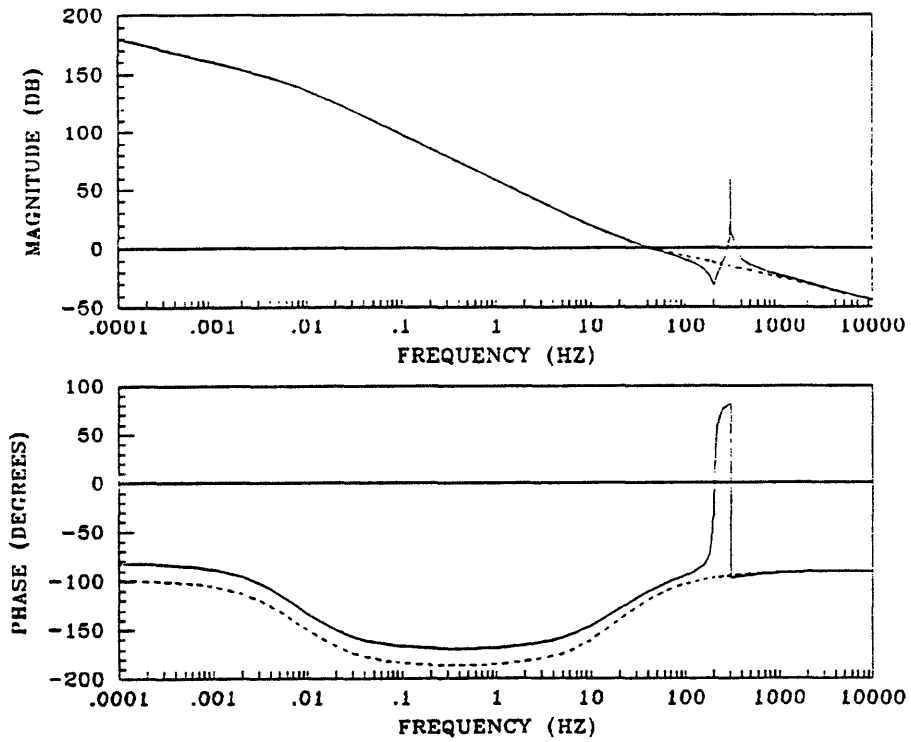


Figure 5.12: Low Bandwidth LQ Target Open Loop Bode Plot

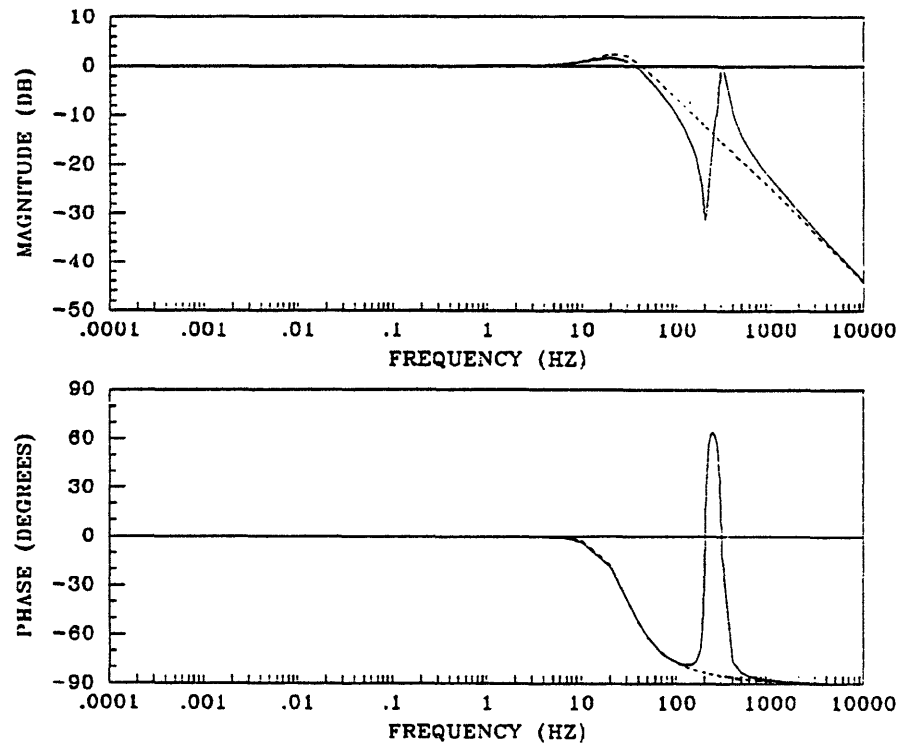


Figure 5.13: Low Bandwidth LQ Target Closed Loop Bode Plot

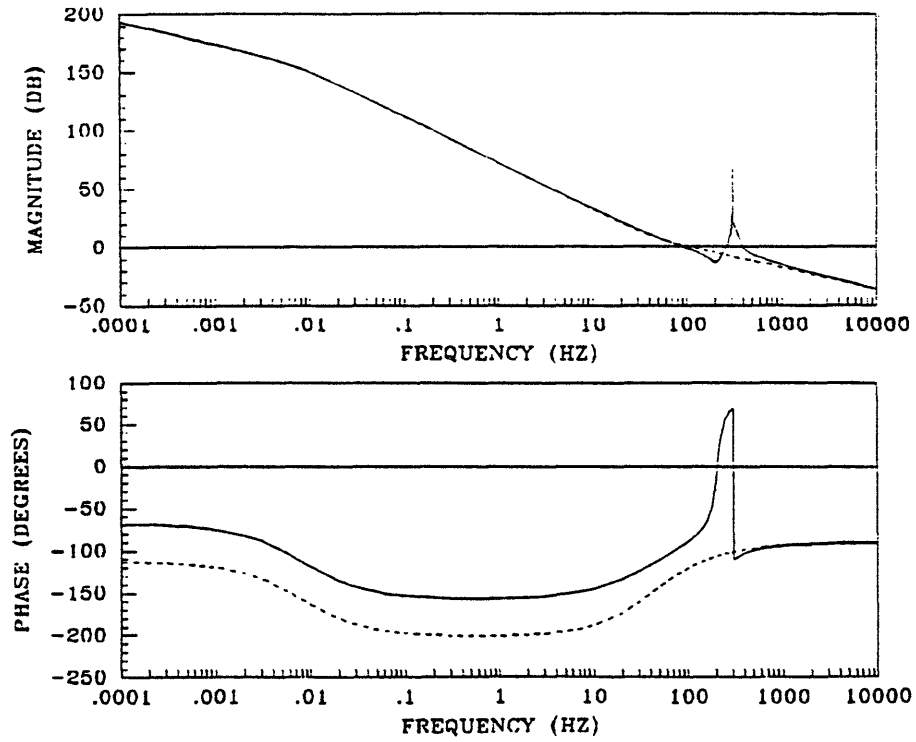


Figure 5.14: High Bandwidth LQ Target Open Loop Bode Plot

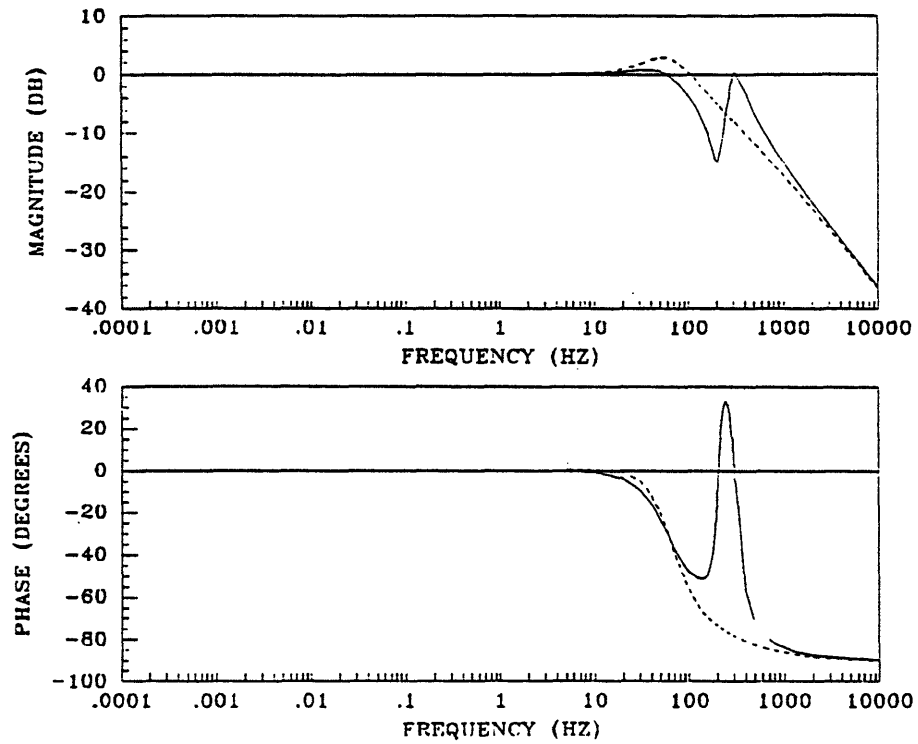


Figure 5.15: High Bandwidth LQ Target Closed Loop Bode Plot

lead compensator design in Section 5.3.2, this indicates that the feedback gain at low frequencies is complex. Furthermore, since the phase is near  $-90^\circ$ , this would indicate a gain with a small real part and a large, negative imaginary part, corresponding to a small auto feedback gain and a large cross feedback gain. For example, the element of  $G_x$  corresponding to the integrator state for the low bandwidth target is  $41.110 - j275.94$ ; the phase angle of which is  $-81^\circ$ , which can be read off of the Bode plot of the forward transfer function.

#### 5.4.4 Recovery of the LQ Target Loops

A family of compensators is generated by the recovery process, each one better approximating the target loop, as  $\mu \rightarrow 0$ . Two compensators are recovered for each target loop, one in which the  $-90^\circ$  bandwidth of the feedback loop matches the  $-3\text{ dB}$  bandwidth of the target and one in which the target is recovered about one decade beyond the nutation frequency.

##### Recovery Zero Locus

One surprising and non-intuitive feature of the recovery of the target loops for this system is the locus of compensator transmission zeros during recovery. Figures 5.16 and 5.17 show the zero loci for the recovery of each target loop. For both target loops the zeros of  $K_{MBC}(s)$  start at open loop poles of the system for large  $\mu$  and approach the zeros of the target as  $\mu \rightarrow 0$ . The locus of the zero that starts at the nutation pole is very striking, however, since it spirals away from the pole and enters the right half plane twice before approaching the target zero.

In view of the discussion in Section 5.3.3 the reason for this behavior is apparent. During recovery, the compensator poles move out in frequency, increasing the phase at low frequencies. In order to maintain stability, the phase cannot increase to the point that the phase before nutation is greater than  $-180^\circ$ . This is prevented by the zero moving into the right half plane, introducing a phase lag in order to hold the phase at nutation below  $-180^\circ$ . Once the poles have moved out in frequency sufficiently, the zero moves back into the left half plane, introducing phase lead to bring the phase above  $0^\circ$ . This process actually occurs twice during recovery, the first time the phase is kept below  $-540^\circ$  and is brought up above  $-360^\circ$  when the zero moves back into the left half plane.

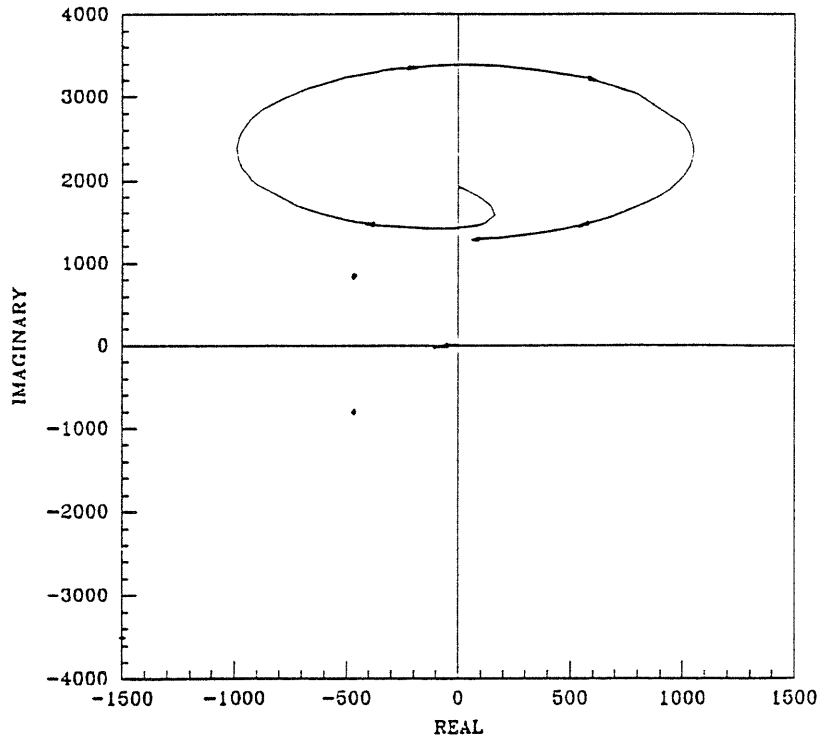


Figure 5.16: Zero Locus During Recovery of the Low Bandwidth Target

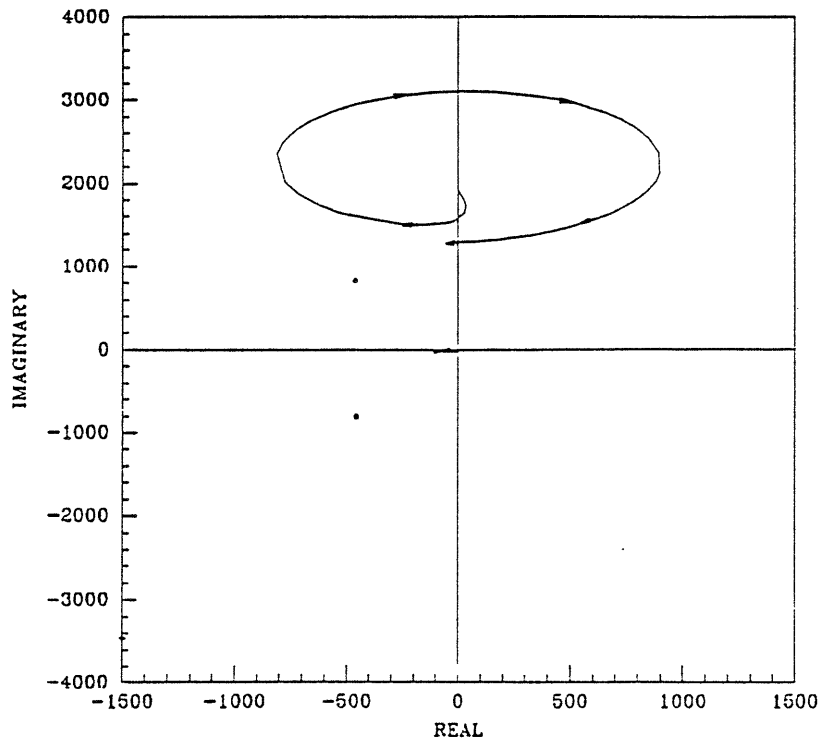


Figure 5.17: Zero Locus During Recovery of the High Bandwidth Target

This behavior has a significant effect on the recovery of the phase characteristic of the LQ target loop. Take, for example, the recovery of the high bandwidth target. The Bode plot of the open loop system for low bandwidth recovery in Figure 5.29 indicates that the magnitude characteristic is recovered well beyond nutation but the phase characteristic is not recovered. However, examination of the high bandwidth recovery in Figure 5.34 shows that once the zero crosses back into the left half plane, the phase is suddenly recovered beyond nutation as well. There are discontinuities in phase during recovery that depend on the value of  $\mu$  and the nutation frequency. Therefore the nutation frequency must be known well in order to have confidence in the recovery of the target phase characteristic.

### Compensator Designs

A compensator design which provides a  $-90^\circ$  bandwidth of  $50\text{ Hz}$  for the low bandwidth LQ target, is achieved with values of the Kalman filter design parameters  $\mu = 10^{-7}$  and  $\Xi = 10^6$ . This design is referred to as LQG/LTR-1a. A Bode plot of the overall compensator,  $K(s)$ : the model based compensator,  $K_{MBC}(s)$ , modified with the notch filter, and augmented with the demodulation filter and integrator, is shown in Figure 5.18. The compensator poles and zeros are listed in Table 5.6, and the compensator Bode gain is  $18.1 - j227.8$  which yields a velocity error constant,  $K_v$ , of  $113.5\text{ dB}$ . Note that this compensator has a zero in the right half plane. A Bode plot of the compensated open loop system is shown in Figure 5.19 while a Bode plot of the closed loop system is shown in Figure 5.20. The system has a  $-90^\circ$  bandwidth of just over  $50\text{ Hz}$  and a  $-3\text{ dB}$  bandwidth of  $70\text{ Hz}$ . The  $M_p$  of the forward transfer function is  $2.51\text{ dB}$  while the  $M_p$  of the backward transfer function is  $3.02\text{ dB}$ , and the attenuation at  $10\text{ kHz}$  is  $-170\text{ dB}$ . The closed loop system poles are listed in Table 5.7.

The response of the system to a  $1\text{ deg/sec}$  step in the  $y$ -axis inertial angular rate, or  $\dot{\phi}_c = j \cdot 1\text{ deg/sec}$ , is shown in Figure 5.21. The real and imaginary parts of the pickoff angle and the real and imaginary parts of the commanded moments are plotted versus time. Related to the TITOBS system, the real and imaginary parts are the  $x$ -axis and  $y$ -axis pickoff angles and  $x$ -axis and  $y$ -axis moment commands, respectively. The solid lines denote the  $x$ -axis response and the broken lines denote the  $y$ -axis response. The maximum deviation of the  $y$ -

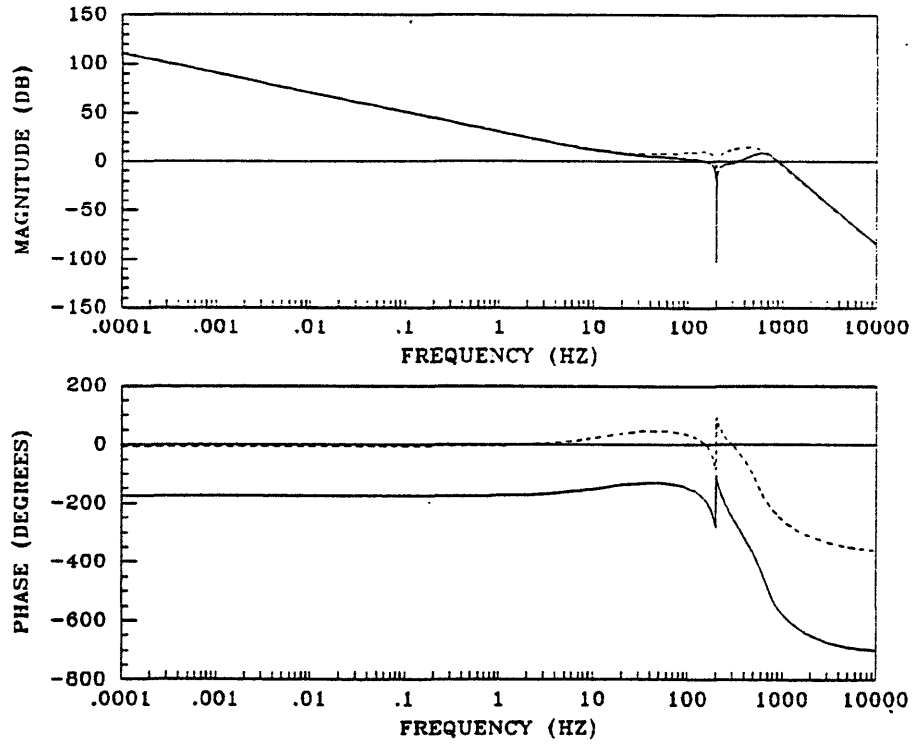


Figure 5.18: Design LQG/LTR-1a Augmented Compensator Bode Plot

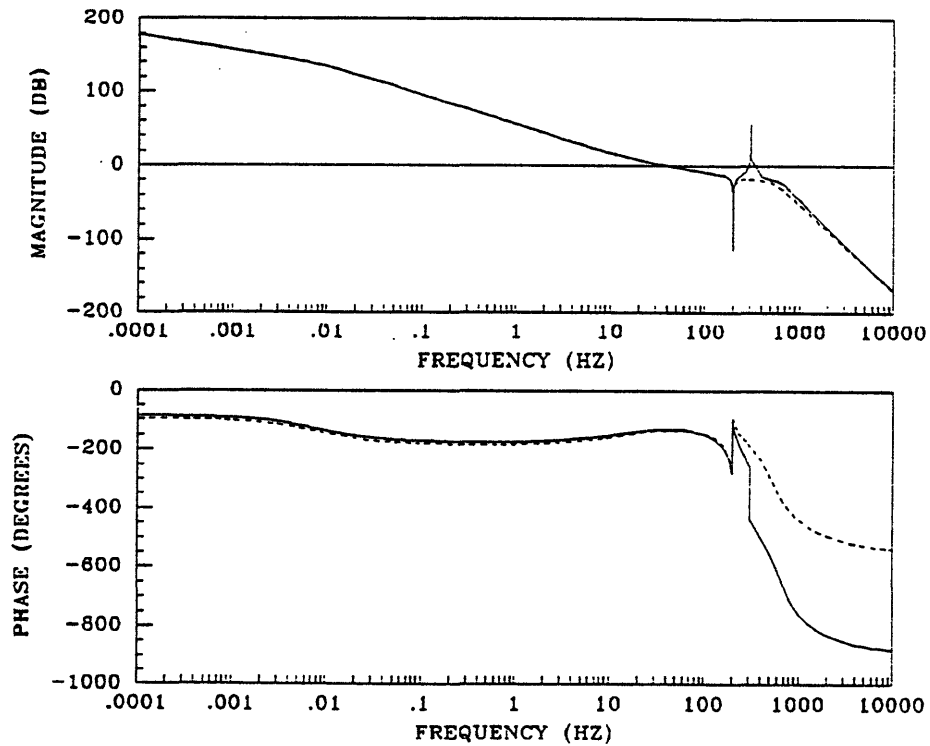


Figure 5.19: Design LQG/LTR-1a Open Loop Bode Plot

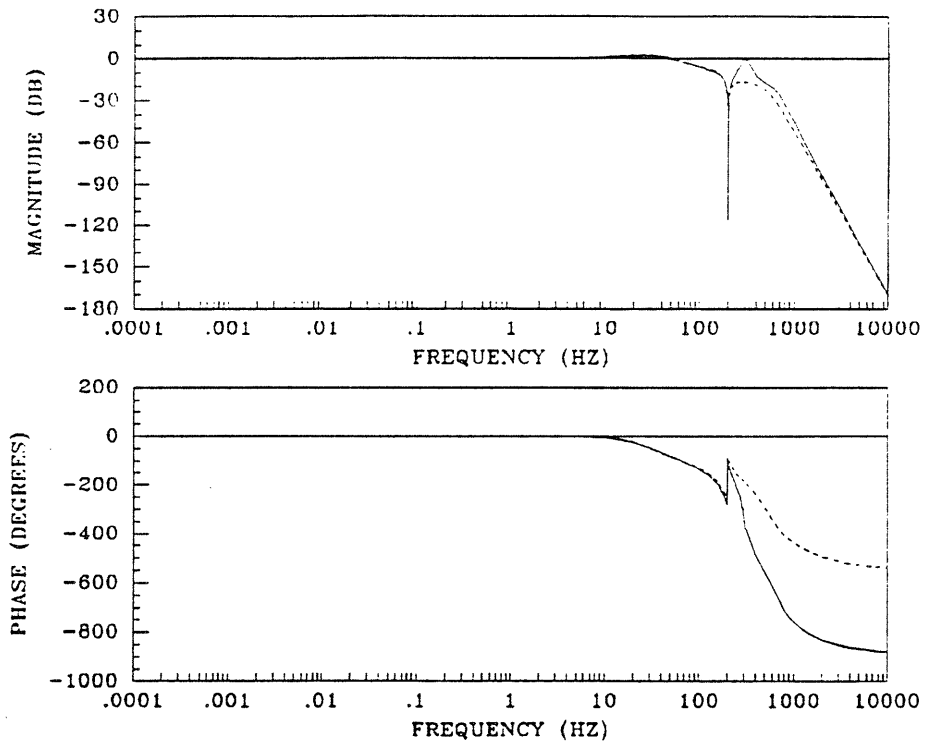


Figure 5.20: Design LQG/LTR-1a Closed Loop Bode Plot

Table 5.6: Design LQG/LTR-1a Compensator Poles and Zeros

Poles	Zeros
0.0	$71.133 + j1577.9$
$-471.00 + j816.35$	$-471.19 + j817.51$
$-471.00 - j816.35$	$-467.41 - j812.93$
$-153.56 + j1236.5$	$-0.001256 + j1256.6$
$-160.18 - j1213.2$	$-0.001256 - j1256.6$
$-955.70 + j4005.0$	$-108.01 - j6.2367$
$-952.56 - j3170.9$	
$-2987.3 + j2929.5$	
$-2914.6 - j2193.0$	
$-4012.8 + j322.98$	



Table 5.7: Design LQG/LTR-1a Closed Loop Poles

Closed Loop Poles	
$-3501.7 + j372.06$	$-201.82 - j1185.8$
$-475.05 + j819.44$	$-1072.8 + j3925.1$
$-470.66 - j815.43$	$-1088.6 - j3138.4$
$-140.16 + j127.01$	$-2820.4 + j2559.9$
$-123.55 - j129.15$	$-2842.4 - j1802.1$
$-116.66 + j1870.0$	$-225.15 + j1230.7$

axis pickoff angle is  $0.0039^\circ$  while the  $x$ -axis moment command has an overshoot of 31% and a settling time of about 0.03 seconds.

A Nyquist plot of the compensated system is shown in Figure 5.22. The stability margins obtained from the plot indicate a negative phase margin of  $48^\circ$ , a positive phase margin of  $50^\circ$ , an upward gain margin of  $12.40 \text{ dB}$ , and a downward gain margin of  $48.16 \text{ dB}$ . The LQG/LTR designs all have downward gain margins as opposed to the lead compensation design in Section 5.3 which has an infinite downward gain margin.

A compensator design which recovers the magnitude characteristic of the low bandwidth LQ target loop a decade beyond nutation, but does not recover the phase characteristic beyond nutation is achieved with values of the Kalman filter design parameters  $\mu = 10^{-15}$  and  $\Xi = 10^6$ . This design is referred to as LQG/LTR-1b. A Bode plot of the overall compensator,  $K(s)$ : the model based compensator,  $K_{MBC}(s)$ , modified with the notch filter, and augmented with the demodulation filter and integrator, is shown in Figure 5.23. The compensator poles and zeros are listed in Table 5.8, and the compensator Bode gain is  $42.1 - j258.3$  which yields a velocity error constant,  $K_v$ , of  $115.5 \text{ dB}$ . Note that this compensator also has a zero in the right half plane, so the phase is not recovered beyond nutation. A Bode plot of the compensated open loop system is shown in Figure 5.24 while a Bode plot of the closed loop system is shown in Figure 5.25. The system has a  $-90^\circ$  bandwidth of  $80 \text{ Hz}$  and a  $-3 \text{ dB}$  bandwidth of  $50 \text{ Hz}$ . The  $M_p$  of the forward transfer function is  $1.85 \text{ dB}$  while the  $M_p$  of the backward transfer function is  $2.59 \text{ dB}$ , and the attenuation at  $10 \text{ kHz}$  is  $-90 \text{ dB}$ . The closed loop system poles are listed in Table 5.9.

The response of the system to a  $1 \text{ deg/sec}$  step in the  $y$ -axis inertial angular

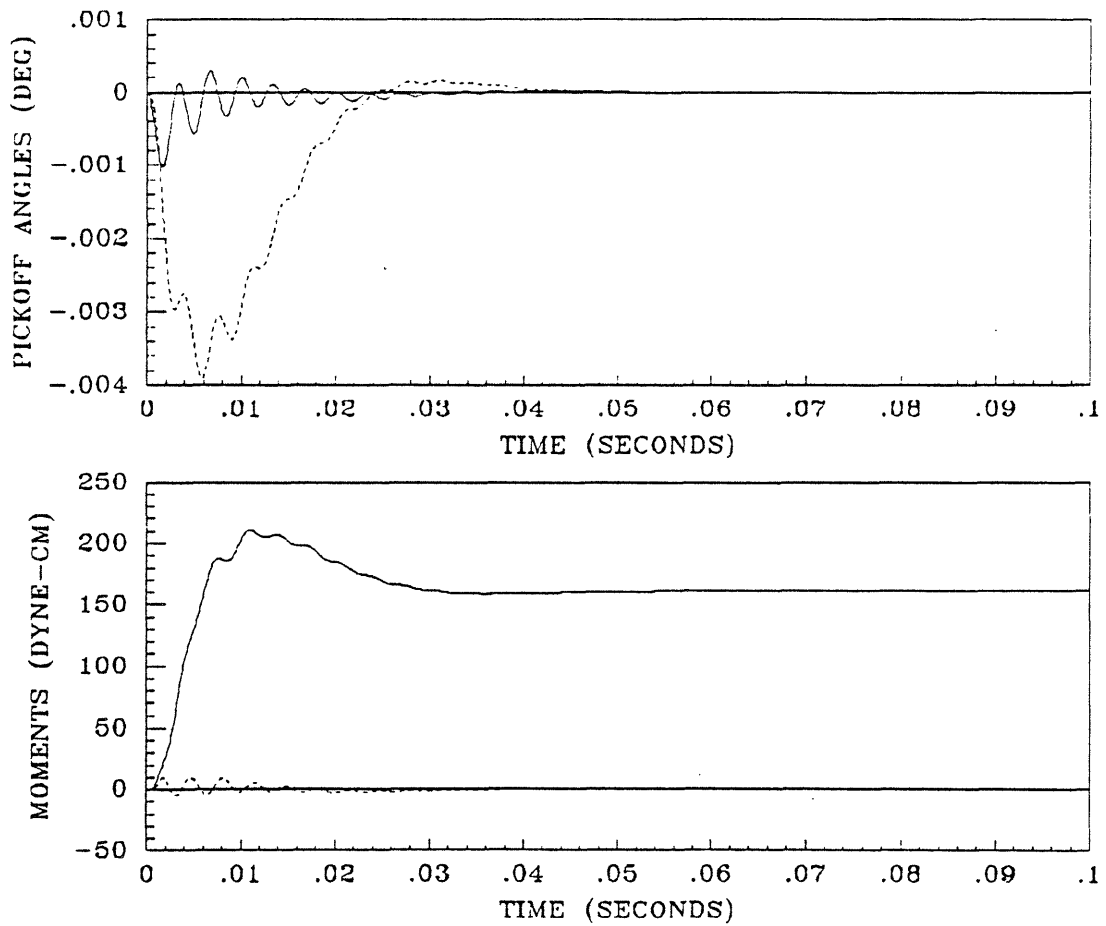


Figure 5.21: Design LQG/LTR-1a Step Response

Table 5.8: Design LQG/LTR-1b Compensator Poles and Zeros

Poles	Zeros
0.0	$56.421 + j1280.1$
$-471.00 + j816.35$	$-469.94 + j817.74$
$-471.00 - j816.35$	$-465.61 - j806.15$
$-198.48 + j1240.4$	$-0.001256 + j1256.6$
$-198.42 - j1239.4$	$-0.001256 - j1256.6$
$-5422.6 + j21838.$	$-119.80 - j11.447$
$-5444.6 - j20894.$	
$-17366. + j11330.$	
$-17610. - j10308.$	
$-29952. - j133.23$	

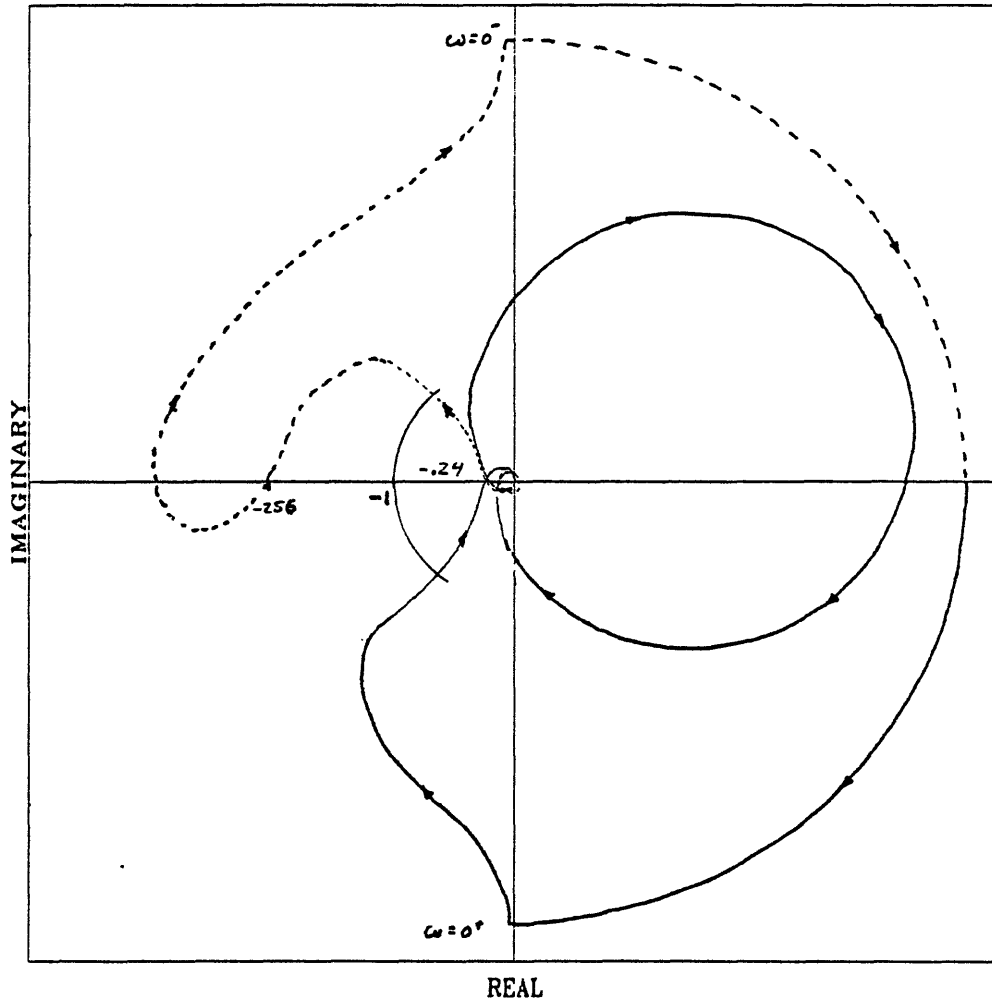


Figure 5.22: Design LQG/LTR-1a Nyquist Plot

Table 5.9: Design LQG/LTR-1b Closed Loop Poles

Closed Loop Poles	
$-27831. - j188.72$	$-225.15 + j1230.7$
$-475.05 + j819.44$	$-201.82 - j1185.8$
$-470.66 - j815.43$	$-5654.9 + j21543.$
$-140.16 + j127.01$	$-5677.2 - j20641.$
$-123.55 - j129.15$	$-17963. + j11069.$
$-116.66 + j1870.0$	$-18255. - j9948.1$

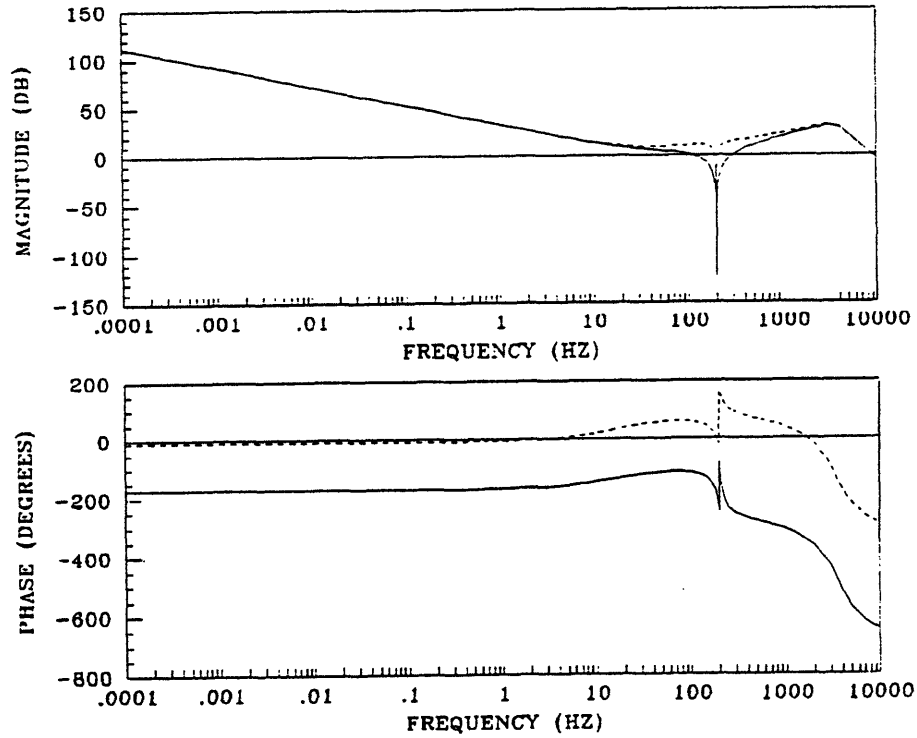


Figure 5.23: Design LQG/LTR-1b Augmented Compensator Bode Plot

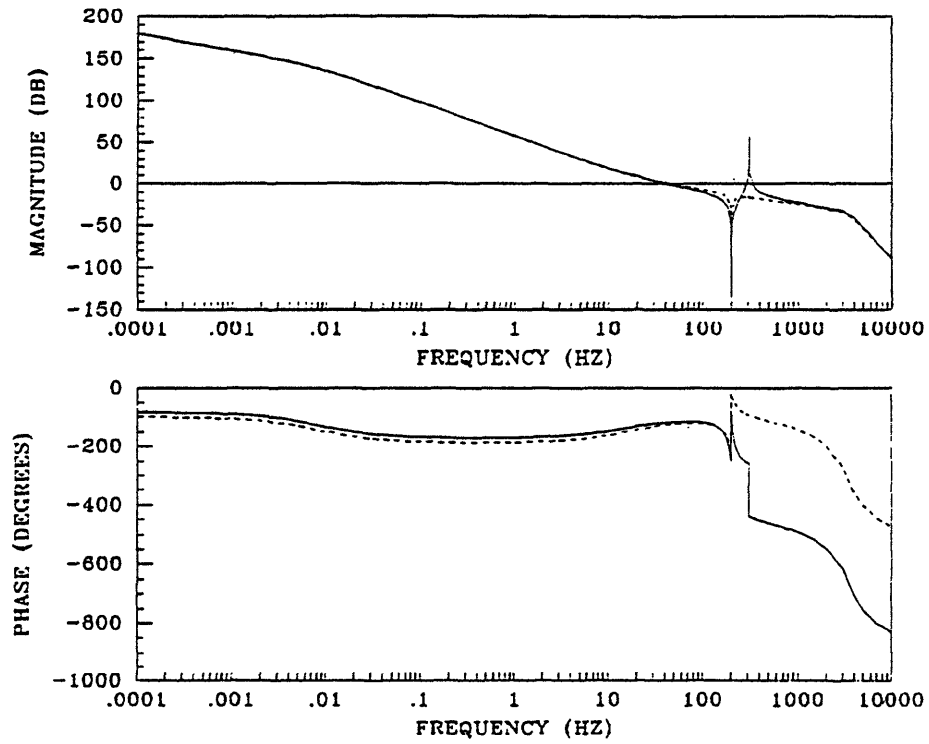


Figure 5.24: Design LQG/LTR-1b Open Loop Bode Plot

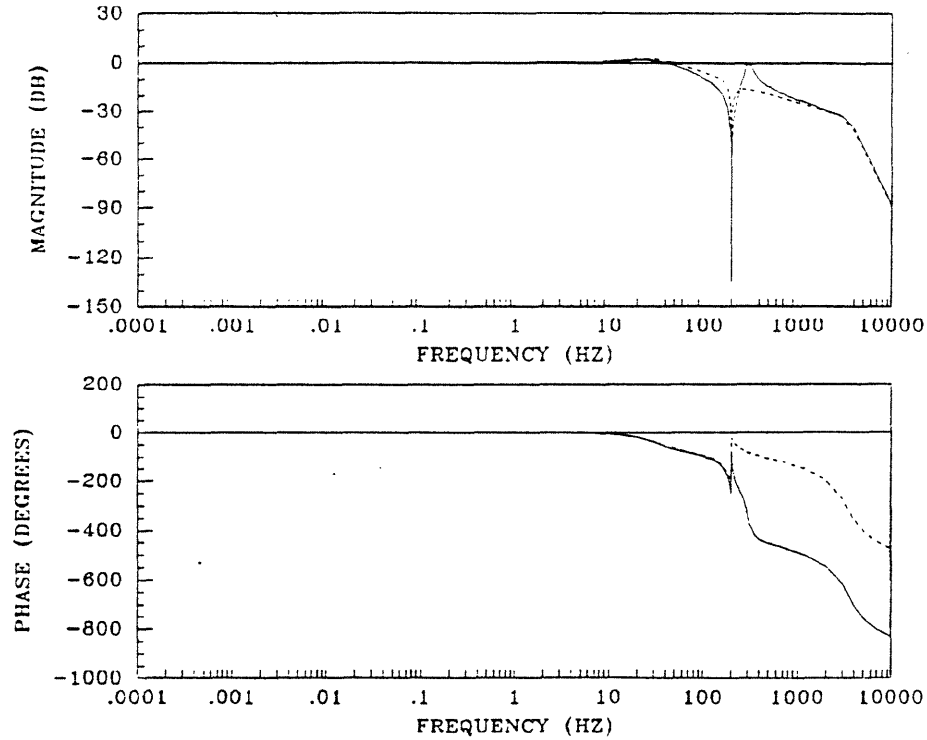


Figure 5.25: Design LQG/LTR-1b Closed Loop Bode Plot

rate, or  $\dot{\phi}_c = j \cdot 1 \text{ deg/sec}$ , is shown in Figure 5.26. The maximum deviation of the  $y$ -axis pickoff angle is  $0.0031^\circ$  while the  $x$ -axis moment command has an overshoot of 25% and a settling time of about 0.03 seconds. The improved overshoot over the low bandwidth recovery design is due to the increased phase margins provided by the recovery of the LQ phase characteristic to a higher frequency.

A Nyquist plot of the compensated system is shown in Figure 5.27. The stability margins obtained from the plot indicate a negative phase margin of  $56^\circ$ , a positive phase margin of  $62^\circ$ , an upward gain margin of  $20.00 \text{ dB}$ , and a downward gain margin of  $39.08 \text{ dB}$ . Note that the Nyquist plot for this design is rotated slightly in a counterclockwise manner compared to design LQG/LTR-1a, and that the downward gain margin has been correspondingly reduced.

A compensator design which provides a  $-90^\circ$  bandwidth of  $100 \text{ Hz}$  for the high bandwidth LQ target, is achieved with values of the Kalman filter design parameters  $\mu = 10^{-9}$  and  $\Xi = 10^6$ . This design is referred to as LQG/LTR-2a. A Bode plot of the overall compensator,  $K(s)$ : the model based compensator,  $K_{MBC}(s)$ , modified with the notch filter, and augmented with the demodulation

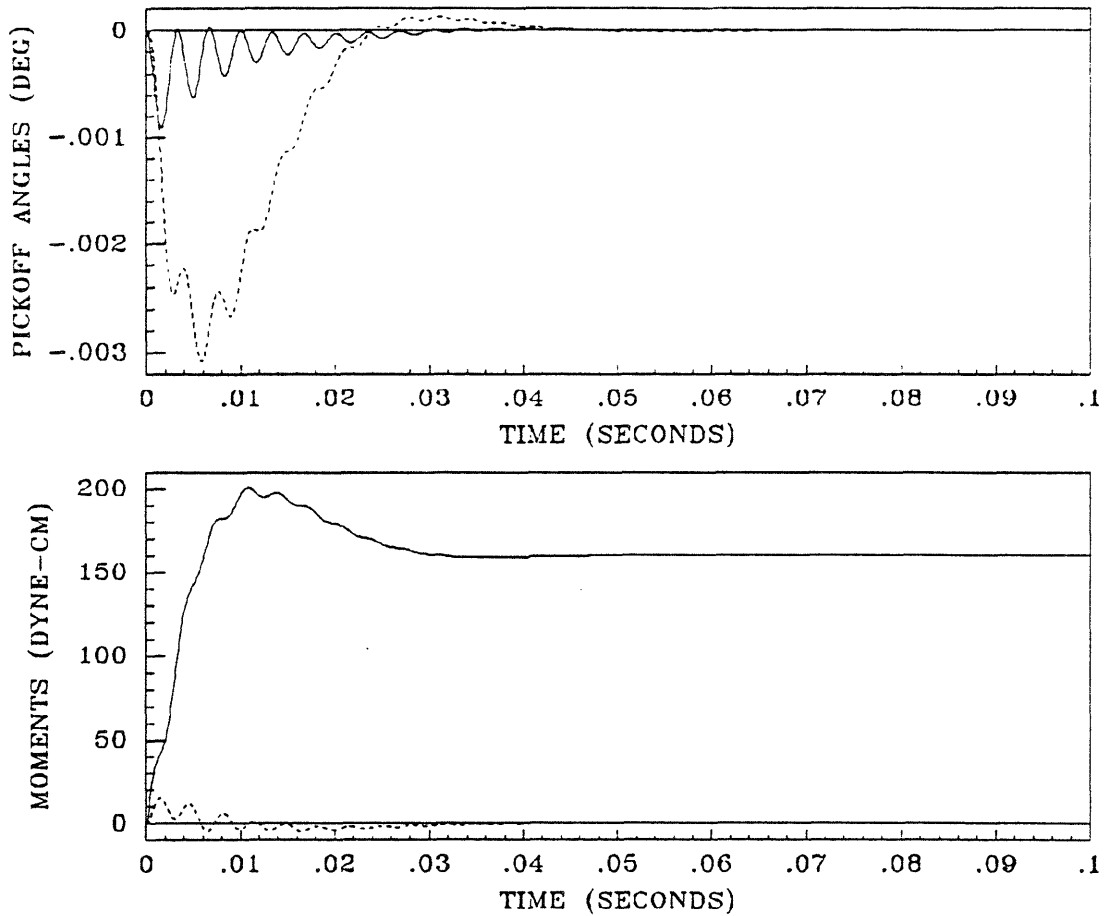


Figure 5.26: Design LQG/LTR-1b Step Response

filter and integrator, is shown in Figure 5.28. The compensator poles and zeros are listed in Table 5.10, and the compensator Bode gain is  $243.9 - j923.3$  which yields a velocity error constant,  $K_v$ , of  $125.9 \text{ dB}$ . Note that this compensator has a relatively well damped zero in the right half plane. A Bode plot of the compensated open loop system is shown in Figure 5.29 while a Bode plot of the closed loop system is shown in Figure 5.30. The system has a  $-90^\circ$  bandwidth of  $100 \text{ Hz}$  and a  $-3 \text{ dB}$  bandwidth of  $120 \text{ Hz}$ . The  $M_p$  of the forward transfer function is  $1.93 \text{ dB}$  while the  $M_p$  of the backward transfer function is  $4.89 \text{ dB}$ , and the attenuation at  $10 \text{ kHz}$  is  $-140 \text{ dB}$ . The closed loop system poles are listed in Table 5.11.

The response of the system to a  $1 \text{ deg/sec}$  step in the  $y$ -axis inertial angular rate, or  $\dot{\phi}_e = j \cdot 1 \text{ deg/sec}$ , is shown in Figure 5.31. The maximum deviation of the  $y$ -axis pickoff angle is  $0.00225^\circ$  while the  $x$ -axis moment command has an

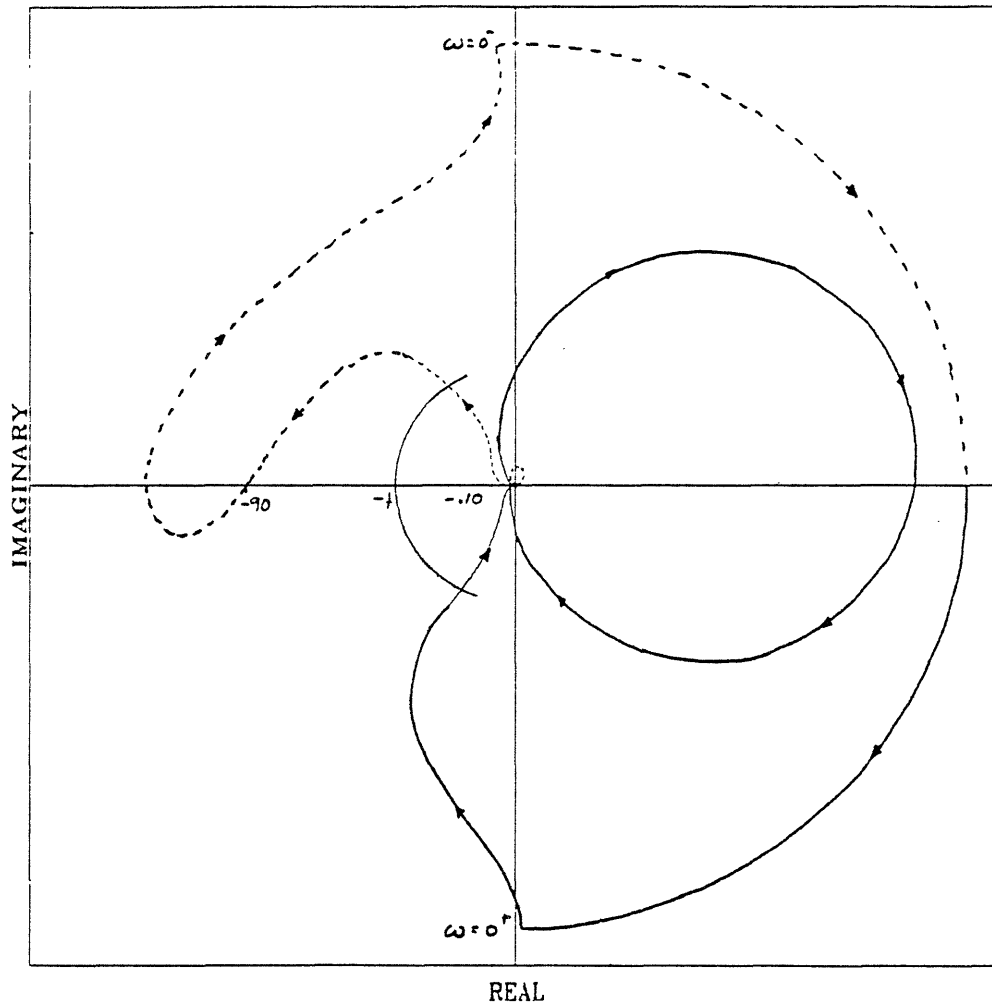


Figure 5.27: Design LQG/LTR-1b Nyquist Plot

Table 5.10: Design LQG/LTR-2a Compensator Poles and Zeros

Poles	Zeros
0.0	$254.87 + j1348.5$
$-471.00 + j816.35$	$-470.05 + j822.68$
$-471.00 - j816.35$	$-460.76 - j790.35$
$-130.24 + j1242.7$	$-0.001256 + j1256.6$
$-132.03 - j1221.0$	$-0.001256 - j1256.6$
$-1398.1 + j6103.5$	$-211.89 - j34.268$
$-1366.7 - j5207.9$	
$-4980.3 + j4687.5$	
$-4793.4 - j3972.7$	
$-6855.9 + j280.59$	

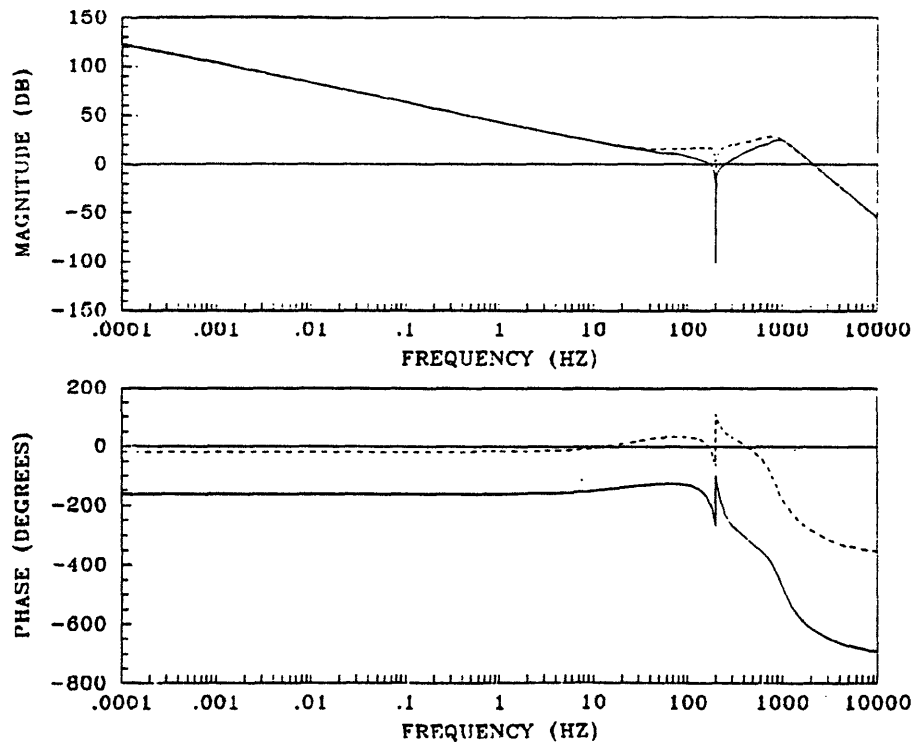


Figure 5.28: Design LQG/LTR-2a Augmented Compensator Bode Plot

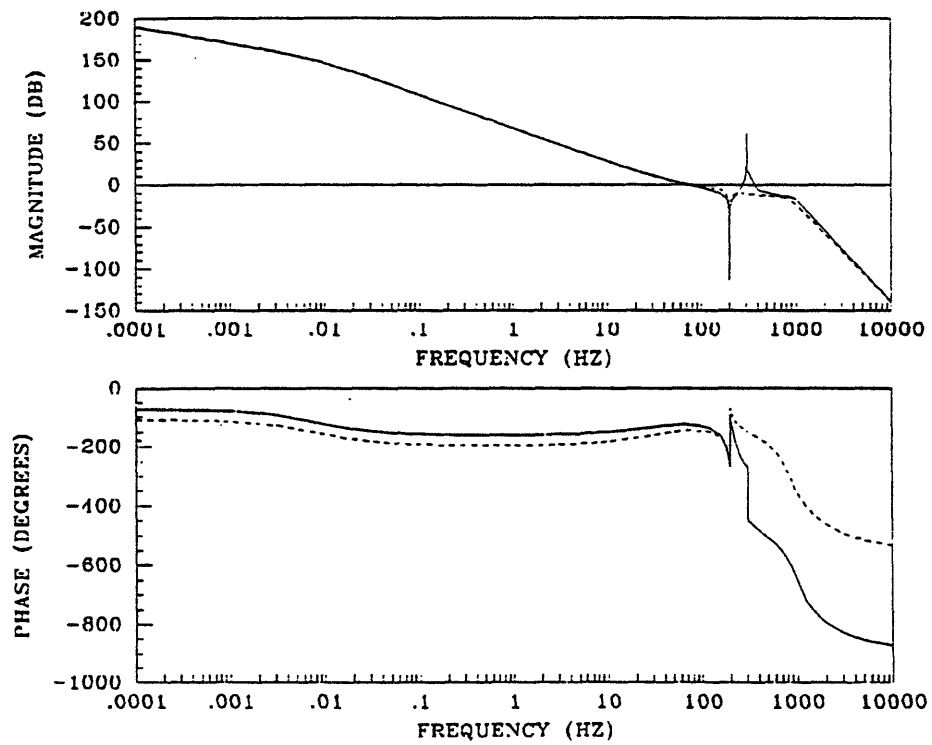


Figure 5.29: Design LQG/LTR-2a Open Loop Bode Plot



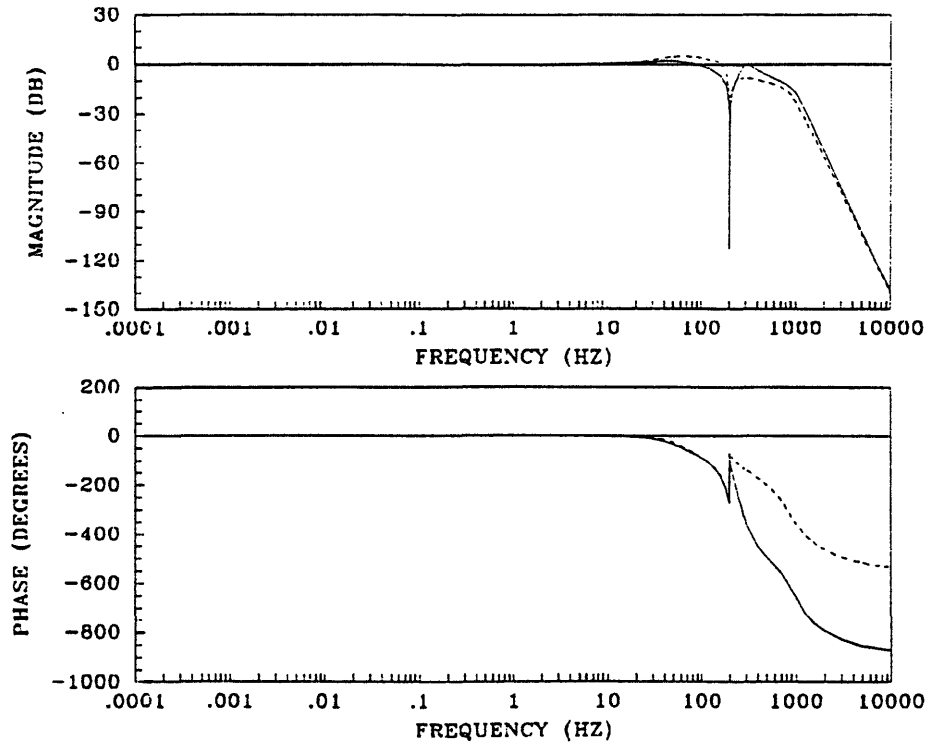


Figure 5.30: Design LQG/LTR-2a Closed Loop Bode Plot

overshoot of 40% and a settling time of about 0.02 seconds. The faster response compared to the 50 Hz bandwidth designs is due to the higher bandwidth of the system, but this causes more control authority to be used by both the  $x$ -axis and  $y$ -axis torquers.

A Nyquist plot of the compensated system is shown in Figure 5.32. The stability margins obtained from the plot indicate a negative phase margin of  $34^\circ$ , a positive phase margin of  $52^\circ$ , an upward gain margin of 6.38 dB, and a downward gain margin of 24.35 dB. Note that the low frequency portion

Table 5.11: Design LQG/LTR-2a Closed Loop Poles

Closed Loop Poles	
$-5649.8 + j378.24$	$-308.61 + j1785.4$
$-525.19 + j865.18$	$-165.05 - j1116.7$
$-459.57 - j805.35$	$-1742.6 + j5887.4$
$-350.70 + j258.15$	$-1748.3 - j5113.0$
$-288.78 - j292.45$	$-4565.0 + j3780.7$
$-220.93 + j1218.6$	$-4574.4 - j3016.7$

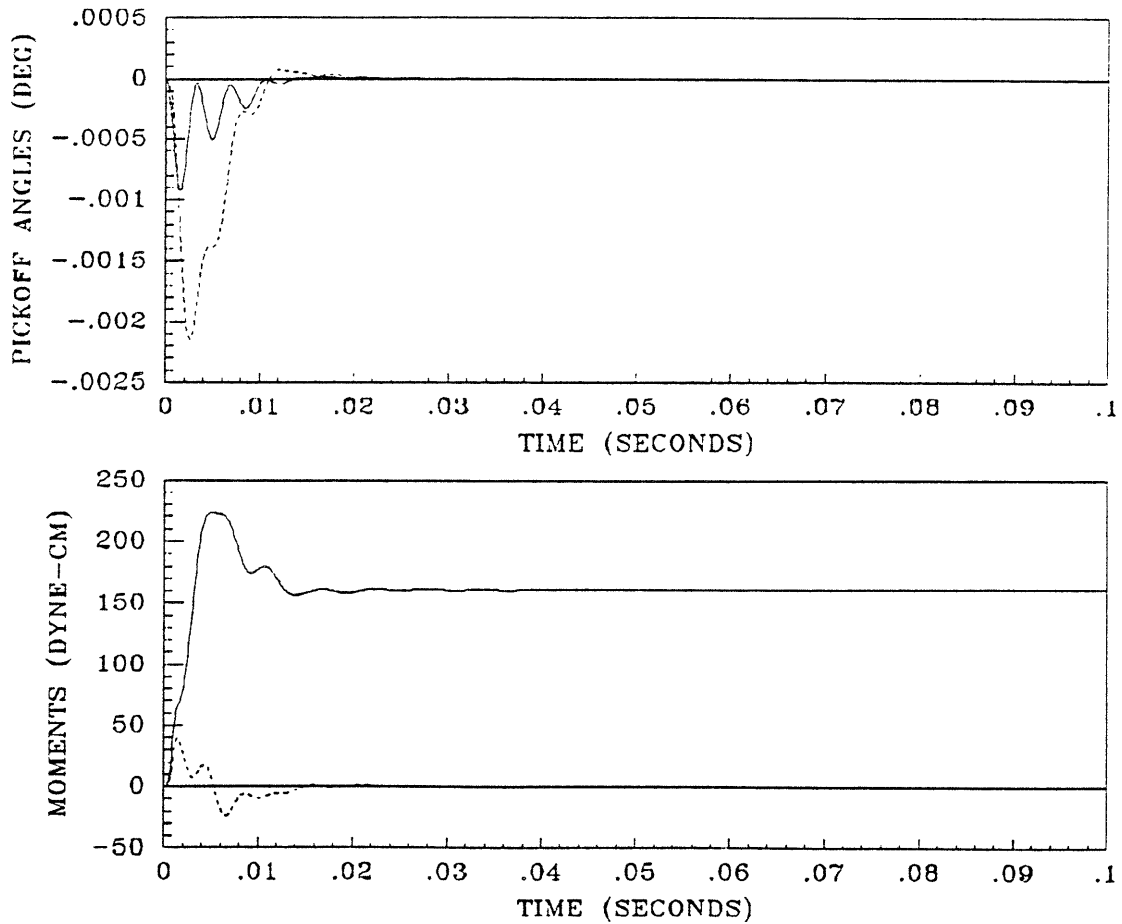


Figure 5.31: Design LQG/LTR-2a Step Response

of the Nyquist plot is rotated counterclockwise somewhat. This is due to the combination of cross and auto feedback at low frequencies. This effect tends to reduce downward gain margins and negative phase margins, and increase positive phase margins. The upward gain margin for this design is also significantly lower than those of the other LQG/LTR designs.

A compensator design which recovers the magnitude characteristic of the high bandwidth LQ target loop a decade beyond nutation and recovers the phase characteristic slightly beyond nutation is achieved with values of the Kalman filter design parameters  $\mu = 10^{-15}$  and  $\Xi = 10^6$ . This design is referred to as LQG/LTR-2b. A Bode plot of the overall compensator,  $K(s)$ : the model based compensator,  $K_{MBC}(s)$ , modified with the notch filter, and augmented with the demodulation filter and integrator, is shown in Figure 5.33. The compensator poles and zeros are listed in Table 5.12, and the compensator Bode gain is

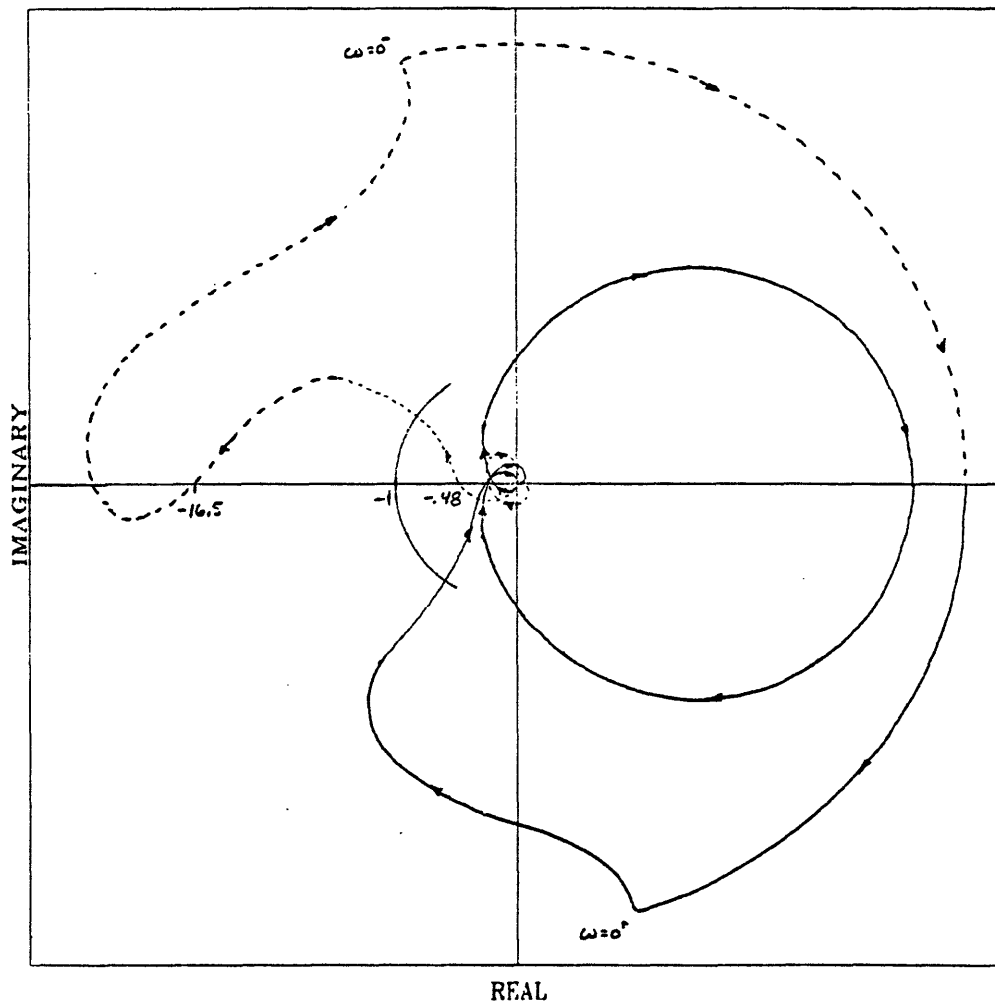


Figure 5.32: Design LQG/LTR-2a Nyquist Plot

455.1 -  $j1167$  which yields a velocity error constant,  $K_v$ , of 128.3 dB. This is the only minimum phase LQG/LTR compensator of those presented here. A Bode plot of the compensated open loop system is shown in Figure 5.34 while a Bode plot of the closed loop system is shown in Figure 5.35. The system has a  $-90^\circ$  bandwidth of 125 Hz and a  $-3$  dB bandwidth of just over 100 Hz. The  $M_p$  of the forward transfer function is 1.18 dB while the  $M_p$  of the backward transfer function is 3.95 dB, and the attenuation at 10 kHz is  $-90$  dB. The closed loop system poles are listed in Table 5.13.

The response of the system to a 1 deg/sec step in the  $y$ -axis inertial angular rate, or  $\dot{\phi}_c = j \cdot 1 \text{ deg/sec}$ , is shown in Figure 5.36. The maximum deviation of the  $y$ -axis pickoff angle is  $0.00156^\circ$  while the  $x$ -axis moment command has an overshoot of 34% and a settling time of about 0.02 seconds. The improved

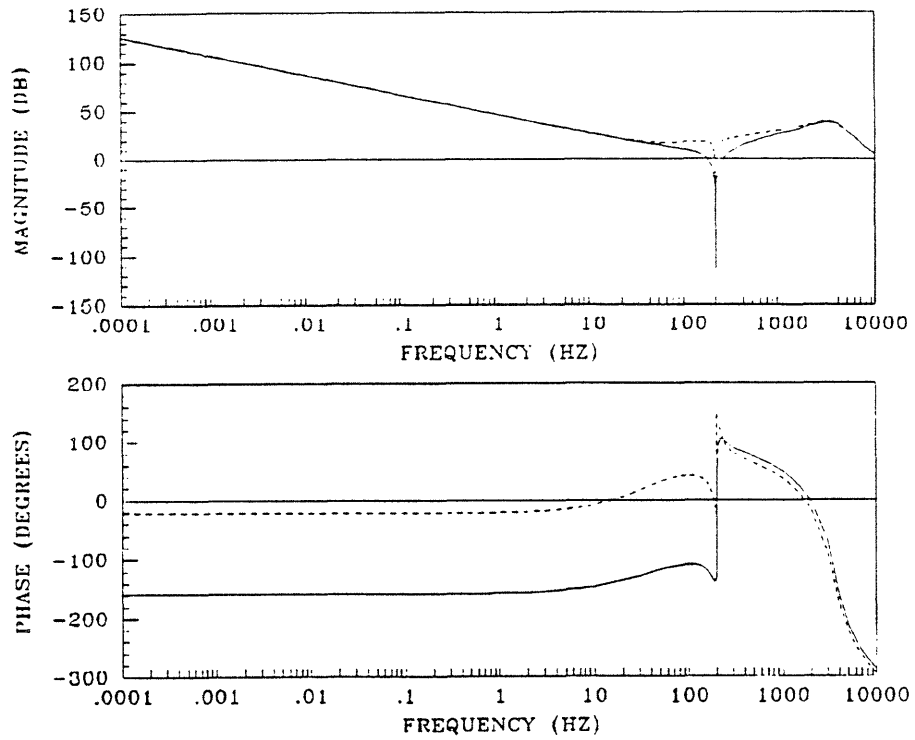


Figure 5.33: Design LQG/LTR-2b Augmented Compensator Bode Plot

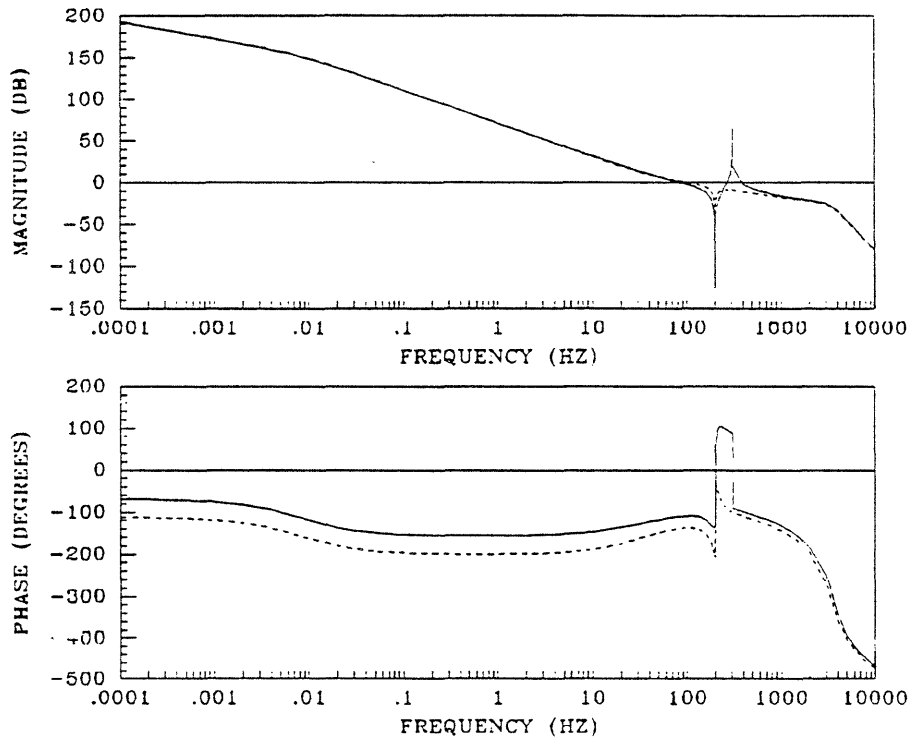


Figure 5.34: Design LQG/LTR-2b Open Loop Bode Plot

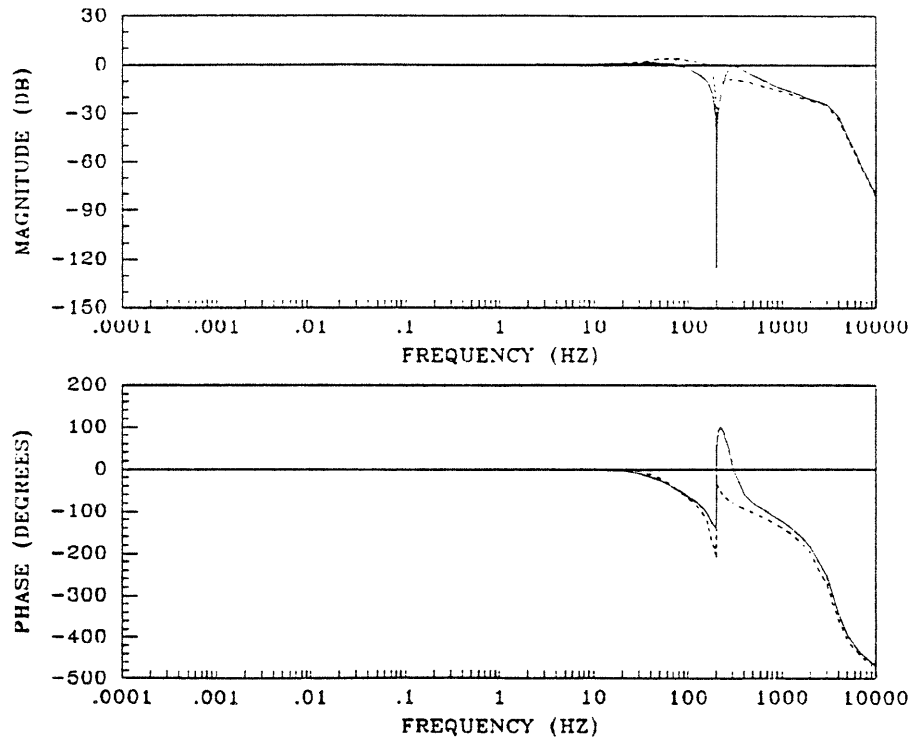


Figure 5.35: Design LQG/LTR-2b Closed Loop Bode Plot

Table 5.12: Design LQG/LTR-2b Compensator Poles and Zeros

Poles	Zeros
0.0	$-56.568 + j1284.3$
$-471.00 + j816.35$	$-465.60 + j823.77$
$-471.00 - j816.35$	$-463.67 - j765.67$
$-183.72 + j1242.4$	$-0.001256 + j1256.6$
$-183.57 - j1239.7$	$-0.001256 - j1256.6$
$-5227.3 + j21911.$	$-241.12 - j49.201$
$-5246.0 - j20947.$	
$-17692. + j12080.$	
$-17879. - j11100.$	
$-30347. - j116.76$	

Table 5.13: Design LQG/LTR-2b Closed Loop Poles

Closed Loop Poles	
$-29487. - j595.43$	$-308.61 + j1785.4$
$-525.19 + j865.18$	$-165.05 - j1116.7$
$-459.57 - j805.35$	$-5633.5 + j21787.$
$-350.70 + j258.15$	$-5537.5 - j20823.$
$-288.78 - j292.45$	$-17184. + j10987.$
$-220.93 + j1218.6$	$-17539. - j9521.4$

overshoot over the low bandwidth recovery design is due to the increased phase margins provided by the recovery of the LQ phase characteristic to a higher frequency.

A Nyquist plot of the compensated system is shown in Figure 5.37. The stability margins obtained from the plot indicate a negative phase margin of  $43^\circ$ , a positive phase margin of  $70^\circ$ , an upward gain margin of  $10.45 \text{ dB}$ , and a downward gain margin of  $22.92 \text{ dB}$ .

### 5.4.5 Summary

The LQG/LTR design methodology allows the performance and stability properties of a linear quadratic regulator loop to be recovered in the feedback loop. Due to the requirement of a notch filter in the compensator, the compensator resulting from the recovery process must be augmented with a notch filter. This destroys the guaranteed stability properties of the recovered LQ loop, but the stability margins for the designs investigated remain quite large.

Two LQ loops are designs, one with a  $50 \text{ Hz}$  bandwidth and one with a  $100 \text{ Hz}$  bandwidth. Each design is recovered to the LQ bandwidth and also a decade beyond the nutation frequency. The stability and performance parameters for the four LQG/LTR compensator designs are summarized in Table 5.14. The first three compensator designs in the table contain a non-minimum phase zero. The high frequency recovery designs (1b and 2b) provide better performance and stability than the low frequency recovery designs, since the performance and stability properties of the LQ loops are better recovered. However, this comes at a cost of lower attenuation at high frequencies. The high bandwidth designs use more auto feedback than the low bandwidth designs, which results

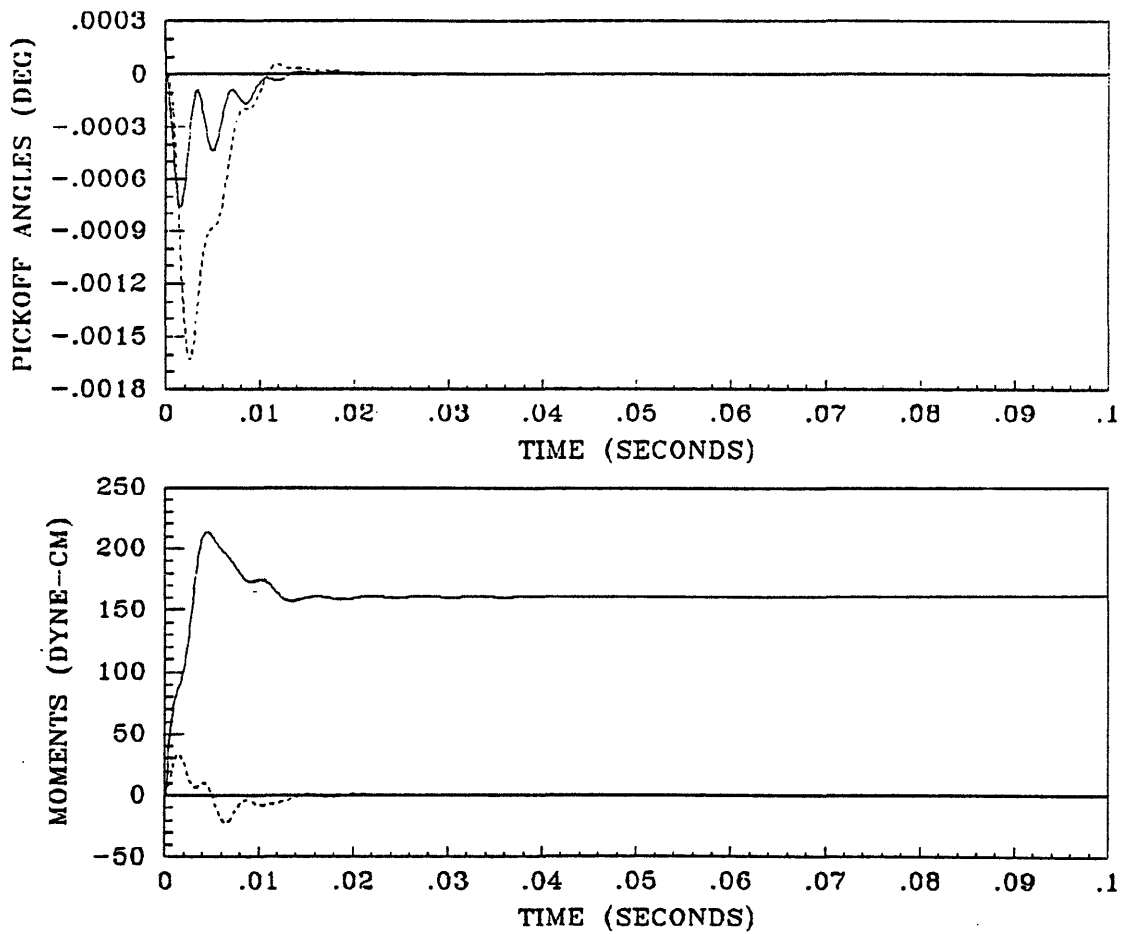


Figure 5.36: Design LQG/LTR-2b Step Response

in a counterclockwise rotation of the Nyquist plot and lower negative phase margins but higher positive phase margins. The downward gain margins of the high bandwidth designs are also lower than those of the low bandwidth designs.

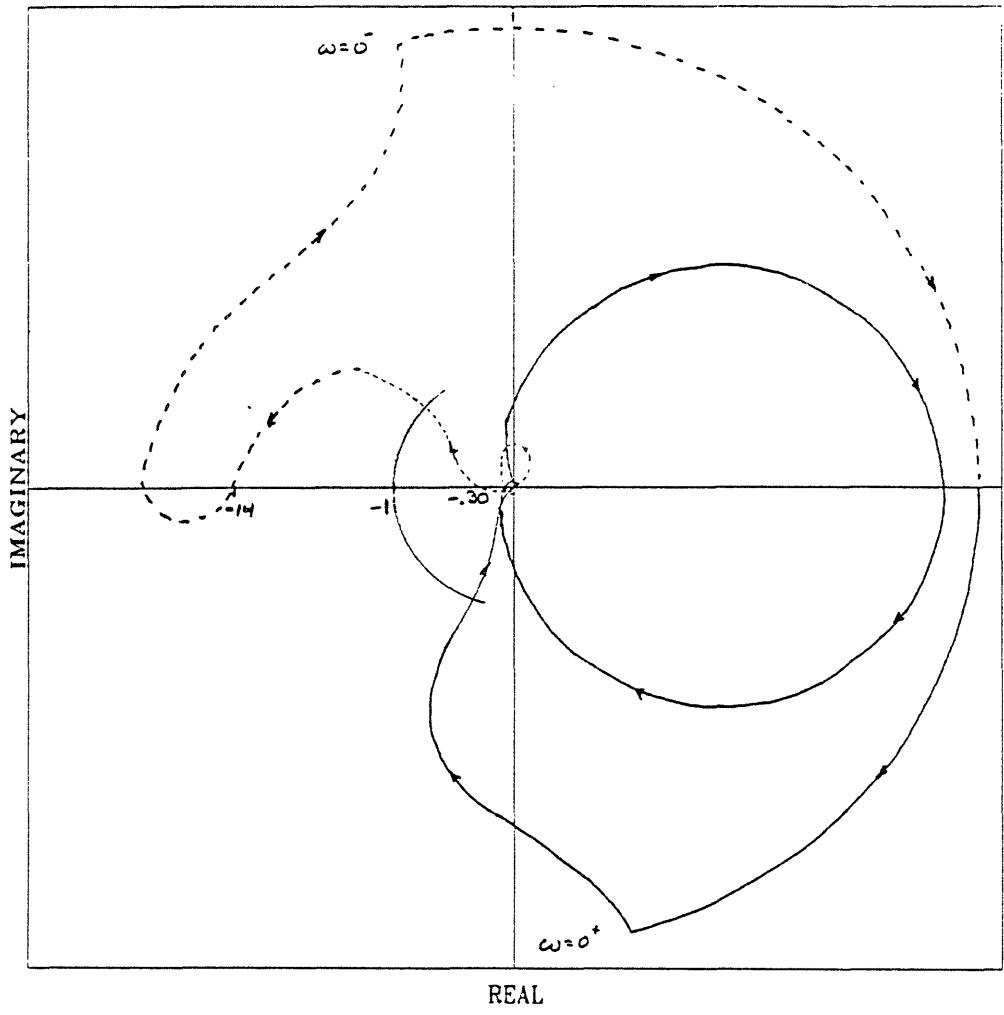


Figure 5.37: Design LQG/LTR-2b Nyquist Plot



Table 5.14: LQG/LTR Compensator Design Parameters

Parameters	Units	LQG/LTR Designs			
		1a	1b	2a	2b
Upward Gain Margin	<i>dB</i>	12.40	20.00	6.38	10.45
Downward Gain Margin	<i>dB</i>	48.16	39.08	24.35	22.92
Negative Phase Margin	<i>deg</i>	48	56	34	43
Positive Phase Margin	<i>deg</i>	50	62	52	70
$-90^\circ$ Bandwidth	<i>Hz</i>	50	80	100	125
$-3$ <i>dB</i> Bandwidth	<i>Hz</i>	70	50	120	100
Forward TF $M_p$	<i>dB</i>	2.51	1.85	1.93	1.18
Backward TF $M_p$	<i>dB</i>	3.02	2.59	4.89	3.95
Velocity Error Constant	<i>dB</i>	113.5	115.5	125.9	128.3
CL Gain at 10 <i>kHz</i>	<i>dB</i>	-170	-90	-140	-90
Moment Command Overshoot	%	31	25	40	34
Settling Time	<i>sec</i>	0.03	0.03	0.02	0.02
Pickoff Angle Deviation	<i>deg</i>	0.0039	0.0031	0.00225	0.00156

## 5.5 FW/LQG Design

### 5.5.1 Description of Design Methodology

The frequency weighted linear quadratic Gaussian design methodology was derived by Gupta [9] and has been found useful in the control of flexible space structures [10]. The methodology generates a linear quadratic regulator which minimizes a cost functional of the state variables and controls weighted as functions of frequency instead of time as in the traditional LQR formulation. The main advantage of FW/LQG is that it can be used to create special LQ loop shapes, such as notch filters, that are not possible with a time domain weighting function. The dual of the frequency weighted LQ problem is the correlated noise Kalman filter problem. This Kalman filter problem is derived in Appendix C.

Consider the frequency based cost functional

$$J = \frac{1}{2} \int_{-\infty}^{\infty} [\underline{x}^H(j\omega) Q_{xx}(j\omega) \underline{x}(j\omega) + u_p^*(j\omega) Q_{uu}(j\omega) u_p(j\omega)] d\omega \quad (5.28)$$

constrained by the augmented system dynamics

$$\dot{\underline{x}}(t) = A_x \underline{x}(t) + B_x u_p(t) \quad (5.29)$$

and the control law,

$$u_p(t) = -G_x \underline{x}(t) \quad (5.30)$$

where  $\underline{x}$  is the augmented state vector discussed in Section 4.3. The state vector weighting matrix,  $Q_{xx}(j\omega)$ , is a function of frequency, and the control weighting matrix,  $Q_{uu}(j\omega)$ , is also a function of frequency. The superscript  $H$  in Equation (5.28) denotes complex conjugate transpose, and the control,  $u_p$ , is a scalar for the gyro problem described by a complex coefficient transfer function.

The state vectors and control variables are weighted in the frequency domain by the generally complex coefficient filters  $N(s)$  and  $P(s)$

$$\underline{z}(s) = N(s) \underline{x}(s) \quad (5.31)$$

$$u(s) = P(s) u_p(s) \quad (5.32)$$

which have the state space representations shown in Equations (5.33) and (5.34) and Equations (5.35) and (5.36).

$$\dot{\underline{x}}_z(t) = A_z \underline{x}_z(t) + B_z \underline{x}(t) \quad (5.33)$$

$$\underline{z}(t) = C_z \underline{x}_z(t) + D_z \underline{x}(t) \quad (5.34)$$

$$\dot{\underline{x}}_u(t) = A_u \underline{x}_u(t) + B_u u_p(t) \quad (5.35)$$

$$u(t) = C_u \underline{x}_u(t) + D_u u_p(t) \quad (5.36)$$

The state and control weighting matrices are formed by

$$Q_{xx}(j\omega) = N(j\omega)^H N(j\omega) \quad (5.37)$$

$$Q_{uu}(j\omega) = P(j\omega)^H P(j\omega) \quad (5.38)$$

where  $s$  has been replaced by  $j\omega$ . The cost functional in Equation (5.28) can now be written as

$$J = \frac{1}{2} \int_{-\infty}^{\infty} [\underline{z}^H(j\omega) \underline{z}(j\omega) + u^*(j\omega) u(j\omega)] d\omega. \quad (5.39)$$

Augmenting the design plant model dynamics with the state vector and control weighting dynamics yields the new complex system dynamics in Equation (5.40)

$$\dot{\underline{X}}(t) = A \underline{X}(t) + B u_p(t) \quad (5.40)$$

which is partitioned as

$$\begin{bmatrix} \dot{\underline{x}} \\ \dot{\underline{x}}_z \\ \dot{\underline{x}}_u \end{bmatrix} = \begin{bmatrix} A_x & 0 & 0 \\ B_z & A_z & 0 \\ 0 & 0 & A_u \end{bmatrix} \begin{bmatrix} \underline{x} \\ \underline{x}_z \\ \underline{x}_u \end{bmatrix} + \begin{bmatrix} B_x \\ 0 \\ B_u \end{bmatrix} u_p(t).$$

The frequency based cost functional in Equation (5.39) is expressed in the time domain by application of Parseval's theorem, and is shown in Equation (5.41).

$$J = \lim_{T \rightarrow \infty} \frac{1}{2T} \int_0^T [\underline{X}^H(t) Q_{xx} \underline{X}(t) + 2 \underline{X}^H(t) Q_{xu} u_p(t) + u_p^*(t) Q_{uu} u_p(t)] dt \quad (5.41)$$

The new, constant weighting matrices are partitioned as

$$Q_{xx} = \begin{bmatrix} D_z^H D_z & D_z^H C_z & 0 \\ C_z^H D_z & C_z^H C_z & 0 \\ 0 & 0 & C_u^H C_u \end{bmatrix} \quad Q_{xu} = \begin{bmatrix} 0 \\ 0 \\ C_u^H D_u \end{bmatrix} \quad Q_{uu} = D_u^H D_u$$

where  $Q_{xx}$  is a positive semi-definite matrix and  $Q_{uu}$  is positive definite.

The optimal feedback gain matrix comes from the solution to the algebraic Riccati equation

$$0 = SA + A^H S + Q_{xx} - (SB + Q_{xu}) Q_{uu}^{-1} (B^H S + Q_{xu}^H) \quad (5.42)$$

$$G = Q_{uu}^{-1} (B^H S) \quad (5.43)$$

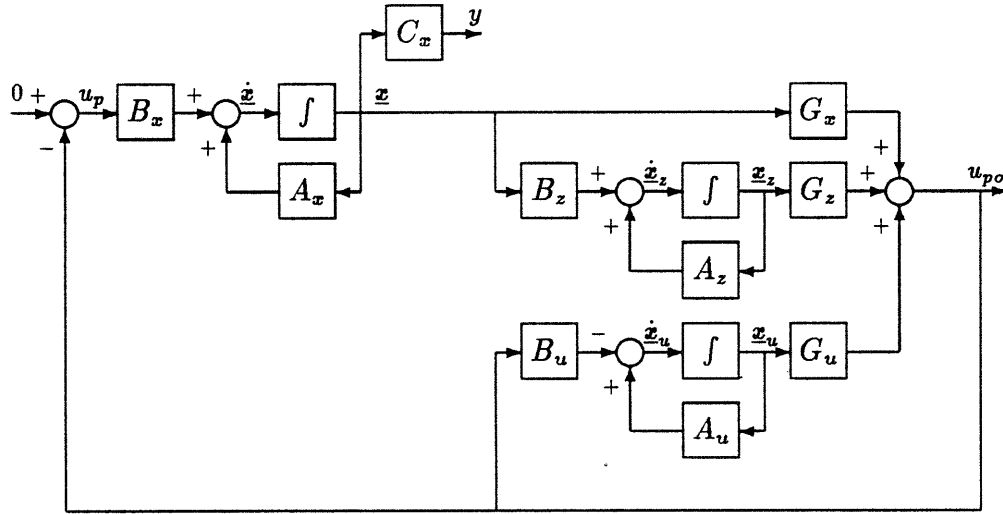


Figure 5.38: Frequency Weighted LQ Loop Block Diagram

where  $G$  is partitioned as

$$G = \begin{bmatrix} G_x & G_z & G_u \end{bmatrix}$$

with the new control law

$$u_p(t) = -G\underline{X}(t). \quad (5.44)$$

A block diagram of the FW/LQ loop is shown in Figure 5.38. The controller contains the dynamics of the state and control variable weighting functions of Equations (5.31) and (5.32).

To complete the FW/LQG design, a Kalman filter is used to form estimates of the plant states,  $\hat{x}(t)$ , from the output of the design plant model. The filter gain matrix,  $H_x$ , comes from the standard Kalman filter problem described in Equations (5.9) through (5.12) where the intensities of the measurement and process noises are chosen to place the closed loop filter poles about a decade beyond the crossover of the LQ loop. A block diagram of the complete FW/LQG system is shown in Figure 5.39. The FW/LQG compensator is a model based compensator including the dynamics of the plant as well as the state and control weighting function dynamics.

The FW/LQG controller has several interesting properties. As noted by Gupta [9], poles of the control weighting function,  $P(s)$ , are zeros of the com-

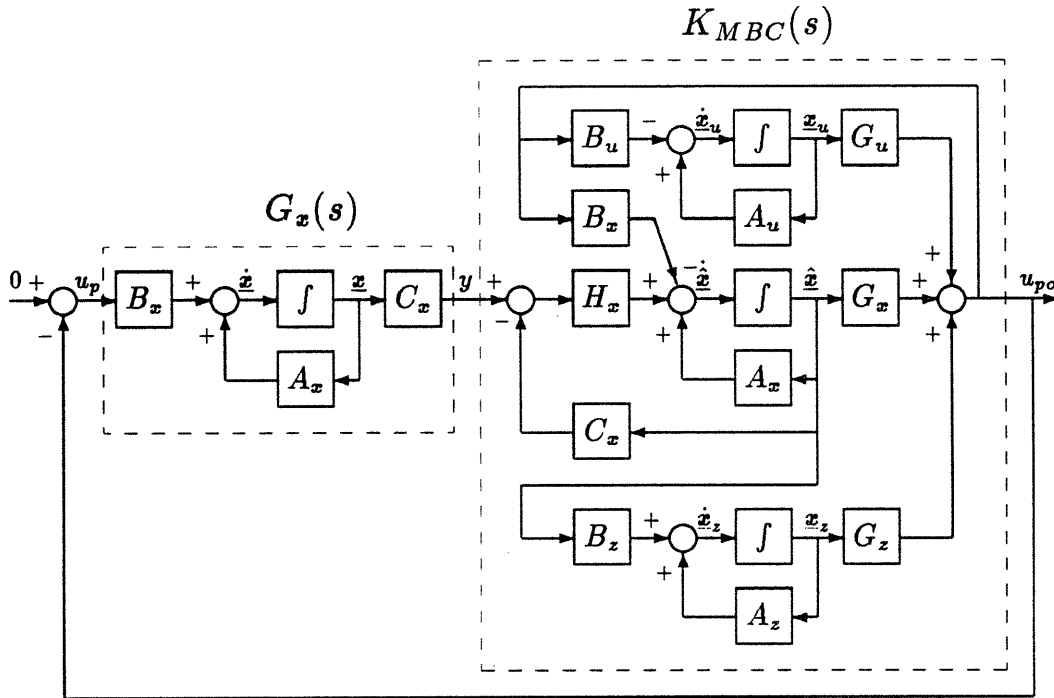


Figure 5.39: Complete FW/LQG Feedback Loop Block Diagram

compensator, and poles of the state weighting function,  $N(s)$ , are poles of the compensator. In addition, some of the closed loop system poles approach the stable zeros of  $N(s)$  and  $P(s)$  even though these zeros do not explicitly appear in the compensator. These properties give some indication of how  $N(s)$  and  $P(s)$  should be chosen to place some closed loop poles and zeros.

### 5.5.2 Design Approach

Two FW/LQG designs are examined. One compensator design provides a bandwidth of 50 Hz, and the other provides a bandwidth of 100 Hz. Both designs have estimator poles placed far enough beyond the LQ loop crossover frequency such that the bandwidth of the original LQ loop is preserved.

The LQ loop is shaped by the choice of the weighting functions,  $P(s)$  and  $N(s)$ . The control weighting is chosen to introduce a notch filter into the compensator and allow large control at low frequencies. A number of different choices are available for the state weighting, and three different functions are presented to illustrate the effects of  $N(s)$  on the 50 Hz bandwidth controller design.

For the designs considered here, both  $N(s)$  and  $P(s)$  are real coefficient SISO transfer functions. Only the output of the design plant model,  $y$ , is weighted by  $N(s)$  since direct weighting of individual states is considered to be too complicated. There is only one control variable in the complex representation of the system so  $P(s)$  is also a scalar function. They have real coefficients because the weighting functions are applied equally to each output and control of the real TITOBS system.

### Control Weighting Function Selection

The control weighting function,  $P(s)$ , is chosen to satisfy the requirement for a notch filter in the compensator and also to allow large control values at low frequencies to make it easy to generate high bandwidth LQ loops. A Bode plot of  $P(s)$  is shown in Figure 5.40. It has the form shown in Equation (5.45)

$$P(s) = \frac{s(s + \omega_z)}{s^2 + 2\zeta_n\omega_n s + \omega_n^2} \quad (5.45)$$

where

$$\begin{aligned} \omega_z &= 2\pi \cdot 1000 \text{ Hz} \\ \omega_n &= 2\pi \cdot 200 \text{ Hz} \\ \zeta_n &= 10^{-6}. \end{aligned}$$

Since there is expected to be noise in the gyro output at the spin frequency of 200 Hz, it is not desirable for the gyro moment command to contain this noise. Therefore, the control variable is weighted very heavily at 200 Hz, by placing a lightly damped pair of poles at that frequency. Since the poles of the control weighting function are zeros of the compensator, this guarantees that the compensator will have a notch filter at that frequency. The notch at 200 Hz created by the control weighting can be seen in the closed loop Bode plot for one design in Figure 5.41.

Additionally, control at low frequencies is weighted less than at high frequencies so that high bandwidths can be obtained without requiring overly large state weightings. The zero at 1000 Hz is included so that the response of the weighting function is flat at high frequencies. This causes  $D_u = 1$  since there are the same number of zeros as poles in the control weighting function, forcing  $Q_{uu}$  to be positive definite. A closed loop pole will approach this zero. This control weighting is used for both FW/LQG designs.

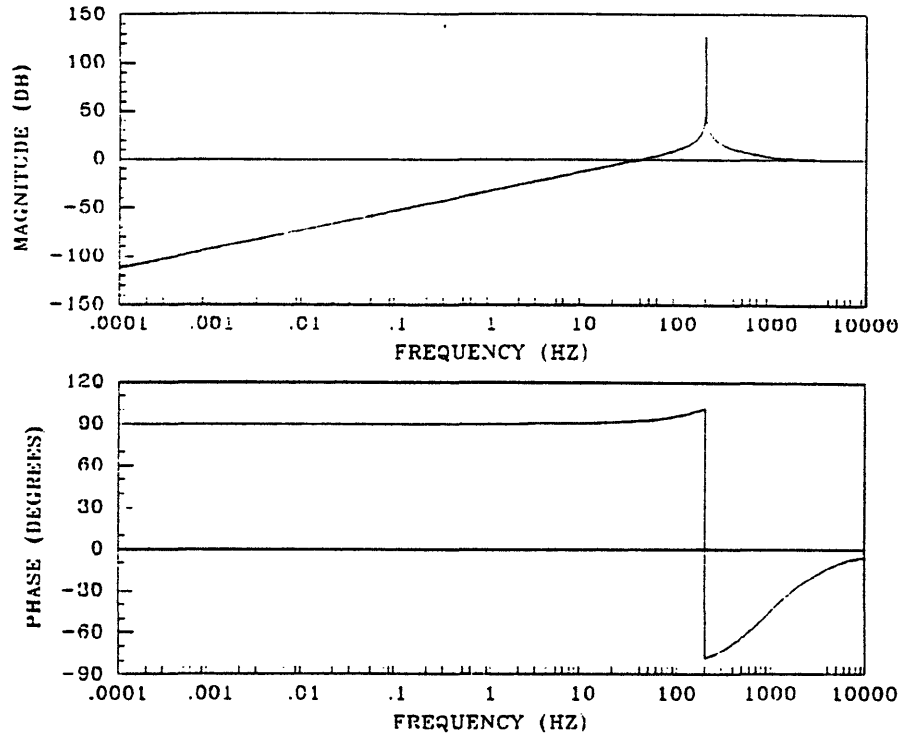


Figure 5.40: Control Weighting Function Bode Plot

### State Weighting Function Selection

Once  $P(s)$  is fixed, the state weighting function is used to further control the shape and bandwidth of the LQ loop by weighting the plant output as a function of frequency. Three different choices of  $N(s)$  for the 50 Hz bandwidth design which illustrate how the loop can be shaped in a systematic manner are presented.

The simplest choice of state weighting is a constant weight on the output for all frequencies. This results in no state weighting dynamics, leaving

$$N(s) = \sqrt{\rho} \quad (5.46)$$

or

$$\underline{z}(t) = D_z \underline{x}(t) = (\sqrt{\rho} C_x) \underline{x}(t) = \sqrt{\rho} y(t) \quad (5.47)$$

where  $\rho$  is a design parameter used to select the bandwidth of the loop. A larger  $\rho$  weights state deviations more heavily, and thus increases the bandwidth.

A value of  $\rho = 7 \times 10^5$  generates a 50 Hz bandwidth LQ loop. A Bode plot of the closed loop system is shown in Figure 5.41. Note how closely the magnitudes and phases of the forward and backward transfer functions are matched. This

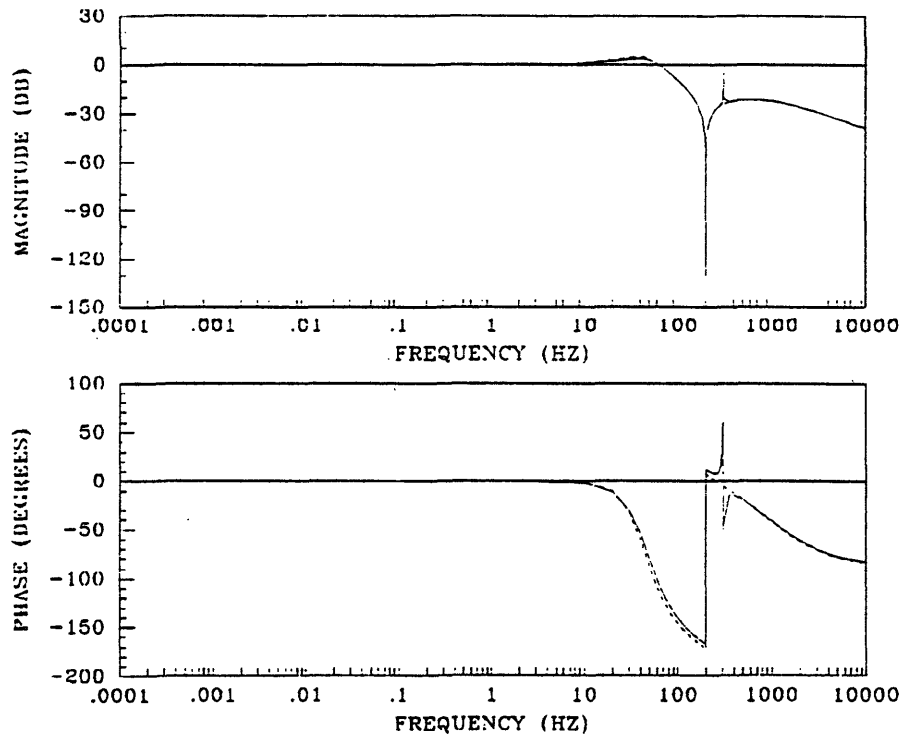


Figure 5.41: Closed Loop LQ Bode Plot: Constant State Weighting

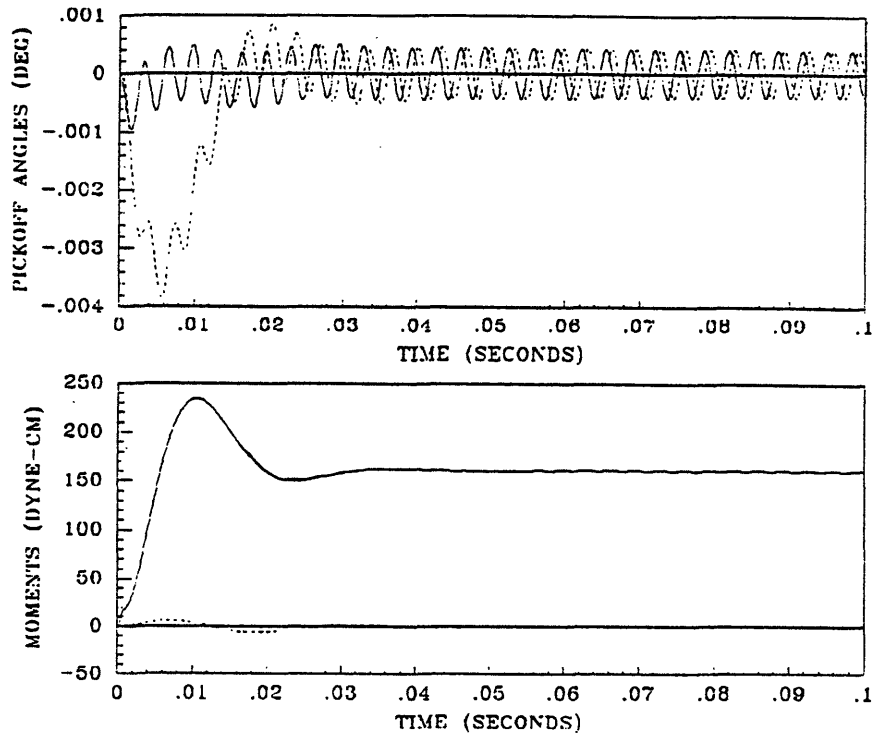


Figure 5.42: Step Response: Constant State Weighting



indicates that the two channels of the TITOBS system are nearly decoupled, producing the near inversion of the plant nutation dynamics. The LQ loop has a zero near the nutation pole of the plant, and cancellation of resonant poles near the  $j\omega$ -axis should be avoided, as noted in [2]. The resulting response of the feedback loop based on this LQ loop for a step in inertial angular rate applied to the gyro case about the  $y$ -axis is shown in Figure 5.42. Since the compensator nearly cancels the nutation pole, the moment command does not work to dampen the nutation oscillation of the pickoff angles. Also note the very small  $y$ -axis moment command, a result of the nearly decoupled channels.

The oscillation of the pickoff angles can be reduced by penalizing output deviations at the nutation frequency very heavily. This state weighting function has the form

$$N(s) = \frac{\sqrt{\rho}\omega_r^2}{s^2 + 2\zeta_r\omega_r s + \omega_r^2} \quad (5.48)$$

where  $\omega_r$  is the nutation frequency, and  $\zeta_r$  is the plant nutation damping. Since the poles of  $N(s)$  are poles of the compensator, the compensator has poles corresponding to the plant nutation mode. This ensures that the compensator will have nutation dynamics that are not cancelled, so the moment command will have authority at that frequency. A Bode plot of this weighting function with  $\rho = 1$  is shown in Figure 5.43.

A value of  $\rho = 5 \times 10^5$  with this resonant state weighting produces an LQ loop with a bandwidth of 50 Hz as shown in Figure 5.44. The corresponding step response is shown in Figure 5.45, and as can be seen, the nutation oscillations in the pickoff angle response have been greatly attenuated.

A problem that remains is the large closed loop peaking of the LQ loop. In this case, the forward transfer function has an  $M_p = 3.35 \text{ dB}$ , and the backward transfer function has an  $M_p = 4.35 \text{ dB}$ . This peaking corresponds to a large overshoot in the moment command step response of the system.

The peaking can be reduced by increasing the weighting on the output at the crossover frequency and above. This is done by including a zero in the state weighting function below the crossover frequency. The resulting weighting function is

$$N(s) = \frac{\sqrt{\rho}(s + \omega_l)\omega_r^2/\omega_l}{s^2 + 2\zeta_r\omega_r s + \omega_r^2} \quad (5.49)$$

where  $\omega_l$  is the frequency of the zero location. A closed loop pole will approach this zero, so  $\omega_l$  cannot be too near the origin or the system step response will be

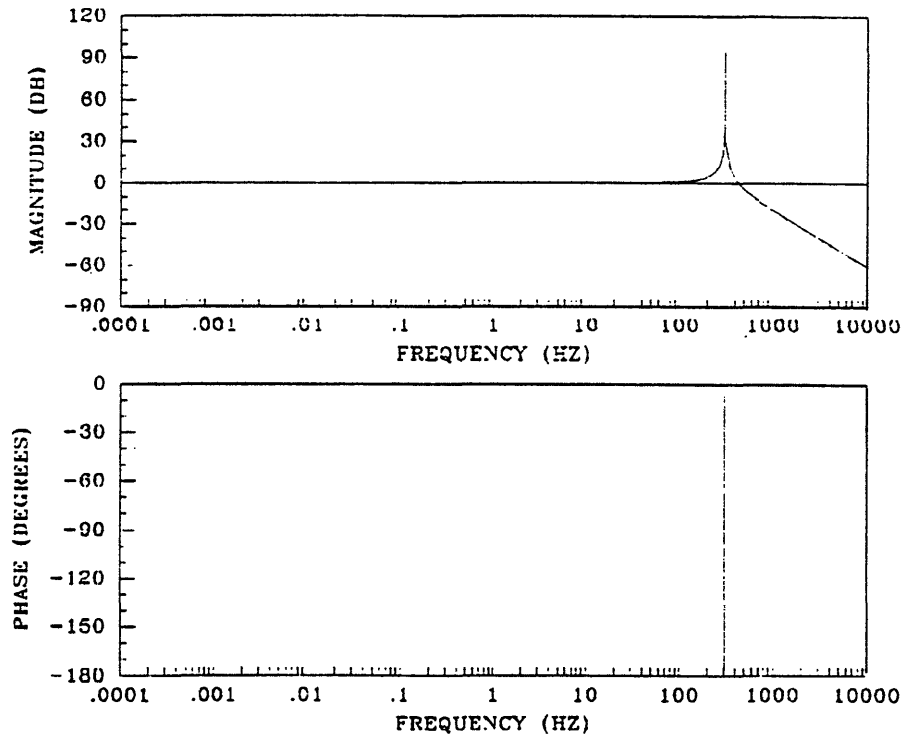


Figure 5.43: Resonant State Weighting Bode Plot

slowed. This is the form of  $N(s)$  that is used in the FW/LQG designs below.

Values of  $\rho = 10^5$  and  $\omega_l = 150$  produce the closed loop LQ Bode plot in Figure 5.48 and the corresponding step response is shown in Figure 5.55. A Bode plot of  $N(s)$  with  $\rho = 1$  is shown in Figure 5.46. Note that the  $M_p$  of both transfer functions has been reduced; the new values are  $1.85 \text{ dB}$  and  $3.05 \text{ dB}$ , respectively. Also, the overshoot of the moment command is reduced, and the damping of the pickoff angle response is improved.

### 5.5.3 FW/LQ Loops

As stated above, the low ( $50 \text{ Hz}$ ) bandwidth LQ design uses the control weighting function in Equation (5.45) and the state weighting function of Equation (5.49) with  $\rho = 10^5$  and  $\omega_l = 150$ . A Bode plot of  $N(s)$  with  $\rho = 1$  is shown in Figure 5.46.

Bode plots of the open and closed loop low bandwidth LQ design are shown in Figures 5.47 and 5.48. The LQ design parameters shown above are chosen to give a  $-90^\circ$  bandwidth of  $50 \text{ Hz}$ . The resulting closed loop LQ poles and zeros are shown in Table 5.15.

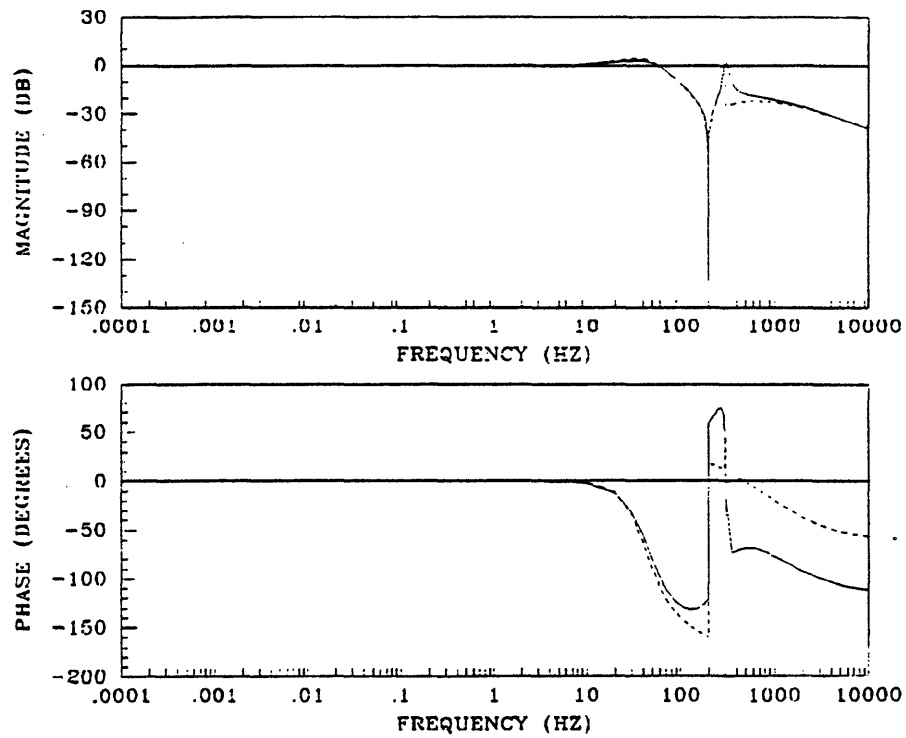


Figure 5.44: Closed Loop LQ Bode Plot: Resonant State Weighting

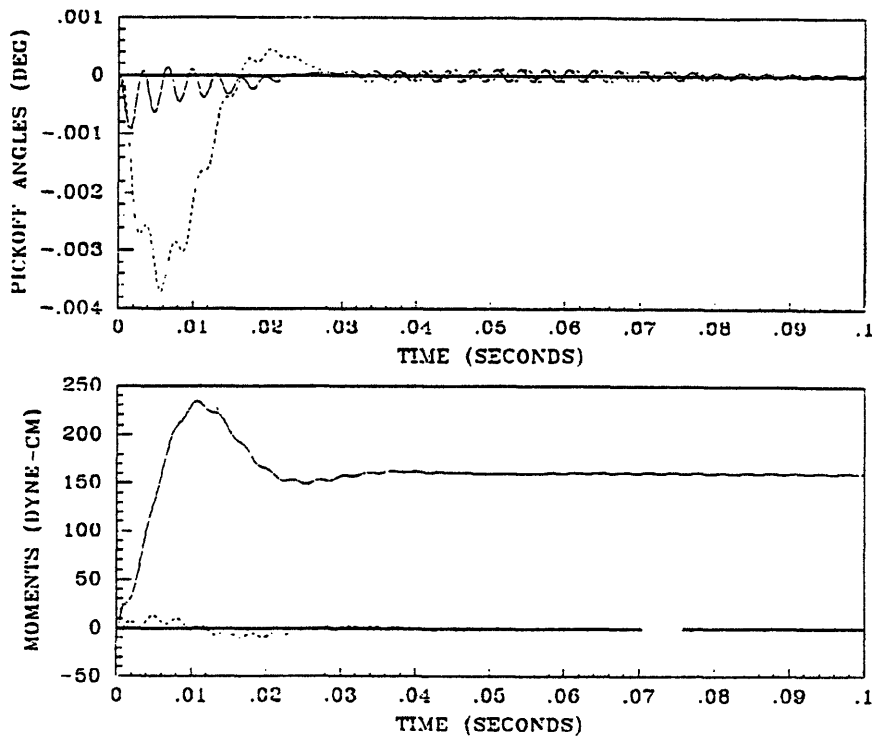


Figure 5.45: Step Response: Resonant State Weighting

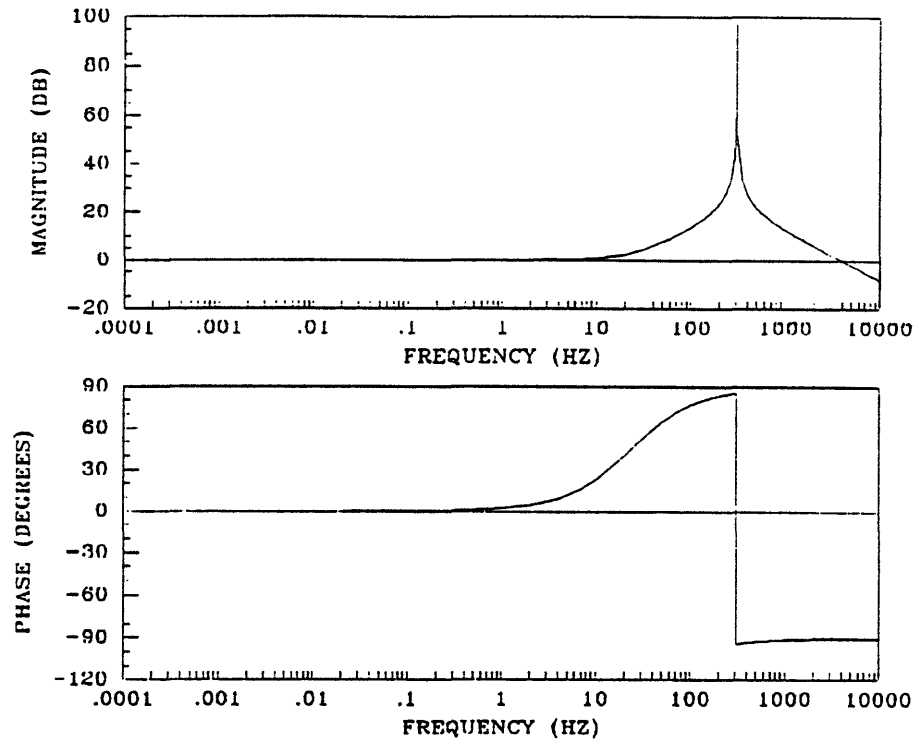


Figure 5.46: Low Bandwidth State Weighting Function Bode Plot

Table 5.15: Low Bandwidth Design LQ Closed Loop Poles and Zeros

Poles	Zeros
$-74.721 + j1845.0$	$-70.468 + j1926.4$
$-68.080 + j1988.2$	$-39.011 - j1942.7$
$-468.78 + j817.83$	$-493.76 + j818.77$
$-470.78 - j815.91$	$-475.04 - j815.53$
$-181.47 + j188.69$	$-0.001256 + j1256.6$
$-150.76 - j189.55$	$-0.001256 - j1256.6$
$-6283.2 + j0.0067$	$-88.331 - j5.1365$
$-2.6650 - j1916.7$	$-655.27 + j392.10$
$-142.11 - j0.8969$	

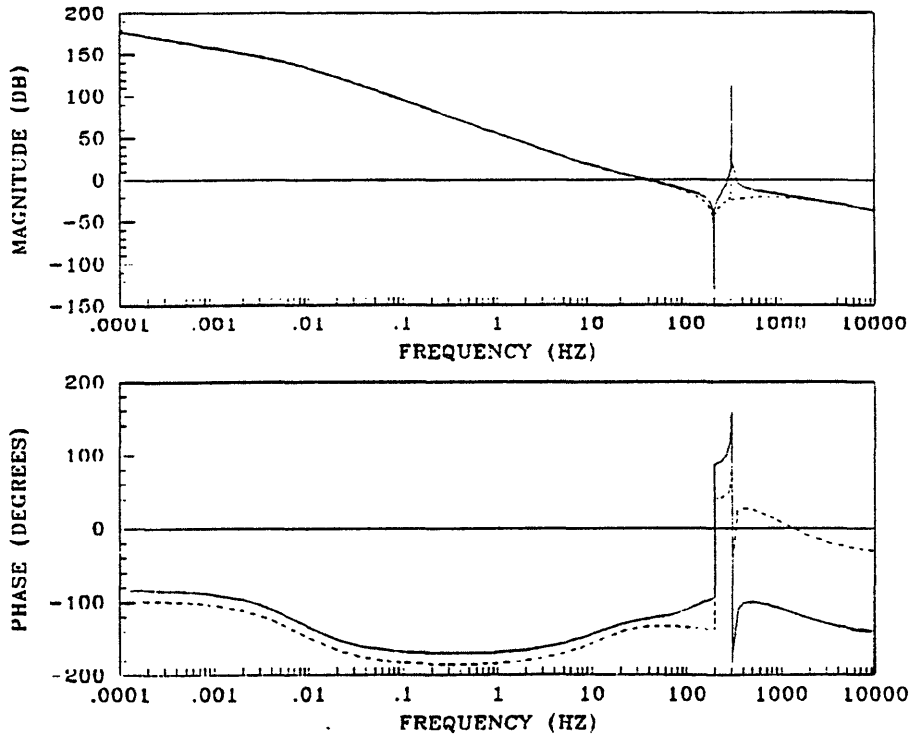


Figure 5.47: Low Bandwidth LQ Design Open Loop Bode Plot

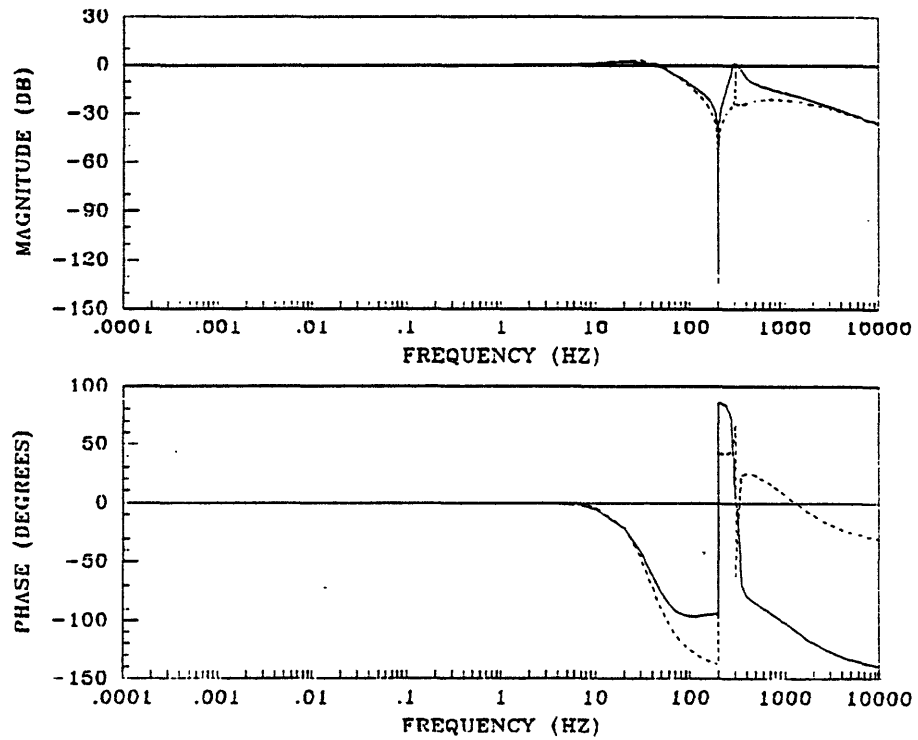


Figure 5.48: Low Bandwidth LQ Design Closed Loop Bode Plot

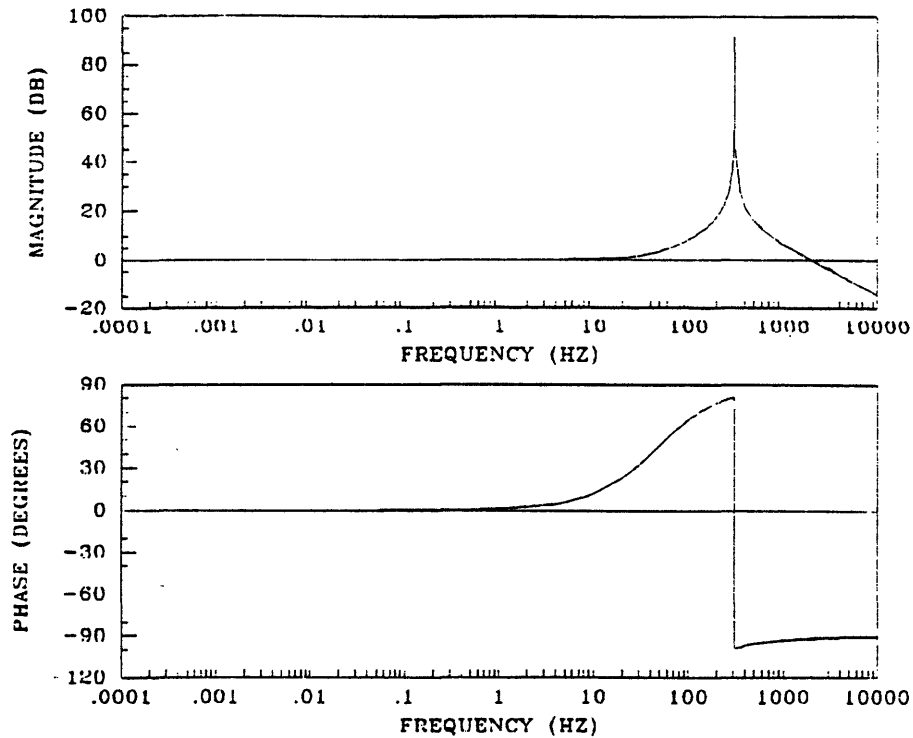


Figure 5.49: High Bandwidth State Weighting Function Bode Plot

The high bandwidth LQ design uses the control weighting function in Equation (5.45) and the state weighting function of Equation (5.49) with  $\rho = 1.5 \times 10^7$  and  $\omega_l = 300$ . A Bode plot of  $N(s)$  with  $\rho = 1$  is shown in Figure 5.49.

Bode plots of the open and closed loop high bandwidth LQ design are shown in Figures 5.50 and 5.51. The LQ design parameters shown above are chosen to give a  $-90^\circ$  bandwidth of 100 Hz. The resulting closed loop LQ poles and zeros are shown in Table 5.16.

#### 5.5.4 Compensator Designs

A compensator design which provides a bandwidth of slightly less than 50 Hz for the low bandwidth LQ design is achieved with values of the Kalman filter design parameters  $\mu = 10^{-14}$  and  $\Xi = 10^4$ . This design is referred to as FW/LQG-1. A Bode plot of the overall compensator,  $K(s)$ : the model based compensator,  $r_{MBC}(s)$ , augmented with the demodulation filter and integrator, is shown in Figure 5.52. The compensator poles and zeros are listed in Table 5.17, and the compensator Bode gain is  $36.8 - j195.7$  which yields a velocity error constant,  $K_v$ , of 112.4 dB. A Bode plot of the compensated open

Table 5.16: High Bandwidth Design LQ Closed Loop Poles and Zeros

Poles	Zeros
$-156.83 + j2093.7$	$-169.07 + j1972.3$
$-198.19 + j1733.4$	$-71.926 - j1950.9$
$-410.18 + j893.46$	$-563.83 + j720.91$
$-450.62 - j803.66$	$-494.61 - j812.76$
$-531.39 + j367.13$	$-0.001256 + j1256.6$
$-360.42 - j448.17$	$-0.001256 - j1256.6$
$-6283.2 + j0.1387$	$-187.71 - j15.648$
$-16.484 - j1916.9$	$-1020.0 + j1142.6$
$-292.02 - j2.1662$	

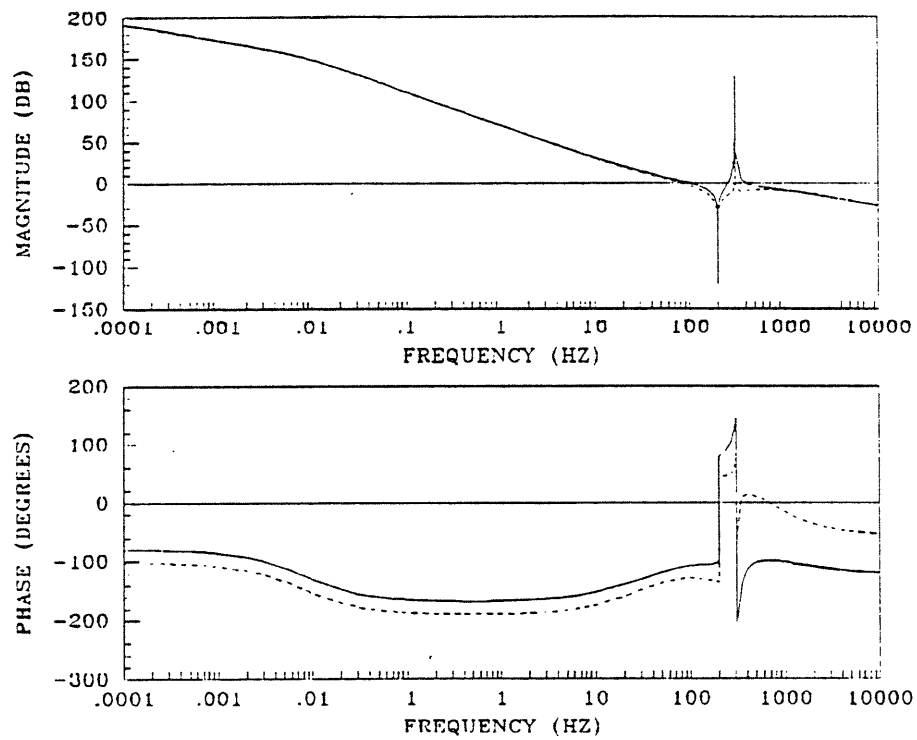


Figure 5.50: High Bandwidth LQ Design Open Loop Bode Plot

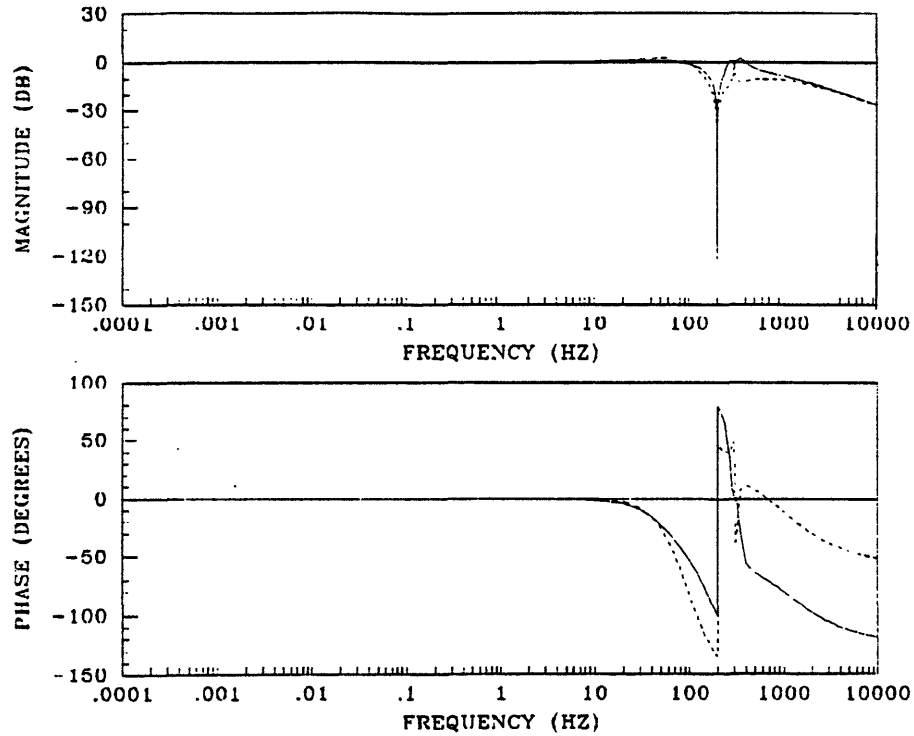


Figure 5.51: High Bandwidth LQ Design Closed Loop Bode Plot

loop system is shown in Figure 5.53 while a Bode plot of the closed loop system is shown in Figure 5.54. The system has a  $-90^\circ$  bandwidth of  $48 \text{ Hz}$  and a  $-3 \text{ dB}$  bandwidth of  $48 \text{ Hz}$ . The  $M_p$  of the forward transfer function is  $1.59 \text{ dB}$  while the  $M_p$  of the backward transfer function is  $3.98 \text{ dB}$ , and the attenuation at  $10 \text{ kHz}$  is  $-109 \text{ dB}$ . The closed loop system poles are listed in Table 5.18.

The response of the system to a  $1 \text{ deg/sec}$  step in the  $y$ -axis inertial angular rate, or  $\dot{\phi}_c = j \cdot 1 \text{ deg/sec}$ , is shown in Figure 5.55. The real and imaginary parts of the pickoff angle and the real and imaginary parts of the commanded moments are plotted versus time. Related to the TITOBS system, the real and imaginary parts are the  $x$ -axis and  $y$ -axis pickoff angles and  $x$ -axis and  $y$ -axis moment commands, respectively. The solid lines denote the  $x$ -axis response and the broken lines denote the  $y$ -axis response. The maximum deviation of the  $y$ -axis pickoff angle is  $0.0034^\circ$  while the  $x$ -axis moment command has an overshoot of  $31\%$  and a settling time of about  $0.03$  seconds.

A Nyquist plot of the compensated system is shown in Figure 5.56. The stability margins obtained from the plot indicate a negative phase margin of  $41^\circ$ , a positive phase margin of  $59^\circ$ , an upward gain margin of  $16.83 \text{ dB}$ , and a



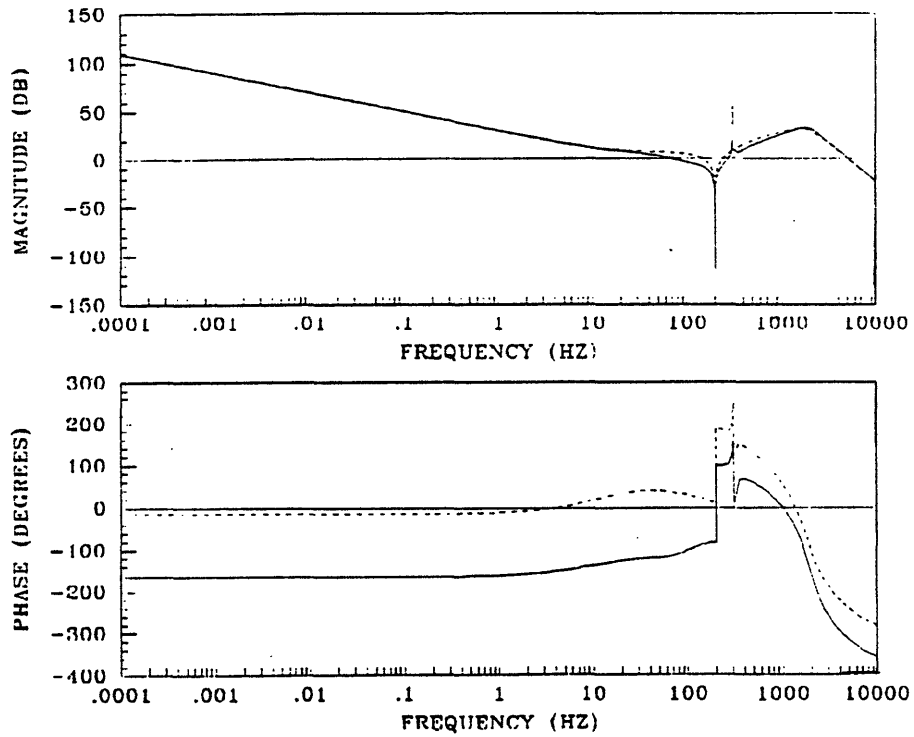


Figure 5.52: Design FW/LQG-1 Augmented Compensator Bode Plot

Table 5.17: Design FW/LQG-1 Compensator Poles and Zeros

Poles	Zeros
0.0	$-83.428 - j8.5933$
$-0.1589 + j1916.7$	$-68.694 + j1926.6$
$-0.1589 - j1916.7$	$-35.739 - j1908.5$
$-471.24 + j816.21$	$-0.001256 + j1256.6$
$-471.24 - j816.21$	$-0.001256 - j1256.6$
$-444.04 + j125.81$	$-484.12 + j838.81$
$-3582.9 - j1391.1$	$-473.32 - j814.82$
$-8972.0 + j8761.4$	$-372.29 + j545.03$
$-13417. + j890.57$	
$-2982.2 + j11420.$	
$-10864. - j7298.2$	
$-3403.5 - j10755.$	

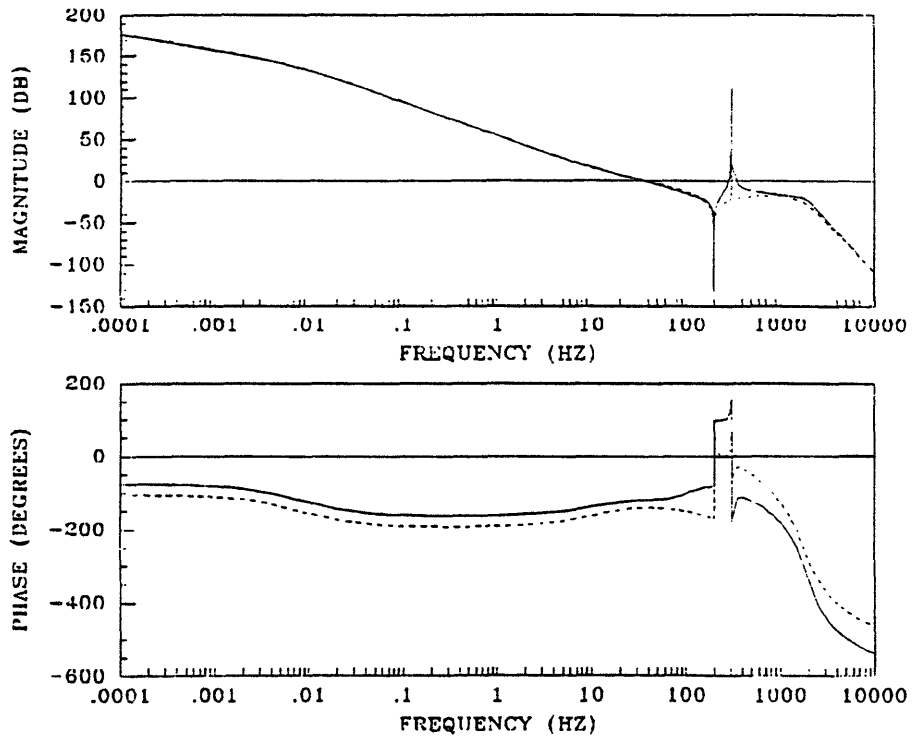


Figure 5.53: Design FW/LQG-1 Open Loop Bode Plot

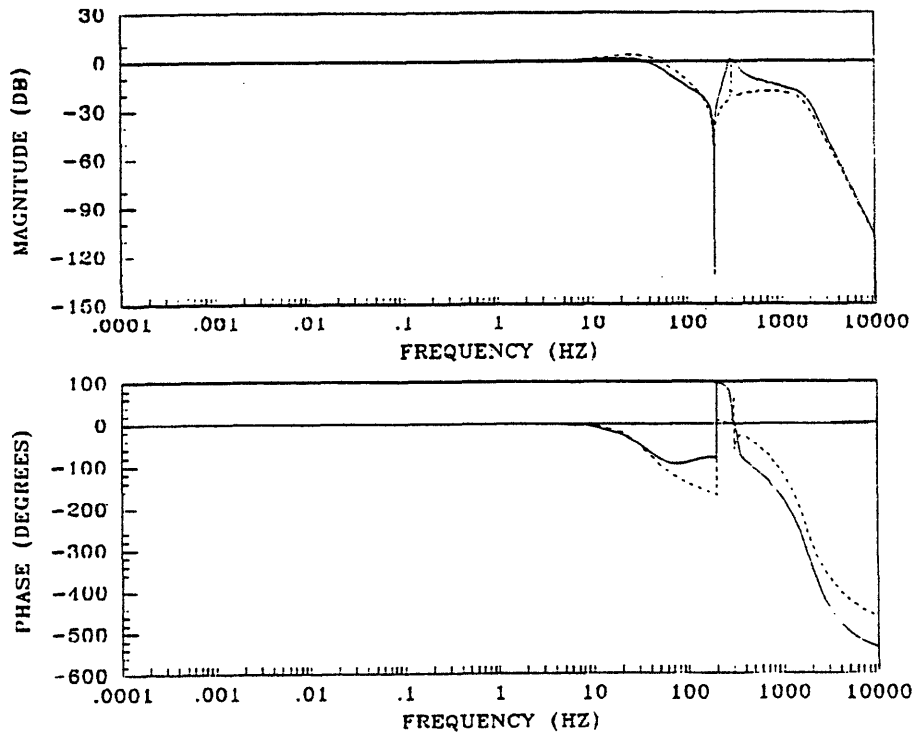


Figure 5.54: Design FW/LQG-1 Closed Loop Bode Plot

Table 5.18: Design FW/LQG-1 Closed Loop Poles

Closed Loop Poles	
$-3505.0 + j11440.$	$-468.76 + j817.83$
$-3528.1 - j10327.$	$-470.78 - j815.91$
$-74.721 + j1988.2$	$-8811.8 + j7140.7$
$-68.080 + j1845.0$	$-9653.6 - j6357.3$
$-2.6650 - j1916.7$	$-11274. - j142.94$
$-181.47 + j188.69$	$-142.11 - j0.8968$
$-150.77 - j189.55$	$-6283.2 + j0.0063$

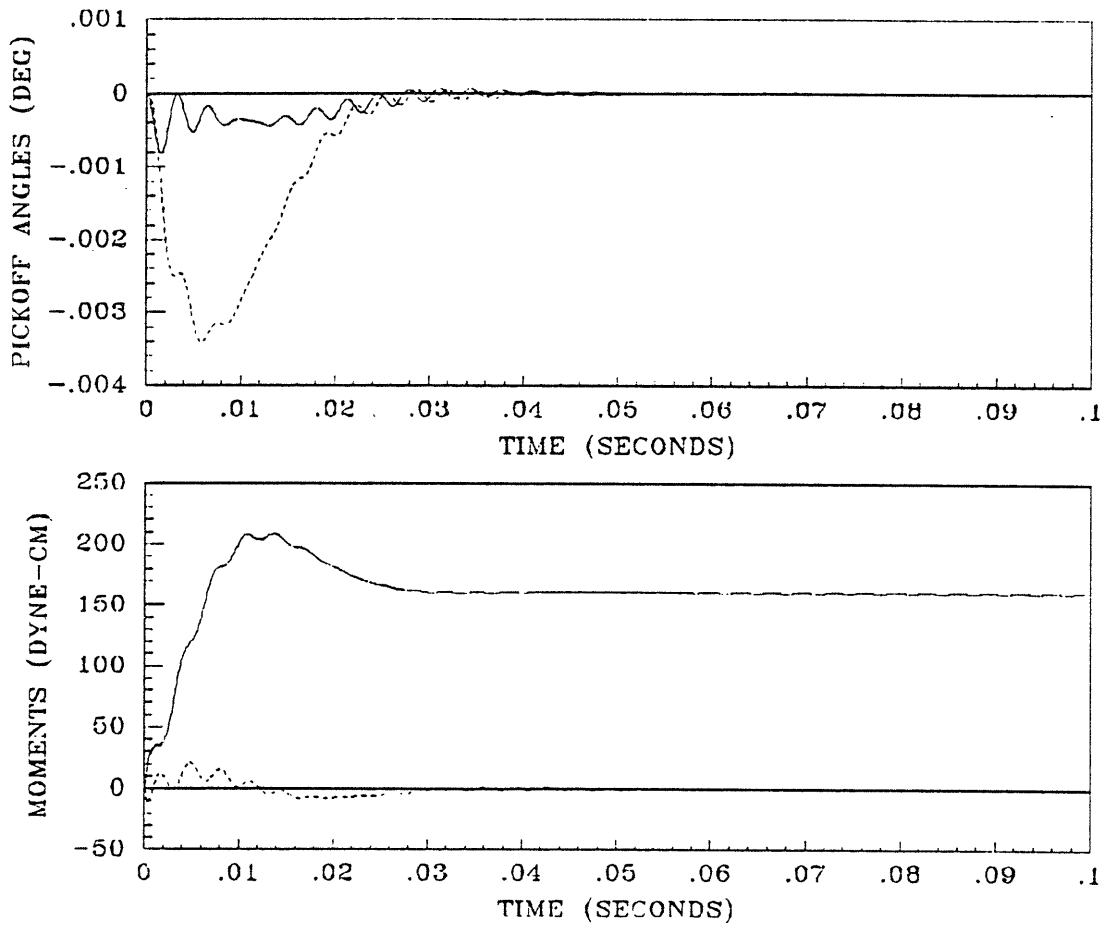


Figure 5.55: Design FW/LQG-1 Step Response

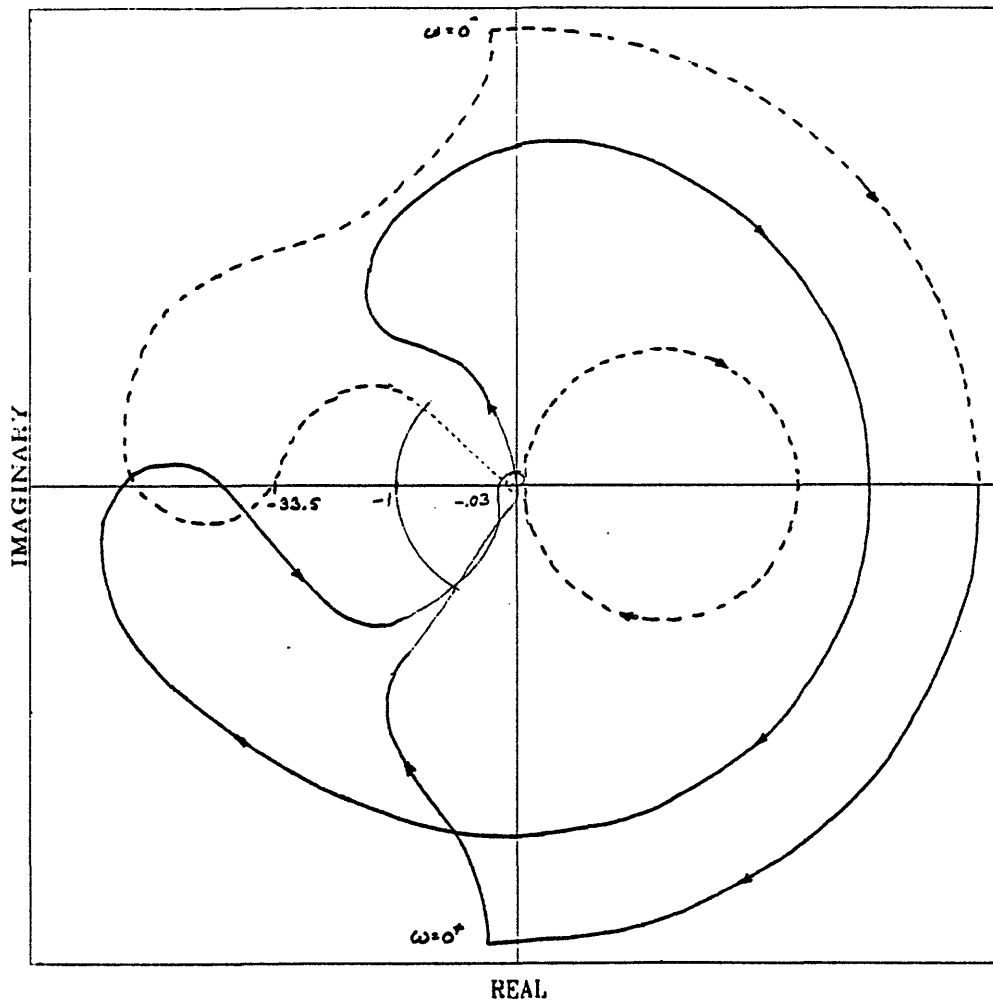


Figure 5.56: Design FW/LQG-1 Nyquist Plot

downward gain margin of 30.50 *dB*.

A compensator design which provides a bandwidth of 100 *Hz* for the high bandwidth LQ design is achieved with values of the Kalman filter design parameters  $\mu = 10^{-14}$  and  $\Xi = 10^5$ . This design is referred to as FW/LQG-2. A Bode plot of the overall compensator,  $K(s)$ : the model based compensator,  $K_{MBC}(s)$ , augmented with the demodulation filter and integrator, is shown in Figure 5.57. The compensator poles and zeros are listed in Table 5.19, and the compensator Bode gain is  $309.6 - j1000.3$  which yields a velocity error constant,  $K_v$ , of 126.7 *dB*. A Bode plot of the compensated open loop system is shown in Figure 5.58 while a Bode plot of the closed loop system is shown in Figure 5.59. The system has a  $-90^\circ$  bandwidth of 100 *Hz* and a  $-3$  *dB* bandwidth of 105 *Hz*. The  $M_p$  of the forward transfer function is 0.95 *dB* while the  $M_p$  of the backward

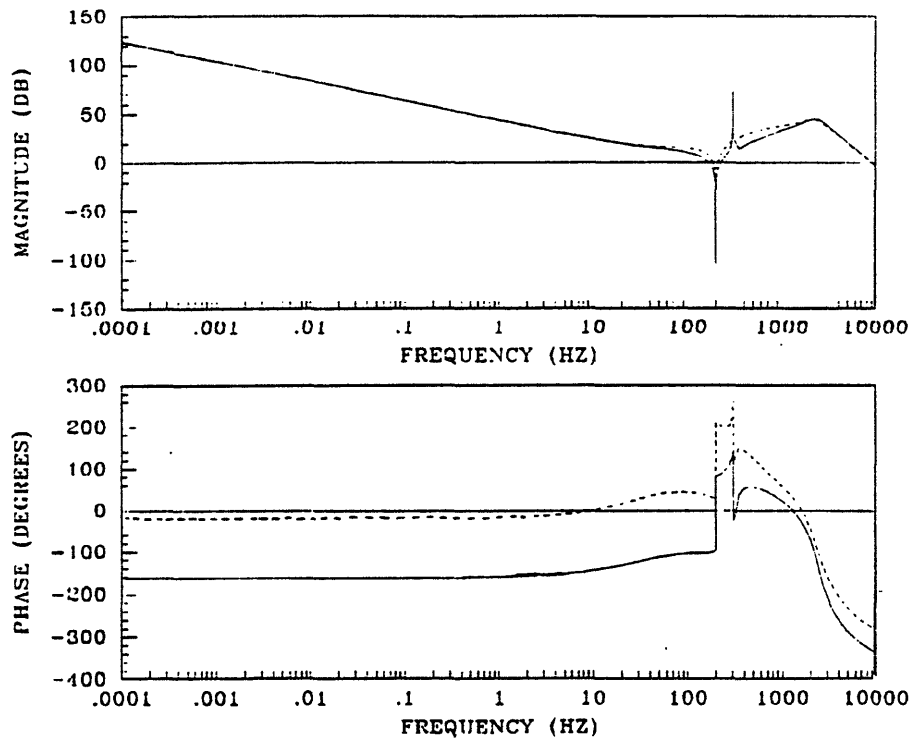


Figure 5.57: Design FW/LQG-2 Augmented Compensator Bode Plot

transfer function is  $3.46 \text{ dB}$ , and the attenuation at  $10 \text{ kHz}$  is  $-89 \text{ dB}$ . The closed loop system poles are listed in Table 5.20.

The response of the system to a  $1 \text{ deg/sec}$  step in the  $y$ -axis inertial angular rate, or  $\dot{\phi}_c = j \cdot 1 \text{ deg/sec}$ , is shown in Figure 5.60. The maximum deviation of the  $y$ -axis pickoff angle is  $0.00152^\circ$  while the  $x$ -axis moment command has an overshoot of 25% and a settling time of about 0.015 seconds.

A Nyquist plot of the compensated system is shown in Figure 5.61. The stability margins obtained from the plot indicate a negative phase margin of  $43^\circ$ , a positive phase margin of  $55^\circ$ , an upward gain margin of  $10.45 \text{ dB}$ , and a downward gain margin of  $16.25 \text{ dB}$ .

### 5.5.5 Summary

In this section, the frequency weighted linear quadratic Gaussian design methodology is described and used to generate two controllers for the gyro. The controls and states of the design plant model are weighted as functions of frequency, allowing the generation of special LQ loop shapes. The control weighting function is used to generate a notch filter in the compensator. The

Table 5.19: Design FW/LQG-2 Compensator Poles and Zeros

Poles	Zeros
0.0	$-177.52 - j21.676$
$-0.1589 + j1916.7$	$-158.01 + j1974.7$
$-0.1589 - j1916.7$	$-62.233 - j1914.3$
$-471.24 + j816.21$	$-0.001256 + j1256.6$
$-471.24 - j816.21$	$-0.001256 - j1256.6$
$-1008.3 + j734.35$	$-506.37 + j674.95$
$-18466. - j9725.8$	$-487.61 - j811.02$
$-14158. - j10481.$	$-653.52 + j1160.0$
$-12020. + j12125.$	
$-3069.3 + j14532.$	
$-3775.1 - j14170.$	
$-1646.5 - j1973.9$	

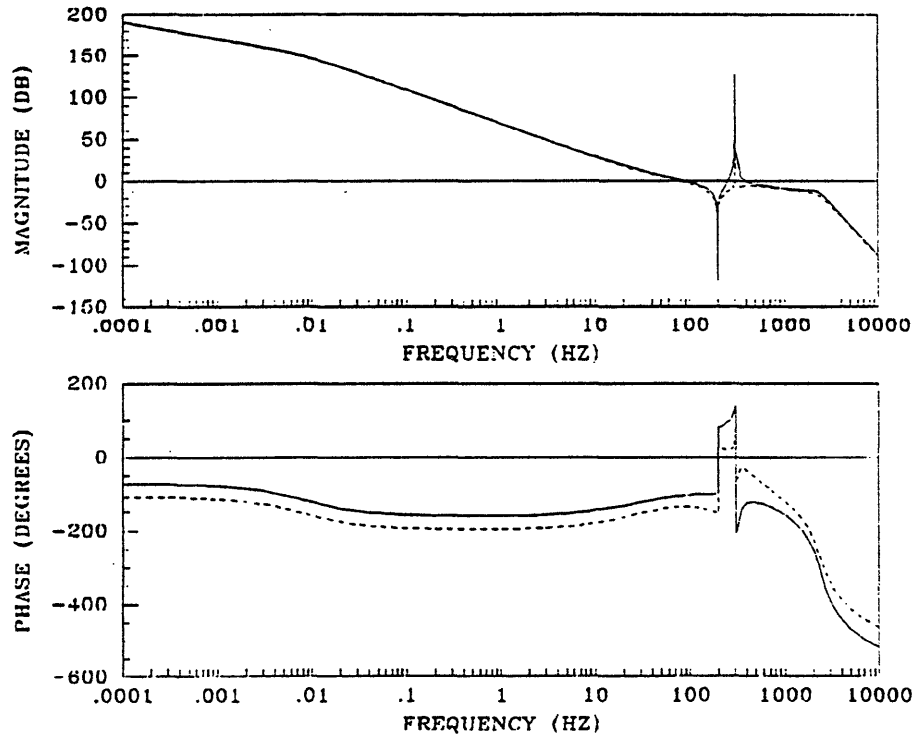


Figure 5.58: Design FW/LQG-2 Open Loop Bode Plot

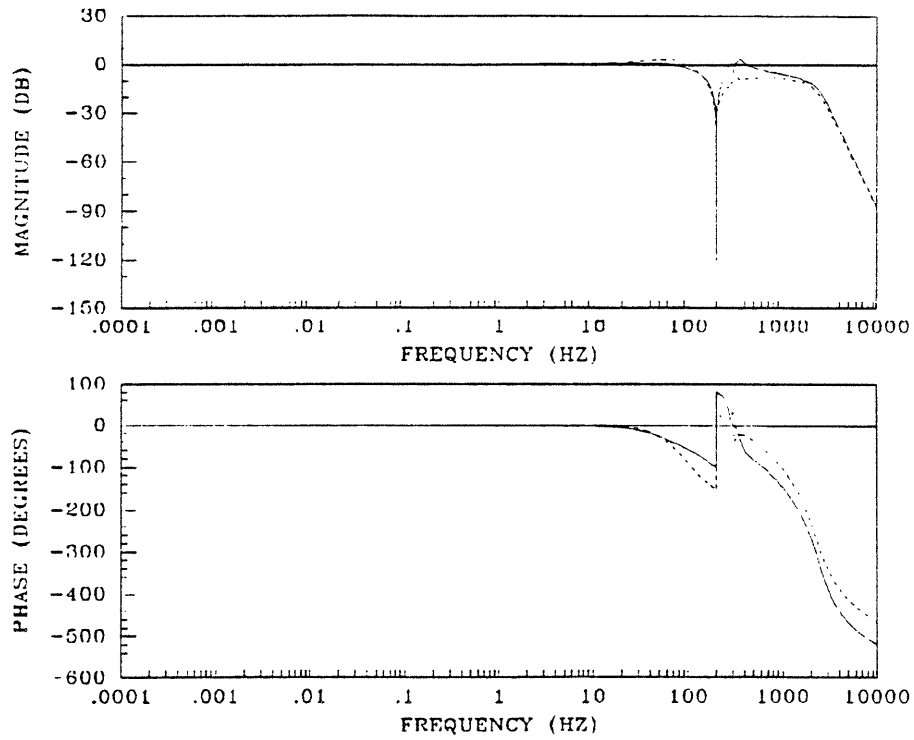


Figure 5.59: Design FW/LQG-2 Closed Loop Bode Plot

effects of different state weighting functions are examined, and an evolutionary design example is presented. The state weighting function is used to guarantee pickoff angle damping and reduce step response overshoot. The performance parameters of the designs are summarized in Table 5.21.

Table 5.20: Design FW/LQG-2 Closed Loop Poles

Closed Loop Poles	
$-4378.0 + j14251.$	$-531.39 + j367.13$
$-4397.5 - j13110.$	$-450.61 - j803.67$
$-198.19 + j1733.4$	$-11162. + j8796.2$
$-156.83 + j2093.7$	$-12096. - j7963.7$
$-16.484 - j1916.9$	$-14354. - j234.43$
$-410.18 + j893.46$	$-292.01 - j2.1683$
$-360.42 - j448.17$	$-6283.1 + j0.1394$

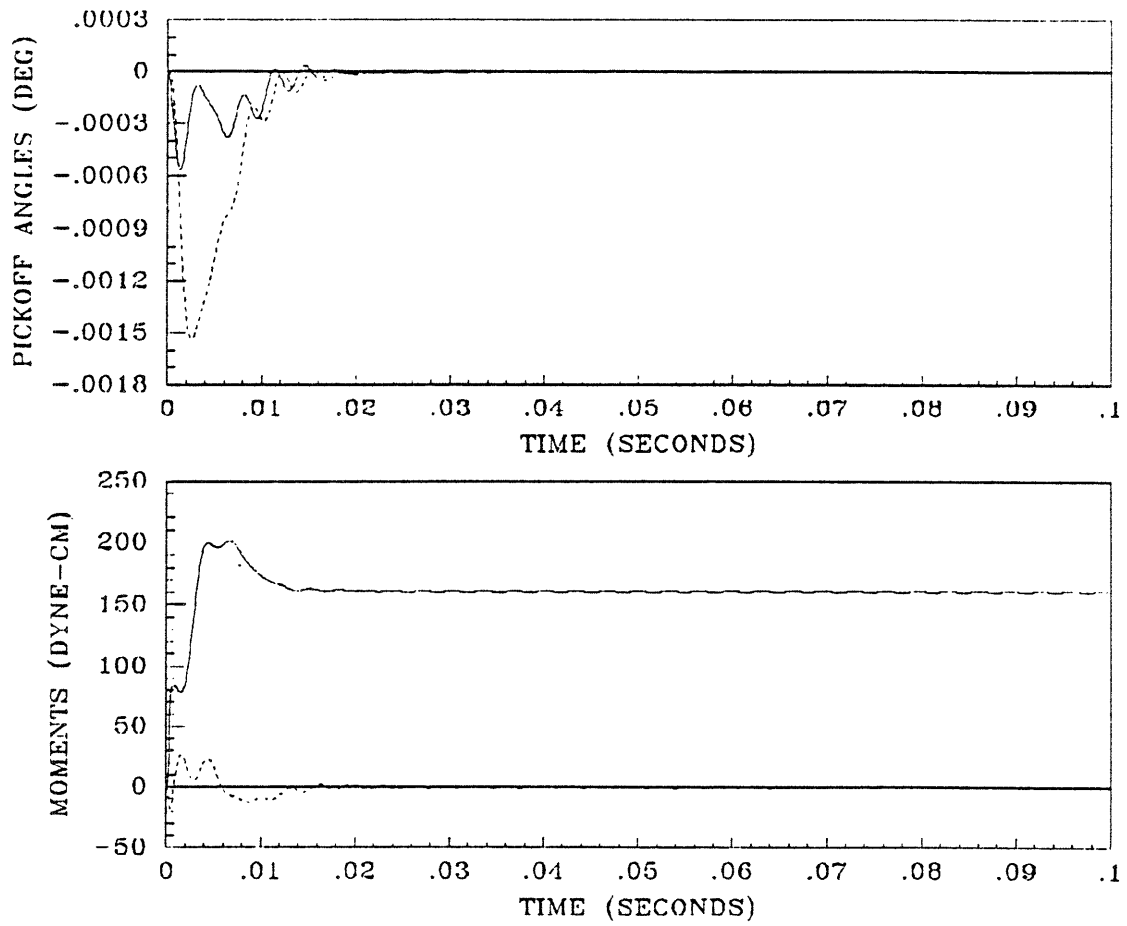


Figure 5.60: Design FW/LQG-2 Step Response



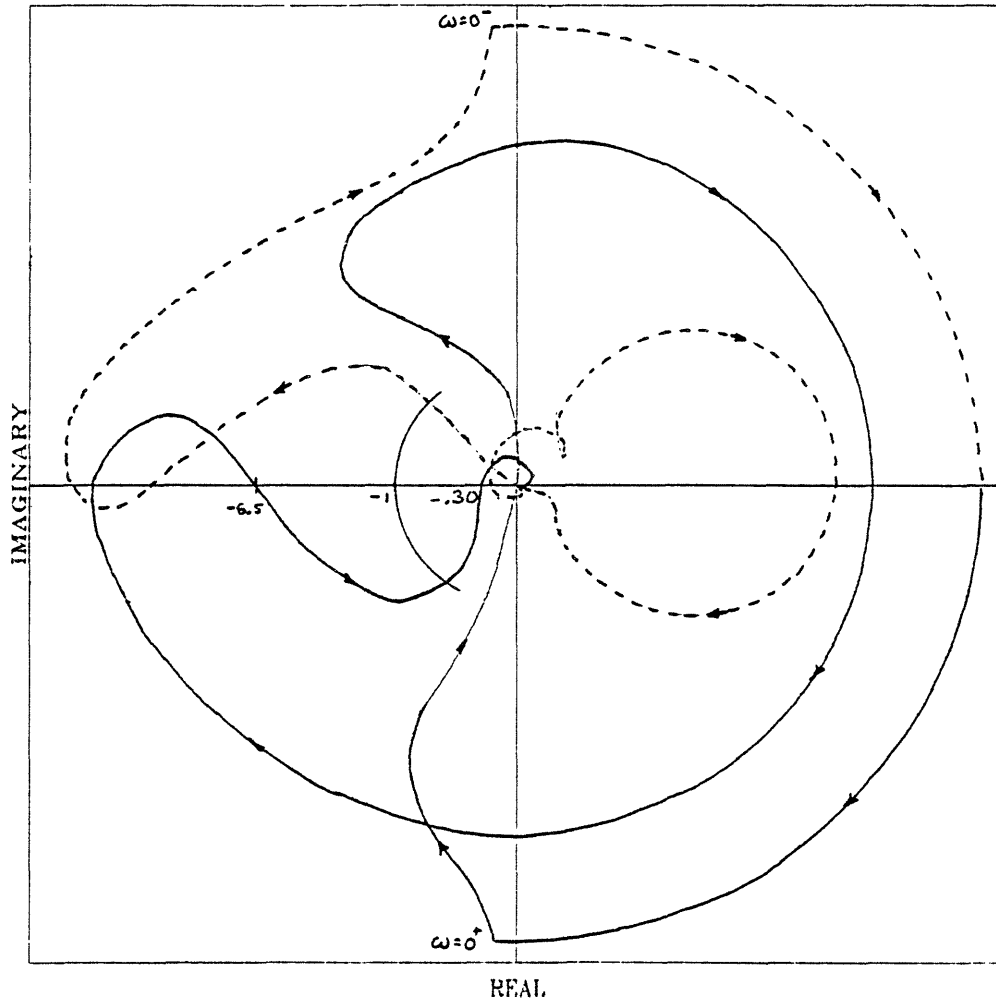


Figure 5.61: Design FW/LQG-2 Nyquist Plot

Table 5.21: FW/LQG Compensator Design Parameters

Parameters	Units	FW/LQG Designs	
		FW/LQG-1	FW/LQG-2
Upward Gain Margin	<i>dB</i>	30.50	10.45
Downward Gain Margin	<i>dB</i>	16.83	16.25
Negative Phase Margin	<i>deg</i>	41	43
Positive Phase Margin	<i>deg</i>	59	55
$-90^\circ$ Bandwidth	<i>Hz</i>	48	100
$-3$ <i>dB</i> Bandwidth	<i>Hz</i>	48	105
Forward TF $M_p$	<i>dB</i>	1.59	0.95
Backward TF $M_p$	<i>dB</i>	3.98	3.46
Velocity Error Constant	<i>dB</i>	112.4	126.7
CL Gain at 10 <i>kHz</i>	<i>dB</i>	-109	-89
Moment Command Overshoot	%	31	25
Settling Time	<i>sec</i>	0.03	0.015
Pickoff Angle Deviation	<i>deg</i>	0.0034	0.00152

## 5.6 FLS/LQG/LTR Design

### 5.6.1 Description of Design Methodology

The LQG/LTR with formal loop shaping (FLS/LQG/LTR) design methodology is described in [1] and in [2]. A limitation of the LQG/LTR design methodology described in Section 5.4 is that the target loop that is recovered must be made up of the dynamics of the design plant model. The FLS/LQG/LTR methodology extends the loop transfer recovery result so that arbitrary stable target loops, not only those based on the plant dynamics, may be recovered in the feedback loop. This methodology produces a model based compensator, containing the dynamics of the target loop to be recovered as well as the dynamics of the design plant model, that inverts the plant dynamics and inserts the recovered dynamics of the target loop.

Consider the design plant model,  $G_x(s)$ , factorable as shown in Equation (5.50)

$$G_x(s) = G_{xs}(s)\Omega(s) \quad (5.50)$$

where  $G_{xs}(s)$  contains the strictly stable, minimum phase dynamics of  $G_x(s)$  and  $\Omega(s)$  contains the dynamics directly on the  $j\omega$ -axis. In this case, with the loop broken at the plant input, the formal loop shaping procedure consists of simply incorporating the desired loop shape, the target loop  $W(s)$ , at the plant input as shown in Figure 5.62. The target loop must also be factorable as shown in Equation (5.51)

$$W(s) = W_s(s)\Omega(s) \quad (5.51)$$

where  $W_s(s)$  contains the strictly stable, minimum phase dynamics of  $W(s)$ . Inclusion of  $\Omega(s)$  in  $W(s)$  is required because the formal procedure produces compensators that completely invert the stable dynamics of the plant, and forming  $W(s)$  in this manner prevents the compensator from inverting dynamics on the  $j\omega$ -axis, which could result in an unstable system. The factorization in (5.50) is clearly possible in the case of the gyro problem where  $G_{xs}(s)$  consists of the gyro and demodulation filter dynamics, and  $\Omega(s)$  is an integrator. This factorization, however, may not be possible for cases in which the  $\Omega(s)$  dynamics are part of the plant and not added to the loop as part of the design plant model. A factorization similar to the one in (5.50) is required for plants with open right half plane poles and zeros and is discussed in [2].

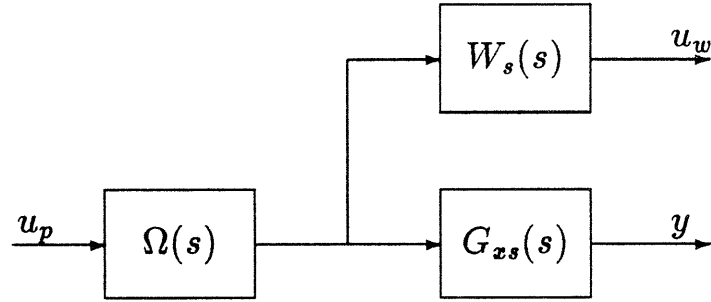


Figure 5.62: Incorporation of the Target Loop Shape at the Plant Input

It is desirable that the target loop,  $W(s)$ , come from the solution to a linear quadratic regulator problem for some desired target dynamics. The guaranteed stability properties of the LQ loop can then be recovered in the feedback loop. It is also suggested [2] that  $W(s)$  be constructed as much as possible out of the plant dynamics, especially highly resonant dynamics with poles close to the  $j\omega$ -axis. Poles and zeros on the  $j\omega$ -axis are forced to be included in the target as discussed above.

The FLS/LQG/LTR design methodology generates a model based compensator,  $K_{MBC}(s)$ , with the structure shown in Figure 5.63. The compensator contains the strictly stable dynamics of the augmented plant, the strictly stable dynamics of the target, and the dynamics directly on the  $j\omega$ -axis which are shared by both the augmented plant and the target. The target loop,  $W(s)$ , is the transfer function from  $u_p$  to  $u_w$  as shown in Figure 5.62, which has the time domain representation

$$\dot{\mathbf{x}}_w(t) = A_w \mathbf{x}_w(t) + B_w u_p(t) \quad (5.52)$$

$$u_w(t) = G_w \mathbf{x}_w(t) \quad (5.53)$$

which is partitioned as

$$\begin{bmatrix} \dot{\mathbf{x}}_{ws} \\ \dot{\mathbf{x}}_{\Omega} \end{bmatrix} = \begin{bmatrix} A_{ws} & B_{ws} C_{\Omega} \\ 0 & A_{\Omega} \end{bmatrix} \begin{bmatrix} \mathbf{x}_{ws} \\ \mathbf{x}_{\Omega} \end{bmatrix} + \begin{bmatrix} 0 \\ B_{\Omega} \end{bmatrix} u_p \quad (5.54)$$

$$u_w = \begin{bmatrix} G_{ws} & G_{\Omega} \end{bmatrix} \begin{bmatrix} \mathbf{x}_{ws} \\ \mathbf{x}_{\Omega} \end{bmatrix}. \quad (5.55)$$

The elements of the output matrix in Equation (5.55) could be the feedback gains that are the solution to a linear quadratic regulator problem based on  $A_w$

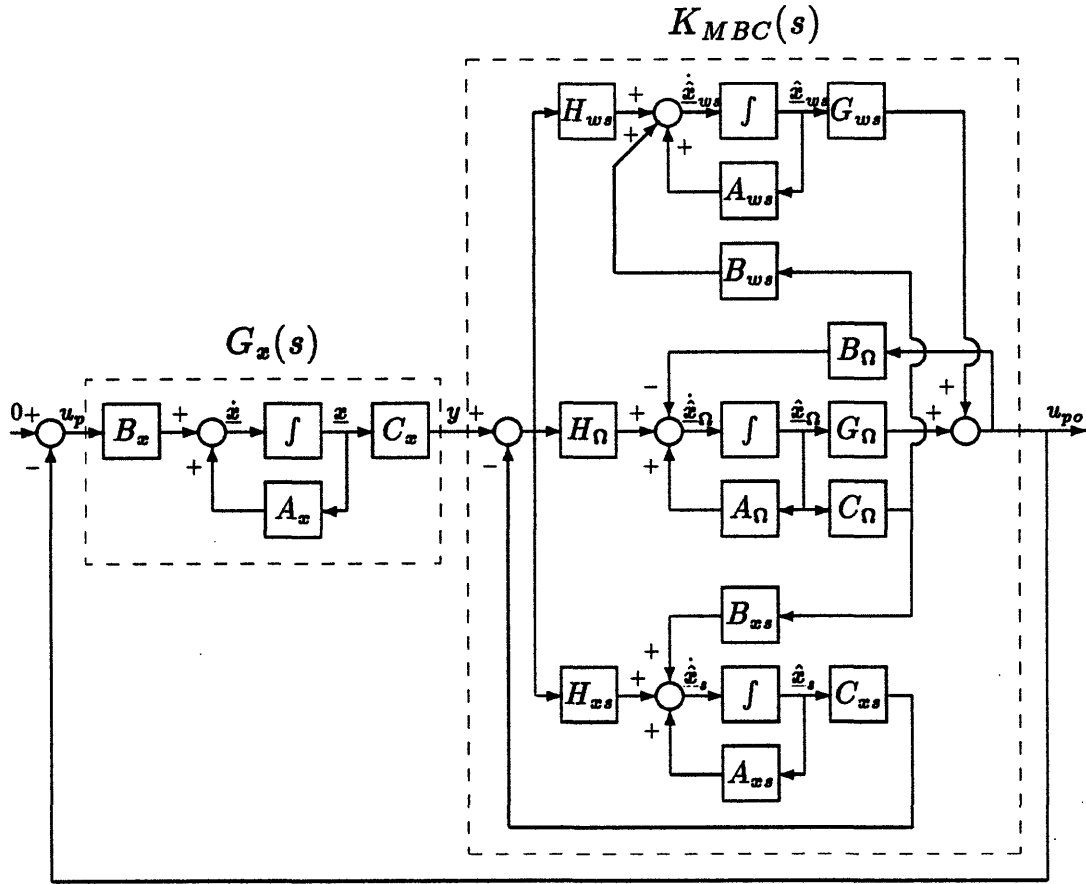


Figure 5.63: FLS/LQG/LTR Feedback Loop Block Diagram

and  $B_w$ . The design plant model discussed in Section 4.3 is partitioned as

$$\begin{bmatrix} \dot{\underline{x}}_s \\ \dot{\underline{x}}_\Omega \end{bmatrix} = \begin{bmatrix} A_{xs} & B_{xs}C_\Omega \\ 0 & A_\Omega \end{bmatrix} \begin{bmatrix} \underline{x}_s \\ \underline{x}_\Omega \end{bmatrix} + \begin{bmatrix} 0 \\ B_\Omega \end{bmatrix} u_p \quad (5.56)$$

$$y = \begin{bmatrix} C_{xs} & 0 \end{bmatrix} \begin{bmatrix} \underline{x}_s \\ \underline{x}_\Omega \end{bmatrix}. \quad (5.57)$$

The subscript  $\Omega$  denotes matrices corresponding to the dynamics in  $\Omega(s)$ . Note that here the design plant model is the gyro augmented at the input with the integrator ( $\Omega(s)$  dynamic) but at the output with the demodulation filter.

As with the normal LQG/LTR design methodology, the target loop is recovered in the feedback loop with the “accurate measurement” Kalman filter problem. Consider the stochastic system in Figure 5.64 which has the state

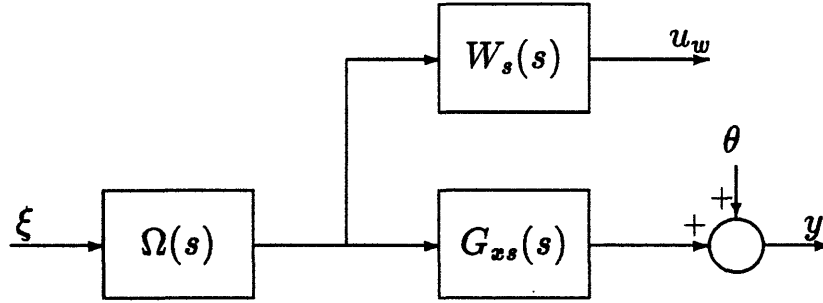


Figure 5.64: FLS/LQG/LTR Stochastic Model

space representation

$$\dot{\underline{X}}(t) = A\underline{X}(t) + L\xi(t) \quad (5.58)$$

$$y(t) = C\underline{X}(t) + \theta(t) \quad (5.59)$$

which is partitioned as

$$\begin{bmatrix} \dot{\underline{x}}_s \\ \dot{\underline{x}}_{ws} \\ \dot{\underline{x}}_\Omega \end{bmatrix} = \begin{bmatrix} A_{xs} & 0 & B_{xs}C_\Omega \\ 0 & A_{ws} & B_{ws}C_\Omega \\ 0 & 0 & A_\Omega \end{bmatrix} \begin{bmatrix} \underline{x}_s \\ \underline{x}_{ws} \\ \underline{x}_\Omega \end{bmatrix} + \begin{bmatrix} 0 \\ 0 \\ B_\Omega \end{bmatrix} \xi \quad (5.60)$$

$$y = \begin{bmatrix} C_{xs} & 0 & 0 \end{bmatrix} \begin{bmatrix} \underline{x}_s \\ \underline{x}_{ws} \\ \underline{x}_\Omega \end{bmatrix} + \theta. \quad (5.61)$$

The process noise,  $\xi(t)$ , is a scalar, zero mean, Gaussian, white noise process with covariance,

$$E\{\xi(t)\xi(t-\tau)\} = \Xi\delta(\tau),$$

and the measurement noise,  $\theta(t)$ , is a scalar, zero mean, Gaussian, white noise process with covariance,

$$E\{\theta(t)\theta(t-\tau)\} = \mu\delta(\tau),$$

and the process noise input matrix is identical to the control input matrix.

Assuming  $[A, L]$  stabilizable and  $[A, C]$  detectable, the Kalman filter gain matrix,  $H$ , comes from the solution to the algebraic Riccati equation

$$0 = \Sigma A^H + A\Sigma + LEL^H - \frac{1}{\mu}\Sigma C^H C\Sigma \quad (5.62)$$

$$H = \frac{1}{\mu}\Sigma C^H \quad (5.63)$$

where  $H$  is partitioned as

$$H = \begin{bmatrix} H_{xs} \\ H_{ws} \\ H_{\Omega} \end{bmatrix}$$

Under the assumption of a plant,  $G_x(s)$ , with no poles or zeros in the open right half plane, pointwise in  $s$ ,

$$\lim_{\mu \rightarrow 0} K_{MBC}(s)G_x(s) = W(s). \quad (5.64)$$

As with LQG/LTR, since the CCTF of a TITOBS system is a scalar transfer function, the loop broken at the plant input,  $K_{MBC}(s)G_x(s)$ , has the same transfer function as the loop broken at the plant output,  $G_x(s)K_{MBC}(s)$ , so the target loop,  $W(s)$ , can be recovered in the feedback loop broken at either point. The value of  $\mu$  determines the frequency to which the target loop is recovered. This is referred to as the recovery bandwidth.

The FLS/LQG/LTR design procedure for a plant with no open right half plane poles or zeros is as follows:

1. Choose a target loop  $W(s)$  which shares the plant dynamics on the  $j\omega$ -axis and has the desired performance and stability properties.
2. Recover the target target loop in the feedback loop to the desired bandwidth by choosing the design parameter  $\mu$ .

The model based compensator has the following properties:

- All of the poles in  $G_{xs}(s)$ , the strictly stable dynamics of the design plant model, are cancelled by zeros of  $K_{MBC}(s)$ .

During the recovery process, as  $\mu \rightarrow 0$ :

- The remaining zeros of  $K_{MBC}(s)$  start at some open loop poles of  $G_{xs}(s)$  and approach the zeros of  $W_s(s)$ .
- Some of the poles of  $K_{MBC}(s)$  cancel the undesirable zeros of  $G_{xs}(s)$ .
- Some of the poles of  $K_{MBC}(s)$  approach poles of  $W_s(s)$ .
- The rest of the poles of  $K_{MBC}(s)$  go to infinity in a stable manner.

## 5.6.2 Design Approach

The ability of the FLS/LQG/LTR design methodology to recover any target loop, not just those based exclusively on the plant dynamics, provides a wide choice of design options. The only restriction on the target loop is that it must contain the closed right half plane plant dynamics [2]. Two design approaches for the gyro are described below.

One design approach would be to recover an LQ target loop based on an FW/LQ regulator design. The methodology could be applied to some very simple  $A_w$  dynamics, with the control and output weighted with functions similar to those chosen in Section 5.5. This would allow an LQ target loop with a notch filter and large state weighting at nutation so that the target loop contains the resonant nutation dynamics. A disadvantage of this approach is the recovery of the notch filter. Since the zeros of the compensator only approach the target zeros as  $\mu \rightarrow 0$ , the notch may not be sufficiently recovered with practical values of  $\mu$ , leading to a notch filter that is at the wrong frequency with the wrong depth.

A second approach would be to recover a target loop, preferably an LQ loop based on a normal time weighted design, and to incorporate the notch filter into the compensator after recovery. The  $A_w$  matrix in this case would contain simpler dynamics than the gyro but should include the nutation dynamics, since these poles are close to the  $j\omega$ -axis. This *ad hoc* implementation of the notch filter destroys the optimality and guaranteed stability properties of a recovered LQ loop, but does guarantee that the notch in the compensator will have the desired properties.

This second approach is used in the LQG/LTR designs in Section 5.4 and two different FLS/LQG/LTR designs based on this approach are presented below. Both of the designs are based on real coefficient target loops,  $W(s)$ . The corresponding TITOBS target loop then has the dynamics of  $W(s)$  on each channel with no coupling between the channels. Recovery of these target loops generates compensators that tend to decouple the torque-rebalance loop channels. The result is that an inertial input on one gyro axis produces a moment command on the opposite axis only.

The first design recovers an LQ target loop based on a real  $A_w$  matrix consisting of an integrator and dynamics corresponding to the gyro nutation dynamics.



This design provides excellent frequency domain characteristics due to the single integrator behavior at low frequencies, but because the quadrature dynamics are inverted by the compensator, the step response of the pickoff angles is unacceptable. This design is referred to as FLS-0 and is discussed in Sections 5.6.3 and 5.6.4.

The second design recovers a target loop based on a real  $A_w$  matrix consisting of an integrator and dynamics corresponding to both the gyro nutation and quadrature dynamics in order to address the problem of the first design. Low and high bandwidth designs are generated, denoted FLS-1 and FLS-2 respectively, and are discussed in Sections 5.6.5 and 5.6.6.

### 5.6.3 Linear Quadratic Target Loop

The LQ target loop for design FLS-0, the target based on a real  $A_w$  matrix consisting of an integrator and a complex pair of poles corresponding to the gyro nutation dynamics, is of the form shown in Equation (5.52) and partitioned as shown in Equation (5.54). The numerical values of the elements in (5.54) are shown below.

$$A_{ws} = \begin{bmatrix} 0 & 1 \\ -3.6737 \times 10^6 & -0.3166 \end{bmatrix} \quad B_{ws} = \begin{bmatrix} 0 \\ 3.6737 \times 10^6 \end{bmatrix}$$

$$A_{\Omega} = 0 \quad B_{\Omega} = 1 \quad C_{\Omega} = 1$$

The eigenvalues of the  $A_w$  matrix are

$$\lambda_1 = 0.0$$

$$\lambda_{2,3} = -0.15833 \pm j1916.7.$$

The output gain matrix,  $G_w$ , comes from the solution of the standard LQR problem outlined in Equations (5.3) through (5.7). The LQ design parameters shown below are chosen to give a  $-3 \text{ dB}$  bandwidth of  $50 \text{ Hz}$ .

$$Q_{uu} = 8 \times 10^{-6}$$

$$N = \begin{bmatrix} -1 & 8.619 \times 10^{-8} & 10^{-8} \end{bmatrix}$$

The resulting gain matrix is

$$G_w = \begin{bmatrix} -331.34 & 0.06384 & 684.90 \end{bmatrix},$$

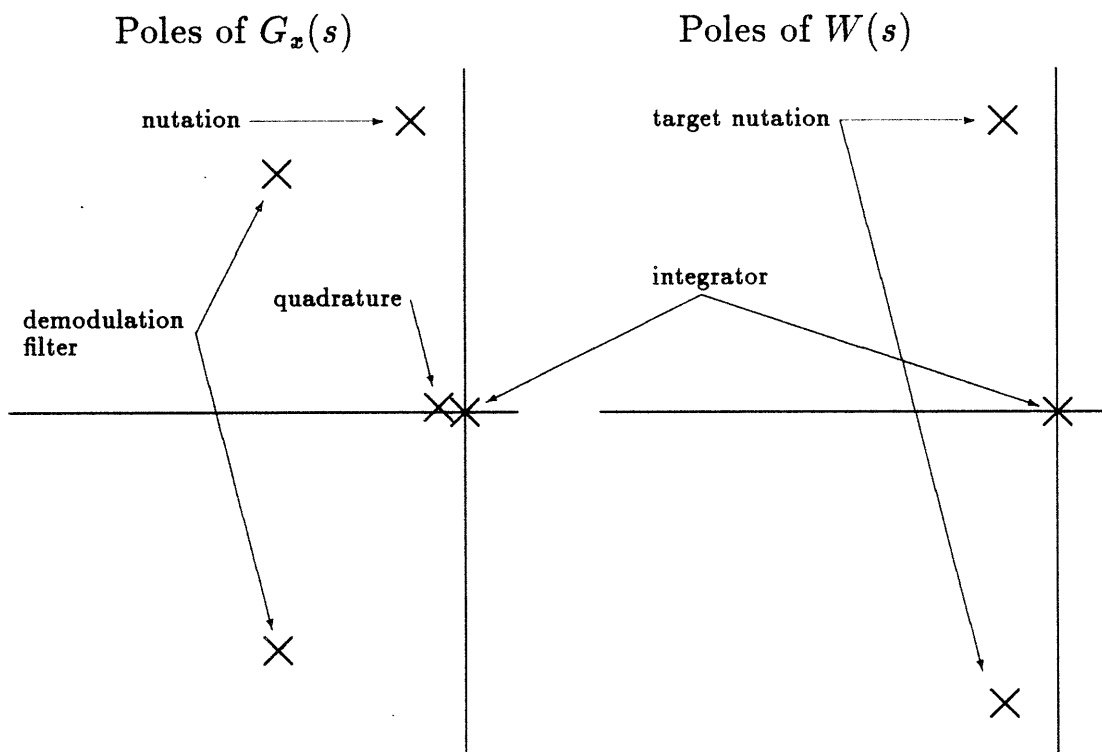


Figure 5.65: Poles of  $G_x(s)$  and  $W(s)$  for Design FLS-0

and

$$W(s) = G_w (sI - A_w)^{-1} B_w.$$

Figure 5.65 shows the pole locations of the design plant model and those of  $W(s)$ . The target loop and the design plant model share the integrator, but the remainder of the poles of  $G_x(s)$  are cancelled by the FLS/LQG/LTR compensator of the next section. The compensator then asymptotically replaces the cancelled nutation pole with the complex pole pair of the target loop. In this way, the feedback loop retains dynamics at the nutation frequency so that the controller can generate moment commands to null pickoff angle deviations at this frequency.

Bode plots of the open and closed loop FLS-0 LQ target,  $W(s)$ , are shown in Figures 5.66 and 5.67. Note that this target, like the subsequent ones in Section 5.6.5, is a real coefficient transfer function. Therefore, the TITOBs target has the transfer function  $W(s)$  on each channel, with no cross coupling, and the

Table 5.22: Design FLS-0 LQ Target Closed Loop Poles and Zeros

Poles	Zeros
$-171.30 + j1939.5$	$-171.38 + j1366.4$
$-171.30 - j1939.5$	$-171.38 - j1366.4$
$-342.61$	

forward and backward transfer functions are identical. The compensator generated by the recovery process will tend to decouple the torque-rebalance loop channels. The resulting closed loop LQ poles and zeros are shown in Table 5.22.

### 5.6.4 Recovery of the LQ Target Loop

A family of compensators is generated by the recovery process, each one better approximating the target loop as the design parameter  $\mu \rightarrow 0$ . The compensator presented below is recovered to provide a  $-90^\circ$  bandwidth of  $50 \text{ Hz}$ . The behavior of the compensator zero locus during recovery is very similar to that of the LQG/LTR design methodology discussed in Section 5.4.4, with the locus crossing into the right half plane. After the target loop is recovered to the desired bandwidth, the compensator is augmented at its output with the notch filter in Equation (4.9) in an analogous way to the augmented LQG/LTR compensator shown in Figure 5.11. As noted in Section 5.6.3, the compensator cancels the stable dynamics of the design plant model and replaces them asymptotically with the decoupled dynamics of the target loop. This yields torque-rebalance loop dynamics with decoupled channels through the recovery bandwidth.

A compensator design which provides a  $-90^\circ$  bandwidth of  $60 \text{ Hz}$  for the LQ target in Section 5.6.3, is achieved for values of the Kalman filter design parameters  $\mu = 10^{-7}$  and  $\Xi = 10^6$ . This design is referred to as FLS-0. (The loop bandwidth is higher than the target bandwidth due to the addition of the notch filter to the compensator.) A Bode plot of the overall compensator,  $K(s)$ : the model based compensator,  $K_{MBC}(s)$ , modified with the notch filter, and augmented with the demodulation filter and integrator, is shown in Figure 5.68. The compensator poles and zeros are listed in Table 5.23, and the compensator Bode gain is  $0.00016 - j0.1040$  which yields a velocity error constant,  $K_v$ , of

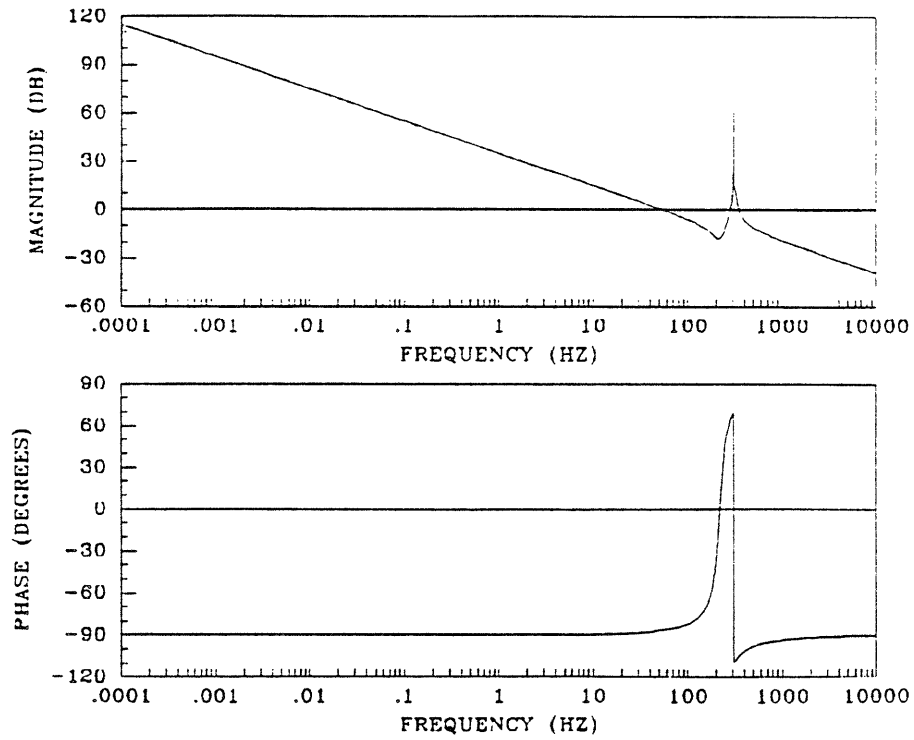


Figure 5.66: Design FLS-0 LQ Target Open Loop Bode Plot

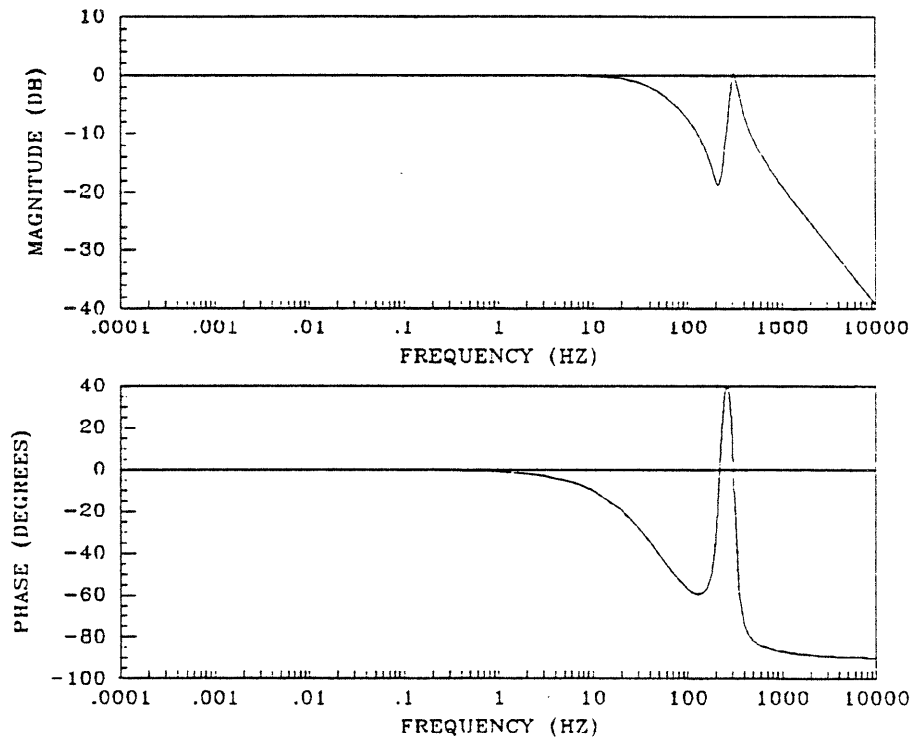


Figure 5.67: Design FLS-0 LQ Target Closed Loop Bode Plot

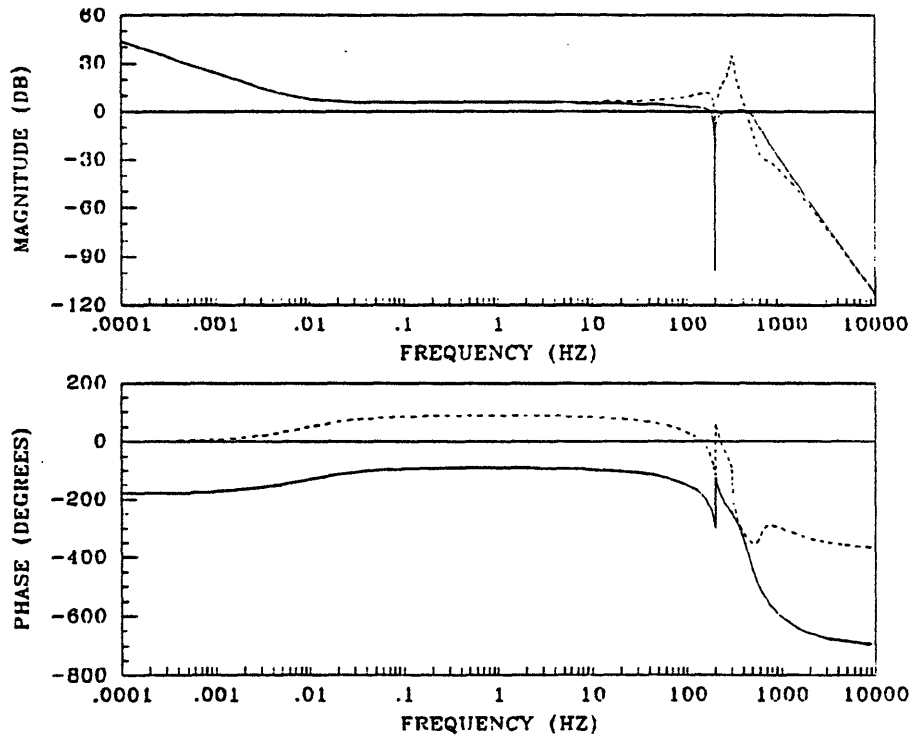


Figure 5.68: Design FLS-0 Augmented Compensator Bode Plot

46.7 dB. Note that this compensator has a zero in the right half plane. A Bode plot of the compensated open loop system is shown in Figure 5.69 while a Bode plot of the closed loop system is shown in Figure 5.70. From the open loop Bode plot, it can be seen that the forward and backward transfer functions are almost identical up to nutation, indicating that the channels of the feedback loop have been decoupled up to that frequency. Moreover, both transfer functions have the characteristic of an integrator for frequencies through crossover, indicating that the quadrature dynamics of the gyro have been inverted by the compensator. The system has a  $-90^\circ$  bandwidth of 60 Hz and a  $-3$  dB bandwidth of 65 Hz. Since the open loop system has a low frequency characteristic of an integrator, the closed loop system has no peaking within the bandwidth. The attenuation at 10 kHz is  $-195$  dB. The closed loop system poles are listed in Table 5.24. Note that the two gyro poles and the poles of the demodulation filter have been cancelled by zeros of the compensator.

The response of the system to a 1 deg/sec step in the  $y$ -axis inertial angular rate, or  $\dot{\phi}_c = j \cdot 1 \text{ deg/sec}$ , to 0.1 seconds is shown in Figure 5.71, and the response to 40 seconds is shown in Figure 5.72. The real and imaginary parts of the pickoff

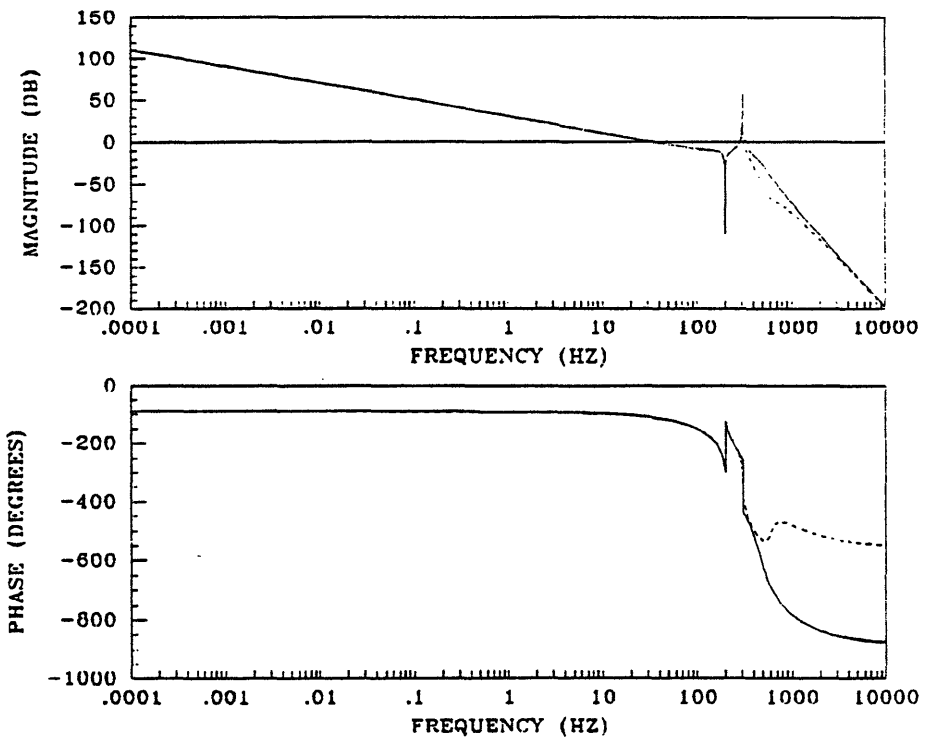


Figure 5.69: Design FLS-0 Open Loop Bode Plot

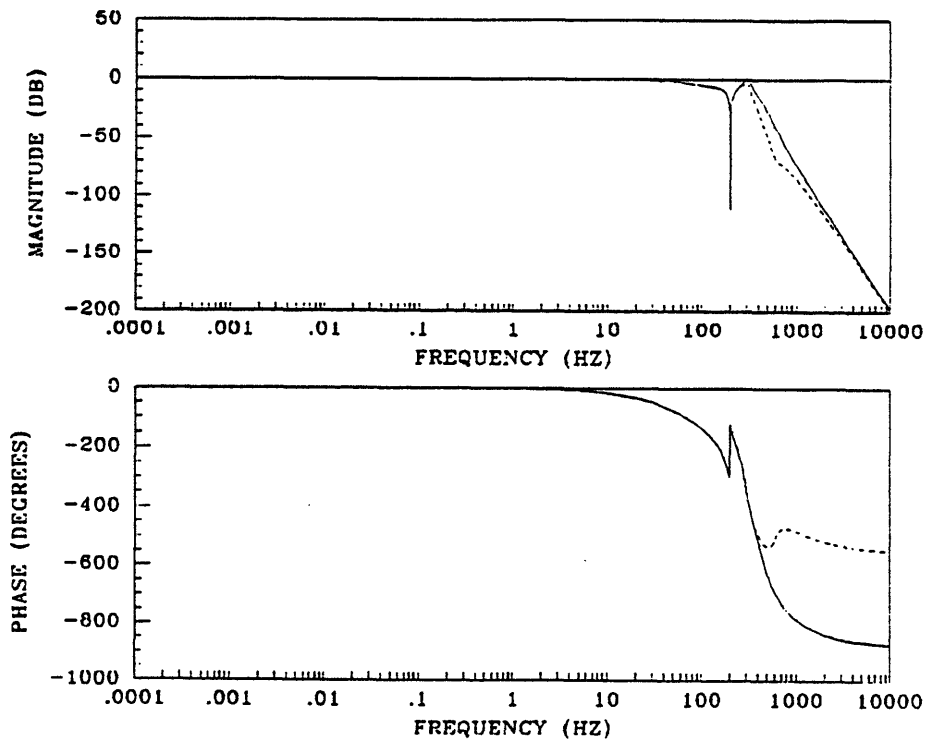


Figure 5.70: Design FLS-0 Closed Loop Bode Plot

Table 5.23: Design FLS-0 Compensator Poles and Zeros

Poles	Zeros
0.0	$1875.7 + j2547.1$
$-471.24 + j816.21$	$-471.24 + j816.21$
$-471.24 - j816.21$	$-467.24 - j816.21$
$-125.45 + j1220.3$	$-0.001256 + j1256.6$
$-127.82 - j1222.3$	$-0.001256 - j1256.6$
$-0.1583 + j1916.7$	$-0.1583 + j1916.7$
$-41.577 - j1902.6$	$-0.05 - j0.00000413$
$-591.00 + j2839.5$	$-83.091 - j3033.6$
$-1859.4 + j2064.4$	
$-2511.3 + j372.65$	
$-1938.2 - j1286.3$	
$-724.14 - j2085.6$	

Table 5.24: Design FLS-0 Closed Loop Poles

Closed Loop Poles	
$-670.37 - j1917.8$	$-208.03 + j1218.7$
$-155.71 + j1879.0$	$-208.03 - j1218.7$
$-155.71 - j1879.0$	$-471.24 + j816.21$
$-1728.8 - j1061.5$	$-471.24 - j816.21$
$-625.07 + j2736.9$	$-0.1538 + j1916.7$
$-2112.7 + j358.01$	$-0.05 + j0.00000413$
$-1677.2 + j1801.0$	$-377.4 + j0.00000030$

angle and the real and imaginary parts of the commanded moments are plotted versus time. Related to the TITOBs system, the real and imaginary parts are the  $x$ -axis and  $y$ -axis pickoff angles and  $x$ -axis and  $y$ -axis moment commands, respectively. The solid lines denote the  $x$ -axis response and the broken lines denote the  $y$ -axis response.

The step response of the system indicates the problem with this design approach. In order to recover a loop with a frequency response of an integrator for frequencies below crossover, the FLS/LQG/LTR compensator cancels the quadrature mode pole of the plant, making that mode unobservable in the moment command output of the torque-rebalance loop. The response of the  $x$ -axis moment command is essentially first order with some nutation oscillation, and

has a settling time of about 0.02 seconds with no overshoot. However, the pick-off angles return to null only with a first order decay at the quadrature time constant of  $\tau = 20 \text{ sec}$  after a maximum deviation of  $0.0046^\circ$ .

A Nyquist plot of the compensated system is shown in Figure 5.73. The stability margins obtained from the plot indicate a negative phase margin of  $62^\circ$ , a positive phase margin of  $71^\circ$ , an upward gain margin of  $9.90 \text{ dB}$ , and an infinite downward gain margin.

### 5.6.5 Target Loops Based on Real Coefficient Gyro Dynamics

The target loops of this section are similar to the target of Section 5.6.3 except that a complex pair of poles corresponding to the gyro quadrature mode is included to rectify the problems discussed above in Section 5.6.4.

The poles of the design plant model and the target are compared in Figure 5.74. Again, the target loop,  $W(s)$ , is a real coefficient transfer function so that the dynamics of  $W(s)$  appear on each channel of the corresponding TITOBs target with no cross coupling. The target loop shares the integrator with the design plant model, but the rest of the poles are cancelled by zeros of the compensators of the next section. The two cancelled poles of the CCTF gyro description are then replaced asymptotically by the two complex pole pairs of the target loop, which are at the same locations as the gyro poles. Therefore, the cancelled, coupled gyro dynamics are asymptotically replaced by the uncoupled target dynamics.

Two target loops, a low bandwidth loop (FLS-1) and a high bandwidth loop (FLS-2), are considered. The dynamics of  $W(s)$  are of the form shown in Equation (5.52) and partitioned as shown in Equation (5.54). The numerical values of the elements in (5.54) are shown below.

$$A_{ws} = \begin{bmatrix} 0 & 1 & 0 & 0 \\ -0.0025 & -0.1 & -0.0025 & 0 \\ 0 & 0 & 0 & 1 \\ 0 & 0 & -3.6737 \times 10^6 & -0.3166 \end{bmatrix} \quad B_{ws} = \begin{bmatrix} 0 \\ 0 \\ 0 \\ 3.6737 \times 10^6 \end{bmatrix}$$

$$A_\Omega = 0 \quad B_\Omega = 1 \quad C_\Omega = 1$$



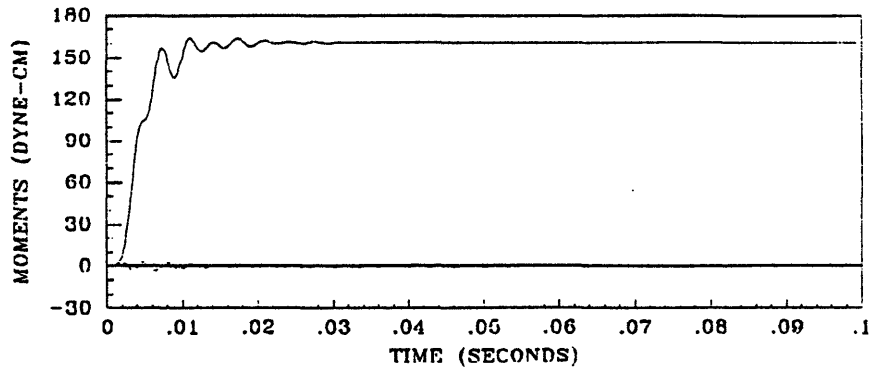
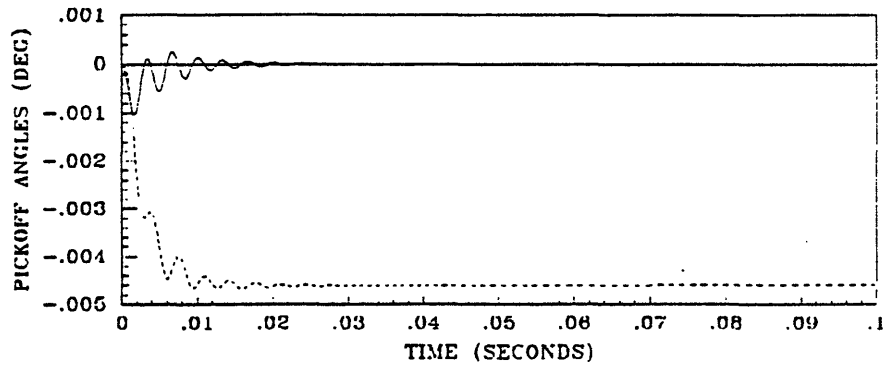


Figure 5.71: Design FLS-0 Step Response to  $t = 0.1 \text{ sec}$

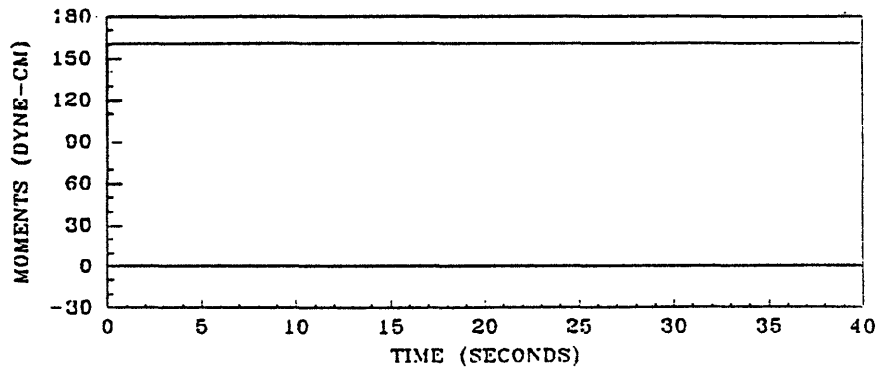
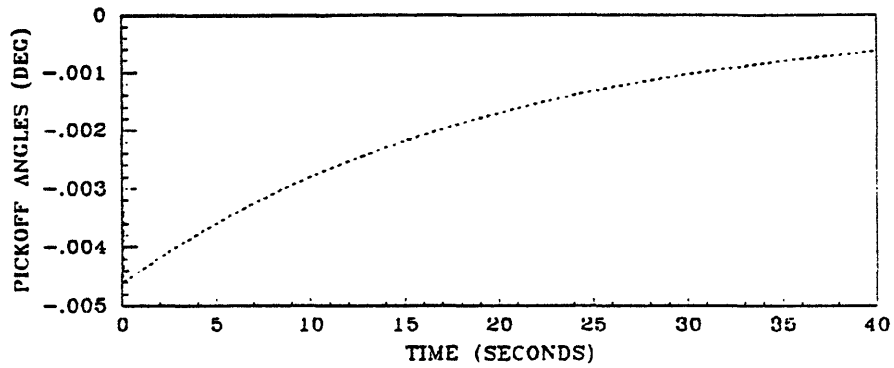


Figure 5.72: Design FLS-0 Step Response to  $t = 40 \text{ sec}$

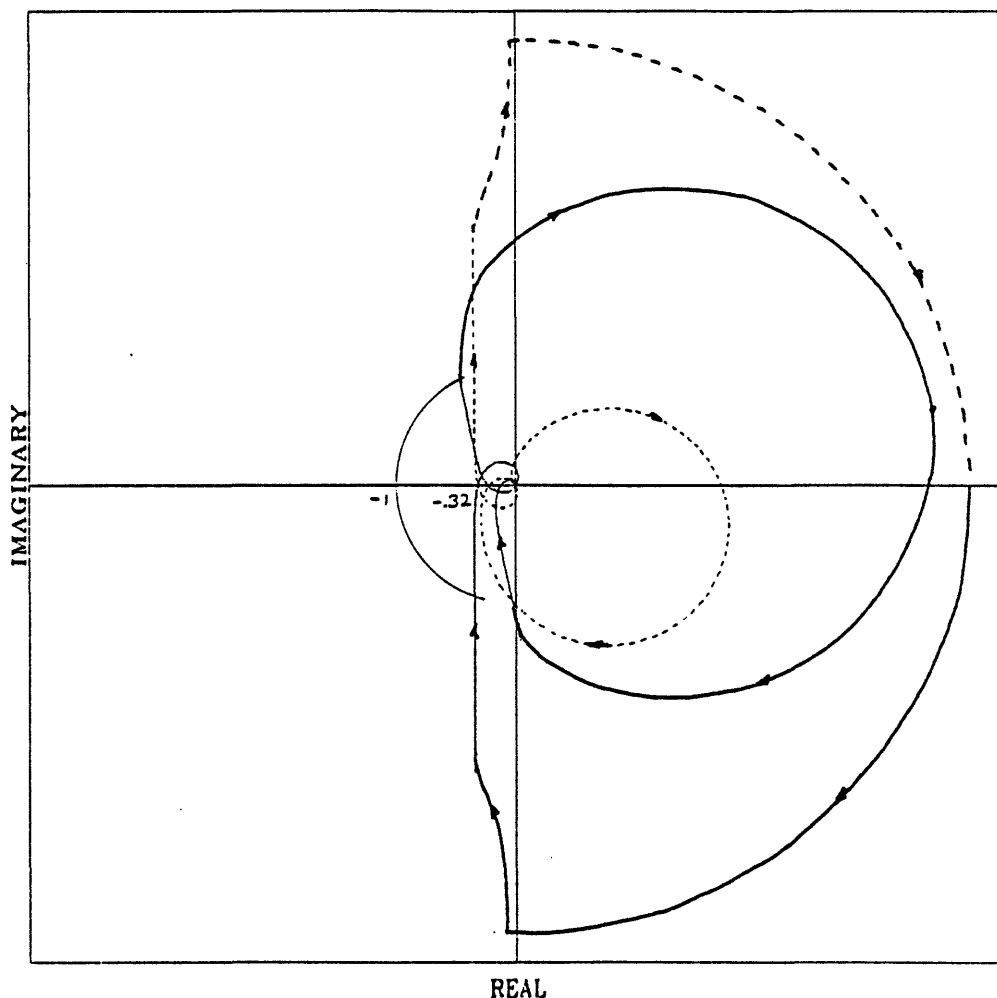


Figure 5.73: Design FLS-0 Nyquist Plot

The eigenvalues of the  $A_w$  matrix are

$$\begin{aligned}\lambda_1 &= 0.0 \\ \lambda_{2,3} &= -0.05 \pm j0.00000413 \\ \lambda_{4,5} &= -0.15833 \pm j1916.7\end{aligned}$$

The output gain matrix,  $G_w$ , is chosen to generate two target loops, one with a bandwidth of 50 Hz (FLS-1) and one with a bandwidth of 100 Hz (FLS-2). It is difficult to choose LQ state weighting matrices that do not place zeros on or near the quadrature poles of  $A_w$ . The goal of this approach is to include these dynamics in the target in order to avoid the problems discussed in Section 5.6.4, so they must not be cancelled in the target loop. Therefore, a pole placement algorithm is used to place the closed loop poles of the target,  $W(s)$ . Since the

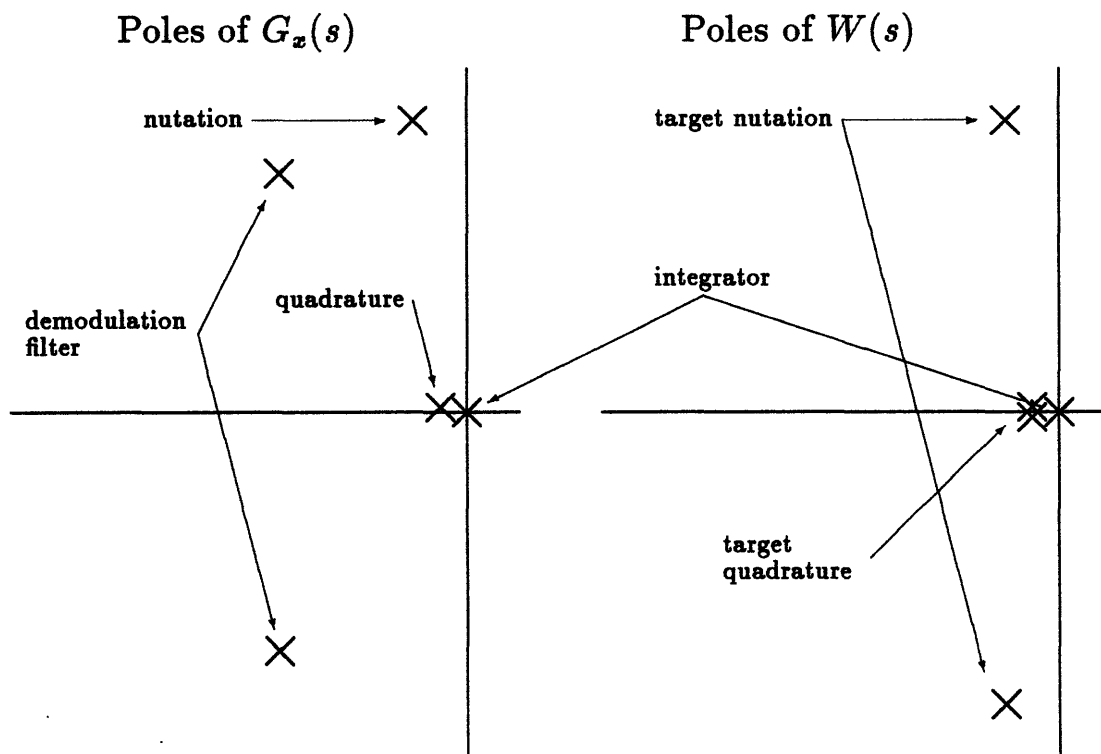


Figure 5.74: Poles of  $G_z(s)$  and  $W(s)$  for Designs FLS-1 and FLS-2

performance of the compensators discussed in Section 5.6.6 depends directly on the performance of the recovered target loop, different choices for the closed loop poles could provide better results. Also, since these designs are not based on a linear quadratic regulator solution, they would be more properly referred to as FLS/LTR designs.

A target with a  $-3\text{ dB}$  bandwidth of  $50\text{ Hz}$  is produced by specifying the closed loop poles in Table 5.25, generating the gain matrix,

$$G_w = \begin{bmatrix} 4.3566 \times 10^8 & 1.0086 \times 10^7 & -359.12 & 0.0238 & 619.58 \end{bmatrix}.$$

Bode plots of the open and closed loop low bandwidth target,  $W(s)$ , are shown in Figures 5.75 and 5.76. The resulting closed loop LQ poles and zeros are shown in Table 5.25.

A target with a  $-3\text{ dB}$  bandwidth of  $100\text{ Hz}$  is produced by specifying the

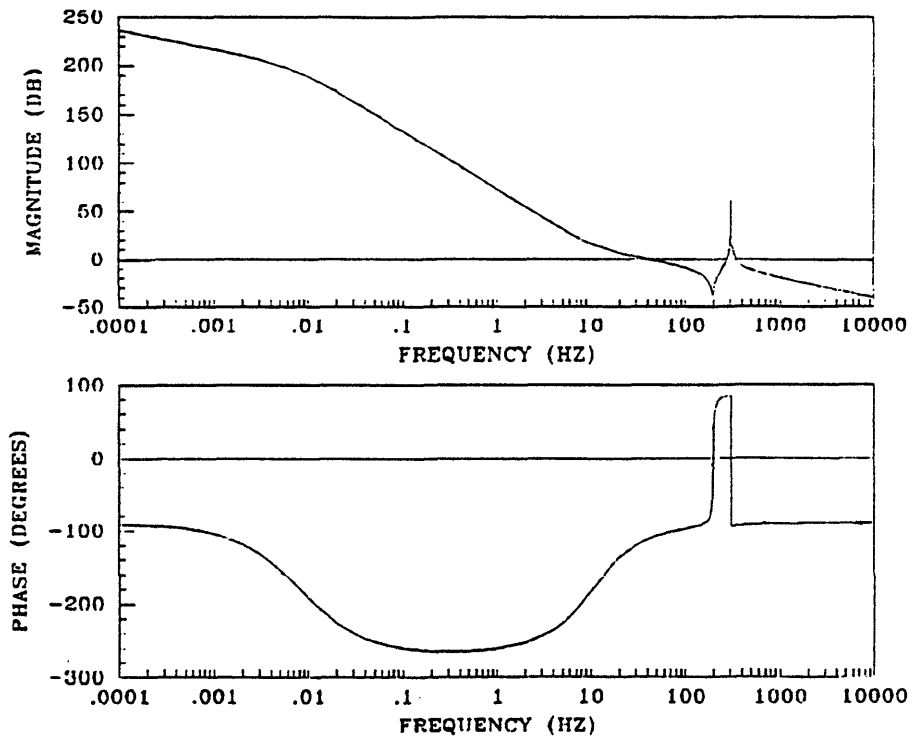


Figure 5.75: Low Bandwidth Target Open Loop Bode Plot

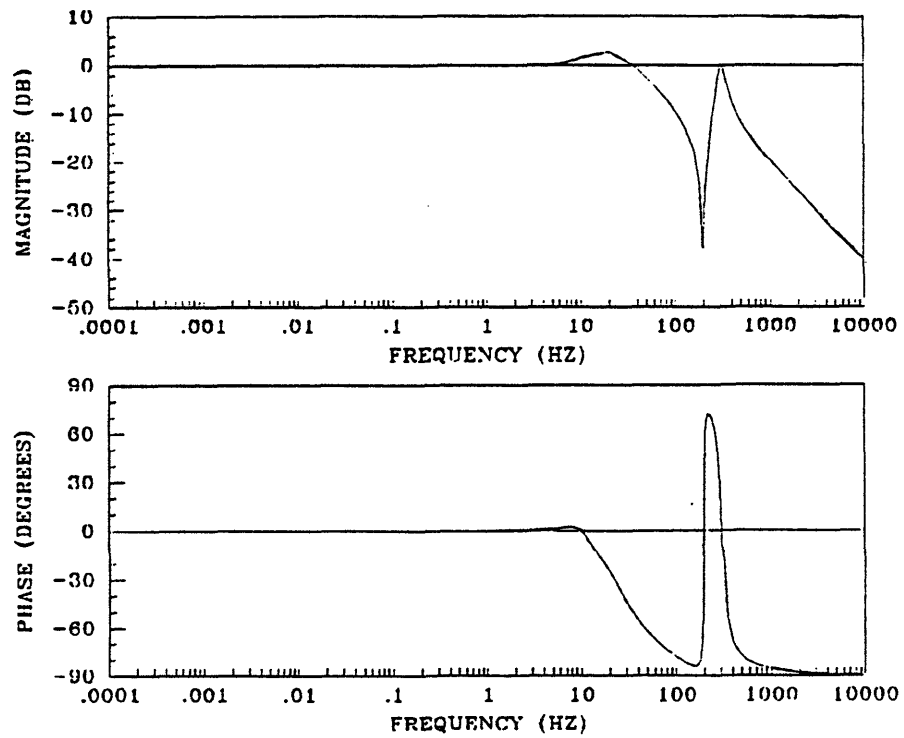


Figure 5.76: Low Bandwidth Target Closed Loop Bode Plot

Table 5.25: Low Bandwidth Target Closed Loop Poles and Zeros

Poles	Zeros
$-180.00 \pm j1900.0$	$-22.085 \pm j1239.1$
$-65.000 \pm j65.000$	$-48.662 \pm j42.857$
$-130.00$	

Table 5.26: High Bandwidth Target Closed Loop Poles and Zeros

Poles	Zeros
$-375.00 \pm j1870.0$	$-97.041 \pm j1275.0$
$-130.00 \pm j130.00$	$-101.55 \pm j92.907$
$-340.00$	

closed loop poles in Table 5.26, generating the gain matrix,

$$G_w = \begin{bmatrix} 4.5516 \times 10^9 & 4.9312 \times 10^7 & -727.53 & 0.1457 & 1349.6 \end{bmatrix}.$$

Bode plots of the open and closed loop high bandwidth target,  $W(s)$ , are shown in Figures 5.77 and 5.78. The resulting closed loop LQ poles and zeros are shown in Table 5.26.

### 5.6.6 Decoupling Compensators

Two compensators are examined in this section that are recovered from the two target loops in Section 5.6.5. A family of compensators is generated by the recovery process, each one better approximating the target loop as the design parameter  $\mu \rightarrow 0$ . The behavior of the compensator zero locus during recovery is very similar to that of the LQG/LTR design methodology discussed in Section 5.4.4, with the locus crossing into the right half plane. In addition, compensator poles that approach the target quadrature poles also go into the right half plane, potentially creating an unstable compensator. After the target loop is recovered to the desired bandwidth, the compensator is augmented at its output with the notch filter in Equation (4.9) in an analogous way to the augmented LQG/LTR compensator shown in Figure 5.11.

A compensator design which provides a  $-90^\circ$  bandwidth of  $50 \text{ Hz}$  for the low bandwidth target in Section 5.6.5, is achieved for values of the Kalman

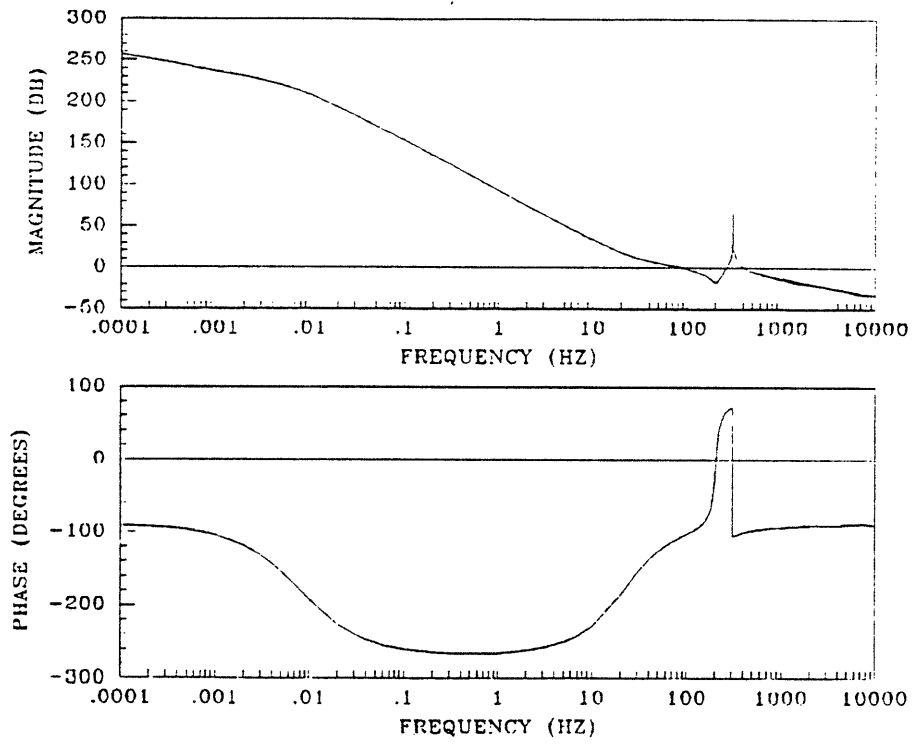


Figure 5.77: High Bandwidth Target Open Loop Bode Plot

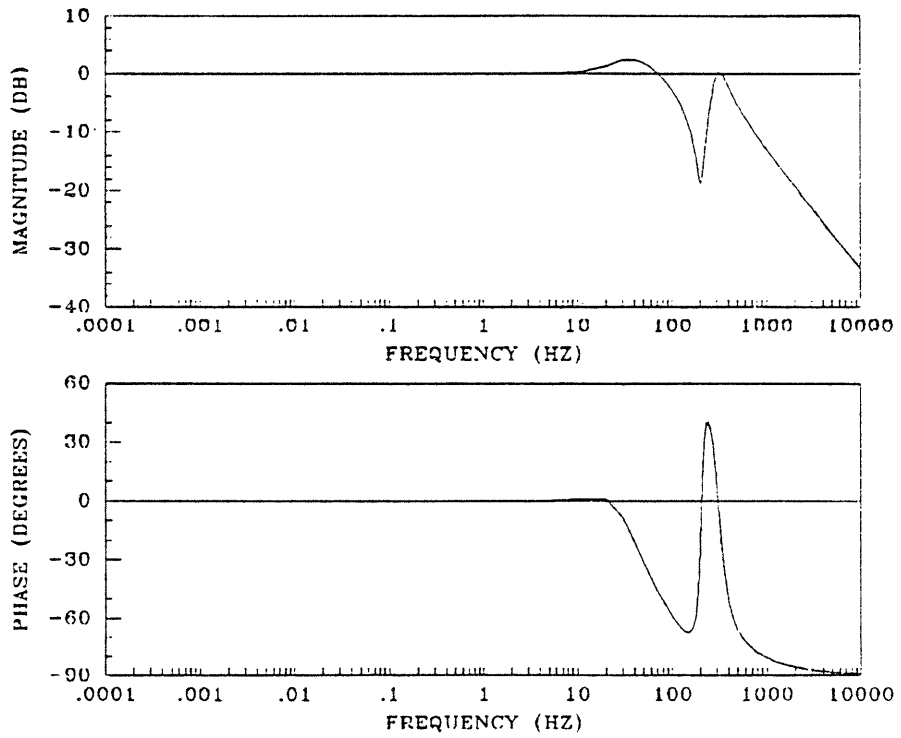


Figure 5.78: High Bandwidth Target Closed Loop Bode Plot

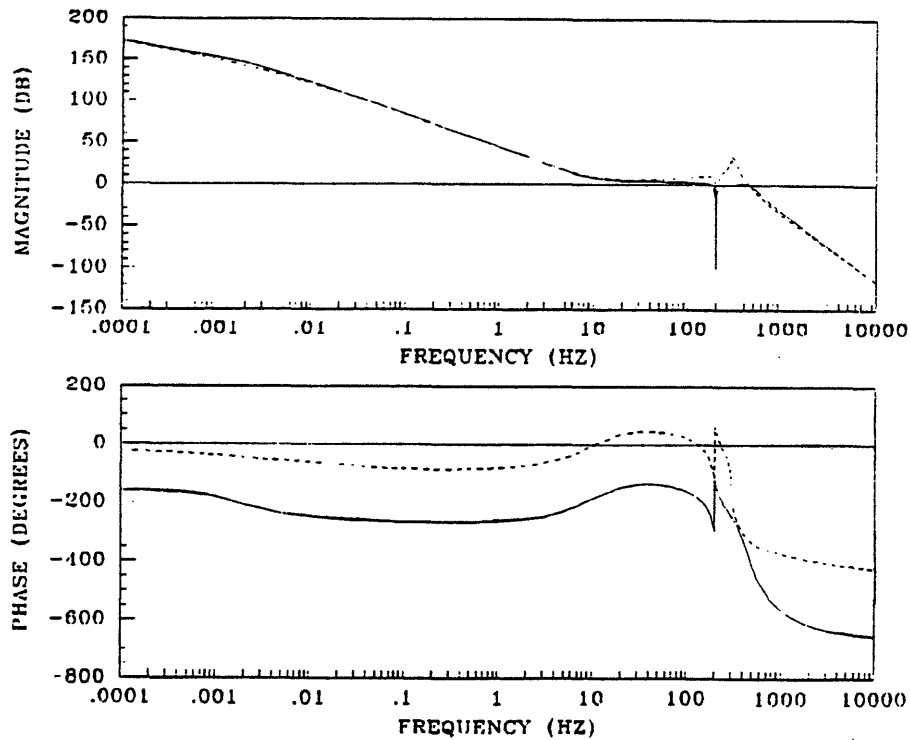


Figure 5.79: Design FLS-1 Augmented Compensator Bode Plot

filter design parameters  $\mu = 10^{-5}$  and  $\Xi = 10^6$ . This design is referred to as FLS-1. A Bode plot of the overall compensator,  $K(s)$ : the model based compensator,  $K_{MBC}(s)$ , modified with the notch filter, and augmented with the demodulation filter and integrator, is shown in Figure 5.79. The compensator poles and zeros are listed in Table 5.27, and the compensator Bode gain is  $1.044 \times 10^5 - j2.830 \times 10^5$  which yields a velocity error constant,  $K_v$ , of 176.0 dB. Note that this compensator has a zero in the right half plane. A Bode plot of the compensated open loop system is shown in Figure 5.80 while a Bode plot of the closed loop system is shown in Figure 5.81. From the open loop Bode plot, it can be seen that the forward and backward transfer functions are almost identical for frequencies from about 0.01 Hz up to nutation, indicating that the channels of the feedback loop have been decoupled in this frequency range. The system has a  $-90^\circ$  bandwidth of 50 Hz and a  $-3$  dB bandwidth of 75 Hz. Both the forward and backward transfer functions have an  $M_p = 4.0$  dB, and the attenuation at 10 kHz is  $-200$  dB. The closed loop system poles are listed in Table 5.28. Note that the two gyro poles and the poles of the demodulation filter have been cancelled by zeros of the compensator.

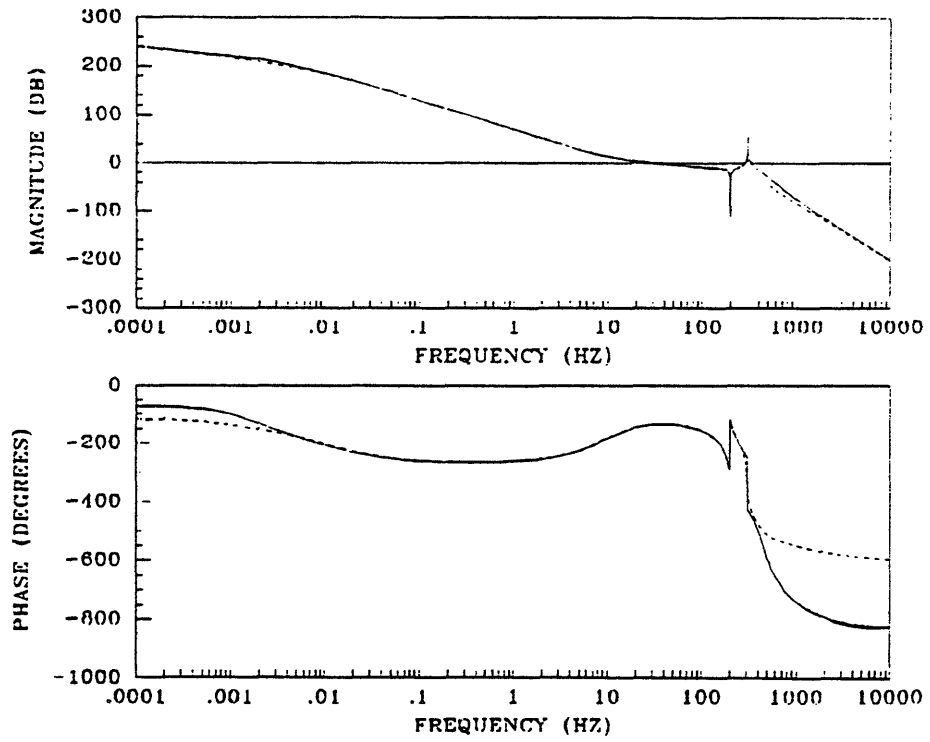


Figure 5.80: Design FLS-1 Open Loop Bode Plot

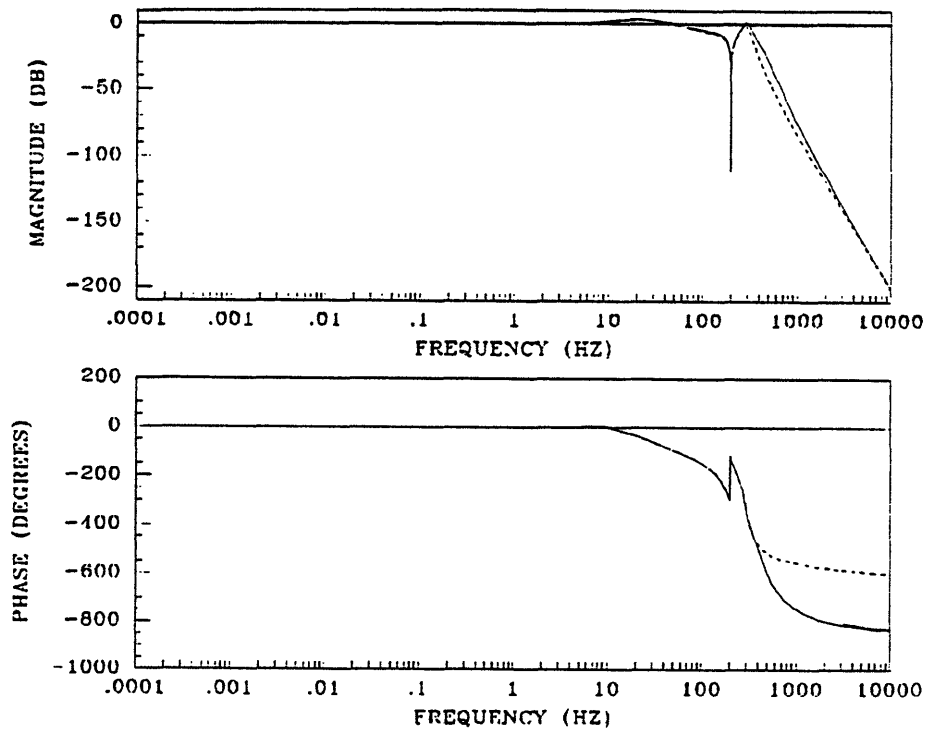


Figure 5.81: Design FLS-1 Closed Loop Bode Plot



Table 5.27: Design FLS-1 Compensator Poles and Zeros

Poles	Zeros*
0.0	$-143.79 + j562.01$
$-471.24 + j816.21$	$-471.24 + j816.21$
$-471.24 - j816.21$	$-471.24 - j816.21$
$-139.82 + j1228.2$	$-0.001256 + j1256.6$
$-146.72 - j1230.8$	$-0.001256 - j1256.6$
$-0.1583 + j1916.7$	$-0.1583 + j1916.7$
$-40.691 - j1894.6$	$-0.05 - j0.00000413$
$-629.84 + j2836.3$	$-40.390 - j45.731$
$-1874.4 + j1972.2$	
$-2392.2 + j316.97$	
$-1858.0 - j1194.0$	
$-771.88 - j2034.4$	
$-0.0121 + j0.006377$	
$-0.0878 - j0.006347$	

\* Two additional zeros could not be found accurately.

Table 5.28: Design FLS-1 Closed Loop Poles

Closed Loop Poles	
$-670.37 - j1917.8$	$-235.63 + j1230.8$
$-147.87 + j1836.6$	$-235.63 - j1230.8$
$-147.87 - j1836.6$	$-471.24 + j816.21$
$-1728.8 - j1061.5$	$-471.24 - j816.21$
$-625.07 + j2736.9$	$-0.1538 + j1916.7$
$-2112.7 + j358.01$	$-0.05 + j0.00000413$
$-1677.2 + j1801.0$	$-140.54 - j0.00000052$
$-66.091 + j63.763$	$-66.091 - j63.763$

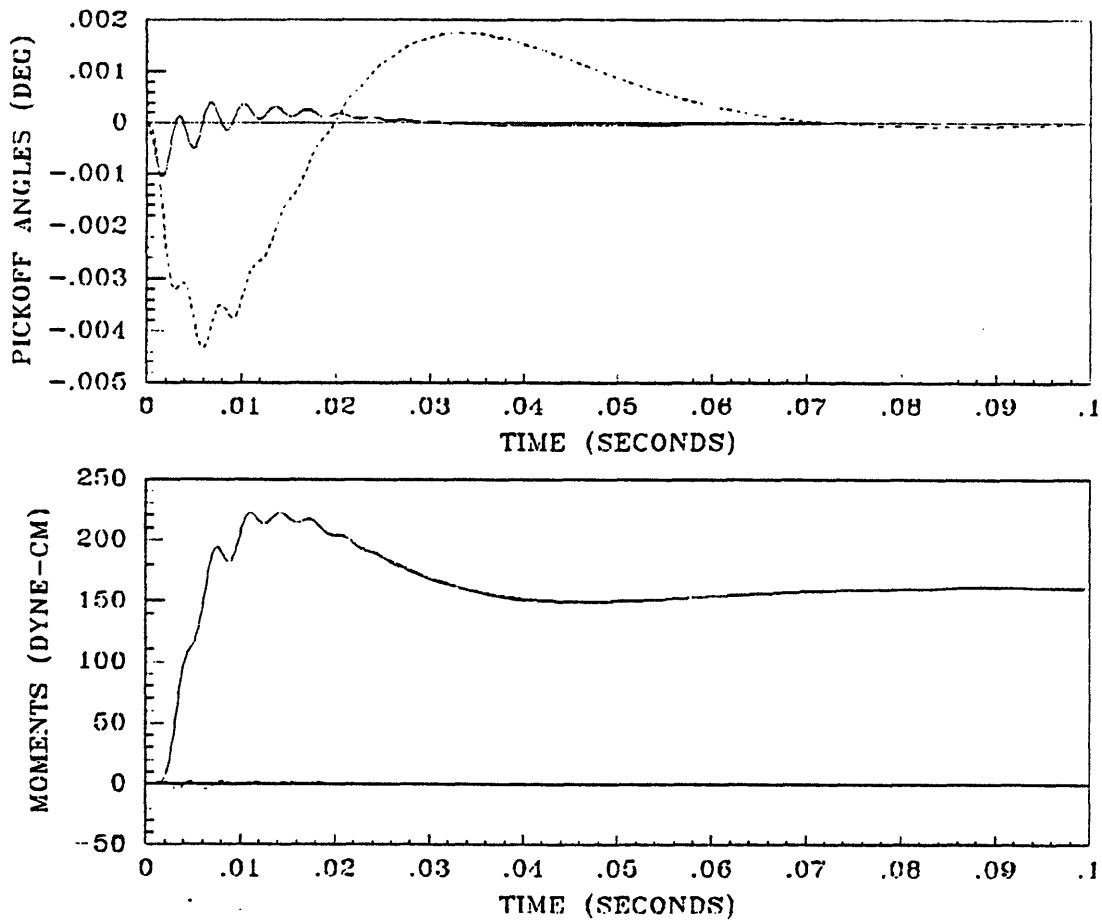


Figure 5.82: Design FLS-1 Step Response

The response of the system to a  $1 \text{ deg/sec}$  step in the  $y$ -axis inertial angular rate, or  $\dot{\phi}_c = j \cdot 1 \text{ deg/sec}$ , is shown in Figure 5.82. The maximum deviation of the  $y$ -axis pickoff angle is  $0.0044^\circ$  while the  $x$ -axis moment command has an overshoot of 41% and a settling time of about 0.066 seconds. Note that there is very little  $y$ -axis moment command, as the TITOBS loop channels are nearly decoupled. The response time of the loop is slow because only one torquer is working to null the pickoff angles. The loop performance is also not optimal since the target is not a solution to a linear quadratic regulator problem and could probably be improved significantly.

A Nyquist plot of the compensated system is shown in Figure 5.83. The stability margins obtained from the plot indicate positive and negative phase margins of  $46^\circ$ , an upward gain margin of  $9.90 \text{ dB}$ , and a downward gain margin of  $12.71 \text{ dB}$ .

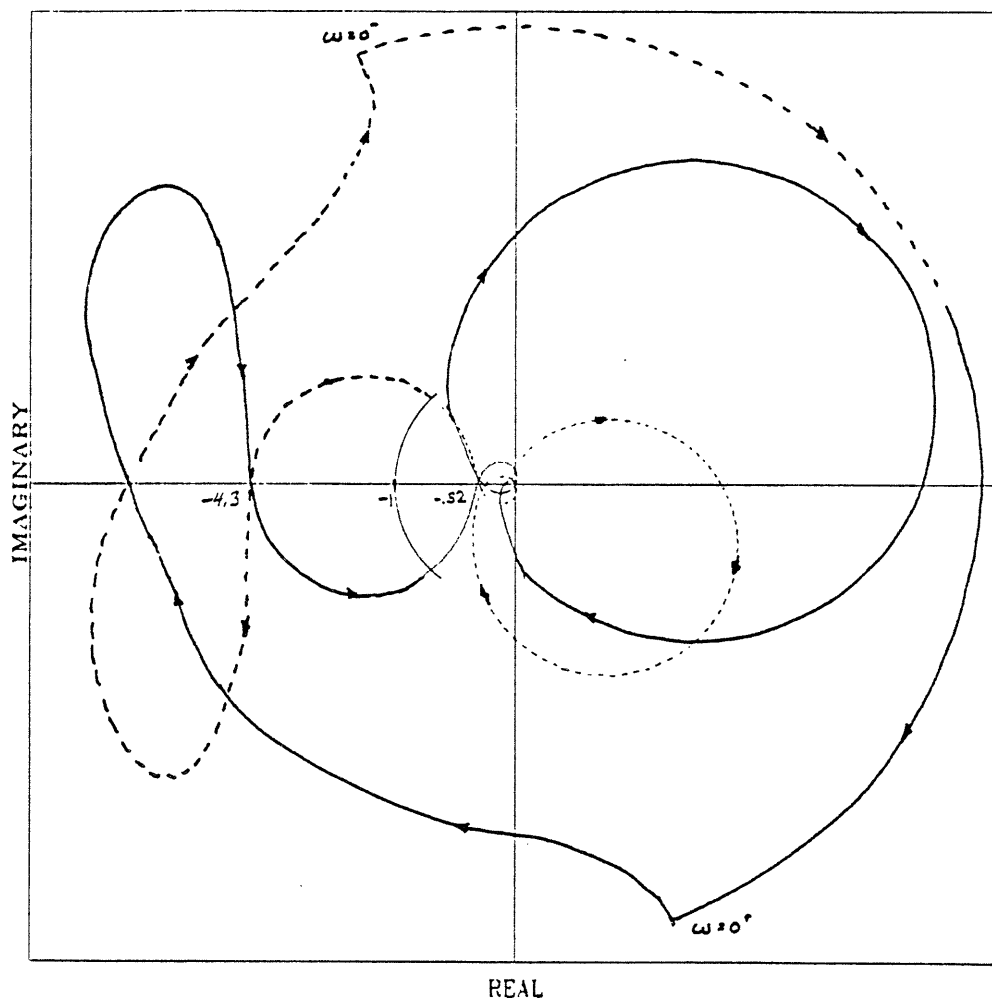


Figure 5.83: Design FLS-1 Nyquist Plot

A compensator design which provides a  $-90^\circ$  bandwidth of  $100\text{ Hz}$  for the high bandwidth target in Section 5.6.5, is achieved for values of the Kalman filter design parameters  $\mu = 10^{-10}$  and  $\Xi = 10^8$ . This design is referred to as FLS-2. A Bode plot of the overall compensator,  $K(s)$ : the model based compensator,  $K_{MBC}(s)$ , modified with the notch filter, and augmented with the demodulation filter and integrator, is shown in Figure 5.84. The compensator poles and zeros are listed in Table 5.29, and the compensator Bode gain is  $-7818 - j5077$  which yields a velocity error constant,  $K_v$ , of  $145.7\text{ dB}$ . Note that this is an unstable compensator, and it has a zero in the right half plane. A Bode plot of the compensated open loop system is shown in Figure 5.85 while a Bode plot of the closed loop system is shown in Figure 5.86. From the open loop Bode plot, it can be seen that the forward and backward transfer function magnitudes are almost

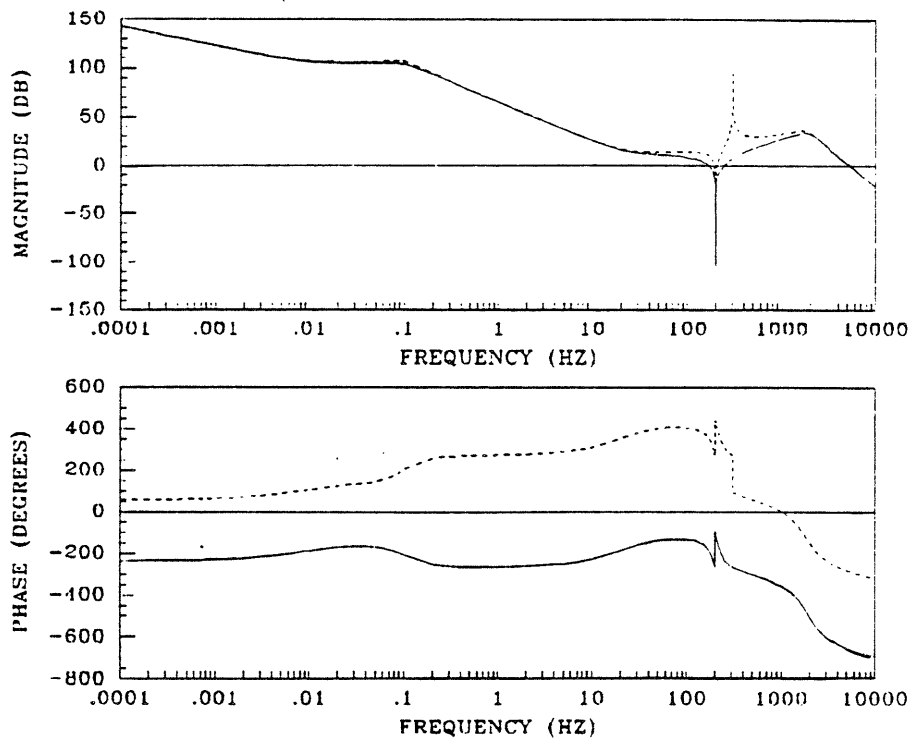


Figure 5.84: Design FLS-2 Augmented Compensator Bode Plot

identical for frequencies from about 0.1 Hz up to nutation, but the phases are different due to the unstable compensator. The system has a  $-90^\circ$  bandwidth of 100 Hz and a  $-3$  dB bandwidth of 125 Hz. Both the forward and backward transfer functions have an  $M_p = 3.68$  dB, and the attenuation at 10 kHz is  $-107$  dB. The closed loop system poles are listed in Table 5.30. Note that the two gyro poles and the poles of the demodulation filter have been cancelled by zeros of the compensator.

The response of the system to a 1 deg/sec step in the  $y$ -axis inertial angular rate, or  $\dot{\phi}_c = j \cdot 1 \text{ deg/sec}$ , is shown in Figure 5.87. The maximum deviation of the  $y$ -axis pickoff angle is  $0.0021^\circ$  while the  $x$ -axis moment command has an overshoot of 44% and a settling time of about 0.03 seconds. Note that there is virtually no  $y$ -axis moment command, as the TITOBs loop channels are nearly decoupled. The response time of the loop is slow because only one torquer is working to null the pickoff angles. The loop performance is also not optimal since the target is not a solution to a linear quadratic regulator problem and could probably be improved significantly.

A Nyquist plot of the compensated system is shown in Figure 5.88. The

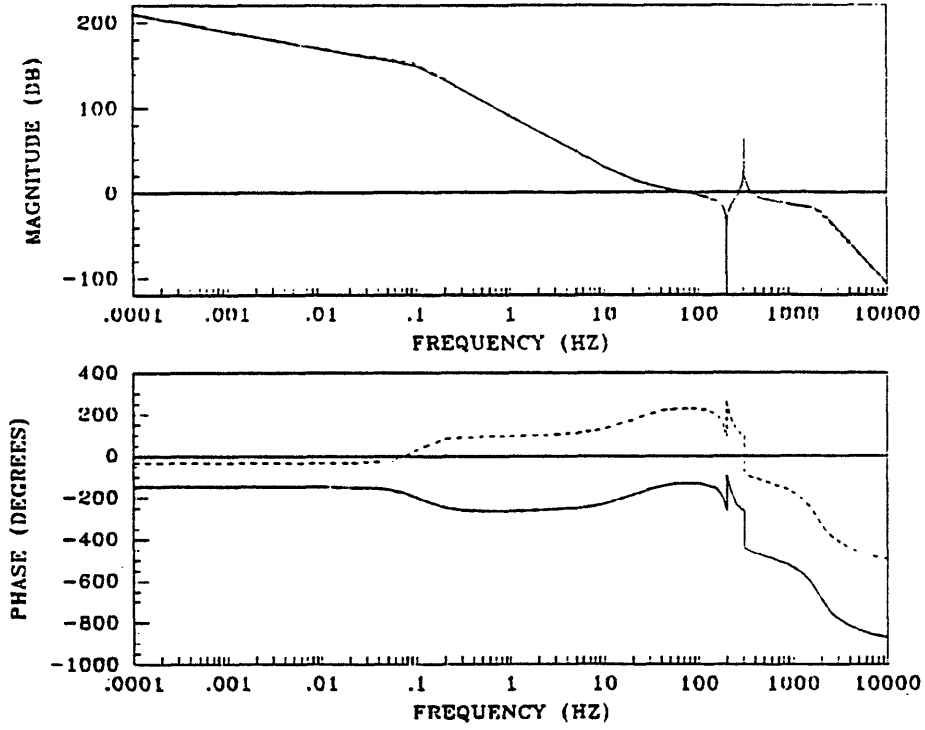


Figure 5.85: Design FLS-2 Open Loop Bode Plot

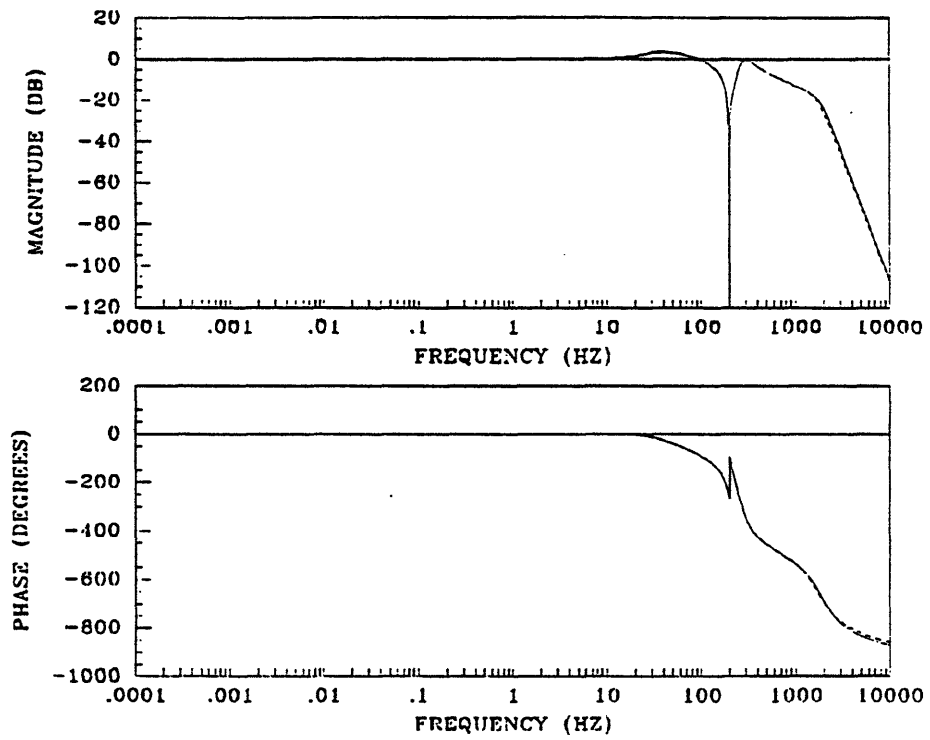


Figure 5.86: Design FLS-2 Closed Loop Bode Plot

Table 5.29: Design FLS-2 Compensator Poles and Zeros

Poles	Zeros
0.0	$186.51 + j1326.7$
$-471.24 + j816.21$	$-471.24 + j816.21$
$-471.24 - j816.21$	$-471.24 - j816.21$
$-149.20 + j1240.0$	$-0.001256 + j1256.6$
$-149.07 - j1240.1$	$-0.001256 - j1256.6$
$-0.1583 + j1916.7$	$-0.1583 + j1916.7$
$-0.1578 - j1916.7$	$-0.05 - j0.00000413$
$-3068.5 + j11438.$	$186.51 - j1326.7$
$-2994.1 - j10809.$	$-95.297 + j88.034$
$-9437.6 + j8771.2$	$-95.297 - j88.034$
$-9474.4 - j7837.0$	
$-12924. - j59.836$	
$-0.3634 + j0.5615$	
$0.2553 - j0.5737$	

stability margins obtained from the plot indicate positive and negative phase margins of  $47^\circ$ , an upward gain margin of  $12.11 \text{ dB}$ , and a downward gain margin of  $13.06 \text{ dB}$ . Note that the  $-1$  point is encircled once due to the unstable compensator.

Table 5.30: Design FLS-2 Closed Loop Poles

Closed Loop Poles	
$-11088. - j51.229$	$-132.16 + j1256.0$
$-248.22 + j1212.0$	$-132.16 - j1256.0$
$-248.22 - j1212.0$	$-471.24 + j816.21$
$-3636.6 + j13140.$	$-471.24 - j816.21$
$-3532.9 - j10607.$	$-0.1538 + j1916.7$
$-9173.6 + j7386.5$	$-0.05 + j0.00000413$
$-8996.6 - j6470.3$	$-421.43 - j0.0060958$
$-293.76 + j1729.9$	$-293.76 - j1729.9$

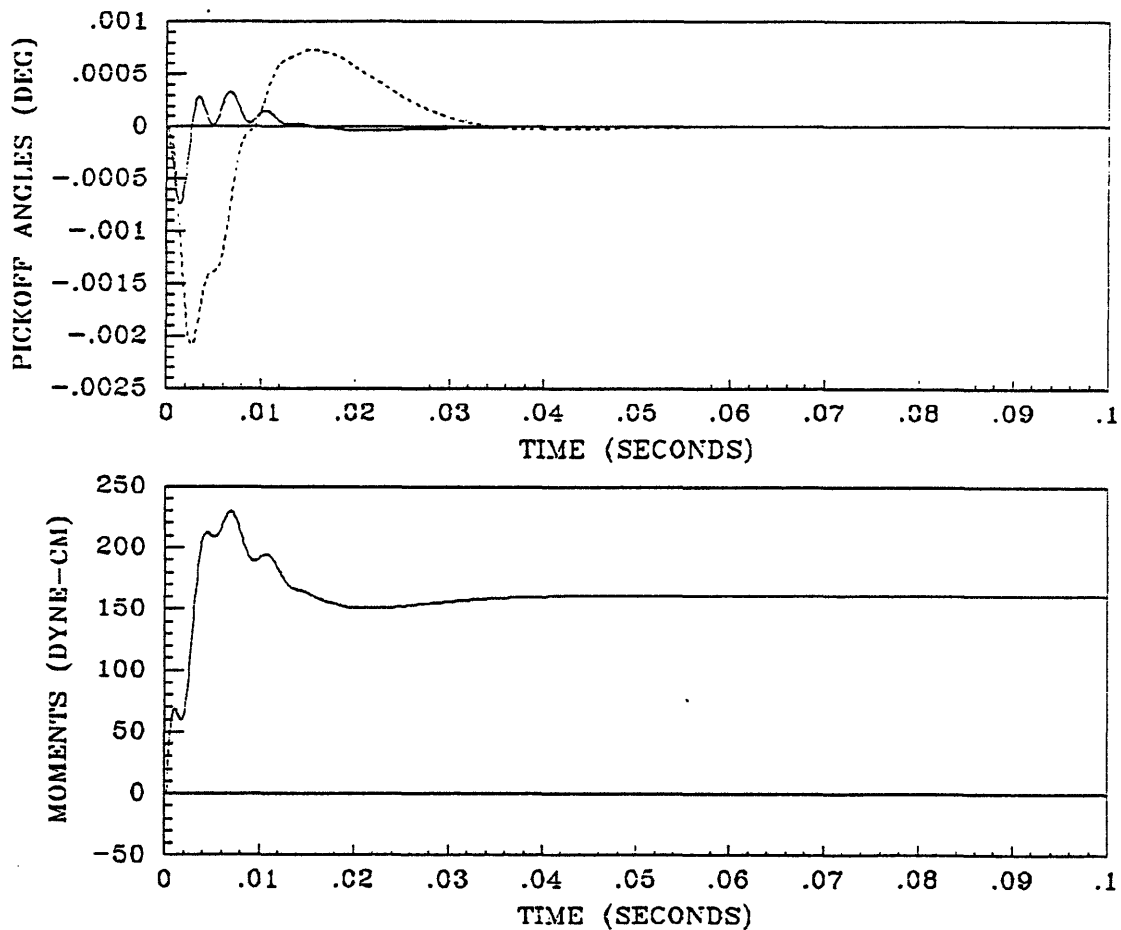


Figure 5.87: Design FLS-2 Step Response

### 5.6.7 Summary

The FLS/LQG/LTR design methodology allows recovery of arbitrary target loops in the feedback loop, by generating a compensator that completely inverts the plant dynamics and recovers the target loop dynamics. Inversion of the plant dynamics causes those dynamics to be unobservable at the output torque command. The result is that if the target loop does not contain these dynamics, the gyro pickoff angles are not driven to null by the controller. Recovery of a target loop that does not contain the gyro quadrature dynamics is investigated in Section 5.6.4, demonstrating the poor step response of the pickoff angles even though the recovered loop has excellent frequency domain characteristics.

Controllers with better time domain characteristics are generated by recovery of real coefficient target loops that are based on decoupled dynamics corresponding to both the gyro nutation and quadrature modes as shown in Section 5.6.6.

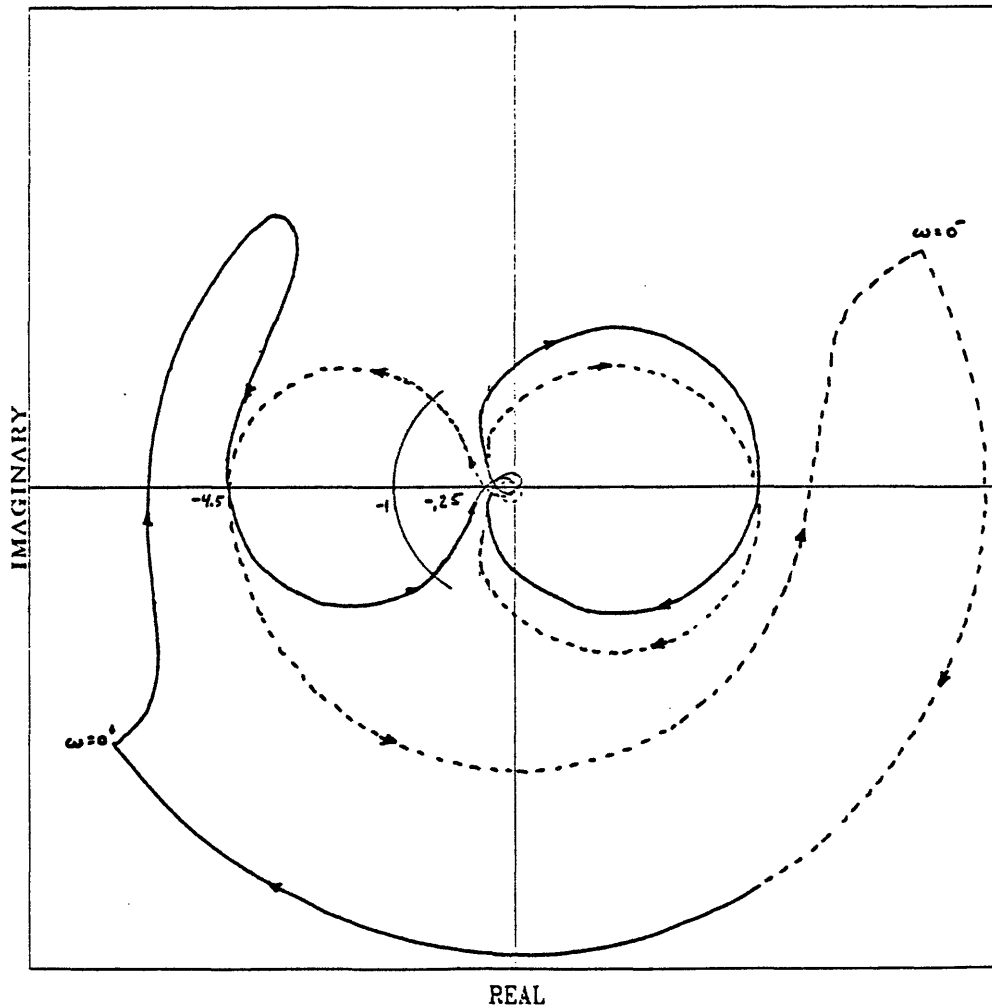


Figure 5.88: Design FLS-2 Nyquist Plot

Recovery of these targets produces compensators that tend to decouple the  $x$  and  $y$ -axes of the torque-rebalance loop so that an input in inertial angular rate on the  $y$ -axis produces only  $x$ -axis torque commands.

The performance parameters of the low and high bandwidth decoupling designs of Section 5.6.6 are shown in Table 5.31. The performance of the recovered loops depends on the performance of the targets. Since the target loops for these designs do not come from the solution to an optimal regulator problem, their performance is expected to be relatively low.



Table 5.31: FLS/LQG/LTR Compensator Design Parameters

Parameters	Units	FLS/LQG/LTR Designs	
		FLS-1	FLS-2
Upward Gain Margin	<i>dB</i>	9.90	12.11
Downward Gain Margin	<i>dB</i>	12.71	13.06
Negative Phase Margin	<i>deg</i>	46	47
Positive Phase Margin	<i>deg</i>	46	47
$-90^\circ$ Bandwidth	<i>Hz</i>	50	100
$-3\text{ dB}$ Bandwidth	<i>Hz</i>	75	125
Forward TF $M_p$	<i>dB</i>	4.00	3.68
Backward TF $M_p$	<i>dB</i>	4.00	3.68
Velocity Error Constant	<i>dB</i>	176.0	145.7
CL Gain at 10 <i>kHz</i>	<i>dB</i>	-200	-107
Moment Command Overshoot	%	41	44
Settling Time	<i>sec</i>	0.066	0.030
Pickoff Angle Deviation	<i>deg</i>	0.0044	0.0021

## 5.7 Summary

In this chapter, four design methodologies are used to generate controllers for the TDF-DTG torque-rebalance loop. The design methodologies used are classical first order lead compensation, LQG/LTR, FW/LQG, and FLS/LQG/LTR. Classical first order lead compensation is used to generate one design with a 50 Hz bandwidth, which is near the maximum achievable bandwidth for that design methodology due to the nutation phase characteristic of the gyro. LQG/LTR is used to generate four controller designs, two with a bandwidth of 50 Hz and two with a bandwidth of 100 Hz. These designs illustrate the effect of the recovery bandwidth on the loop performance parameters. The LQG/LTR compensators allow non-minimum phase zeros which provide additional negative phase margin by introducing phase lag at nutation when required during the recovery process. FW/LQG is used to generate two controllers, one with a 50 Hz bandwidth and one with a 100 Hz bandwidth. In this methodology the states and controls are weighted as functions of frequency. This provides great flexibility in shaping the LQ loop and allows the inclusion of a notch filter directly in the LQ loop. In addition, the effects of different state weighting transfer functions are examined to present a systematic design approach. Two different design approaches are examined for the the FLS/LQG/LTR design methodology. One provides good frequency domain characteristics but has a poor time response. The other approach is used to generate two controllers, one with a 50 Hz bandwidth and one with a 100 Hz bandwidth, which provide acceptable time response behavior. These designs decouple the torque-rebalance loop channels so that an inertial angular rate input on one axis produces a moment command on the opposite axis only. The design methodologies and the designs are compared in Chapter 6.

## Chapter 6

# Comparison of Design Methodologies and Conclusions

In this chapter, the controller designs presented in Chapter 5 are compared. First, the performance of the designs is compared, and second, the design procedures and special characteristics of the designs are compared. Finally, some recommendations for future work in torque-rebalance loop compensation are made.

## 6.1 Performance Comparisons

### 6.1.1 Overview

The general design requirements for strapdown torque-rebalance loops are described in Section 1.3. The primary points of comparison are:

- stability margins with respect to block symmetric plant perturbations;
- $M_p$ , the maximum closed loop peaking within the bandwidth as a measure of how close the closed loop gain within the bandwidth is to unity;
- $K_v$ , the velocity error constant as a measure of steady state error in moment command and pickoff angle due to a step in inertial angular acceleration;
- the closed loop gain at 10 *kHz* as a measure of high frequency attenuation for high frequency noise rejection;
- time response characteristics including overshoot and settling time of the moment command and maximum deviation from null of the pickoff angles due to a 1 *deg/sec* step in inertial angular rate.

Table 6.1: Low (50 Hz) Bandwidth Compensator Design Parameters

Parameters	Units	Compensator Designs				
		1st Order Lead	LQG/LTR		FW/LQG	FLS/LTR
			1a	1b	1	1
Upward GM	<i>dB</i>	4.73	12.40	20.00	30.50	9.90
Downward GM	<i>dB</i>	$\infty$	48.16	39.08	16.83	12.71
Negative PM	<i>deg</i>	50	48	56	41	46
Positive PM	<i>deg</i>	49	50	62	59	46
$-90^\circ$ BW	<i>Hz</i>	50	50	80	48	50
$-3$ dB BW	<i>Hz</i>	145	70	50	48	75
Forward TF $M_p$	<i>dB</i>	3.95	2.51	1.85	1.59	4.00
Backward TF $M_p$	<i>dB</i>	2.37	3.02	2.59	3.98	4.00
$K_v$	<i>dB</i>	110.9	113.5	115.5	112.4	176.0
10 kHz Gain	<i>dB</i>	-170	-170	-90	-109	-200
Overshoot	%	31	31	25	31	41
Settling Time	<i>sec</i>	0.035	0.03	0.03	0.03	0.066
Max. PO Ang.	<i>deg</i>	0.0042	0.0039	0.0031	0.0034	0.0044
Order of $K(s)$		6	10	10	12	14

All four designs, first order lead, LQG/LTR, FW/LQG, and FLS/LQG/LTR, are compared for the low (50 Hz) bandwidth case while the multivariable designs, LQG/LTR, FW/LQG, and FLS/LQG/LTR, are compared for the high (100 Hz) bandwidth case. The performance parameters for the designs of Chapter 5 are summarized in Table 6.1 and Table 6.2 for the low and high bandwidth designs respectively.

The differences between the low and high bandwidth designs are essentially that stability margins, high frequency attenuation and moment command overshoot are traded for improved bandwidth,  $K_v$ , and response time. Clearly all of the designs presented could be improved with further iteration of the respective design parameters or weighting functions. However, they are designs that are representative of the performance attainable for each of the methodologies.

A performance parameter not discussed in Section 1.3 is the order of the compensator itself. The augmented classical lead compensator has 6 states while all of the multivariable, model based compensators have many more. This parameter could be important because it is desirable to have compensators with as few states as possible. If a high order compensator is implemented with ana-

Table 6.2: High (100 Hz) Bandwidth Compensator Design Parameters

Parameters	Units	Compensator Designs			
		LQG/LTR		FW/LQG	FLS/LTR
		2a	2b	2	2
Upward GM	<i>dB</i>	6.38	10.45	10.45	12.11
Downward GM	<i>dB</i>	24.35	22.92	16.25	13.06
Negative PM	<i>deg</i>	34	43	43	47
Positive PM	<i>deg</i>	52	70	55	47
$-90^\circ$ BW	<i>Hz</i>	100	125	100	100
$-3$ dB BW	<i>Hz</i>	120	100	105	125
Forward TF $M_p$	<i>dB</i>	1.93	1.18	0.95	3.68
Backward TF $M_p$	<i>dB</i>	4.89	3.95	3.46	3.68
$K_v$	<i>dB</i>	125.9	128.3	126.7	145.7
10 kHz Gain	<i>dB</i>	-140	-90	-89	-107
Overshoot	%	40	34	25	44
Settling Time	<i>sec</i>	0.02	0.02	0.015	0.030
Max. PO Ang.	<i>deg</i>	0.00225	0.00156	0.00152	0.0021
Order of $K(s)$		10	10	12	14

log electronics, more components are required, and if it is implemented in a digital computer, more processing time is required, leading to time delays that could degrade the performance of the torque-rebalance loop. Therefore, there is a tradeoff between the loop performance achievable with the particular design methodology and the order of the resulting compensator.

### 6.1.2 Low Bandwidth Designs

The performance parameters of the low bandwidth designs are shown in Table 6.1. The designs are compared with respect to each of the performance parameters of interest.

#### Stability Margins

The phase margins of all of the designs are comparable, with the high bandwidth recovery LQG/LTR design (LQG/LTR-1b) having the largest phase margins as well as the largest gain margins. Although the downward gain margin of the lead compensation design is infinite, the upward gain margin is only 4.73 dB. The downward gain margins of the multivariable designs are very large, and the

upward gain margins of the designs, between  $9.90\text{ dB}$  and  $30.50\text{ dB}$ , are much larger than that of the lead design. The stability margins of the FLS design are lower than those of the other multivariable designs because the target loop for that case is not based on a linear quadratic regulator so the stability properties of the LQG based designs are not achievable.

### **Bandwidth**

The FW/LQG design has the best bandwidth characteristic in that the  $-3\text{ dB}$  and  $-90^\circ$  bandwidths are identical. The other multivariable designs have between  $20\text{ Hz}$  and  $30\text{ Hz}$  difference between the bandwidths while the lead design has a  $-90^\circ$  bandwidth of  $50\text{ Hz}$  and a  $-3\text{ dB}$  bandwidth of  $145\text{ Hz}$ . If the lower  $-90^\circ$  bandwidth is matched to the attitude algorithm bandwidth, then a larger  $-3\text{ dB}$  bandwidth would pass high frequency motion which could lead to coning errors. Design LQG/LTR-1b has a  $-90^\circ$  bandwidth that is higher than its  $-3\text{ dB}$  bandwidth, so there is a point during recovery where these bandwidths are matched.

### **Closed Loop Peaking**

The  $M_p$  for all of the designs are comparable. The  $M_p$  of design LQG/LTR-1b is somewhat better than the rest, but that of the FW/LQG design could be improved using the technique described in Section 5.5. Since the channels of the FLS design are decoupled, the  $M_p$  for that design is identical for both the forward and backward transfer functions; however, it is higher than the rest, again due to the non-optimal target loop.

### **Velocity Error Constant**

The  $K_v$  of all of the designs is near  $110\text{ dB}$  with the exception of the FLS design which is over 1000 times better, or over  $60\text{ dB}$  higher. A  $K_v$  of  $110\text{ dB}$  yields a pickoff angle steady state hang off error of about  $16\text{ arcsec}$  for a  $100^\circ/\text{sec}^2$  step in inertial angular acceleration, and this would be improved by a factor of about one thousand for the FLS design.

## High Frequency Attenuation

The closed loop gain at  $10\text{ kHz}$  for the lead design is  $-170\text{ dB}$  and that of the FLS design is  $-200\text{ dB}$ . The LQG/LTR closed loop gain at high frequencies is a function of recovery bandwidth so that recovery of the target stability and other performance properties are traded off against high frequency attenuation. Design LQG/LTR-1a has a closed loop gain at  $10\text{ kHz}$  of  $-170\text{ dB}$  while design LQG/LTR-1b has a gain at  $10\text{ kHz}$  of  $-90\text{ dB}$ , but with better stability, step response and  $M_p$  properties. The FW/LQG design has a rather high gain of  $-109\text{ dB}$ .

## Step Response

The response of the designs to a  $1\text{ deg/sec}$  step in inertial angular rate is presented in the table. The step responses of all of the designs, except for the FLS design, are comparable, with that of the LQG/LTR-1b design being slightly better. The FLS design has clearly the worst response in terms of the parameters listed. The settling time in particular is twice as long as the other designs. The characteristic of the design that does not appear in the table is that the moment command response on the opposing channel is very small compared to that of the other designs. The advantage of this is that no rate on the opposing axis is seen by the attitude algorithm. The disadvantage is that the moment and pickoff angle settling times are much longer, due in part to a non-optimal design.

### 6.1.3 High Bandwidth Designs

The performance parameters of the high bandwidth multivariable designs are shown in Table 6.2. The designs are compared with respect to each of the performance parameters of interest.

## Stability Margins

The phase margins of the designs are similar, with design LQG/LTR-2b having the largest margins. The gain margins are also comparable, again with those of design LQG/LTR-2b being the largest. The low bandwidth recovery LQG/LTR design (LQG/LTR-2a) has a downward gain margin of only  $6.38\text{ dB}$  which is very small. Overall, the stability margins for the high bandwidth designs

are lower than for the low bandwidth designs, except for the FLS designs. Again, this is likely to be due to the fact that these FLS designs are not based on an LQ regulator solution as are the other multivariable designs.

### **Bandwidth**

The bandwidth results for these designs are similar to those of the low bandwidth designs. The  $-3\text{ dB}$  and  $-90^\circ$  bandwidths are between  $20\text{ Hz}$  and  $25\text{ Hz}$  apart with the exception of the FW/LQG design, for which they are only  $5\text{ Hz}$  apart.

### **Closed Loop Peaking**

In this case, the LQG/LTR designs have the highest  $M_p$ , with the low bandwidth recovery having an  $M_p$  of  $4.89\text{ dB}$  and the high bandwidth recovery having an  $M_p$  of  $3.95\text{ dB}$ . Here, the advantage of selecting the FW/LQG weighting functions specifically to reduce  $M_p$  is obvious, since this has the lowest  $M_p$  of the high bandwidth designs. Note again that the  $M_p$  of the FLS design is identical for both transfer functions.

### **Velocity Error Constant**

As with the low bandwidth case, the FLS design has the highest  $K_v$ , though not as high as the previous case. This is due to the fact that the high bandwidth FLS/LQG/LTR compensator is unstable. The other designs have a  $K_v$  near  $126\text{ dB}$  which yields a pickoff angle steady state hang off error of about  $3.0\text{ arcsec}$  for a  $100^\circ/\text{sec}^2$  step in inertial angular acceleration.

### **High Frequency Attenuation**

The closed loop gain at  $10\text{ kHz}$  for the LQG/LTR-2a design is  $-140\text{ dB}$  which is between  $40\text{ dB}$  and  $50\text{ dB}$  better than that of the other designs. These values are much higher than those of the low bandwidth designs and represent one of the major trade-offs for higher bandwidth.



## Step Response

In this case the FW/LQG design has superior step response performance to the other designs. Again the moment command overshoot, and settling times for the FLS design are poor for the reasons discussed in the previous section.

### 6.1.4 Summary

No multivariable design has a clear performance advantage over the others, but all out-perform the first order lead compensation design, except in the category of compensator order. The LQG/LTR designs provide superior stability margins with good  $M_p$  and step response characteristics traded for closed loop attenuation at high frequencies. The FW/LQG designs provide good stability,  $M_p$ , and step response with superior bandwidth characteristics, but poor closed loop attenuation at high frequencies. The FW/LQG designs also have two more states than do the LQG/LTR designs. The FLS/LTR designs have superior  $K_v$  and high frequency attenuation with decoupled but slow step response performance.

## 6.2 Design Procedures

In this section, the design procedures for each of the design methodologies are compared. The special characteristics of the compensators are also discussed.

### 6.2.1 Classical Lead Compensation

Classical first order lead compensation requires the selection of three parameters, the compensator gain and the locations of the compensator pole and zero. If the pole location is fixed to be about a decade beyond crossover, then the remaining two parameters must be adjusted to achieve the desired performance and stability properties. Selection of these parameters is fairly straight forward, and designs can be generated quickly using Bode techniques.

The performance achievable with first order lead compensation, discussed in Section 5.3.3, is limited by the gyro nutation. The open loop transfer function phase just before the nutation frequency must be less than  $-180^\circ$ ; therefore, the phase contribution of the lead cannot be such that it increases the phase at nutation above  $-180^\circ$ . This can be avoided to some extent by using a second order

lead network to improve the phase at crossover somewhat, or by including an additional low pass filter to increase phase lag at nutation but not at crossover. An advantage of the addition of a low pass filter is that high frequency attenuation would be improved.

### 6.2.2 LQG/LTR

The performance of the linear quadratic Gaussian with loop transfer recovery designs is limited by the performance of the linear quadratic target loop that is recovered. The degree to which it is recovered directly affects the high frequency attenuation, but the recovery process is simply a “crank turning” process. The shape of the LQ target loop depends on the state and control weighting matrices. In Section 5.4, the selection of the weighting matrices is reduced to the selection of two scalar parameters by matching the magnitudes of the forward and backward transfer functions at high and low frequencies. One parameter, the control weighting, is used to control the bandwidth of the LQ target loop while the other determines the frequency of the maximum attenuation between crossover and nutation. This weighting selection scheme, however, ignores two additional degrees of freedom in loop shaping.

A serious disadvantage of the LQG/LTR design methodology is that notch filters beyond crossover cannot be generated with a time weighted LQ problem. In addition, since the zeros of the compensator approach the zeros of the target only asymptotically, high Q notch filters cannot be accurately recovered for practical recovery bandwidths. These problems require that the notch filter at the spin frequency be included in the compensator after recovery is completed. This solves the requirement for a notch filter but creates two new problems: first, the LQ loop should be designed to take the notch filter into account so that the final feedback loop has the desired characteristics, and second, the notch filter destroys the optimality and guaranteed stability properties of the recovered LQ loop.

An interesting feature of the LQG/LTR compensator for the TDF-DTG problem is that it may be non-minimum phase. This result is discussed in detail in Section 5.4.4. The phase lag of the non-minimum phase zeros is employed by the compensator to keep the phase angle at nutation well below  $-180^\circ$ , maintaining large positive and negative phase margins. Because of this, the LQG/LTR

designs have larger overall stability margins than do the other multivariable designs.

### **6.2.3 FW/LQG**

The frequency weighted linear quadratic Gaussian design methodology allows a linear quadratic regulator loop to be shaped in the frequency domain by the selection of control and state (or output) weighting transfer functions. Since the poles of the state weighting transfer function are poles of the compensator and poles of the control weighting transfer function are zeros of the compensator, loop pole and zero selection is very straight forward.

A notch filter in the LQ loop (and consequently in the compensator) can be generated by penalizing the control variable heavily at the desired frequency by placing resonant poles in the control weighting transfer function at the desired compensator zero locations. As demonstrated in Section 5.5.2, the LQ loop shape and system time response may be further controlled by adding dynamics to either the state or control weighting functions in a straight forward manner. For example, excessive output oscillation at the nutation frequency is corrected by weighting the output more heavily at the nutation frequency.

The FW/LQG design methodology offers great flexibility in the generation of desired LQ loop shapes, limited only by the additional consideration of keeping the compensator order low. In Section 5.5.2 only the output of the design plant model is weighted, and the frequency weighting of individual states is ignored. This may also offer a possibility of increased loop performance and design flexibility without a large increase in the number of compensator states.

### **6.2.4 FLS/LQG/LTR**

The LQG/LTR with formal loop shaping design methodology allows additional design flexibility within the LTR framework. It allows the recovery of any target, even a target loop not based on the plant dynamics or a target not based on the solution to a linear quadratic regulator problem, in which case the methodology should probably be called simply FLS/LTR. The only restrictions on the target loop are that it must contain all of the closed right half plane dynamics of the design plant model, and for the gyro torque-rebalance loop problem, it must include the gyro dynamics in some form.

The design approaches examined in Section 5.6.2 outline some of the advantages and disadvantages of the FLS/LQG/LTR design methodology. As discussed above, the recovery of a target loop is asymptotic, so a high  $Q$  notch filter cannot be accurately recovered. This problem reduces the value of the recovery of a FW/LQ loop with a notch filter which would otherwise be a very attractive design approach. (If the depth and frequency of the notch are less critical, this could still be a valuable approach.) An attempt to recover a target loop that does not contain the low frequency gyro dynamics in an effort to achieve good low frequency loop shapes results in a compensator that cancels those low frequency gyro dynamics, making those modes unobservable in moment command output. The result for the gyro torque-rebalance loop design is that the pickoff angles are not driven back to null by the controller, which is unacceptable for accurate gyro operation. The designs presented are based on target loops that contain decoupled plant dynamics. The recovered loops succeed in decoupling the TITOBs torque-rebalance loop channels, but have slow time response characteristics compared to the other multivariable designs.

### 6.2.5 Summary

In terms of the ability of the design methodologies to directly satisfy the gyro torque-rebalance loop design requirements, the FW/LQG design methodology is clearly superior since the notch filter requirement can be included in the LQ loop. This methodology also provides excellent flexibility in shaping the LQ loop through reasonably straight forward modification of the weighting transfer functions to improve system time and frequency response. The frequency weighted estimator, discussed in Appendix C, could be employed with the FW/LQ design for additional design flexibility.

The LQG/LTR design methodology provides the easiest design approach, with the target loop design reduced to two parameters. The remainder of the design is simply recovery of the target loop to the desired bandwidth, trading off the good qualities of the target loop for high attenuation at high frequencies. Loop transfer recovery with formal loop shaping uses the recovery process to recover arbitrary loop shapes. This methodology offers the greatest flexibility in target loop design, and the designs presented here have only scratched the surface of what may be possible with this methodology. However, with both

LTR design methodologies, the notch filter requirement must be satisfied by augmenting the compensator with the notch filter after recovery, since a notch filter in the target loop may not be sufficiently recovered.

### 6.3 Conclusions and Recommendations

In this thesis multivariable design methodologies are used to design controllers for a two-degree-of-freedom dynamically tuned gyro torque-rebalance loop. The LQG/LTR, FW/LQG, and FLS/LQG/LTR multivariable design methodologies, in addition to classical first order lead compensation are applied to a gyro model described by complex coefficient differential equations. The maximum torque-rebalance loop bandwidth achievable with first order lead compensation is limited by the gyro nutation. For the gyro model considered, this imparts a practical bandwidth limit of about 50 Hz. All of the design methodologies are used to generate 50 Hz designs, and the multivariable design methodologies are also used to generate 100 Hz bandwidth designs. The performance and stability properties of the resulting designs are compared, as are the design methodologies themselves.

The multivariable design methodologies can be used to double the bandwidth achievable with classical means. A comparison of the performance of the designs shows that while the multivariable design methodologies out-perform classical lead compensation, none provides a clear performance advantage over the others. In terms of the ability of the design methodologies to produce compensators which satisfy the typical gyro torque-rebalance loop design requirements, the FW/LQG design methodology is superior. The LQG/LTR design procedure is probably the most straight forward, with the target loop design problem reduced to the selection of two scalar parameters. The FLS/LQG/LTR design methodology holds promise, but the best way to select target loops in this case is not clear.

There are several areas where further work could be performed. The performance of the FLS/LQG/LTR design methodology could be improved by finding improved target loops for the gyro torque-rebalance loop problem, only a few of which are presented in this thesis. Additional design methodologies could be compared. In particular,  $H_\infty$  optimization could be examined. It is expected that it would produce results similar to those of the FW/LQG design method-

ology.

Another area of interest is a type II torque-rebalance loop. The designs presented here are all type I, with the high bandwidth designs allowing a steady state error in pickoff angle of about  $3 \text{ arcsec}$  for a step input of  $100^\circ/\text{sec}^2$  in inertial angular acceleration. For some applications, this hang off error may be too large for accurate operation of the gyro and could be eliminated with a type II loop. For this gyro model, first order lead compensation cannot be used to stabilize a type II loop for useful bandwidths, so second order lead compensation or multivariable designs must be used.

Finally, since many torque-rebalance loops are implemented digitally, direct discrete time controller designs could be examined and compared to discretized versions of the continuous time designs described in this thesis.

## References

- [1] M. Athans, "Lecture Notes for Multivariable Control Systems II," January 1987.
- [2] M. Athans and G. Stein, "The LQG/LTR Procedure for Multivariable Feedback Control Design," *IEEE Transactions on Automatic Control*, vol. AC-32, pp. 105–114, February 1987.
- [3] D. E. Coffman, "Feasibility Study of a Digital Rebalance Loop for a Dry Tuned TDF Gyro," Scientific Report S-28, Dept. of Electrical Engineering, University of Tennessee, Knoxville, May 1974. NASA-CR-144089.
- [4] R. J. Craig, "Dynamically Tuned Gyros in Strapdown Systems," in *AGARD Conference No. 116 on Inertial Navigation Components and Systems*, February 1972.
- [5] R. J. Craig, "Theory of Errors of a Multigimbal, Elastically Supported, Tuned Gyroscope," *IEEE Transactions on Aerospace and Electronic Systems*, vol. AES-8, pp. 289–297, May 1972.
- [6] R. J. Craig, "Theory of Operation of an Elastically Supported, Tuned Gyroscope," *IEEE Transactions on Aerospace and Electronic Systems*, vol. AES-8, pp. 280–288, May 1972.
- [7] J. Doyle and G. Stein, "Multivariable Feedback Designs: Concepts for a Classical/Modern Synthesis," *IEEE Transactions on Automatic Control*, vol. AC-26, pp. 4–16, February 1981.
- [8] A. Gelb, ed., *Applied Optimal Estimation*. Cambridge, Ma.: MIT Press, 1986.
- [9] N. K. Gupta, "Frequency-Shaped Cost Functionals: Extension of Linear-Quadratic-Gaussian Design Methods," *AIAA Journal of Guidance and Control*, vol. 3, pp. 529–535, November 1980.

- [10] N. K. Gupta *et al.*, "Frequency-Shaping Methods in Large Space Structures Control," in *AIAA Guidance and Control Conference*, August 1981. paper no. 81-1783.
- [11] J. C. Hung, M. K. Kao, and E. H. Berry, "A Pseudo Root-Locus Method for the Design of a Class of Two-Input-Two-Output Systems," in *8th Annual Southeastern Symposium on System Theory*, pp. 264-268, April 1976.
- [12] B. G. Johnson, *Active Control of a Flexible, Two-Mass Rotor: The Use of Complex Notation*. PhD thesis, Massachusetts Institute of Technology, September 1986.
- [13] D. S. Lipman, "Application of the Complex Method to Transform Analysis of Spinning Systems With Rotating Nonsymmetries," in *Joint Automatic Control Conference*, June 1968.
- [14] P. H. Savet, "Dynamics of Ideal Suspensions Applied to Rotating Bodies in Space," in *AIAA 2nd Annual Meeting*, July 1965. paper no. 65-435.
- [15] Teledyne Systems Co., "Investigation of Application of Two-Degree-of-Freedom Dry Tuned-Gimbal Gyroscopes to Strapdown Navigation Systems," Final Report, Teledyne Systems Co., 1974. NASA-CR-132419.
- [16] M. Weinberg, "Wide Band DTG Control Loops," September 1982. CSDL Intralab Memorandum.



# Appendix A

## List of Symbols

Vectors are underlined, with lower case usually denoting vectors that are functions of time and upper case usually denoting vectors that are functions of the Laplace variable  $s$ . Scalars are usually lower case. Matrices are upper case.

### Operators

$\frac{d^a}{dt}()$	derivative with respect to time in frame a
$\det()$	determinant
$()^*$	complex conjugate
$()^T$	matrix transpose
$()^H$	complex conjugate transpose
$L\{\}$	Laplace transform
$L^{-1}\{\}$	inverse Laplace transform
$\times$	vector cross product
$  $	determinant or magnitude
$(\dot{\quad})$	derivative with respect to time
$(\hat{\quad})$	estimated value
$(\prime)$	(1) variable dimensioned in mV (2) discretized matrix
$\sigma_k\{\}$	singular value

### Subscripts

$c$	complex variable
$d$	variable associated with the demodulation filter
$i$	explicitly imaginary

$k$	one of a series
$n$	variable associated with the notch filter
$p$	variable associated with the plant model
$r$	explicitly real
$s$	strictly stable dynamics
$u$	variable associated with the FW/LQG control weighting function
$ws$	variable associated with the FLS/LQG/LTR strictly stable target dynamics
$x$	(1) $x$ -direction component (2) variable associated with the augmented plant model (design plant model)
$xs$	variable associated with the strictly stable dynamics of the design plant model
$y$	$y$ -direction component
$z$	(1) $z$ -direction component (2) variable associated with the FW/LQG state weighting function
$\Omega$	variable associated with the dynamics on the $j\omega$ -axis
$\theta$	variable associated with the CN/KF measurement noise shaping filter
$\xi$	variable associated with the CN/KF process noise shaping filter

### Superscripts

$i$	inertial reference frame
$c$	gyro case-fixed frame
$g$	gimbal-fixed frame
$n$	non-rotating rotor-fixed frame
$r$	rotor-fixed frame
$s$	shaft-fixed frame

### Variables

$a$	lead compensator zero location
$A$	state dynamics matrix
$b$	lead compensator pole location

$B$	control input matrix
$C$	system output matrix
$C_a^b$	direction cosine matrix relating the a-frame to the b-frame
$D$	control feed through matrix
$D_R$	gyro rotor viscous damping term
$f_n$	nutation frequency in $Hz$
$f_s$	rotor spin speed in $Hz$
$G$	feedback gain matrix
$G(s)$	transfer function
$G_c(s)$	explicitly complex coefficient transfer function
$G_{LQ}(s)$	linear quadratic regulator loop transfer function
$H$	Kalman filter gain matrix
$\underline{H}$	rotor angular momentum vector
$I$	identity matrix
$I_g$	gimbal moment of inertia
$I_{rr}$	rotor moment of inertia about its $x$ and $y$ -axes
$I_{rz}$	rotor moment of inertia about its $z$ -axis
$j$	$\sqrt{-1}$
$k_h$	LQ loop shaping parameter
$K$	(1) compensator Bode gain (2) suspension flexure torsional spring constant (3) block symmetric gain perturbation
$K(s)$	compensator transfer function
$K_L(s)$	lead compensator transfer function
$K_{MBC}(s)$	model based compensator transfer function
$K_{PO}$	pickoff gain
$K_T$	torquer gain
$K_v$	velocity error constant
$L_i(s)$	$i$ th noise or disturbance input matrix
$\underline{M}$	moment or torque applied to the rotor
$\underline{M}_c$	complex moment
$\underline{M}_s$	moment on rotor due to a physical suspension system
$N$	(1) auxiliary output matrix (2) number of encirclements of the $-1$ point
$N(s)$	FW/LQG state weighting transfer function

$N_R$	Nyquist contour
$P$	number of ORHP poles of $G_c(s)$
$P(s)$	FW/LQG control weighting transfer function
$Q_{uu}$	LQR control weighting matrix
$Q_{xu}$	LQR cross weighting matrix
$Q_{xx}$	LQR state weighting matrix
$s$	Laplace variable
$S$	LQR Riccati equation solution
$t$	time
$\underline{u}$	control variable
$u_{po}$	controller output
$u_{pi}$	control reference
$\underline{v}$	time correlated measurement noise
$\underline{v}_k$	$k$ th eigenvector
$\underline{w}$	time correlated process noise
$\underline{W}$	augmented white process noise
$\underline{x}$	generally complex state vector
$\underline{X}$	state vector augmented with weighting or shaping filter dynamics
$\underline{y}$	system output variable
$z_k$	$k$ th transmission zero
$Z$	number of closed loop ORHP poles of $G_c(s)$
$\gamma$	block symmetric phase perturbation
$\zeta_n$	nutation damping
$\underline{\theta}$	(1) pickoff angle (2) white measurement noise
$\underline{\theta}_c$	complex pickoff angle
$\Theta$	measurement noise intensity matrix
$\lambda_k$	$k$ th eigenvalue
$\mu$	scalar measurement noise intensity parameter
$\xi$	white process noise
$\Xi$	process noise intensity matrix
$\rho$	(1) LQR scalar control weighting parameter (2) FW/LQG scalar state weighting parameter
$\Sigma$	Kalman filter Riccati equation solution
$\tau$	gyro quadrature time constant

$\dot{\phi}$	inertial angular rate
$\underline{\varphi}$	attitude of the shaft relative to the rotor in the spinning coordinate frame
$\omega$	frequency in radians/second
$\omega_s$	gyro shaft (or rotor) spin frequency
$\underline{\omega}_{ab}^c$	angular rate of frame b with respect to frame a, written in frame c

# Appendix B

## Computer Software

The numerical analyses contained in this thesis were performed using the matrix and control analysis package `MATRIX $\chi$`  from Integrated Systems, Inc. Listings of `MATRIX $\chi$`  macros used in this thesis may be obtained from the author. The verification of many algebraic results and some analysis of complex matrices were performed using the symbolic manipulation program `MACSYMA`. The text of this thesis was formatted using the `LATEX` document preparation system.

# Appendix C

## Correlated Noise Kalman Filter Problem

The derivation of the Kalman filter dual to the frequency weighted linear quadratic regulator problem discussed in Section 5.5 is presented in this appendix. This Kalman filter problem corresponds to that for a plant driven by independent, time correlated process and measurement noise. The filter can also be used for the design of a class of compensators that is the dual of the FW/LQG compensator.

### C.1 Correlated Noise Kalman Filter Derivation

Consider the real, linear, time invariant, stochastic system

$$\dot{\underline{x}}(t) = A_x \underline{x}(t) + B_x \underline{u}(t) + L_x \underline{w}(t) \quad (\text{C.1})$$

$$\underline{y}(t) = C_x \underline{x}(t) + \underline{v}(t) \quad (\text{C.2})$$

where  $\underline{w}(t)$  and  $\underline{v}(t)$  are independent, Gaussian, time correlated noise processes, and  $\underline{u}(t)$  is a deterministic control input. The noise inputs are generated from Gaussian white noise by the shaping filters in Equations (C.3) and (C.4) and Equations (C.5) and (C.6).

$$\dot{\underline{x}}_\xi(t) = A_\xi \underline{x}_\xi(t) + L_\xi \underline{\xi}(t) \quad (\text{C.3})$$

$$\underline{w}(t) = C_\xi \underline{x}_\xi(t) + D_\xi \underline{\xi}(t) \quad (\text{C.4})$$

$$\dot{\underline{x}}_\theta(t) = A_\theta \underline{x}_\theta(t) + L_\theta \underline{\theta}(t) \quad (\text{C.5})$$

$$\underline{v}(t) = C_\theta \underline{x}_\theta(t) + D_\theta \underline{\theta}(t) \quad (\text{C.6})$$

The shaping filter inputs are the independent white noise processes  $\underline{\xi}(t)$  and  $\underline{\theta}(t)$ , which have intensities  $\Xi$  and  $\Theta$  respectively.

The plant dynamics are augmented with the shaping filter dynamics to form the system shown in Equations (C.7) and (C.8), where the deterministic input, which does not affect the solution to the problem, has been dropped.

$$\dot{\underline{X}}(t) = A\underline{X}(t) + L\underline{W}(t) \quad (\text{C.7})$$

$$\underline{y}(t) = C\underline{X}(t) + D_\theta \underline{\theta}(t) \quad (\text{C.8})$$

These equations are partitioned as

$$\begin{bmatrix} \dot{\underline{x}} \\ \dot{\underline{x}}_\xi \\ \dot{\underline{x}}_\theta \end{bmatrix} = \begin{bmatrix} A_x & L_x C_\xi & 0 \\ 0 & A_\xi & 0 \\ 0 & 0 & A_\theta \end{bmatrix} \begin{bmatrix} \underline{x} \\ \underline{x}_\xi \\ \underline{x}_\theta \end{bmatrix} + \begin{bmatrix} L_x D_\xi & 0 \\ L_\xi & 0 \\ 0 & L_\theta \end{bmatrix} \begin{bmatrix} \underline{\xi} \\ \underline{\theta} \end{bmatrix} \quad (\text{C.9})$$

$$\underline{y} = \begin{bmatrix} C_x & 0 & C_\theta \end{bmatrix} \begin{bmatrix} \underline{x} \\ \underline{x}_\xi \\ \underline{x}_\theta \end{bmatrix} + D_\theta \underline{\theta}. \quad (\text{C.10})$$

From Equations (C.9) and (C.10) it can be seen that the process noise of the augmented system,  $\underline{W}(t)$ , and the measurement noise,  $\underline{\theta}(t)$  are correlated,

$$\Gamma = E \{ \underline{W}(t) \underline{\theta}^T(\tau) \} = \begin{bmatrix} 0 \\ \Theta(t - \tau) \end{bmatrix}.$$

The process and measurement noises can be made to be uncorrelated by making use of the method in [8] of adding  $D(\underline{y}(t) - C\underline{X}(t) - D_\theta \underline{\theta}(t)) = 0$  to the right side of (C.7). The result is

$$\dot{\underline{X}}(t) = (A - DC) \underline{X}(t) + D\underline{y}(t) + (L\underline{W}(t) - DD_\theta \underline{\theta}(t)) \quad (\text{C.11})$$

where  $D\underline{y}(t)$  is a deterministic term, and  $L\underline{W}(t) - DD_\theta \underline{\theta}(t)$  is a new process noise. The parameter  $D$  is chosen to make the new process noise and the measurement noise uncorrelated,

$$E \{ [L\underline{W}(t) - DD_\theta \underline{\theta}(t)] \underline{\theta}^T(t) \} = 0$$

if

$$D = L\Gamma\Theta^{-1}D_\theta^{-1}.$$

The problem can now be solved by ordinary means. The steady state Kalman filter gains come from the Riccati equation

$$0 = A\Sigma + \Sigma A^T + \Xi_1 - (\Sigma C^T + \Gamma_1^T) \Theta_1^{-1} (\Gamma_1 + C\Sigma) \quad (\text{C.12})$$

$$H = (\Sigma C^T + \Gamma_1^T) \Theta_1^{-1} \quad (\text{C.13})$$



where

$$\begin{aligned}\Xi_1 &= \begin{bmatrix} L_x D_\xi \Xi D_\xi^T L_x^T & L_x D_\xi \Xi L_\xi^T & 0 \\ L_\xi \Xi D_\xi^T L_x^T & L_\xi \Xi L_\xi^T & 0 \\ 0 & 0 & L_\theta \Theta L_\theta^T \end{bmatrix} \\ \Gamma_1 &= \begin{bmatrix} 0 & 0 & D_\theta \Theta L_\theta^T \end{bmatrix} \\ \Theta_1 &= D_\theta \Theta D_\theta^T\end{aligned}$$

and  $H$  is partitioned as

$$H = \begin{bmatrix} H_x \\ H_\xi \\ H_\theta \end{bmatrix}.$$

The resulting filter equations are shown below, where the deterministic control input has been included.

$$\begin{aligned}\dot{\hat{\mathbf{x}}}(t) &= (A_x - H_x C_x) \hat{\mathbf{x}}(t) + L_x C_\xi \hat{\mathbf{x}}_\xi(t) - H_x C_\theta \hat{\mathbf{x}}_\theta(t) + H_x \underline{\mathbf{y}}(t) + \\ &\quad B_x \underline{\mathbf{u}}(t)\end{aligned}\tag{C.14}$$

$$\dot{\hat{\mathbf{x}}}_\xi(t) = A_\xi \hat{\mathbf{x}}_\xi(t) - H_\xi C_x \hat{\mathbf{x}}(t) - H_\xi C_\theta \hat{\mathbf{x}}_\theta(t) + H_\xi \underline{\mathbf{y}}\tag{C.15}$$

$$\dot{\hat{\mathbf{x}}}_\theta(t) = (A_\theta - H_\theta C_\theta) \hat{\mathbf{x}}_\theta(t) - H_\theta C_x \hat{\mathbf{x}}(t) + H_\theta \underline{\mathbf{y}}(t)\tag{C.16}$$

## C.2 The CN/KF Model Based Compensator

A feedback loop with a model based compensator based on the correlated noise Kalman filter is shown in Figure C.1. The process and measurement noise shaping filter dynamics as well as the plant dynamics appear in the compensator. The shaping filters can be used to model true noise inputs to the system, or they can be used to place the poles and zeros of the compensator. The gain  $G_x$  is a regulator state feedback gain matrix. In the setting of a standard LQG problem, a typical time domain weighted LQ regulator can be designed using the original plant dynamics,  $A_x$ , to place the regulator poles, and the shaping filters of the CN/KF problem can be used to model the actual process and measurement noise to obtain optimal estimates of the plant state.

A dual design procedure to the FW/LQG design methodology for the loop broken at the plant input is the use of the CN/KF shaping filters to shape the loop by including desired dynamics in the compensator. These shaping filters create correlated measurement and process noises in the same way that the weighting functions of the FW/LQ problem weight the states and controls as

functions of frequency. This CN/KF compensator has dual properties of the FW/LQ compensator. The poles of the measurement noise shaping filter are zeros of the compensator, and the poles of the process noise shaping filter are poles of the compensator. Also, the closed loop poles approach the zeros of both shaping filters. Therefore, the measurement noise shaping filter is the dual of the control weighting, and the process noise shaping filter is the dual of the state weighting. The LQ gain matrix,  $G_x$ , is then the solution to a time domain weighted linear quadratic regulator problem designed using the original plant dynamics,  $A_x$ , the input matrix,  $B_x$ , and output matrix,  $C_x$ . The poles of which are placed beyond the CN/KF loop crossover frequency.

Another possible compensator design combines the FW/LQ regulator with the CN/KF to achieve further flexibility in pole-zero placement. Some advantages of combining FW/LQ regulators with frequency based state estimators are discussed in [10].

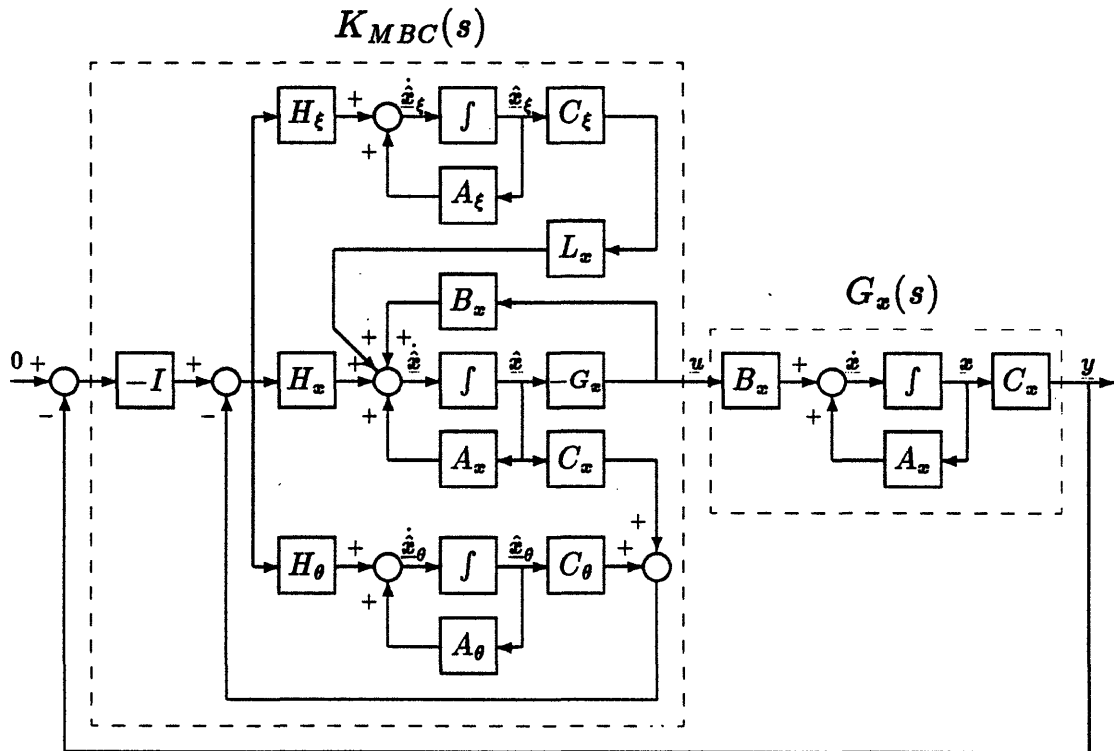


Figure C.1: CN/KF Feedback Loop Block Diagram

### C.3 Summary of Duality

The duality between the frequency weighted linear quadratic regulator and the correlated noise Kalman filter is summarized in Table C.1. The duality between the augmented systems for these frequency based problems is identical to the standard duality between the linear quadratic regulator and the Kalman filter problems, with the addition of the duality between the state-control cross weighting and the process-measurement noise cross correlation.

Table C.1: Duality Between the FW/LQ and the CN/KF Problems

FW/LQ	Duality	CN/KF
Augmented System Matrix	$A \Leftrightarrow A^T$	Augmented System Matrix
Augmented Input Matrix	$B \Leftrightarrow C^T$	Augmented Output Matrix
Control Weighting Matrix	$Q_{uu} \Leftrightarrow \Theta_1$	Measurement Noise Covariance
State Weighting Matrix	$Q_{xx} \Leftrightarrow \Xi_1$	Process Noise Covariance
Cross Weighting Matrix	$Q_{xu} \Leftrightarrow \Gamma_1$	Cross Correlation
Linear Quadratic Gain	$G \Leftrightarrow H^T$	Kalman Gain